PART I: ON THE STRUCTURE IN SEPARATRIX-SWEPT REGIONS OF SLOWLY-MODULATED HAMILTONIAN SYSTEMS
PART II: ON THE QUANTIFICATION OF MIXING IN CHAOTIC STOKES' FLOWS: THE ECCENTRIC JOURNAL BEARING

Thesis by

Tasso J. Kaper

In Partial Fulfillment of the Requirements

for the Degree of

Doctor of Philosophy

California Institute of Technology

Pasadena, California

1992

(Defended June 20, 1991)

Dedicated to Antonella and to my parents, Hans and Hillegonde

ACKNOWLEDGEMENTS

There are a number of people who have made these years as a graduate student rewarding. I thank my advisor Steve Wiggins for his guidance, which has enabled me to develop a firm foundation in the field of slowly-modulated Hamiltonian systems. He has allowed me a great deal of freedom to work on what interests me, and at the same time, has helped me to concentrate on completing my work. Over the course of two years, I enjoyed many conversations with Paco Lagerstrom about mathematics and classical music. In addition, at various stages Greg Forest, Darryl Holm, Gary Leal, and Tony Leonard have discussed various parts of my research. Their enthusiasm and patience has been a great source of encouragement for me.

I am very happy to have started a collaboration with David Bruhwiler in the last year and have learned a lot from him about separatrix-crossing orbits. Also, I wish to thank Howie Weiss for discussing the problem of persistence of hyperbolic sets in nonstationary systems.

I have learned a lot about myself and about others from Spyros Pandis. I am also fortunate that I got to know and work closely with my friends Gregor Kovacic and Roberto Camassa.

Finally, I would like to acknowledge generous financial support from the ONR and the NSF (via my advisor's ONR Young Investigator Award and PYI Award, respectively). In addition, part of this work was funded through the DOE while I worked at the CNLS in Los Alamos for one year.

Tot slot, bedank ik mijn familie, vooral opa en oma, pap en mam, en Bertrand, die ieder in hun eigen wijze mij geholpen hebben om beiden poten op de grond te houden. Io ringrazio anche Antonella per il suo amore e incorragiamento. Questa these e per lei.

ABSTRACT FOR PART I

In this work, we establish the structure of the large $\mathcal{O}(1)$-sized separatrix-swept regions in Hamiltonian systems which depend on a slow-varying parameter z: $H = H(p, q, z = \epsilon t)$, where $0 < \epsilon \ll 1$. These regions are complementary to those in which the theory of adiabatic invariance and Arnold's extension of the KAM Theorem to adiabatic systems apply. We prove the following theorem about the structure of lobes, which, being regions of phase space bounded by segments of intersecting stable and unstable manifolds terminating on principal homoclinic points, are the fundamental building blocks of homoclinic tangles. Theorem: The area of a lobe in (1.1) is: $A = \int_{Z_0}^{Z_1} M_A(z)dz + \mathcal{O}(\epsilon)$, where Z_0 and Z_1 are two adjacent simple zeroes of $M_A(z)$, the adiabatic Melnikov function of the system. We also derive a corollary: The area of a lobe in these systems is given to leading order by the difference between the areas enclosed by two sequential extremal instantaneous separatrices, Γ^{Z_0} and Γ^{Z_1}. The remaining terms are $\mathcal{O}(\epsilon)$. Theorem 1 and the corollary establish several important results: First, the area occupied by the homoclinic tangles formed by the intersection of the stable and unstable manifolds is $\mathcal{O}(1)$ to leading order. Second, Theorem 1 implies that the flux between regions separated by instantaneous separatrices is $\mathcal{O}(1)$ asymptotically, see Part II for an application. Third, for systems in which H depends periodically or quasiperiodically on z, Theorem 1 states that the region in which orbits evolve chaotically is $\mathcal{O}(1)$ in the limit of $\epsilon \to 0$. This result stands in marked contrast to the known examples of chaotic systems in which the "stochastic" regions are either of $\mathcal{O}(\epsilon)$ or $\mathcal{O}(\sqrt{\epsilon})$ and vanish as $\epsilon \to 0$. Finally, since islands must lie outside of the lobes, Theorem 1 shows that the phase space area in which islands must lie vanishes with ϵ as $\epsilon \to 0$. We remark that we lower the upper bounds on island size presented

in Elskens and Escande [1991] using asymptotic expansions of the exact resonance-zone area formula of MacKay and Meiss [1986]. We also derive an exact lobe area formula for general time-dependent Hamiltonian systems, which eliminates the need for the existence of a recurrent $p-q$ section in the extended phase space assumed in the previous work. A direct measurement of the type used on weakly-perturbed Hamiltonian systems is not possible in adiabatic systems since the pieces of stable and unstable manifold defining the boundary of the lobe cannot be expressed as graphs over the unperturbed separatrix. Therefore, the shape-independence of this exact formula is needed. We illustrate our results on the adiabatic pendulum: $H = \frac{p^2}{2} + (1 - \gamma \cos(z = \epsilon t)) \cos q$ and on a model due to Hastings and McLeod. Finally, for z-periodic H, we show for the first time in an example that a Smale horseshoe map can be created in one iteration of the Poincaré map.

Abstract for Part II

We study the transport of tracer dye in a low Reynolds number flow in the two-dimensional eccentric journal bearing. Modulation of the angular velocities of the cylinders continuously, slowly, and periodically in time causes the integrable steady-state flow to become nonintegrable. In stark contrast to the flows usually studied with dynamical systems, however, these slowly-varying systems are singular-perturbation problems in which the nonintegrability is due to the slow $\mathcal{O}(1)$ modulation of the position of the saddle stagnation point and the two streamlines stagnating on it. We establish an analytical technique to determine the location and size of the region in which mixing occurs. This technique gives us explicit control over the mixing process. We also develop a transport theory based on the lobes formed by the segments of stable and unstable manifolds of the fixed points of the Poincaré map, which are responsible for the transport of tracer in the mixing zone. In particular, we show that the radically different shape of these lobes, as compared to the shape of the lobes studied in the usual flows, readily makes them identifiable as the mechanism by which the modulation causes the patches of tracer to develop into elaborately striated and folded lamellar structures. When the modulation frequency is small we apply the tools developed in Part I to analytically predict several important quantities associated with the lobes and transport theory for the first time. From the measurement of these quantities, we determine the combination of the flow parameters with which one achieves the most efficient mixing possible. Furthermore, we use an extension of the KAM theory to explain the highly-regular appearance of islands in quasi-steady Stokes' flows for the first time. Finally, we we show that diffusion enhances stretching, discuss the robustness of our model by analyzing the influence of the inertial terms, and compare our results to those obtained experimentally using so-called blinking protocols.

TABLE OF CONTENTS

Abstract for Part I iv

Abstract for Part II vi

Table of Contents vii

List of Figures for Part I x

List of Figures for Part II xi

PART I. ON THE STRUCTURE OF THE SEPARATRIX-SWEPT REGIONS IN SLOWLY-MODULATED HAMILTONIAN SYSTEMS . . . 1

CHAPTER 1. Introduction 2

CHAPTER 2. Geometric and Analytic Structural Preliminaries 16

2.1 Geometry of the Perturbed System 18

2.2 The Adiabatic Melnikov Function 21

2.3 Behavior of the Derivatives of Solutions on Manifolds with Respect to ϵ 27

2.4 The Angle Between the Manifolds at h_0 30

CHAPTER 3. Lobe Area and the Proof of Theorem 1 36

3.1 Exact Action-Theoretic Formula for Lobe Area 36

3.2 Approximate Lobe Area 46

3.3 Asymptotic Accuracy of the Approximation 53

3.4 A Maximum Property for the Lobe Area 63

3.5 Action-Minimizing and Minimax Homoclinic Orbits 65

CHAPTER 4. Two Paradigm Problems in Adiabatic Chaos 67

4.1 The Adiabatic Pendulum 67

4.1.1 The Homoclinic Tangles of Adiabatic Systems 70

4.2 The Example of Hastings and McLeod 75

CHAPTER 5. On Obtaining Upper Bounds on the Size of Islands 82

APPENDIX A. New Technique for Generating the Unstable Manifolds in Singularly-Perturbed Systems Numerically 84

APPENDIX B. Use of Symplectic Integration Schemes for Stiff Non--Autonomous Systems 88

APPENDIX C. Derivation of $M_A(z)$ 90

APPENDIX D. Brief Review of Adiabatic Invariance Theory 93

REFERENCES 96

PART II. ON THE QUANTIFICATION OF TRANSPORT IN CHAOTIC STOKES' FLOWS: THE ECCENTRIC JOURNAL BEARING 101

CHAPTER 1. Introduction 102

CHAPTER 2. Transport Theory 111

2.1 Governing Equations and Modulation Protocols 111

2.2 Mixing Zone Location and Size 118

2.3 Transport Theory 135

2.3.1 Structures Governing Stretching and Transport 138

2.3.2 Transport in Intervals of Half Periods 148

2.3.3 Transport in Intervals of Unit Periods 155

2.3.4 Exponential Stretching of Material Interfaces and Lobes . . . 164

CHAPTER 3. Applications of Results from Adiabatic Dynamical Systems Theory 171

3.1 Analytical Estimates of Lobe Areas, Lengths, Stretching and the Average Striation Thickness 171

3.2 Chaotic Fluid Particle Motion 176

3.3 Regular Zones and Islands 179

CHAPTER 4. Robustness of the Model and Comparison to Experiment . 186

4.1 Inclusion of Molecular Diffusivity 186

4.2 Inclusion of Inertial Terms 191

4.3 Comparison to Results from Blinking Experiments 193

4.4 Rigorous Proof of the Statement that Quasi-steady Stokes' Flows Constitute Adiabatic Dynamical Systems 194

4.5 Application to Other Interesting Mixing Problems 198

APPENDIX A. The Stream Function Ψ 200

APPENDIX B. Asymptotic Expansion for $\gamma_\epsilon(z)$ 202

REFERENCES 204

LIST OF FIGURES FOR PART I

1.1 An orbit which may cross the separatrix. On top, $z = \pi$; on bottom $z = 0$. . 9

2.1 Geometry of the unperturbed system $(1.1)_0^z$ 19

2.2 Geometry of the perturbed system $(1.1)_\epsilon$ in $U \times \mathbb{R}$ 22

2.3 Measuring the distance for $M_A(z)$ 24

2.4 The angle α at h_0 31

3.1 Illustration of what is a pip 38

3.2 The lobe L^{PQ} 39

3.3 The strips Σ_T^S and Σ_{-T}^U for Theorem 1 43-44

3.4 The section Σ used to get the approximation A_0 47

3.5 The surfaces $\Omega^{\mathcal{P}}$ and $\Omega^{\mathcal{Q}}$. 55-56

4.1 Region A_S for pendulum with $\gamma = 0.75$ 71

4.2 Poincaré maps for the adiabatic pendulum $\epsilon = \frac{2\pi}{12}, \frac{2\pi}{20}, \frac{2\pi}{25}$ 72-74

4.3 Turnstile lobes and their first images in the adiabatic pendulum. 76

4.4 A horsehoe in one period 78-81

A.1 The segments of the unstable manifolds generated numerically 86

Table 4.1 Lobe area for various ϵ 69

List of Figures for Part II

2.1 Typical steady state counterrotating flow 114

2.2 The bipolar coordinate system 115

2.3 Potential mixing zone for various eccentricities and modulation protocols 121-123

2.4 Actual mixing zone with $\epsilon = \frac{2\pi}{50}$, $\bar{e} = 0.1$, $\bar{r} = 0.3$, (MP1) 124

2.5 Actual mixing zone $\epsilon = \frac{2\pi}{60}$ 129

2.6 Actual mixing zone with $\epsilon = \frac{2\pi}{120}$ 129

2.7 Actual mixing zone with $\epsilon = \frac{2\pi}{180}$ 131

2.8 Actual mixing zone with $\epsilon = \frac{2\pi}{40}$ 131

2.9 Actual mixing zone with $\epsilon = \frac{2\pi}{20}$ 132

2.10-2.13 More pictures of mixing zones 133-134

2.14 Typical unstable manifolds 139-141

2.15 The orbit $\gamma_\epsilon(z)$ for various ϵ 142

2.16 Segments of the stable and unstable manifolds and the region boundaries 144-146

2.17 The turnstile lobes and their intersections 149-152

2.18 Transport in half-period intervals 156-160

2.20 Basic and second Birkhoff signatures for the simple example of Chapter 2.3.4 167

3.1 The period of the steady state periodic orbits 184

3.2 Before the global bifurcation 185

4.1 The neighborhood $\mathcal{N}$ used in the diffusion example of Chapter 4. 189

Tables 2.1-2.5 Area of three domains, potential mixing zone area, and thickness of Σ_ϵ 169-170

PART I: ON THE STRUCTURE OF SEPARATRIX-SWEPT REGIONS IN SLOWLY-MODULATED HAMILTONIAN SYSTEMS

CHAPTER 1. INTRODUCTION.

In the first part of this thesis, we consider the dynamics of orbits in the separatrix-swept regions of slowly-modulated Hamiltonian systems which arise in many physical, chemical, and fluid mechanical applications. For simplicity of the presentation in this introduction, we begin by classifying six of the various types of orbits which exist in a prototypical slowly-modulated system, namely a slowly-modulated nonlinear pendulum, which we studied in Kaper and Wiggins [1991a]. This classification progresses from the fundamental periodic orbits of the slowly-modulated pendulum, through its quasiperiodic orbits, on to the special asymptotic orbits and the large classes of separatrix-crossing orbits that exist in this (and similar) problems. We use this progressive classification to lead the reader to consider the large, $\mathcal{O}(1)$-sized regions of the vector field (restricted to the $p-q$ components) in which orbits cross the slowly-varying separatrices. It is for these orbits and the structure of these regions that we present new results in Part I of this thesis. The main results we obtain, which are actually valid for a large class of slowly-modulated Hamiltonian systems where the modulation can have quite general time dependence, are presented after the classification for the pendulum, later in this introduction.

The Slowly-Modulated Pendulum.

For the standard nonlinear pendulum, the angle the pendulum makes with the vertical is the coordinate q. When the pendulum hangs vertically downward, it is at the stable equilibrium point $q = 0$; and, when it stands vertically upward it is at the unstable equilibrium point $q = \pi$. In addition to these stationary configurations, there are two types of periodic orbits the pendulum can execute. The pendulum either rotates (either clockwise or counterclockwise) so that q runs through the

angles $[0, 2\pi)$ every period or it oscillates periodically with $q \in [q_{\min}, q_{\max}] \subset [0, 2\pi]$ for all time. Finally, there are two orbits which take an infinite amount of time to depart from the unstable equilibrium and return to it. These correspond to the separatrices that connect $(p, q) = (0, \pi)$ and $(p, q) = (0, -\pi)$, and they constitute the boundary between the oscillatory and rotational regimes. These dynamics are all contained in the Hamiltonian for the standard nonlinear pendulum:

$$H(p, q) = \frac{p^2}{2} + 1 - \cos q,$$

and the phase portrait showing all of these features is well known. With out loss of generality we absorb the constant one in to H.

Now, for various reasons which we discuss later on in this introduction, we want to study the dynamics of a slightly more complicated pendulum. In the standard pendulum, the point from which the pendulum is suspended stays fixed. The complication we now add is to force the suspension point to move up and down an $\mathcal{O}(1)$ distance in a periodic fashion such that the frequency, ϵ, of this *periodic modulation* satisfies $0 < \epsilon \ll 1$. The Hamiltonian for this more complicated pendulum is:

$$H(p, q, \epsilon t) = \frac{p^2}{2} - g(\epsilon t) \cos q,$$

where $g(\epsilon t)$ is periodic in t with $\mathcal{O}(\frac{1}{\epsilon})$ period. For simplicity, we may assume that the amplitude of the potential energy $g(\epsilon t) > 0$ for all t, so that the sign of this term is determined solely by the function $\cos q$. We note that the possibility of g vanishing leads to interesting bifurcation questions which are beyond the scope of this work.

The dynamics of the modulated pendulum are much richer than those of the standard pendulum, due to the addition of the slow-time scale, which we denote $z = \epsilon t$. In order to discuss the different types of orbits which exist for these modulated

systems, we consider the system obtained from the following particular choice:

$$g(\epsilon t) = 1 - \gamma \cos(\epsilon t),$$

where the constant $\gamma \in (0, 1)$. This system, which we term the adiabatic pendulum, exhibits the same types of dynamics as many other slowly-modulated systems, although the details for a particular orbit, *e.g.*, the coefficients in a matched asymptotic expansion representation of the orbit, depend on the choice of $g(\epsilon t)$.

We now classify six of the different orbits which exist in this system.

First, as the suspension point moves slowly up and down, the two equilibrium positions become periodic orbits of the modulated system. In particular, the modulated system has one stable periodic orbit which corresponds to the pendulum always hanging straight down ($q = 0$); the other periodic orbit is unstable and corresponds to the pendulum always standing straight up ($q\pi$). We give references to the proofs of these statements for both this special periodic case and the general time-dependent case in Chapter 2. Although this unstable periodic orbit occurs with probability zero, it plays a central role in understanding the dynamics of many other orbits, as we will see further along in this classification and in the following chapters.

Second, the adiabatic pendulum possesses three large families of quasiperiodic orbits. The first of these families lies in the oscillatory region, inside the well of the slowly-modulating potential surrounding the stable periodic orbit identified above. The position and momentum coordinates of these orbits are confined to lie well within the intervals $(-\pi, \pi)$ and $(-\sqrt{1-\gamma}, \sqrt{1-\gamma})$, respectively. The other two families lie in the two rotational regions, one in the upper region where $p > \sqrt{1+\gamma}$, and the other in the lower region where $p < -\sqrt{1+\gamma}$. The existence of these families of quasiperiodic orbits has been established in at least three different ways:

constructing the series for the adiabatic invariant that Kruskal [1962] proved these orbits have; using Arnold's extension of the KAM Theorem to slowly-modulated systems which states that periodic orbits of the initial unmodulated system sufficiently far away from the separatrices persist under the modulation as invariant tori on which the orbits are quasiperiodic, see Arnold [1963]; or using the Kuzmak-Luke method, see for example Chapter 3.6 of Kevorkian and Cole [1981]. We return to these results and discuss why they cannot be used for orbits too near the separatrices when we list the fifth type of orbit. We also remark that for general periodic adiabatic Hamiltonian systems, the number and locations of these families depend on the details of the Hamiltonian.

Third, there are resonant subharmonic and superharmonic responses to the periodic modulation. The subharmonics are periodic orbits with a period equal to some integral multiple of the modulation period $T = \frac{2\pi}{\epsilon}$. In fact, subharmonics of all integral multiples exist, and they can rotate or oscillate. Realizing that the outer solution corresponds to when the orbit is near the unstable equilibrium and that the inner solution corresponds to when the pendulum swings from being near the unstable equilibrium through $q = 0$ and back again to being near the unstable equilibrium, *i.e.*, makes a near-separatrix excursion whose duration is $\mathcal{O}(\epsilon)$ in the slow time z, one can construct the subharmonic orbits using matched asymptotic expansions. The problem may be classified as a stiff, non-autonomous two-point boundary value problem. Furthermore, the subharmonics are either stable (locally elliptic) or unstable (locally hyperbolic) orbits. As we will see in Chapter 5, the orbit's action determines its stability, because the action measures whether the near-separatrix excursions from π to $-\pi$ (or, vice versa) occur near $z = 0$ or $z = \pi$. Recently, there have also been attempts to prove the existence of the orbits constructed by matched asymptotics using shooting methods; we refer the reader

to Hastings and McLeod [1991].

The superharmonics are also periodic orbits but have a period which is some rational fraction of T. Orbits of all rational fractional multiples exist. Since these orbits make more than one rotation or oscillation per period, one can construct them by matching the "middle" rotations or oscillations, which are farthest away from the unstable equilibrium and instantaneous separatrix, to an orbit obtained by adiabatic invariance theory (or the Kuzmak-Luke method), see Ockendon, *et al.* [1986] for an example. Again, action theory can be used to determine the orbit's stability type, and the value of the slow time z at which it makes its excursions.

The **fourth** type of orbit is quasiperiodic just as the second type. However, rather than lying on a persistent torus as the second type of orbits do, these quasiperiodic orbits are created in the same global bifurcation as the resonant elliptic periodic orbits and form a tube around them. One can establish their existence rigorously using the theory of the Birkhoff normal form. These families of quasiperiodic orbits make up the so-called island chains that lie in the middle of the stochastic- appearing separatrix-swept regions. These islands are most $\mathcal{O}(\epsilon)$ in size asymptotically, see Elskens and Escande [1991] and the implications of Theorem 1 below. We return to the topic of islands when we sharpen this upper bound on their size in Chapter 5.

Separatrix-Crossing Orbits.

Now that we have arrived at the **fifth** type of orbit in our classification, we can discuss some exciting, bounded, yet seemingly unpredictable orbits, namely separatrix-crossing orbits. We remark that we will shortly arrive at the end of the classification for the slowly-modulated pendulum when we discuss the sixth orbit type on the next page. We follow the evolution of a pendulum orbit with initial condition

$(p_0, q_0, z_0 = \pi)$ which lies on the instantaneous periodic orbit enclosing an area equal to $A_{\rm po}$, where $A_{\rm sep}^{\rm min} < A_{\rm po} < A_{\rm sep}^{\rm max}$. The first term, the action I of the orbit, in the series for the adiabatic invariant J, is exactly the area $A_{\rm po}$ enclosed by the instantaneous periodic orbit at $z = \pi$.

Adiabatic invariance theory states that, even though the path of the orbit may deform considerably, it will evolve in such a way that numerically J is equal to $A_{\rm po}$ to within $\mathcal{O}(\epsilon)$. Now, as the system evolves (*i.e.*, as z increases from π), the area enclosed by the instantaneous separatrix decreases. Hence, by our choice of $A_{\rm po}$, there exists a value of z, label it z_*, such that

1. $\pi < z_* < 2\pi$
2. $A_{\rm sep}(z_*) = A_{\rm po}$
3. $A_{\rm sep}(z) < A_{\rm po}$ for $z \in (z_*, \bar{z})$, where $\bar{z} = 4\pi - \bar{z}$.

Therefore, our orbit must have crossed the instantaneous separatrix near $z = z_*$ and changed type from being an oscillating pendulum to being a rotating pendulum, because there is no longer enough area inside the separatrices when $z > z_*$ for it to maintain its initial adiabatic invariant. Its adiabatic invariant also changed. We sketch the location of the initial condition and illustrate the above argument in Figure 1.1, where we acknowledge Bruhwiler [1990] for the idea of making this figure.

Besides illustrating why orbits must cross instantaneous separatrices, this example also identifies the fundamental problem of analyzing near-separatrix orbits. The ratio of successive terms in the series for J is $\frac{\epsilon}{\omega_0}$, which is $\ll 1$ if $\omega_0(I, z)$ is bounded away from zero uniformly in I and z. However, when an orbit gets too near an instantaneous separatrix, *i.e.*, when $\omega_0(i, z)$ is of the same order as ϵ for some z, then adiabatic invariance theory is no longer applicable. The Kuzmak-Luke method and Arnold's Theorem do not apply either, because the two time scales, which must

be asymptotically distinct for these methods to apply, are no longer separated. We recall that ω_0 decays logarithmically to zero as the separatrix is approached. Note that we briefly review the theory of adiabatic invariance in Appendix D.

The particular orbit we focused on above is not an isolated case. Rather, it is one of a large class of separatrix-crossing orbits, orbits not included in any of the previous types in our classification. One is lead to suspect that the class separatrix-crossing orbits is large simply because the difference between the areas enclosed by the maximum instantaneous separatrix and the minimum instantaneous separatrix is $\mathcal{O}(1)$. Recall for the pendulum that the value of p on the separatrix is $\sqrt{1-\gamma}$ at $z = 0$ and $\sqrt{1+\gamma}$ at $z = \pi$. As we will see shortly, the size of this separatrix-swept region is $\mathcal{O}(1)$ as $\epsilon \to 0$. Therefore, methods must be devised to understand these orbits. We also add a explanatory note here about the concept of instantaneous separatrices. These do not exist in the modulated system, rather they are the separatrices which one gets if one freezes the parameter z at its instantaneous value and then lets the system evolve in the steady state corresponding to that z value. Thus, they are a convenient, and commonly used, fiction.

There are two types of results, which are distinct yet complementary, one can obtain about separatrix-swept regions. First, one can seek representations for individual separatrix-crossing orbits. This goal has been pursued successfully using asymptotic matching analysis in action-angle coordinates, which is referred to as separatrix-crossing theory, see Cary, *et al.*, [1986], Cary and Skodje [1989], and Neishtadt [1986], or the concise review in Bruhwiler [1990]. Using this basis a description of large classses of these orbits in terms of a diffusion process has been made, see Bruhwiler and Cary [1989].

Second, one can try to determine the geometry of the invariant structures which govern the dynamics of the orbits in these regions. Although this second program

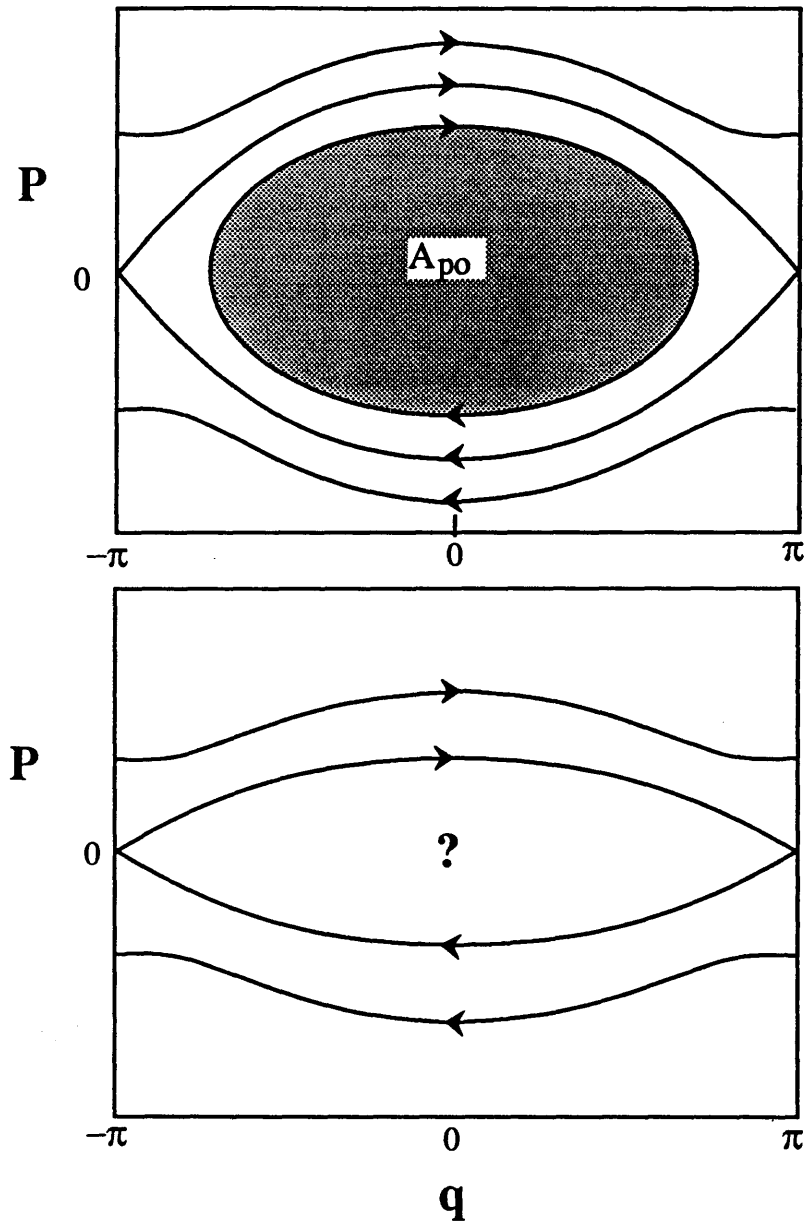

Fig. 1.1. A separatrix-crossing orbit. The instantaneous (or "frozen") portrait at $z = \pi \bmod 2\pi$ is in the top figure; and, the instantaneous (or "frozen") portrait at $z = 0 \bmod 2\pi$ is in the bottom figure. The orbit may have crossed an instantaneous separatrix, Υ^{z_*}, with $\pi < z_* < 2\pi$, because the area inside Υ^z for all $z_* < z < 4\pi - z_*$ is smaller than $A_{\rm po}$.

yields fewer details about each individual orbit, it provides important information about large classes of orbits, so many that they can not all be calculated individually using the first approach. We establish the global approach in this thesis for the first time.

The two principal governing structures are the homoclinic tangles formed by the **sixth** type of orbit in these systems and the families of quasiperiodic orbits, or "islands," created around resonant elliptic periodic orbits, see the fourth orbit type discussed above. The **sixth** orbit type comprises those which are backward and forward asymptotic in time to the main unstable periodic orbit (in which the pendulum is always standing up). Looking in the extended $p - q - t$ phase space, the union of all of the orbits forward asymptotic to this periodic orbit constitutes a two-dimensional surface which we refer to as its stable manifold. Similarly, the union of all of the orbits backward asymptotic to this periodic orbit constitutes a two-dimensional surface which we call its unstable manifold. Due to the local hyperbolic structure of this unstable periodic orbit, each of these manifolds has two branches. We analyze the geometry exactly in Chapter 2. The case which is of most interest in the applications is when the branches of the stable and unstable manifolds intersect, because the intersection implies the existence of orbits which are biasymptotic to the hyperbolic periodic orbit corresponding to the pendulum always standing straight up. These biasymptotic orbits have asymptotic phase.

Having discussed six different types of orbits which exist in this pendulum example, we now stop our classification. We turn our attention to general slowly-modulated systems with Hamiltonian $H = H(p, q, z = \epsilon)$, in which H is not necessarily periodic in z.

Main Results for General Slowly-Modulating Systems.

We now present the main results of Part I of this thesis. The equations of motion of the general slowly-modulated Hamiltonian systems we consider are:

$$\begin{aligned} \dot{q} &= \frac{\partial H}{\partial p}(p,q,z) \\ \dot{p} &= -\frac{\partial H}{\partial q}(p,q,z) \\ \dot{z} &= \epsilon, \end{aligned} \tag{1.1}_\epsilon$$

where $p, q, z \in \mathbb{R}$ and $0 < \epsilon \ll 1$. Assuming that H is at least C^3 and that $(1.1)_0$ has one hyperbolic fixed point for every value of z with a homoclinic orbit, Υ^z, attaching it to itself, we prove the following theorem about the structure of lobes, which, being regions of phase space bounded by segments of intersecting stable and unstable manifolds terminating on principal homoclinic points, are the fundamental building blocks of homoclinic tangles:

Theorem 1. *The area of a lobe in* $(1.1)_\epsilon$ *is:*

$$A = \int_{Z_0}^{Z_1} M_A(z)dz + \mathcal{O}(\epsilon), \tag{1.2}$$

where Z_0 *and* Z_1 *are two adjacent simple zeroes of* $M_A(z)$*, the adiabatic Melnikov function of* $(1.1)_\epsilon$ *which we define below.*

We prove this theorem in Chapter 3 and remark that it appears in Kaper and Wiggins [1991b]. From the proof of Theorem 1 we derive a maximum property for the lobe area:

Corollary. *The area of a lobe in* $(1.1)_\epsilon$ *is given to leading order by the difference between the areas enclosed by two extremal instantaneous separatrices,* Υ^{z_0} *and* Υ^{z_1}*, where* Z_0 *and* Z_1 *are two adjacent simple zeroes of* $M_A(z)$*. The remaining terms are* $\mathcal{O}(\epsilon)$*.*

We remark that Υ^{z_0} and Υ^{z_1} are such that none of the instantaneous separatrices Υ^z with $z \in (z_0, z_1)$ are extremal.

Theorem 1 and the corollary establish several important results:

First, Theorem 1 and the corollary establish that the area occupied by the homoclinic tangles formed by the intersection of the stable and unstable manifolds is $\mathcal{O}(1)$ to leading order, since $M_A(z) = \mathcal{O}(1)$ for all $z \in \mathbb{R}$ and lobes are the fundamental building blocks of the homoclinic tangles. The stable and unstable manifolds therefore form a "backbone" for this $\mathcal{O}(1)$-sized region.

Second, Theorem 1 implies that the flux between regions separated by instantaneous separatrices is $\mathcal{O}(1)$ asymptotically, because lobe area is the fundamental unit of flux in separatrix-crossing transport theories used in the applications, which are often referred to as "lobe-dynamics" theories, see Rom-Kedar and Wiggins [1990b]. For example, in Part II of this thesis, we have used it to make many quantitative predictions about the mixing and transport properties of low Reynolds number fluid flows which were previously only available through extensive experiments or numerical simulations.

Third, for systems in which H depends periodically or quasiperiodically on z, the criterion for the existence of Smale horseshoes in the separatrix– swept regions is established in Wiggins [1988b] using an extension of Melnikov's method to adiabatic systems and the Smale-Birkhoff Homoclinic Theorem. Thus, Theorem 1 states that the region in which orbits evolve chaotically is $\mathcal{O}(1)$ in the limit of $\epsilon \to 0$. This result stands in marked contrast to the known examples of chaotic systems in which the "stochastic" regions are either of $\mathcal{O}(\epsilon)$ or $\mathcal{O}(\sqrt{\epsilon})$ and vanish as $\epsilon \to 0$. The essential reason for this difference is that $(1.1)_\epsilon$ is a singularly-perturbed system, whereas the usual systems are regular perturbations.

Finally, as is discussed in Elskens and Escande [1991], islands must lie outside of the lobes. Hence, Theorem 1 shows that the phase space area in which islands must lie vanishes with ϵ as $\epsilon \to 0$. In these singularly-perturbed systems it appears to be

much easier to estimate the size of islands than it is in the case of the standard map or regularly-perturbed Hamiltonian systems. We remark that we refine the upper bounds presented in Elskens and Escande [1991] using asymptotic expansions of the exact resonance-zone area formula of MacKay and Meiss [1987] for the island size in Chapter 5.

Before proving Theorem 1, we step back from focusing on adiabatic systems and derive an exact lobe area formula for general time-dependent Hamiltonian systems, see Theorem 2 in section 2. This result gives the area of a lobe independently of its shape in terms of the difference in the actions of two distinguished homoclinic orbits. It was motivated by the formula for time-periodic Hamiltonians first derived by MacKay and Meiss [1986] and eliminates the need for the existence of a recurrent $p - q$ section in the extended phase space assumed in the previous work. The shape-independence of the exact result from Theorem 2 is necessary for establishing Theorem 1. A direct measurement of the type used on weakly-perturbed Hamiltonian systems is not possible in adiabatic systems since the pieces of stable and unstable manifold defining the boundary of the lobe cannot be expressed as graphs over the unperturbed separatrix. This difficulty, observed for the first time numerically on the adiabatic pendulum: $H = \frac{p^2}{2} + (1 - \gamma \cos(z = \epsilon t)) \cos q$, see Elskens and Escande [1991] and Kaper and Wiggins [1991a] and the references there, in large part motivated this work. To be precise, it was observed that the lobe area in this example is to leading order the difference between the areas enclosed by the maximal and minimal instantaneous separatrices and, which is the same, the integral of $M_A(z)$ between two consecutive zeroes.

Then the proof of Theorem 1 consists of two steps. First, since we know of no way to evaluate the exact formula in closed form, we develop an approximation using the adiabatic Melnikov function, which gives the leading order term in (1.2).

Second, we prove rigorously that the error made in this approximation vanishes asymptotically with ϵ as $\epsilon \to 0$. This second step constitutes the main difficulty of proving the theorem and relies on measuring the flux of $(1.1)_\epsilon$ through surfaces spanned by special homoclinic orbits of the intermediate systems $H = H(p, q, z = \mu\epsilon t)$, where $\mu \in [0, 1]$.

Part I of this thesis is organized as follows. In Chapter 2 we analyze the geometry of the stable and unstable manifolds. In Chapter 3, we derive the exact action-based lobe area result, prove Theorem 1, and establish a maximal property for lobe area. In Chapter 4, we give two examples, one is the adiabatic pendulum already introduced here, and the other is an equation due to Hastings and McLeod [1991]. Finally, we present new (sharper) upper bounds on the size of islands in these systems in Chapter 5.

Before embarking on Chapter 2, we make three remarks.

Remark 1. With regard to the chaotic orbits in z-periodic H, we show in Chapter 4 for the first time that a Smale horseshoe map is created in one iteration of the Poincaré map of the slowly-varying oscillator. We discuss the orbits that exist in the Smale horseshoe. It is an open problem whether some of the periodic orbits constructed with matched asymptotic expansions are the same or different from the hyperbolic periodic orbits in a horseshoe, see Hastings and McLeod [1991] and Kaper and Wiggins [1991c]. Also, the horseshoe gives the existence of infinitely many bounded, non-periodic orbits. Therefore, one is led to ask: Are these separatrix-crossing orbits of the fifth type in our scheme? or are they different? Finally, a kneading theory, relying on the ordering-property of the line (the q-axis, on which the initial conditions in the equations of Hastings and McLeod [1991] lie, for example), has been developed in Hastings and McLeod [1991]. Can the this be used to further classify separatrix-crossing orbits? We list a number of other open

questions in Kaper and Wiggins [1991c].

Remark 2. Elskens and Escande [1991] have simultaneously and independently established a result related to our corollary using the WKB method and the asymptotic results of separatrix-crossing theory, by defining a "crossing-ribbon" and then using it to estimate lobe area. Their result is a formal one, and it is somewhat weaker than ours because they calculate that the remainder terms are $\mathcal{O}(\epsilon^{\frac{2}{3}-a})$ for some $a > 0$, whereas we prove rigorously that they are $\mathcal{O}(\epsilon)$. Furthermore, they do not discuss the role of the adiabatic Melnikov function in these results, and $M_A(z)$ makes *a priori* verification of the existence of these $\mathcal{O}(1)$ tangles possible using only information from the reduced (unperturbed) system.

Remark 3. The use of perturbation theory to approximate the exact, action-based formula was first made in MacKay and Meiss [1988] in the context of weakly-perturbed, time-periodic Hamiltonian systems: $H = H_0(p,q) + \delta H_1(p,q,t)$, where $0 < \delta \ll 1$. They showed that lobe area is given to leading order by integrating the usual Melnikov function between two adjacent zeroes. The fact that the remaining terms are of higher order was established for time-periodic H_1 in Rom-Kedar and Wiggins [1990] using a direct measurement on the Poincaré map and for general time-dependent H_1 in Kovacic [1991] using action theory as in MacKay and Meiss [1988], which was inspirational for our work.

CHAPTER 2. GEOMETRIC AND ANALYTIC STRUCTURAL PRELIMINARIES.

In this chapter we identify the geometrical structures of adiabatic systems which are essential to Theorem 1. We have already identified these structures in the introductory chapter as being the hyperbolic orbit (along which the flow is slow) and the two-dimensional surfaces spanned by orbits which are either forward or backward asymptotic to it (the stable and unstable manifolds). However, we want to make the necessary statements mathematically precise, and so we spend a few pages doing so in the beginning of this chapter and in Section 2.1.

Next, we briefly review the theory of the adiabatic Melnikov function in Section 2.2. The adiabatic Melnikov function constitutes a tool with which one can detect the existence of lobes and homoclinic tangles based exclusively on information about the unmodulated system. We relegate its derivation to Appendix C.

We do, however, give an alternative derivation of $M_A(z)$ in Section 2.2, different from that reviewed in Appendix C. This alternative definition shows that $M_A(z)$ is equivalent to the closure condition on the energy modulation equation for these systems, *i.e.*, a Fredholm Alternative solvability condition for this equation in the hierarchy of perturbation equations for a homoclinic orbit.

Finally, in Section 2.3, we establish analytically a technical result which we need concerning the asymptotic ($t \to \pm\infty$) behavior of the derivatives of solutions on the stable and unstable manifolds of the hyperbolic orbit with respect to ϵ.

We begin by stating precisely the assumptions we make on $(1.1)_\epsilon$. As stated in Chapter 1, these assumptions are minimal and are satisfied by most physical systems with an unstable equlibrium. For convenience we recall the equations governing

adiabatic systems:

$$\dot{q} = \frac{\partial H}{\partial p}(p, q; z)$$
$$\dot{p} = -\frac{\partial H}{\partial q}(p, q; z)$$
$$\dot{z} = \epsilon.$$

H is defined for all (p, q) in a large open subset $U \subset \mathbf{R}$ and for all $z \in \mathbf{R}$. We assume

Assumption A1. *$H(p, q, z)$ is C^r, with $r \geq 2$, and that H and all of its first and second derivatives are uniformly bounded in $U \times \mathbf{R}^2$.*

We pick the solution parametrizing an orbit by setting $z = \epsilon t$, a convention we use throughout this thesis because it is consistent with our definition of action. We refer to $(1.1)_\epsilon$ as the perturbed system. We denote the unperturbed systems, $(1.1)_\epsilon$ with $\epsilon = 0$ and $z = z_0$ fixed, by $(1.1)_0$. The time variable of $(1.1)_0$ is s and $'$ indicates a derivative with respect to s. We use s for the time of the unperturbed system to distinguish it from t, that of the perturbed system.

We make the following structural assumptions on $(1.1)_0$:

Assumption A2. *For every $z \in \mathbf{R}$ the autonomous planar system $(1.1)_0^z$ possesses a hyperbolic fixed point, $X_0^z = (p_0^z, q_0^z)$, which varies smoothly with z and which is connected to itself by a nontrivial homoclinic orbit, Υ^z, lying in U. Furthermore, the set of points X_0^z is uniformly bounded in U for all $z \in \mathbf{R}$ and is uniformly hyperbolic.*

Thus $(1.1)_0^z$ has a one-dimensional hyperbolic invariant manifold,

$$\gamma \equiv \cup_{z \in \mathbf{R}} (p_0^z, q_0^z, z),$$

which is of course just a line of unstable fixed points. We remark that eventhough we also use γ to denote a constant in the adiabatic pendulum example, the context

will always make it clear as to its meaning. In fact, in Chapters 2 and 3, it will always refer to the hyperbolic invariant manifold. We use the homoclinic orbit $(p_0^z(-s_0), q_0^z(-s_0))$ to parametrize Υ^z. We call the point $(p_0^z(0), q_0^z(0))$ on Υ^z the reference point. Furthermore, A2 implies that γ has two-dimensional stable and unstable manifolds which coincide in a homoclinic manifold, $\Gamma \equiv \cup_{z\in\mathbf{R}}(\Upsilon^z, z)$. We refer the reader to Figure 2.1 for an illustration of the unperturbed geometry.

Remark. The assumption A2 is made for simplicity of the analysis. If a planar autonomous Hamiltonian system of the form $(1.1)_0^z$ possesses more than one homoclinic orbit our method can be applied to each isolated one separately, or if it has a heteroclinic orbit then our technique can be applied to it directly, as well.

Furthermore, we suppose:

Assumption A3. *The adiabatic Melnikov function for* (1.1), *which we state below, has at least two distinct simple zeroes.*

We now turn our attention to the geometry of the perturbed system.

2.1 Geometry of the Perturbed System

Assumption A2 allow us to use the theory presented in Sakamoto [1990] and Kaper [1991] (or in the special case in which H depends periodically or quasiperiodically on z, the theory presented in Fenichel [1979] and reviewed in Wiggins [1988]) and conclude:

Theorem 2. *There exists a hyperbolic orbit, γ_ϵ, in $(1.1)_\epsilon$ for ϵ sufficiently small. This orbit is C^{r-1} smooth with respect to p, q, z and ϵ and is $C^{r-1} - \mathcal{O}(\epsilon)$ close to γ. Moreover, $W^S_{\text{loc}}(\gamma_\epsilon)$ and $W^U_{\text{loc}}(\gamma_\epsilon)$ are $C^{r-1} - \mathcal{O}(\epsilon)$ close to $W^S_{\text{loc}}(\gamma)$ and $W^U_{\text{loc}}(\gamma)$, respectively.*

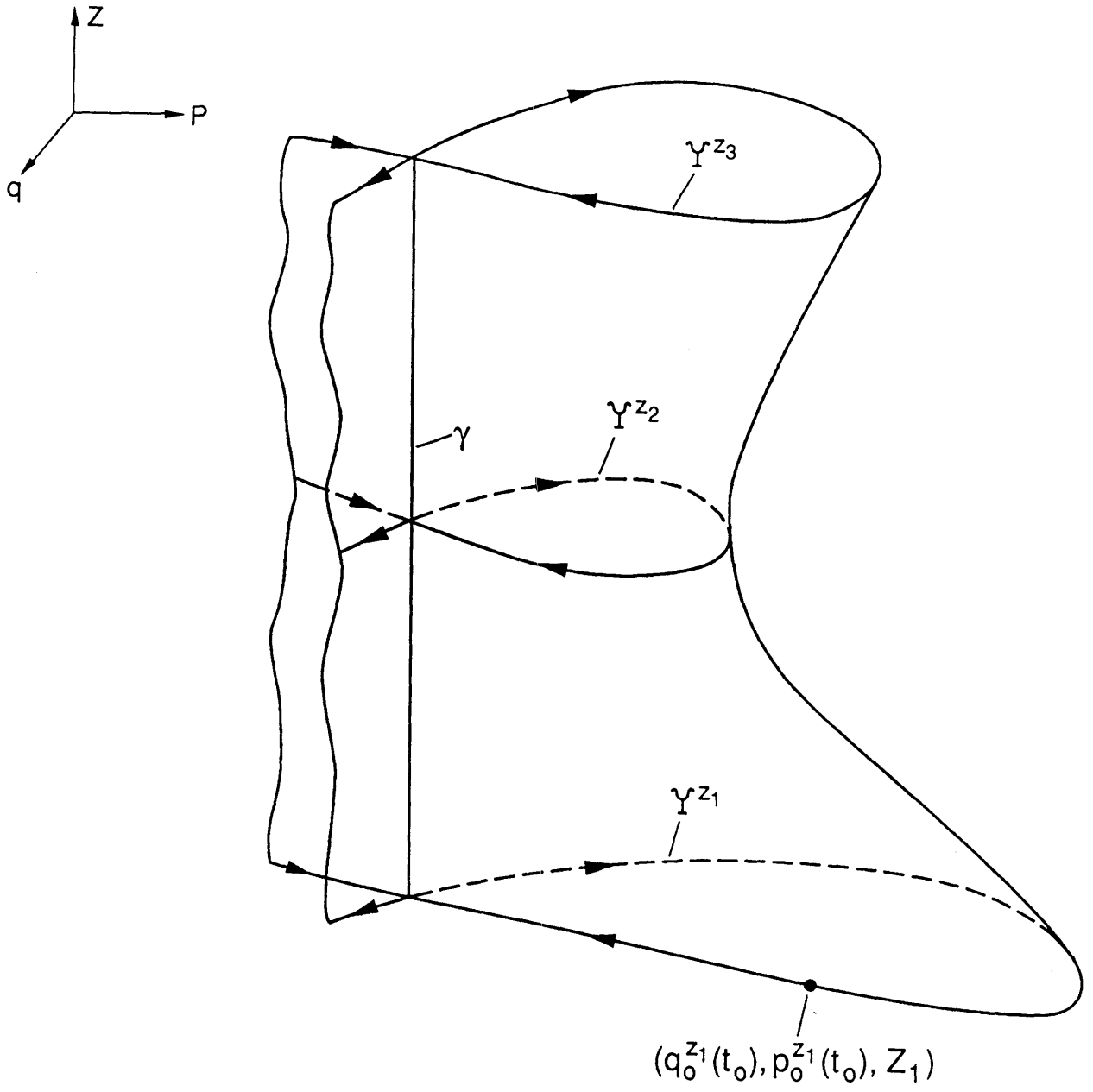

Fig. 2.1. The geometry of the unperturbed system $(1.1)_0$ in the extended $p-q-z$ phase space.

Furthermore, the perturbed manifolds are actually C^r if γ is compact. The proof of this theorem states that solutions on these manifolds converge exponentially to γ_ϵ as $t \to \pm\infty$, and the rates of contraction are bounded away from zero and attributes to γ_ϵ the properties listed below.

Let $X_t \in U$ be the unique intersection point of γ_ϵ and Π_t, the plane $t = \text{const.}$ Also, for any $\rho > 0$, let $D_\rho(X_t) \subset U$ be the disk of radius ρ around X_t, and let $V_\rho(\gamma_\epsilon)$ be the tubular neighborhood of γ_ϵ: $V_\rho(\gamma_\epsilon) \equiv \bigcup_{t\in\mathbb{R}}(D_\rho(X_t), t)$. Hyperbolicity of γ_ϵ implies that for some $\rho > 0$, there exist two-dimensional manifolds $W^S_{\text{loc}}(\gamma_\epsilon)$ and $W^U_{\text{loc}}(\gamma_\epsilon)$ in $V_\rho(\gamma_\epsilon)$ and a positive constant c bounded away from zero such that:

i) $W^S_{\text{loc}}(\gamma_\epsilon)$ (respectively $W^U_{\text{loc}}(\gamma_\epsilon)$), the local stable (unstable) manifold of γ_ϵ, is invariant under the forward (backward) time evolution of (2.1);

ii) $W^S_{\text{loc}}(\gamma_\epsilon)$ and $W^U_{\text{loc}}(\gamma_\epsilon)$ intersect along γ_ϵ, and the angle between the manifolds (defined in terms of the normals to the manifolds) at any point X_t is bounded away from zero uniformly for all $t \in \mathbb{R}$;

iii) every trajectory on $W^S_{\text{loc}}(\gamma_\epsilon)$ (respectively $W^U_{\text{loc}}(\gamma_\epsilon)$) can be continued to the boundary of $V_\rho(\gamma_\epsilon)$ in backward (forward) time;

iv) trajectories starting on $W^S_{\text{loc}}(\gamma_\epsilon)$ (respectively $W^S_{\text{loc}}(\gamma_\epsilon)$) at time $t = t_0$ approach γ_ϵ exponentially in forward (backward) time, $e^{-c|t-t_0|}$;

v) all other trajectories in $V_\rho(\gamma_\epsilon)$ not on either $W^S_{\text{loc}}(\gamma_\epsilon)$ or $W^U_{\text{loc}}(\gamma_\epsilon)$ must leave $V_\rho(\gamma_\epsilon)$ in both forward and backward time.

Remark. Properties **ii)** and **iii)** stem from the uniform hyperbolicity of γ. The exponential contraction listed as property **iv)** is exploited in Chapter 3 and in Section 2.3. For the general theory of hyperbolic orbits (or, more generally, of normally-hyperbolic invariant manifolds) we refer the reader to the following sources: Fenichel [1979] and wiggins [1988] (with Lyapunov type numbers), Coppel [1978], Sakamoto

[1990], and Sell [1978] (with exponential dichotomies), and Hirsch *et al.* [1983] (with hyperbolic splittings).

Also, the global stable and unstable manifolds, $W^S(\gamma_\epsilon)$ and $W^U(\gamma_\epsilon)$, are obtained from the local ones by letting the orbits on them evolve in backward and forward time, respectively. Of course, $W^S(\gamma_\epsilon)$ and $W^U(\gamma_\epsilon)$ will in general not coincide. Instead, we expect them to intersect along isolated orbits. We refer the reader to Figure 2.2 for an illustration of the geometry of the perturbed system.

The existence of these intersection orbits is implied by A3. We turn now to the implications of A3 and define the adiabatic Melnikov function.

2.2. The Adiabatic Melnikov Function.

In this section, we briefly review the theory of the adiabatic Melnikov function. More importantly, we give an alternative derivation of it in order to illustrate that it is equivalent to the closure condition on the energy modulation equation.

Geometrically the adiabatic Melnikov function is the first term, up to a normalization factor, of a Taylor expansion of the distance between the stable and unstable manifolds of a hyperbolic orbit along the normal to the separatrix, Υ^z, of $(1.1)_0^z$, as measured at the reference point $(p_0^z(0), q_0^z(0))$. A zero of the adiabatic Melnikov function corresponds to a principal intersection of the stable and unstable manifolds of a hyperbolic orbit. Now the reason for making Assumption A3 is clear, because we need two principal intersections to define a lobe, as we will show in Chapter 3.

Define $\mathbf{f} \equiv \left(\frac{\partial H}{\partial p}, -\frac{\partial H}{\partial q}\right)$. Let $\mathbf{X}_0^z$ denote the hyperbolic fixed point on Π_z of the unperturbed system in $p-q-z$ space. The orbit $\mathbf{q}_0^z(-t_0) = (p_0^z(-t_0), q_0^z(-t_0))$ is homolinic to $\mathbf{X}_0^z$; we use it to paramatrize Γ^z. The normal to Γ^z on Π_z is $\mathbf{n}(t_0, z) = \mathbf{f}^\perp(\mathbf{q}_0^z(-t_0), z)$. In the rest of this section we need the normal, $\mathbf{n}(0, z)$, to Γ^z at the reference point $\mathbf{q}_0^z(0)$.

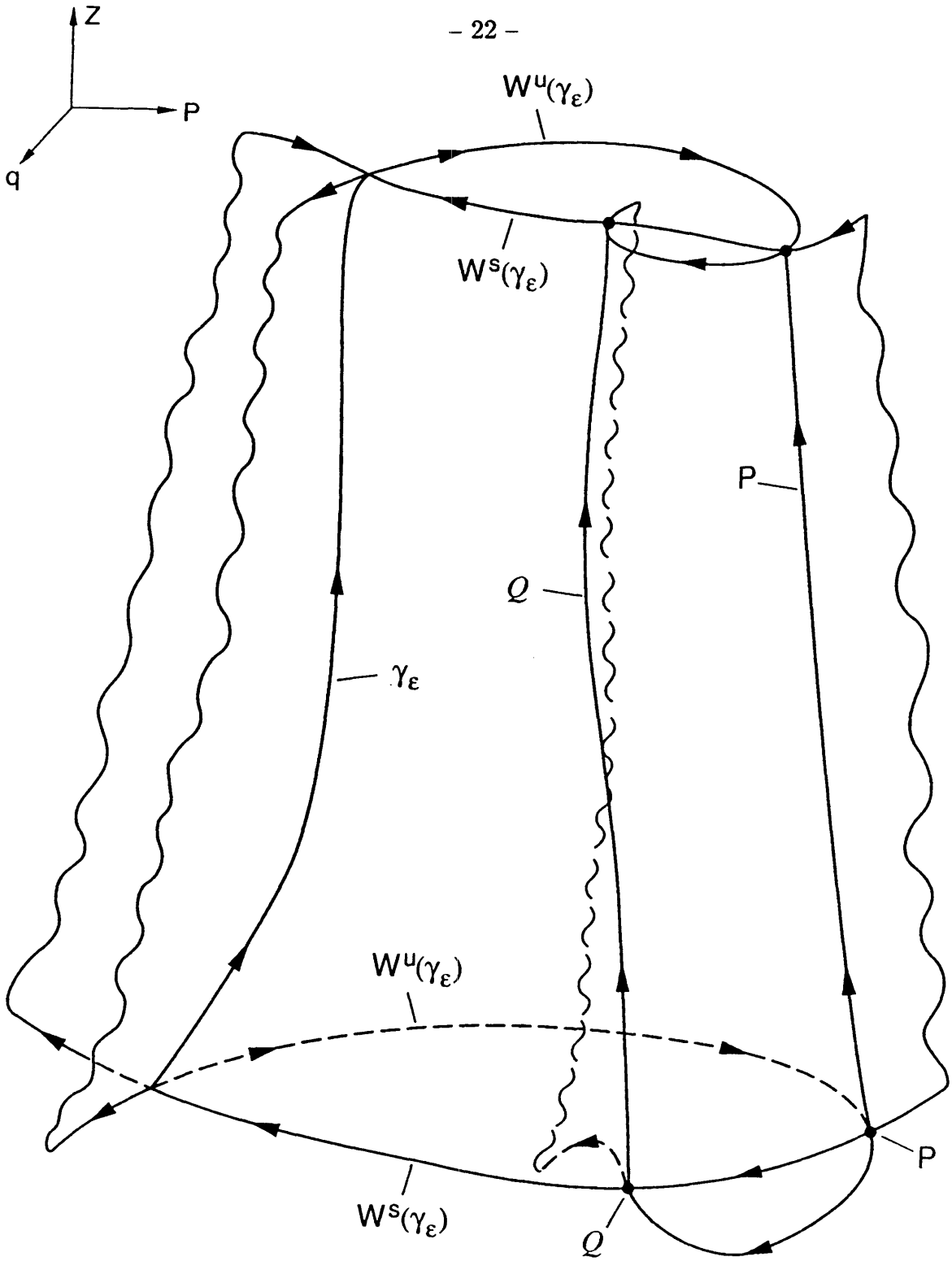

Fig. 2.2. Geometry of the perturbed system $(1.1)_\epsilon$ in the extended $p-q-z$ phase space.

Let $\mathbf{q}_\epsilon^S(0,z;0)$ and $\mathbf{q}_\epsilon^U(0,z;0)$ be solutions on $W^S(\gamma_\epsilon)$ and $W^U(\gamma_\epsilon)$, respectively, which cross $\mathbf{n}(0,z)$ at time $t=0$ closest to γ_ϵ in time-of-flight. The geometry is illustrated in Figure 2.3. The signed distance between $\mathbf{q}_\epsilon^S(0,z;0)$ and $\mathbf{q}_\epsilon^U(0,z;0)$ is given by

$$d(z;\epsilon) = \frac{\mathbf{f}(\mathbf{q}_0^z(0),z) \wedge (\mathbf{q}_\epsilon^U(0,z;0) - \mathbf{q}_\epsilon^S(0,z;0))}{\|\mathbf{f}(\mathbf{q}_0^z(0),z)\|}. \tag{2.1}$$

Asymptotically as $\epsilon \to 0$:

$$\begin{aligned} d(z;\epsilon) &= \epsilon \frac{\mathbf{f}(\mathbf{q}_0^z(0),z) \wedge \left(\frac{\partial \mathbf{q}_\epsilon^U}{\partial \epsilon}(0,z;0)|_{\epsilon=0} - \frac{\partial \mathbf{q}_\epsilon^S}{\partial \epsilon}(0,z;0)|_{\epsilon=0}\right)}{\|\mathbf{f}(\mathbf{q}_0^z(0),z)\|} + \mathcal{O}(\epsilon^2) \\ &\equiv \epsilon \frac{M_A(z)}{\|\mathbf{f}(\mathbf{q}_0^z(0),z)\|} + \mathcal{O}(\epsilon^2) \end{aligned} \tag{2.2}$$

In Appendix A, we give a fairly standard derivation of the following computable expression for $M_A(z)$:

$$M_A(z) = \int_{-\infty}^{\infty} t\{H, \frac{\partial H}{\partial z}\}(\mathbf{q}_0^z(t))\, dt. \tag{2.3}$$

In the derivation there, we follow Robinson [1983] and Wiggins [1988] in several places and also use the result of Lemma 2.1 given in the next section. See also Palmer [1986] and Neishtadt [1975]. We remark that we always measure along $\mathbf{n}(0,z)$ so that our derivation of $M_A(z)$ applies to all systems $(1.1)_\epsilon$, which is a point misunderstood in Elskens and Escande [1991].

Here, however, we give an alternative derivation of $M_A(z)$. We stated the reason for wanting to give this above. We show

$$M_A(z) = \int_{-\infty}^{\infty} \left[\frac{\partial H}{\partial z}(p_0^z(s), q_0^z(s), z) - \frac{\partial H}{\partial z}(\mathbf{X}_0^z)\right] ds, \tag{2.4}$$

which may also be obtained from (2.3) upon using integration by parts and realizing that the boundary terms vanish due to the exponential contraction to γ_ϵ as $t \to \pm\infty$.

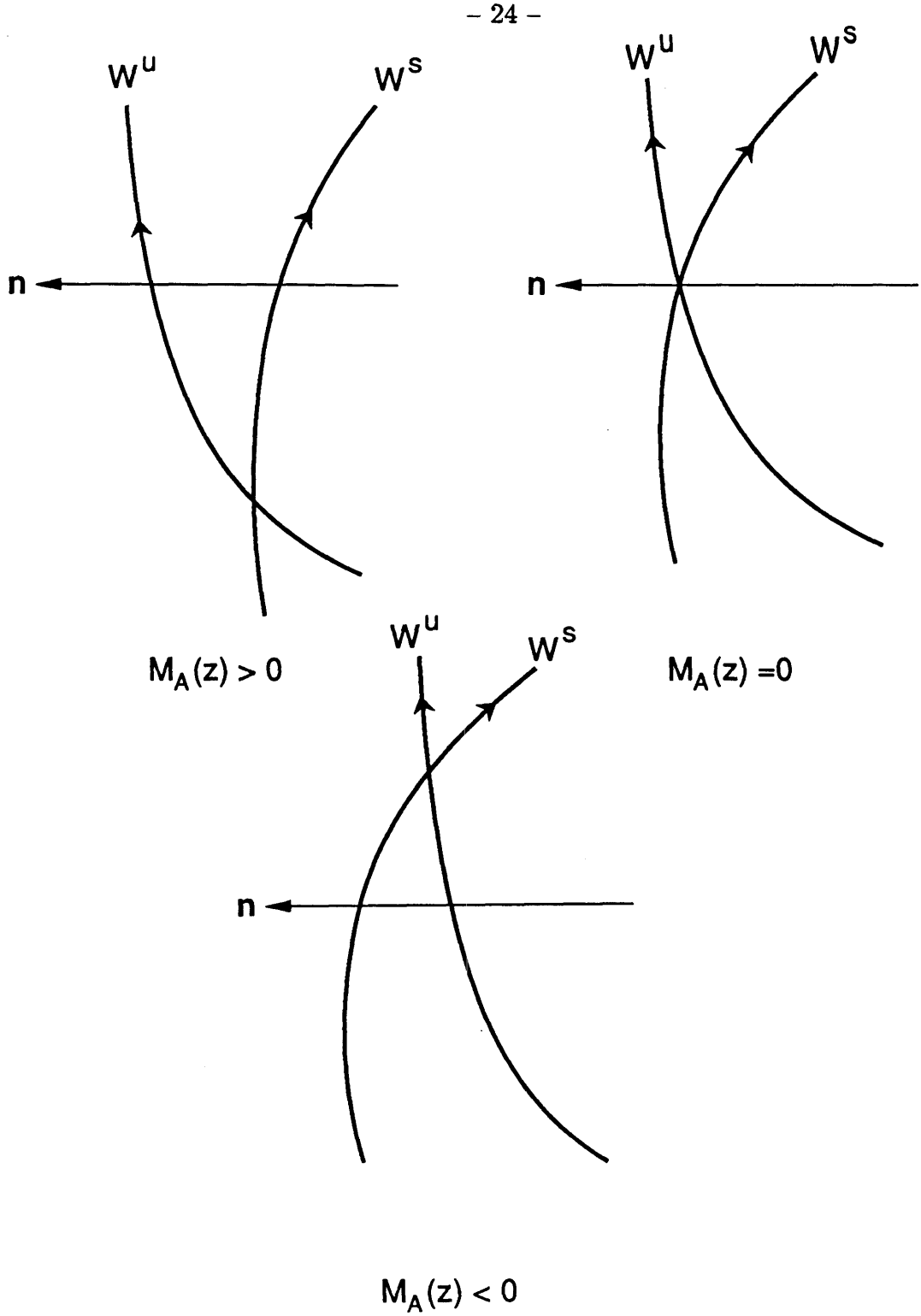

Fig. 2.3 The geometry of the adiabatic Melnikov function.

We now show that an alternative method, one using the unperturbed (z fixed) energy contour lines as a coordinate system, with $H = 0$ on Γ^z for all z, to measure the distance between $\mathbf{q}_\epsilon^U(0,z;0)$ and $\mathbf{q}_\epsilon^S(0,z;0)$ yields the same result, as obtained in the standard derivation.

The energy modulation equation is:

$$\dot{H} = \frac{\partial H}{\partial p}\dot{p} + \frac{\partial H}{\partial q}\dot{q} + \frac{\partial H}{\partial z}\dot{z} = \epsilon\frac{\partial H}{\partial z}, \tag{2.5}$$

where we used the equations of motion to get the last equality. Let

$$H_S \equiv \int_0^\infty \frac{\partial H}{\partial z}(\mathbf{q}_\epsilon^S(t,z;t_0),z)dt \tag{2.6}$$

$$H_U \equiv \int_{-\infty}^0 \frac{\partial H}{\partial z}(\mathbf{q}_\epsilon^U(t,z;t_0),z)dt. \tag{2.7}$$

We remark that these integrals are well-defined because the integrands converge exponentially to zero as $t \to \pm\infty$ respectively. The distance between $\mathbf{q}_\epsilon^U(0,z;0)$ and $\mathbf{q}_\epsilon^S(0,z;0)$ is

$$\Delta H = \epsilon(H_u - H_S). \tag{2.8}$$

Next, we expand ΔH in a series in ϵ. We recall that $z = z_0 - \epsilon t$ and that

$$\begin{aligned}
\mathbf{q}_\epsilon^S(t,z) &= \mathbf{q}_0^{z_0}(t) + \epsilon\mathbf{q}_1^S(t,z) + \epsilon^2\mathbf{q}_2^S(t,z) + \epsilon^3\mathbf{q}_3^S(t,z) + \mathcal{O}(\epsilon^4) \\
\mathbf{q}_\epsilon^U(t,z) &= \mathbf{q}_0^{z_0}(t) + \epsilon\mathbf{q}_1^U(t,z) + \epsilon^2\mathbf{q}_2^U(t,z) + \epsilon^3\mathbf{q}_3^U(t,z) + \mathcal{O}(\epsilon^4)
\end{aligned} \tag{2.9}$$

Therefore, asymptotically as $\epsilon \to 0$,

$$\begin{aligned}
\Delta H = &-\epsilon \int_{-\infty}^{\infty} \frac{\partial H}{\partial z}(\mathbf{q}_0^{z_0}(t), z_0)dt \\
&- \epsilon^2 \left[- \int_{-\infty}^{\infty} \frac{\partial^2 H}{\partial z^2}(\mathbf{q}_0^{z_0}(t), z_0)tdt + \int_0^{\infty} D_{\mathbf{q}} \frac{\partial H}{\partial z}(\mathbf{q}_0^{z_0}(t), z_0) \cdot \mathbf{q}_1^S(t,z)dt \right. \\
&\left. + \int_{-\infty}^{0} D_{\mathbf{q}} \frac{\partial H}{\partial z}(\mathbf{q}_0^{z_0}(t), z_0) \cdot \mathbf{q}_1^U(t,z)dt \right] \\
&- \epsilon^3 \left[- \int_{-\infty}^{\infty} \frac{\partial^3 H}{\partial z^3}(\mathbf{q}_0^{z_0}(t), z_0)t^2 dt - 2\int_0^{\infty} D_{\mathbf{q}} \frac{\partial^2 H}{\partial z^2}(\mathbf{q}_0^{z_0}(t), z_0) \cdot \mathbf{q}_1^S(t,z)tdt \right. \\
&- 2\int_{-\infty}^{0} D_{\mathbf{q}} \frac{\partial^2 H}{\partial z^2}(\mathbf{q}_0^{z_0}(t), z_0) \cdot \mathbf{q}_1^U(t,z)tdt \\
&+ \int_0^{\infty} \left(D_{\mathbf{q}}^2 (\frac{\partial H}{\partial z}(\mathbf{q}_0^{z_0}(t), z_0)) \cdot \mathbf{q}_1^S(t,z) \right) \cdot \mathbf{q}_1^S(t,z)dt \\
&+ \int_{-\infty}^{0} \left(D_{\mathbf{q}}^2 (\frac{\partial H}{\partial z}(\mathbf{q}_0^{z_0}(t), z_0)) \cdot \mathbf{q}_1^U(t,z) \right) \cdot \mathbf{q}_1^U(t,z)dt \\
&+ \int_0^{\infty} D_{\mathbf{q}} \frac{\partial H}{\partial z}(\mathbf{q}_0^{z_0}(t), z_0) \cdot \mathbf{q}_2^S(t,z)dt \\
&+ \int_{-\infty}^{0} D_{\mathbf{q}} \frac{\partial H}{\partial z}(\mathbf{q}_0^{z_0}(t), z_0) \cdot \mathbf{q}_2^U(t,z)dt + \int_0^{\infty} D_{\mathbf{q}} \frac{\partial H}{\partial z}(\mathbf{q}_0^{z_0}(t), z_0) \cdot \frac{d\mathbf{q}_1^S(t,z)}{dt}tdt \\
&\left. + \int_{-\infty}^{0} D_{\mathbf{q}} \frac{\partial H}{\partial z}(\mathbf{q}_0^{z_0}(t), z_0) \cdot \frac{d\mathbf{q}_1^U(t,z)}{dt}tdt \right] + \mathcal{O}(\epsilon^4)
\end{aligned} \tag{2.10}$$

We discuss the computation of $\mathbf{q}_1^U(0,z;0)$ and $\mathbf{q}_1^S(0,z;0)$ in Section 2.4 (on the angle at h_0).

As shown above, via an integration by parts we can rewrite the $\mathcal{O}(\epsilon)$ term in (2.10) as $M_A(z_0)$. Therefore the two calculations lead to the same leading order result. We remark that all of the improper integrals exist because $\mathbf{q}_0^z(t)$ converges exponentially as $t \to \pm\infty$.

Furthermore, this calculation shows that the closure condition on the energy phase modulation equation (or the Fredholm Alternative solvability) is the same as the adiabatic Melnikov criterion for the existence of homoclinic orbits in $(1.1)_\epsilon$.

We have also calculated the first three terms to show (something which has not been noticed before) that for a large class of systems $\Delta H(z_0) = 0$ to all orders in ϵ. This class of systems includes those in the form $H = F(p) + V(q)G(z)$, a group which includes many of the problems studied in the literature, including the two example in Chapter 4. We consider systems of the form $(1.1)_\epsilon$ in which $\frac{\partial H}{\partial z}(\mathbf{q}_0^{z_0}(t), z_0) \equiv 0$ for all t, $\frac{\partial^2 H}{\partial z^2}(\mathbf{q}_0^z(t), z)$ is an even function of t about $t = 0$ for $z \neq z_0 \bmod \pi$, where we assume without loss of generality that H is 2π-periodic in z. For these systems, $D_{\mathbf{q}}^k \frac{\partial H}{\partial z}(\mathbf{q}_0^{z_0}(t), z_0) \equiv 0$ for all t and for all $k \in \mathbb{N}$, $\mathbf{q}_k^{S,U}(t, z) \equiv 0$, $\frac{\partial^{2k+1} H}{\partial z^{2k+1}}(\mathbf{q}_0^{z_0}(t), z_0) \equiv 0$ for all $k \in \mathbb{N}$, and $\frac{\partial^{2k} H}{\partial z^{2k}}(\mathbf{q}_0^{z_0}(t), z_0) t^{2k-1}$ is odd in t about $t = 0$ for all $k \in \mathbb{N}$. Therefore, using these observations in (2.10), we conclude that $\Delta H(z_0)$ vanishes to all orders in ϵ. As a corollary, because $H(\mathbf{q}_0^{z_0}(t), z_0) = 0$, this result implies that the distances between both $\mathbf{q}_\epsilon^U(0, z; 0)$ and $\mathbf{q}_\epsilon^S(0, z; 0)$ and the point $\mathbf{q}_0^{z_0}$ on the unperturbed homoclinic orbit are beyond all orders in ϵ.

Location of pips

All but one of the pips lie inside of a small neighborhood of γ_ϵ. We readily establish this fact by observing that the time-of-flight in between the orbits corresponding to pips is $\mathcal{O}(\frac{1}{\epsilon})$. For an example of this phenomenon in the case of the adiabatic pendulum, we refer the reader to Figure 4.2 in Chapter 4.

2.3. Behavior of Derivatives of Solutions on Manifolds with respect to ϵ.

The reader who is not interested in these details may skip to Chapter 3 without losing the thread of the results. In this section, we establish that the derivatives of solutions on the stable and unstable manifolds with respect to ϵ grow at worst linearly in time as $t \to \pm\infty$. The following lemma says this precisely in mathematical symbols:

Lemma 2.1. a) *For solutions* $\mathbf{x}_\epsilon(t,t_0)$ *on* $W^S_{\rm loc}(\gamma_\epsilon)$, $\frac{\partial \mathbf{x}_\epsilon}{\partial \epsilon}(t,t_0) = \mathcal{O}(t)$ *as* $t \to \infty$, *and for solutions* $\mathbf{x}_\epsilon(t,t_0)$ *on* $W^U_{\rm loc}(\gamma_\epsilon)$, $\frac{\partial \mathbf{x}_\epsilon}{\partial \epsilon}(t,t_0) = \mathcal{O}(|t|)$ *as* $t \to -\infty$; *and b)* $\frac{\partial \mathbf{x}_\epsilon}{\partial \epsilon}|^{\mathbf{x}^{\mathcal{Q}}_\epsilon}_{\mathbf{x}^{\mathcal{P}}_\epsilon} \to 0$ *exponentially as* $t \to \pm\infty$, *where* $\mathbf{x}^{\mathcal{P}}_\epsilon(t,t_0)$ *and* $\mathbf{x}^{\mathcal{Q}}_\epsilon(t,t_0)$ *are adjacent homoclinic orbits.*

The idea of the proof of part a) is to show in the simple case in which γ_ϵ is rectified (*i.e.*, γ_ϵ lies at the origin of $\mathbb{R}^2$ for every z so that $\gamma_\epsilon \cap \Pi_t = (0,0)$ for all t), then these derivatives are uniformly bounded. Thus for general systems of the form $(1.1)_\epsilon$, in which the $p-q$ location of $\gamma_\epsilon \cap \Pi_t$ can change linearly in time (since the location of $\gamma_\epsilon \cap \Pi_t$ can move an $\mathcal{O}(1)$ distance), the derivatives with respect to ϵ of solutions on $W^S_{loc}(\gamma_\epsilon)$ and $W^U_{loc}(\gamma_\epsilon)$ grow at worst linearly in time. Furthermore, as we show in the proof of part b), the difference in any of these derivatives between two sequential intersection orbits decays exponentially in time due to the exponential contraction on the local stable and unstable manifolds.

Now, we perform the detailed calculations for the proof in one limit, namely that of $t \to +\infty$, looking at solutions on $W^S(\gamma_\epsilon)$. Those for the other limit will be the same except that one considers solutions on $W^U(\gamma_\epsilon)$.

In order to proceed with proving the lemma we write the scalar equation for the evolution of orbits on $W^S_{\rm loc}(\gamma_\epsilon)$ which we solve in the proof. The scalar equation may be obtained from $(1.1)_\epsilon$ by rectifying γ_ϵ and using the fact that $y_2 = \phi(y_1,t,\epsilon)$ for orbits on $W^S_{\rm loc}(\gamma_\epsilon)$, where ϕ is C^r smooth in both y_1 and t. Thus we get:

$$\dot{y}_1 = -\lambda^S(z)y_1 + F(y_1,t), \tag{2.11}$$

where $y_1 \in \mathbb{R}$ and $F(y_1,t)$ is a nonlinear function of y_1 satisfying $F(0,t) = 0$. Here $\lambda^S(z)$ is the contraction rate on the stable manifold. $\lambda^S(z)$ varies in the interval $[\lambda^\epsilon_1, \lambda^\epsilon_2]$, where λ^ϵ_1 is bounded away from zero as a consequence of the uniform

hyperbolicity, and λ_2^ϵ is finite. Similarly, for the proof in the other time limit ($t \to -\infty$) and solutions on $W^U(\gamma_\epsilon)$, the expansion rate along $W^U(\gamma_\epsilon)$, $\lambda^U(z)$, varies in the interval $[\lambda_3^\epsilon, \lambda_4^\epsilon]$,

Proof of Lemma 2.1 The above scalar equation for orbits on $W^S(\gamma_\epsilon)$, (2.11), enables us to write down the equation

$$\frac{d}{dt}\frac{\partial y_1}{\partial \epsilon}(t,\epsilon) = A(y_1,t,\epsilon)\frac{\partial y_1}{\partial \epsilon}(t,\epsilon) + B(y_1,t,\epsilon), \tag{2.12}$$

where $A(y_1,t,\epsilon) \equiv -\lambda^S(z) + \frac{\partial F}{\partial y_1}(y_1,t)$ and $B(y_1,t,\epsilon) \equiv -\frac{\partial \lambda^S}{\partial z}(z)ty_1(t,\epsilon) + \frac{\partial F}{\partial z}(y_1,t)t$ and $z = \epsilon t$.

Using variation of constants we can solve this equation:

$$\frac{\partial y_1}{\partial \epsilon}(t,\epsilon) = \frac{\partial y_1}{\partial \epsilon}(0,\epsilon)e^{-\int_0^t A(s,\epsilon,y_1(s,\epsilon))ds} + \int_0^t B(s,\epsilon,y_1(s,\epsilon))e^{-\int_s^t A(r,\epsilon,y_1(r,\epsilon))dr}ds. \tag{2.13}$$

From the persistence theory we know that $y_1(t,\epsilon) = \mathcal{O}(e^{-\lambda_1^\epsilon t})$ as $t \to +\infty$ because λ_1^ϵ is the minimum contraction rate for all t (taken uniformly in z) and thus $y_1(t,\epsilon;y_1(0)) \to 0$ as least as fast as $e^{-\lambda_1^\epsilon t}$. Thus the terms in the functions A and B involving F and its derivatives with respect to y_1 and z are $\mathcal{O}(e^{-\lambda_1^\epsilon t})$. Hence we know that $|A(t,\epsilon,y_1)| > a$ for $|t|$ sufficiently large where $0 < a < \lambda_1^\epsilon$. Also, $|B(t,\epsilon,y_1)| = \mathcal{O}(te^{-\lambda_1^\epsilon t})$ because $\frac{\partial \lambda^S}{\partial z}(z)$ is uniformly bounded. Thus,

$$|\frac{\partial y_1}{\partial \epsilon}(t,\epsilon)| \leq |\frac{\partial y_1}{\partial \epsilon}(0,\epsilon)|e^{-at} + Kt^2e^{-at}, \tag{2.14}$$

and the proof of part a) of the lemma is complete.

Part b) of the lemma follows from the simple observation that the two adjacent homoclinic orbits approach each other exponentially in both backward and forward time because they both approach γ_ϵ exponentially in backward and forward time. Thus, even though each term separately may grow linearly in time, their difference vanishes exponentially.

2.4. The Angle between $W^S(\gamma_\epsilon)$ and $W^U(\gamma_\epsilon)$ at h_0.

Let the homoclinic orbit $\mathbf{q}_0^z(-t_0) = (p_0^z(-t_0), q_0^z(-t_0))$ parametrize the homoclinic loop Γ^z. Let $\mathbf{n}$ denote the normal to Γ^z through the reference point $\mathbf{q}_0^z(0)$ on Π_z. Assume that $W^S(\gamma_\epsilon)$ and $W^U(\gamma_\epsilon)$ intersect transversely at a point h_0 which is ϵ-close in the extended phase space to $\mathbf{q}_0^z(0)$, the reference point on Γ^z. In this section, we derive a computable expression for the angle, α, between $W^S(\gamma_\epsilon)$ and $W^U(\gamma_\epsilon)$ at h_0.

From purely geometrical considerations on the constant z slice Π_z of the extended phase space, one can readily write down the following formula for α:

$$\alpha = \beta_1 - \beta_2 \equiv \cos^{-1}\left(\hat{\mathbf{n}} \cdot \frac{\hat{\partial \mathbf{q}_\epsilon^S}}{\partial t_0}\right) - \cos^{-1}\left(\hat{\mathbf{n}} \cdot \frac{\hat{\partial \mathbf{q}_\epsilon^U}}{\partial t_0}\right) \tag{2.15}$$

where $\frac{\hat{\partial \mathbf{q}_\epsilon^S}}{\partial t_0}$ and $\frac{\hat{\partial \mathbf{q}_\epsilon^U}}{\partial t_0}$ are the unit tangent vectors $\frac{\frac{\partial \mathbf{q}_\epsilon^S}{\partial t_0}(0,z;0)}{\|\frac{\partial \mathbf{q}_\epsilon^S}{\partial t_0}(0,z;0)\|}$ and $\frac{\frac{\partial \mathbf{q}_\epsilon^U}{\partial t_0}(0,z;0)}{\|\frac{\partial \mathbf{q}_\epsilon^U}{\partial t_0}(0,z;0)\|}$ to $W^S(\gamma_\epsilon)$ and $W^U(\gamma_\epsilon)$, respectively, at the intersection point h_0, $\mathbf{q}_\epsilon^S(0,z;0) = \mathbf{q}_\epsilon^U(0,z;0)$, and $\hat{\mathbf{n}}$ is the unit normal $\frac{\mathbf{n}}{\|\mathbf{n}\|}$. We refer the reader to Figure 2.4 where the geometry is explicitly illustrated. Now we derive a computable expression for (2.15).

First, we know that $\alpha \to 0$ as $\epsilon \to 0$. In fact β_1 and β_2 are both near $\frac{\pi}{2}$. Thus we may use the expansion :

$$\cos^{-1} x = \frac{\pi}{2} - x - \frac{x^3}{6} - \frac{3x^5}{40} + \mathcal{O}(x^7) \tag{2.16}$$

with $|x = \hat{\mathbf{n}} \cdot \frac{\hat{\partial \mathbf{q}_\epsilon^S}}{\partial t_0}| < 1$ and with $|x = \hat{\mathbf{n}} \cdot \frac{\hat{\partial \mathbf{q}_\epsilon^U}}{\partial t_0}| < 1$ because $0 < \cos^{-1} x < \pi$.

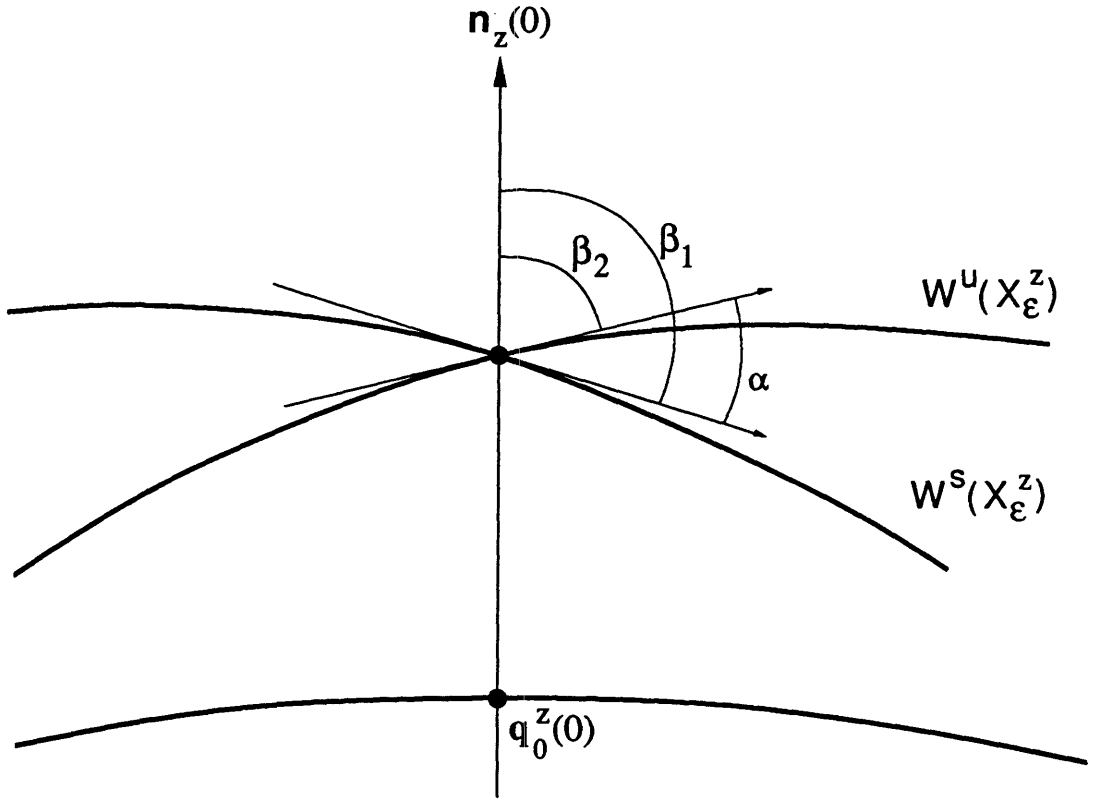

Fig. 2.4. Measurement of the angle between $W^S(\gamma_\epsilon)$ and $W^U(\gamma_\epsilon)$ at the pip h_0.

Therefore, substituting (2.16) into (2.15) we get:

$$\begin{aligned}\alpha = & \hat{\mathbf{n}} \cdot \left(\frac{\hat{\partial \mathbf{q}_\epsilon}^U}{\partial t_0} - \frac{\hat{\partial \mathbf{q}_\epsilon}^S}{\partial t_0} \right) \\ & + \frac{1}{6} \hat{\mathbf{n}} \cdot \left(\frac{\hat{\partial \mathbf{q}_\epsilon}^U}{\partial t_0} - \frac{\hat{\partial \mathbf{q}_\epsilon}^S}{\partial t_0} \right) \left[(\hat{\mathbf{n}} \cdot \frac{\hat{\partial \mathbf{q}_\epsilon}^U}{\partial t_0})^2 + (\hat{\mathbf{n}} \cdot \frac{\hat{\partial \mathbf{q}_\epsilon}^U}{\partial t_0})(\hat{\mathbf{n}} \cdot \frac{\hat{\partial \mathbf{q}_\epsilon}^S}{\partial t_0}) + (\hat{\mathbf{n}} \cdot \frac{\hat{\partial \mathbf{q}_\epsilon}^S}{\partial t_0})^2 \right] \\ & + \mathcal{O}\left((\hat{\mathbf{n}} \cdot \frac{\hat{\partial \mathbf{q}_\epsilon}^S}{\partial t_0})^5, (\hat{\mathbf{n}} \cdot \frac{\hat{\partial \mathbf{q}_\epsilon}^U}{\partial t_0})^5 \right).\end{aligned} \tag{2.17}$$

The leading order contribution to α comes from the first term in (2.17). The contributions from the second term (involving the x^3 terms) and from the remainder terms are all of higher order in ϵ. We demonstrate these two claims now.

We rewrite the first term of (2.17) as follows. On Π_z at $t = 0$, the distance between $\mathbf{q}_\epsilon^S(0, z; 0)$ and $\mathbf{q}_\epsilon^U(0, z; 0)$ is

$$d(t_0 = 0, z, \epsilon) = \hat{\mathbf{n}} \cdot \left(\mathbf{q}_\epsilon^U(0, z; 0) - \mathbf{q}_\epsilon^S(0, z; 0) \right). \tag{2.18}$$

Therefore, since $\frac{\partial \mathbf{q}_\epsilon}{\partial t_0} = \frac{\partial \mathbf{q}_0^z}{\partial t_0} + \epsilon \frac{\partial \mathbf{q}_1}{\partial t_0} + \mathcal{O}(\epsilon^2) = -\mathbf{f}(\mathbf{q}_0^z, z) + \epsilon \frac{\partial \mathbf{q}_1}{\partial t_0} + \mathcal{O}(\epsilon^2)$,

$$\begin{aligned}\hat{\mathbf{n}} \cdot \left(\frac{\hat{\partial \mathbf{q}_\epsilon}^U}{\partial t_0} - \frac{\hat{\partial \mathbf{q}_\epsilon}^S}{\partial t_0} \right) = & \frac{\hat{\mathbf{n}}}{\|\mathbf{f}(\mathbf{q}_0^z(0), z)\|} \cdot \left(\frac{\partial \mathbf{q}^U}{\partial t_0} - \frac{\partial \mathbf{q}^S}{\partial t_0} \right) \\ & + \epsilon \frac{\hat{\mathbf{n}}}{\|\mathbf{f}(\mathbf{q}_0^z(0), z)\|} \cdot \left(\frac{\partial \mathbf{q}^U}{\partial t_0} \cdot \| \frac{\partial \mathbf{q}_1^U}{\partial t_0} + \mathcal{O}(\epsilon) \| - \frac{\partial \mathbf{q}^S}{\partial t_0} \cdot \| \frac{\partial \mathbf{q}_1^S}{\partial t_0} + \mathcal{O}(\epsilon) \| \right) \\ = & \frac{1}{\|\mathbf{f}(\mathbf{q}_0^z(0), z)\|} \left[\frac{\partial d}{\partial t_0} - \frac{\partial \hat{\mathbf{n}}}{\partial t_0} \cdot \left(\mathbf{q}_\epsilon^U(0, z; 0) - \mathbf{q}_\epsilon^S(0, z; 0) \right) \right] + \text{h.o.t.s.}\end{aligned} \tag{2.19}$$

However, $\hat{\mathbf{n}}$ does not depend explicitly on t_0: $\frac{\partial \hat{\mathbf{n}}}{\partial t_0} = 0$. Furthermore, we can rewrite $\frac{\partial d}{\partial t_0}$ using $M_A(z)$. We know from the theory of the adiabatic Melnikov function

given in Section 2.2 that asymptotically as $\epsilon \to 0$,

$$d(0,z,\epsilon) = \epsilon \frac{M_A(z)}{\|\mathbf{f}(\mathbf{q}_0^z(0),z)\|} + \epsilon^2 \frac{1}{\|\mathbf{f}(\mathbf{q}_0^z(0),z)\|} \cdot \left[\int_{-\infty}^{\infty} - \left(\frac{\partial^2 H}{\partial z^2}(\mathbf{X}_0^z) + \frac{\partial^2 H}{\partial z^2}(\mathbf{q}_0^z(t),z) \right) t dt + \int_0^{\infty} \left(D_{\mathbf{q}} \left(\frac{\partial H}{\partial z} \right) (\mathbf{q}_0^z(t),z) \right) \cdot \mathbf{q}_1^S(t,z;0) dt + \int_{-\infty}^{0} \left(D_{\mathbf{q}} \left(\frac{\partial H}{\partial z} \right) (\mathbf{q}_0^z(t),z) \right) \cdot \mathbf{q}_1^U(t,z;0) dt \right] + \mathcal{O}(\epsilon^3), \tag{2.20}$$

where we record $\mathbf{q}_1^S$ and $\mathbf{q}_1^U$ below.

Now,

$$\frac{\partial M_A}{\partial t_0}(z) \approx -\epsilon \frac{dM_A}{dz}(z_0) + \mathcal{O}(\epsilon^2). \tag{2.21}$$

We remark that the $\mathcal{O}(\epsilon)$ term in (2.21) is nonzero because $\frac{dM_A}{dz}(z_0) \neq 0$. As for the $\mathcal{O}(\epsilon^2)$ terms in (2.20), when evaluated at $t_0 = 0$, the second and third integrals vanish to leading order because $D_{\mathbf{q}} \frac{\partial H}{\partial z}(\mathbf{q}_0^{z_0}(t), z_0) = \mathbf{0}$ for all $t \in \mathbb{R}$. Furthermore, the integrand of the first integral is odd about $t = 0$, and so the first integral vanishes. Hence,

$$\frac{\partial d}{\partial t_0}(0,z,\epsilon) = \epsilon^2 \frac{-\frac{dM_A}{dz}(z_0)}{\|\mathbf{f}(\mathbf{q}_0^{z_0}(0),z_0)\|} + \mathcal{O}(\epsilon^3). \tag{2.22}$$

Therefore, plugging (2.22) into (2.19), we get:

$$\hat{\mathbf{n}} \cdot \left(\frac{\hat{\partial} \mathbf{q}_\epsilon^U}{\partial t_0} - \frac{\hat{\partial} \mathbf{q}_\epsilon^S}{\partial t_0} \right) = \epsilon^2 \frac{-\frac{dM_A}{dz}(z_0)}{\|\mathbf{f}(\mathbf{q}_0^{z_0}(0),z_0)\|^2} + \mathcal{O}(\epsilon^3). \tag{2.23}$$

Of course, the result of Section 2.3 leads one to believe that this is only an upper bound on the angle. Furthermore, (2.21) is only an approximation, and the actual result may be much smaller.

To finish, we show that the remaining terms in (2.17) are $\mathcal{O}(\epsilon^3)$. We expand

$\mathbf{q}_\epsilon^S(0,z;0)$ and $\mathbf{q}_\epsilon^U(0,z;0)$ for ϵ sufficiently small near h_0:

$$\frac{\partial \mathbf{q}_\epsilon^S}{\partial t_0}(0,z;0) \sim \frac{\partial \mathbf{q}_0^z(0)}{\partial t_0} + \epsilon \frac{\partial \mathbf{q}_1^S(0,z;0)}{\partial t_0} + \mathcal{O}(\epsilon^2)$$
$$\frac{\partial \mathbf{q}_\epsilon^U}{\partial t_0}(0,z;0) \sim \frac{\partial \mathbf{q}_0^z(0)}{\partial t_0} + \epsilon \frac{\partial \mathbf{q}_1^U(0,z;0)}{\partial t_0} + \mathcal{O}(\epsilon^2).$$

By definition of the normal $\mathbf{n}$,

$$\mathbf{n} \cdot \frac{\partial \mathbf{q}_0^z}{\partial t_0} \equiv 0.$$

Thus the leading terms of $\hat{\mathbf{n}} \cdot \frac{\partial \hat{\mathbf{q}}_\epsilon^S}{\partial t_0}$ and $\hat{\mathbf{n}} \cdot \frac{\partial \hat{\mathbf{q}}_\epsilon^U}{\partial t_0}$ are $\mathcal{O}(\epsilon)$. Hence, using (2.23), the x^3 terms are $\mathcal{O}(\epsilon^3)$ and the remaining terms are all at least $\mathcal{O}(\epsilon^5)$.

Therefore, inserting (2.23) into (2.17), the asymptotic formula for α as $\epsilon \to 0$ is:

$$\alpha = \epsilon^2 \frac{-\frac{dM_A}{dz}(z_0)}{\|\mathbf{f}(\mathbf{q}_0^{z_0}(0), z_0)\|^2} + \mathcal{O}(\epsilon^3). \tag{2.24}$$

We have finished the work of this section.

Just for completeness we record the solutions $\mathbf{q}_1^S$ and $\mathbf{q}_1^U$ here. Recall that $\mathbf{q}_1^S$ and $\mathbf{q}_1^U$ are the coefficients on the $\mathcal{O}(\epsilon)$ terms in the solutions $\mathbf{q}_\epsilon^S$ and $\mathbf{q}_\epsilon^U$. They satisfy the following equation:

$$\begin{aligned} \dot{q}_1 &= \frac{\partial^2 H}{\partial q \partial p}(\mathbf{q}_0^{z_0}, z_0) q_1 + \frac{\partial^2 H}{\partial p^2}(\mathbf{q}_0^{z_0}, z_0) p_1 + \frac{\partial^2 H}{\partial z \partial p}(\mathbf{q}_0^{z_0}, z_0) t \\ \dot{p}_1 &= -\frac{\partial^2 H}{\partial q^2}(\mathbf{q}_0^{z_0}, z_0) q_1 - \frac{\partial^2 H}{\partial p \partial q}(\mathbf{q}_0^{z_0}, z_0) p_1 - \frac{\partial^2 H}{\partial z \partial q}(\mathbf{q}_0^{z_0}, z_0) t. \end{aligned} \tag{2.25}$$

The solution of (2.25) is obtained using the variations of constants formula (see Coddington and Levinson, for example). Let $\mathbf{q}_1(t) = (q_1(t), p_1(t))$. Then the solution is

$$\mathbf{q}_1(t, z_0) = \mathbf{X}(t) \left[\mathbf{X}^{-1}(\tau) \mathbf{q}_1(\tau) - \int_t^\tau \mathbf{X}^{-1}(s) \frac{\partial \mathbf{f}}{\partial z}(\mathbf{q}_0^{z_0}(s), z_0) s ds \right] \tag{2.24}$$

where $\mathbf{X}(t)$ is the fundamental matrix of the homogeneous problem. We remark that the homogeneous part of (2.25) has the solution $(\dot{q}_0^{z_0}, \dot{p}_0^{z_0})$. In the particular

case in which the Hamiltonian is separable, *i.e.*, $H = p^2 + V(q,z)$, (2.25) reduces to:

$$\ddot{q}_1 + \frac{\partial^2 V}{\partial q^2}(q_0^{z_0}(t), z_0)q_1 + \frac{\partial^2 V}{\partial z \partial q}(q_0^{z_0}, z_0)t = 0 \tag{2.27}$$

of which the solution is:

$$q_1^{S,U}(t, z_0) = q_1^{pS,U}(t, z_0) + k^{S,U}\dot{q}_0^{z_0}(t), \tag{2.28}$$

where

$$q_1^{pS,U}(t, z_0) = -\dot{q}_0^{z_0}\int_t^{\pm\infty}\frac{d\tau}{(\dot{q}_0^{z_0})^2}\int_\tau^{\pm\infty}\frac{\partial^2 V}{\partial z \partial q}\dot{q}_0^{z_0}\bar{t}d\bar{t}$$

and where

$$k^{S,U} = -\frac{\dot{q}_1^{pS,U}(0, z_0)}{\ddot{q}_0^{z_0}(0, z_0)}.$$

CHAPTER 3. LOBE AREA AND THE PROOF OF THEOREM 1.

We prove Theorem 1 in this chapter. The proof is split into several parts: First, we derive an action-based formula which gives the lobe area in $(1.1)_\epsilon$ exactly. This formula states that the area of a lobe is given by the difference in the actions of the two biasymptotic orbits which define the lobe. Second, we develop an approximation to this exact formula which may be evaluated using only quantities known from the unmodulated system. Thus, our result offers an easily verifiable test for the existence of rich dynamics in these systems. We find that the lobe area for these systems is $\mathcal{O}(1)$ in the limit of $\epsilon \to 0$. Finally, we prove that the error made in the approximation is $\mathcal{O}(\epsilon)$. This proof is the most difficult part of the work. It involves calculating the flux of the fully perturbed Hamiltonian through surfaces spanned by biasymptotic orbits of the intermediate systems $H = H(p, q, z = \mu\epsilon r)$, where $\mu \in [0, 1]$.

After finishing the proof of Theorem 1, we establish a maximal property for lobe area. To conclude this chapter, we derive some additional results about the orbits defining the lobes using further ideas from action theory.

The chapter is organized into five sections: Section 3.1 contains the exact formula; Section 3.2 the approximation; Section 3.3 the proof of the error; Section 3.4 the maximal property; and Section 3.5 the additional results.

3.1. EXACT ACTION-THEORETIC FORMULA FOR LOBE AREA.

In this section we derive an exact, action-based formula for lobe area in $(1.1)_\epsilon$. In particular, we prove Theorem 3 which states that the difference in action between the orbits of the two homoclinic points defining a lobe gives its area. Before presenting this proof, we give the precise definitions of a primary intersection point

and a lobe, and we briefly review the concept of flux of a Hamiltonian vector field through a two-dimensional surface in the extended phase space.

We define a primary intersection point (pip) as follows. Let X_t denote the point of intersection of γ with the slice Π_t.

Definition 3.1. Let P be a homoclinic point on the slice Π_t. Let $X^S P$ denote the segment of $W^S(\gamma) \bigcap \Pi_t$ between X_t and P, and let $X^U P$ denote the segment of the intersection of $W^U(\gamma) \bigcap \Pi_t$ between X_t and P. We say that P is a *primary intersection point (pip)* if $X^S P$ and $X^U P$ intersect only in P. The reader is referred to Figure 3.1 for an illustration of this concept.

Now we use pip's to define a lobe.

Definition 3.2. If P and Q are two pips such that there are no other pips on the segments of $W^S(\gamma) \bigcap \Pi_t$ and $W^U(\gamma) \bigcap \Pi_t$ connecting them, then the region on the two-dimensional slice Π_t bounded by the pieces of stable and unstable manifold which connect these two points is called a *lobe.*

We label this lobe by L^{PQ} (see Figure 3.2), and we label its perimeter with α_t^S and α_t^U , where α_t^S and α_t^U are pieces of $W^S(\gamma)$ and $W^U(\gamma)$, respectively, on the slice Π_t terminating on P and Q. Also we label the trajectories through P and Q, by $\mathcal{P}$ and $\mathcal{Q}$. The reader is referred to Figure 3.2. We shall refer to P and Q as adjacent pips and remark that our definition of a lobe includes that of Rom-Kedar, *et al*, [1987], Rom-Kedar and Wiggins [1990a], [1990b]. The final consequence of our assumptions we remark upon is that there is at least one lobe to study in $(1.1)_\epsilon$ on every time slice of $U \times \mathbf{IR}$ because by A3 and its immediate consequence there are at least two intersection points on any time slice.

Next, we briefly review the concept of flux of a time-dependent Hamiltonian vector field through a two-dimensional surface in the extended phase space $U \times \mathbf{IR}$.

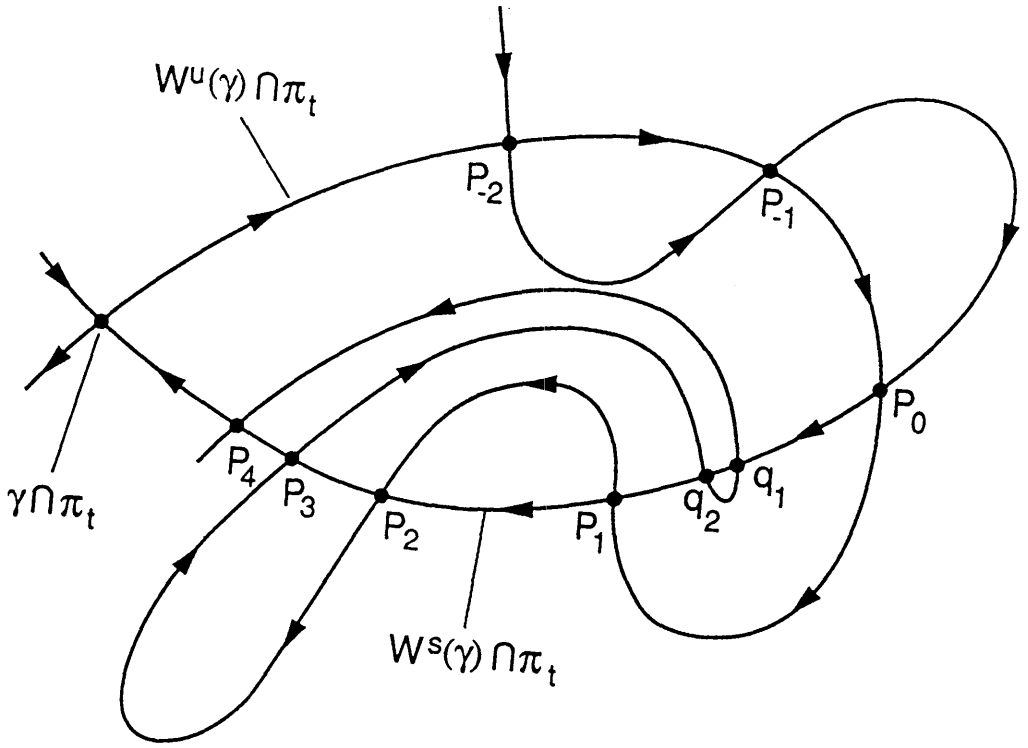

Fig. 3.1 The points p_i are pips. The points q_i are not.

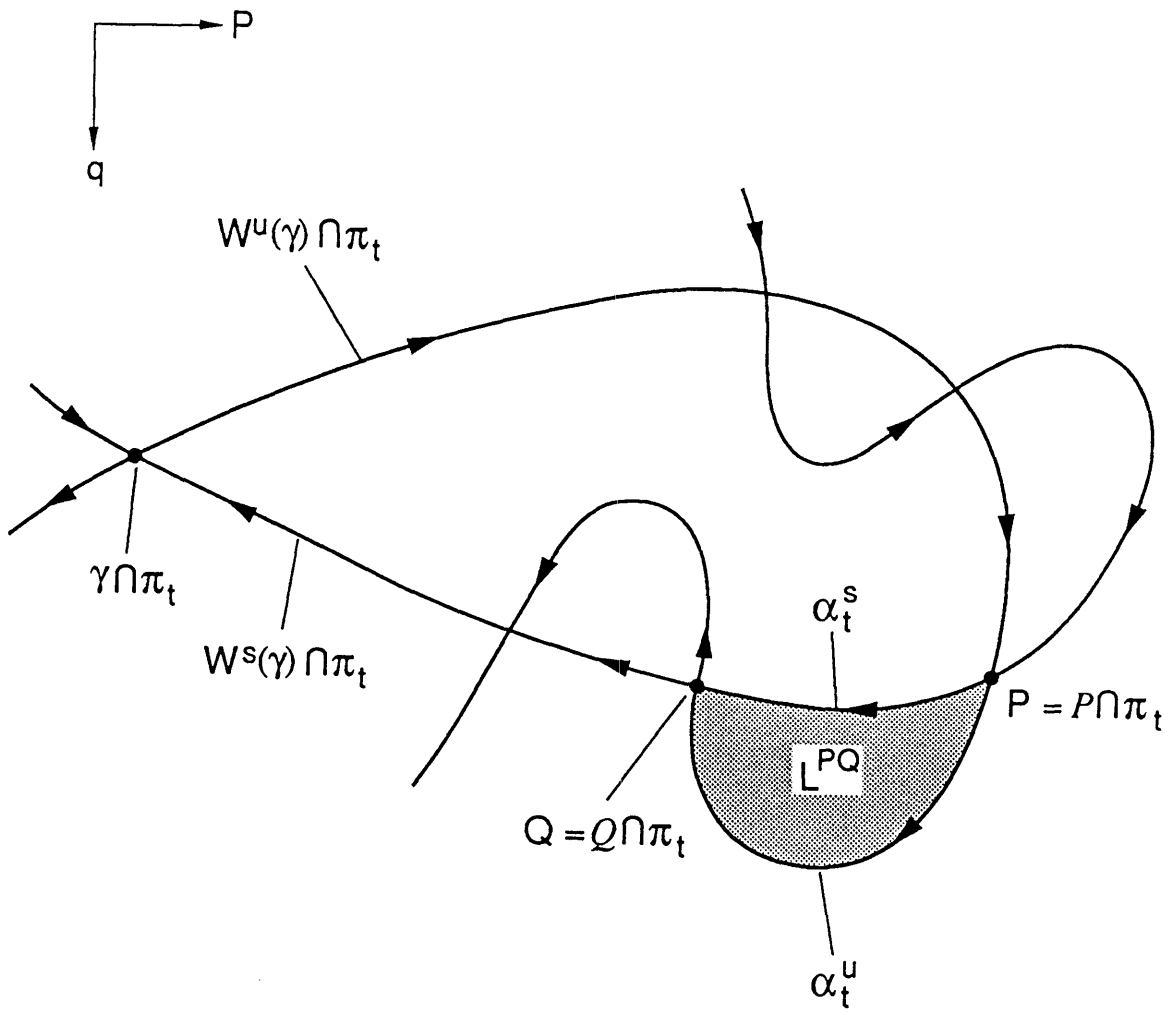

Fig. 3.2 The lobe L^{PQ}.

To study this flux in $(1.1)_\epsilon$ we need the two-form $d\omega_1 = dp \wedge dq - dH \wedge dt$. We refer to $d\omega_1$ as the flux form because the phase space volume crossing a two-dimensional surface Ξ in $U \times \mathbf{IR}$ is defined by the integral

$$\int_\Xi d\omega_1,$$

see Arnold [1978], p.237. The flux form, $d\omega_1$, is evaluated on a pair of vectors in $U \times \mathbf{IR}$. The orientation of these vectors with respect to the tangent spaces of Ξ and their magnitudes determine the value of $d\omega_1$. In particular the value of $d\omega_1$ on a pair of vectors that lie in the tangent plane of a surface spanned by trajectories, a surface that Arnold calls a vortex tube, Ξ_{vt}, is identically zero. Hence

$$\int_{\Xi_{vt}} d\omega_1 = 0.$$

For an arbitrarily chosen surface, Ξ, however, the orbits of $(1.1)_\epsilon$ are transverse to the tangent spaces of Ξ. Hence the integral

$$\int_\Xi d\omega_1$$

will in general be non-zero, indicating a non-zero flux of the vector field $(1.1)_\epsilon$ across the surface Ξ.

We now establish the theorem which gives the area of a lobe in system $(1.1)_\epsilon$:

Theorem 3. *Under assumptions A1-A3 the area of a lobe L^{PQ} in system $(1.1)_\epsilon$ is*

$$A(L^{PQ}) = \int_{\mathcal{P}-\mathcal{Q}} (pdq - Hdt), \tag{3.1}$$

where $\mathcal{P}$ and $\mathcal{Q}$ are the trajectories from $t = -\infty$ to $t = \infty$ of the adjacent pips P and Q which define the lobe L^{PQ} on the given reference time slice Π_{t_1} of $U \times \mathbf{IR}$.

Our proof of (3.1) is based on the hyperbolicity of the orbit γ and Stokes' Theorem. Furthermore, as we will see, the proof of this theorem is independent of the nature of

the time-dependence in H. Thus, although we state the theorem only for the slowly-modulated systems which are the focus of this thesis, it applies to all general time-dependent Hamiltonian systems with a hyperbolic orbit and at least two distinct orbits biasymptotic to it, see Kaper and Wiggins [1991b].

Proof of Theorem 3. Choose an arbitrary time slice, $\Pi_{t_1} = U \times \{t_1\}$, of $U \times \mathbb{R}$. The area of the lobe L^{PQ} on Π_{t_1} is defined by

$$A(L^{PQ}) = \int_{L^{PQ}} dp \wedge dq \,. \tag{3.2}$$

Since the lobe lies entirely on the one time slice Π_{t_1} we can subtract the two-form $dH \wedge dt$, which is identically zero on L^{PQ}, from the integrand to get

$$A(L^{PQ}) = \int_{L^{PQ}} dp \wedge dq - dH \wedge dt \,. \tag{3.3}$$

The area integral (3.3) can be recast as a line integral around the boundary of the compact two-dimensional surface L^{PQ} in Π_{t_1} using Stokes' Theorem

$$A(L^{PQ}) = \int_{\alpha^S_{t_1} - \alpha^U_{t_1}} (pdq - Hdt) \,. \tag{3.4}$$

This result is also illustrated in Figure 3.2 where one replaces t everywhere by t_1. The boundary of the lobe L^{PQ} is $\alpha^S_{t_1} - \alpha^U_{t_1}$. The orientation of the boundary of the lobe is chosen so that the interior of a region lies to the left as one traverses its boundary.

The integrals in (3.4) along $\alpha^S_{t_1}$ and $\alpha^U_{t_1}$ can be evaluated individually by studying the forward and backward semi-orbits of the pips P and Q in $U \times \mathbb{R}$. We use Stokes' Theorem on a strip of $W^S(\gamma)$ to express the integral along $\alpha^S_{t_1}$ in terms of integrals on the positive semi-orbits, $t \in (t_1, \infty)$, of the pips P and Q. Similarly, we use Stokes' Theorem on a strip of $W^U(\gamma)$ to express the integral along $\alpha^U_{t_1}$ in terms of integrals on the negative semi-orbits, $t \in (-\infty, t_1)$, of the pips P and Q.

We first work on the integral along $\alpha^S_{t_1}$. Let $\mathcal{P}^{+T}$ and $\mathcal{Q}^{+T}$ denote the restrictions of the orbits $\mathcal{P}$ and $\mathcal{Q}$ to the time interval (t_1, T), where $T > t_1$. Let Σ^S_{+T} label the strip of $W^S(\gamma)$ between the orbits $\mathcal{P}^{+T}$ and $\mathcal{Q}^{+T}$. Finally let α^S_{+T} denote the curve on $W^S(\gamma) \bigcap \Pi_T$ which connects the points $\mathcal{P} \bigcap \Pi_T$ and $\mathcal{Q} \bigcap \Pi_T$. We refer the reader to Figure 3.3*a* for an illustration of the geometry of Σ^S_{+T}.

An application of Stokes' Theorem on the compact two-dimensional strip Σ^S_{+T}, using the same orientation convention as used above, yields

$$\int_{\Sigma^S_{+T}} dp \wedge dq - dH \wedge dt = \left[\int_{\mathcal{P}^{+T}} + \int_{\alpha^S_{+T}} - \int_{\mathcal{Q}^{+T}} - \int_{\alpha^S_{t_1}} \right] (pdq - Hdt). \qquad (3.5)$$

The integral of $dp \wedge dq - dH \wedge dt$ over Σ^S_{+T} is identically zero because the vector field is tangent to Σ^S_{+T} at every orbit on it, and hence the flux of the vector field $(1.1)_\epsilon$ through Σ^S_{+T} is identically zero. Therefore (3.5) implies:

$$\int_{\alpha^S_{t_1}} pdq - Hdt = \left[\int_{\mathcal{P}^{+T}} + \int_{\alpha^S_{+T}} - \int_{\mathcal{Q}^{+T}} \right] (pdq - Hdt). \qquad (3.6)$$

The same argument can be made to rework the integral along $\alpha^U_{t_1}$ in (3.4). Let $\mathcal{P}^{-T}$ and $\mathcal{Q}^{-T}$ be the restrictions of the orbits of the pips P and Q to $t \in (-T, t_1)$. We refer to the strip of $W^U(\gamma)$ between the orbits $\mathcal{P}^{-T}$ and $\mathcal{Q}^{-T}$ as Σ^U_{-T}, and α^U_{-T} denotes the curve on $W^U(\gamma) \bigcap \Pi_{-T}$ connecting the points $\mathcal{P} \bigcap \Pi_{-T}$ and $\mathcal{Q} \bigcap \Pi_{-T}$. The reader is referred to Figure 3.3*b* for an illustration of the geometry of Σ^U_{-T}.

Stokes' Theorem for the compact two-dimensional strip Σ^U_{-T} in $U \times \mathbb{R}$ yields

$$\int_{\Sigma^U_{-T}} dp \wedge dq - dH \wedge dt = \left[\int_{\mathcal{Q}^{-T}} - \int_{\alpha^U_{t_1}} - \int_{\mathcal{P}^{-T}} + \int_{\alpha^U_{-T}} \right] (pdq - Hdt). \qquad (3.7)$$

The left hand side of (3.7) is identically zero, just as the left hand side of (3.5) is identically zero, because there is no flux of the vector field $(1.1)_\epsilon$ through the surface Σ^U_{-T} lying on $W^U(\gamma)$. Thus (3.7) implies:

$$-\int_{\alpha^U_{t_1}} pdq - Hdt = \left[\int_{\mathcal{P}^{-T}} - \int_{\alpha^U_{-T}} - \int_{\mathcal{Q}^{-T}} \right] (pdq - Hdt). \qquad (3.8)$$

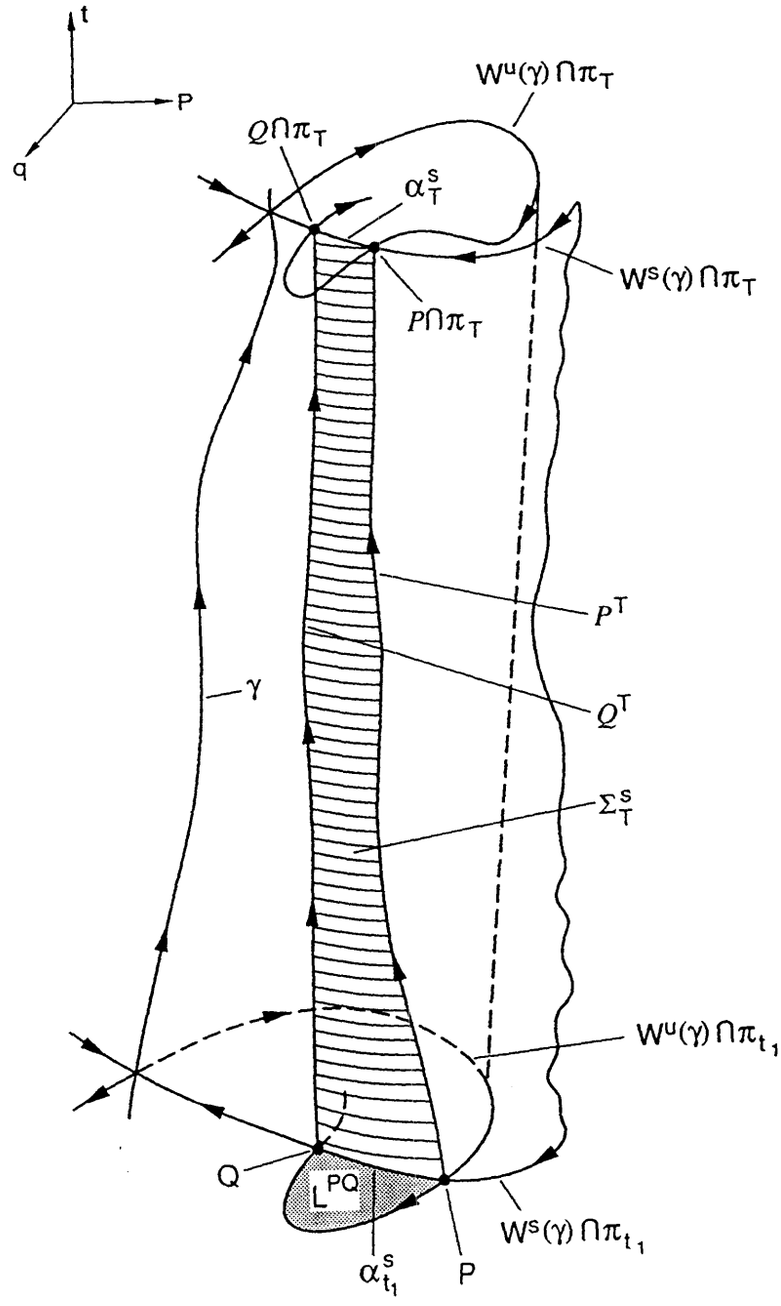

Fig. 3.3.a. The surface Σ_{+T}^S.

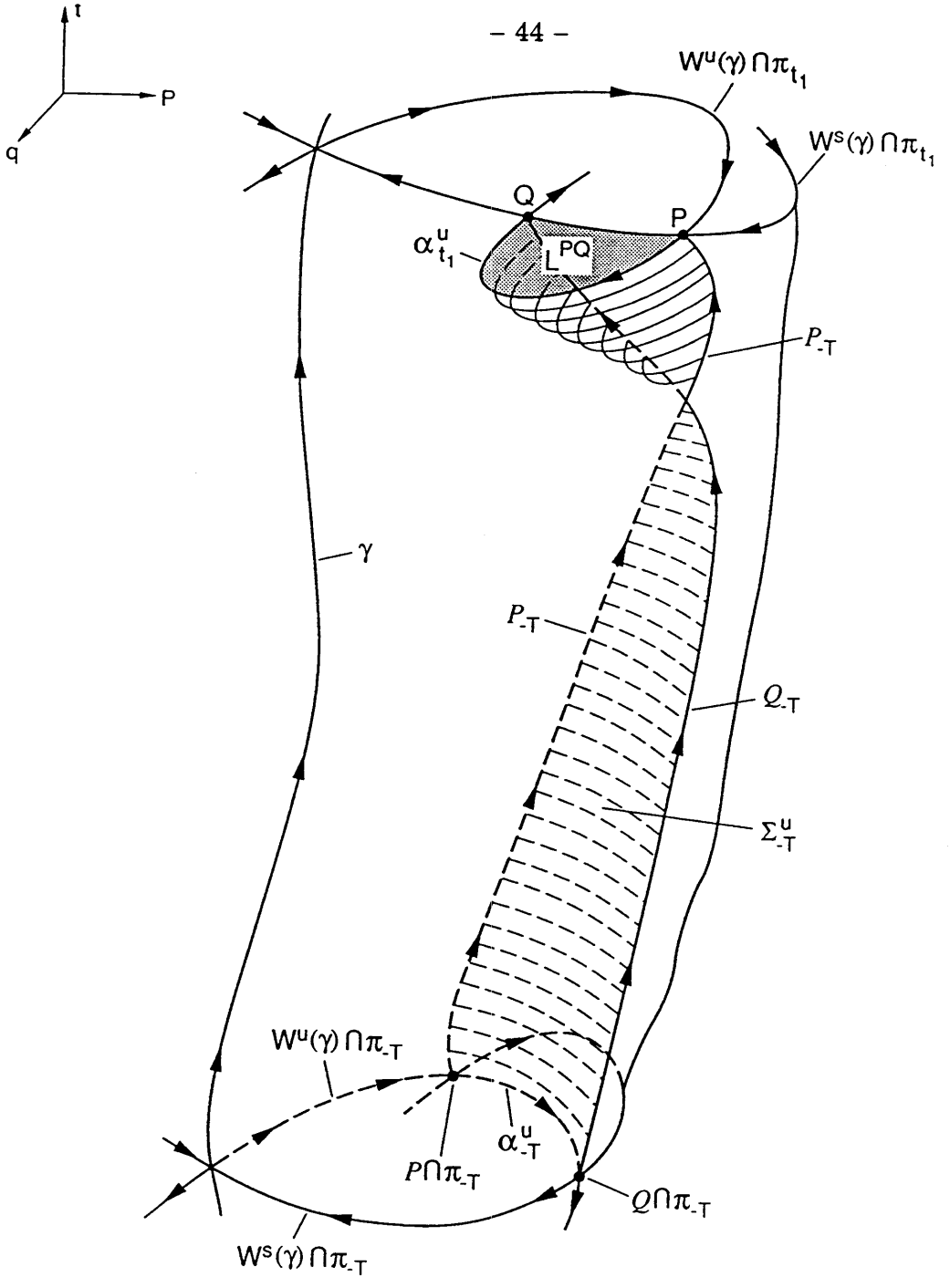

Fig. 3.3.b. The surface Σ^U_{-T}.

Finally we note that the lengths of α^S_{+T} and α^U_{-T} are $\mathcal{O}(e^{-cT})$ as $T \to \infty$. This length contraction follows from hyperbolicity because the orbits of the pips P and Q are orbits on $W^S(\gamma) \bigcap W^U(\gamma)$ and, hence, are biasymptotic to each other. Hence, the integrals over α^S_{+T} and α^U_{-T} vanish exponentially as $T \to \infty$. Therefore we arrive at (3.1) by putting (3.6) and (3.8) into (3.4) and letting $T \to \infty$

$$\begin{aligned} A(L^{PQ}) &= \lim_{T\to\infty} \left[\int_{\mathcal{P}+T} - \int_{\mathcal{Q}+T} + \int_{\mathcal{P}-T} - \int_{\mathcal{Q}-T} \right] (pdq - Hdt) \\ &= \int_{\mathcal{P}-\mathcal{Q}} (pdq - Hdt) \,. \end{aligned} \tag{3.9}$$

Thus we have completed the proof of Theorem 3. As one can see from the proof, Theorem 3 holds for all time-dependent one degree of freedom Hamiltonian systems with a hyperbolic orbit because we require only one time slice of $U \times \mathbf{IR}$.

We conclude this section with two observations about Theorem 3.

Remark 1. We observe that (3.1) is independent of the choice of time slice Π_{t_1} because of the following simple argument based on (3.6) and (3.8): The choice of a reference slice with t different from t_1 lengthens either the pair of semi-orbits $\mathcal{P}^+$ and $\mathcal{Q}^+$ or the pair of semi-orbits $\mathcal{P}^-$ and $\mathcal{Q}^-$ and shortens the other pair by the same piece it lengthens the first pair. Thus in picking a different value of t_1 one does not alter (3.9), and the lobe area, (3.1), is independent of the choice of reference slice.

Remark 2. MacKay and Meiss [1986] developed a formula for time-periodic Hamiltonian systems which is the same as (3.1). Their hypothesis that time-dependent systems possess a pair of homoclinic orbits which are homotopic to zero in the sense defined there is a slightly weaker hypothesis than A1-A3 because it also covers the situation in which the two homoclinic orbits defining the lobe need not be asymptotic to a hyperbolic orbit. They need only be asymptotic to each other or to a degenerate hyperbolic orbit to be homotopic to zero.

3.2. Approximate Lobe Area.

In this section we develop a computable closed form approximation of the lobe area for systems $(1.1)_\epsilon$. The approximation A_0 consists of evaluating the flux of the vector field $(1.1)_\epsilon$ through a piece of the homoclinic manifold Γ of the unperturbed system. The specific piece is determined by applying our homotopy method. However, for the purposes of this section it suffices to identify the piece. We state explicitly how the homotopy method yields it in Section 3.3. After identifying the piece we use, we show in Lemma 3.1 that the flux integral over the piece of Γ can be expressed in closed form in terms of the adiabatic Melnikov function.

Let Σ be the piece of the homoclinic manifold Γ defined by the restriction of the z- component to lie in the interval $[Z_0, Z_1]$, where Z_0 and Z_1 are two adjacent zeroes of the adiabatic Melnikov function whose existence is guaranteed by Assumption A3:

$$\Sigma = \bigcup_{z \in [Z_0, Z_1]} (\Upsilon^z, z).$$

Σ is the surface over which we will integrate the flux form to get A_0. See Figure 3.4. We recall that $z = \epsilon t$ and make two remarks about the piece of Σ: *i*) Σ is a compact two-dimensional surface in $U \times \mathbb{R}$, and *ii*) the value of the two-form $d\omega = dp \wedge dq - dH \wedge dt$ on vectors in $U \times \mathbb{R}$ which intersect Σ is uniformly bounded.

As stated above, we take the difference in action between two homoclinic orbits to get A_0. The two homoclinic orbits we take are the separatrices, Υ^{Z_0} and Υ^{Z_1}, on the two reference slices Π_{Z_0} and Π_{Z_1}, respectively:

$$A_0 = \int_{\Upsilon^{Z_1}} (pdq - Hdt) - \int_{\Upsilon^{Z_0}} (pdq - Hdt).$$

Defining the curves $\mathcal{P}_0$ and $\mathcal{Q}_0$ as the union of each of Υ^{Z_0} and Υ^{Z_1}, respectively,

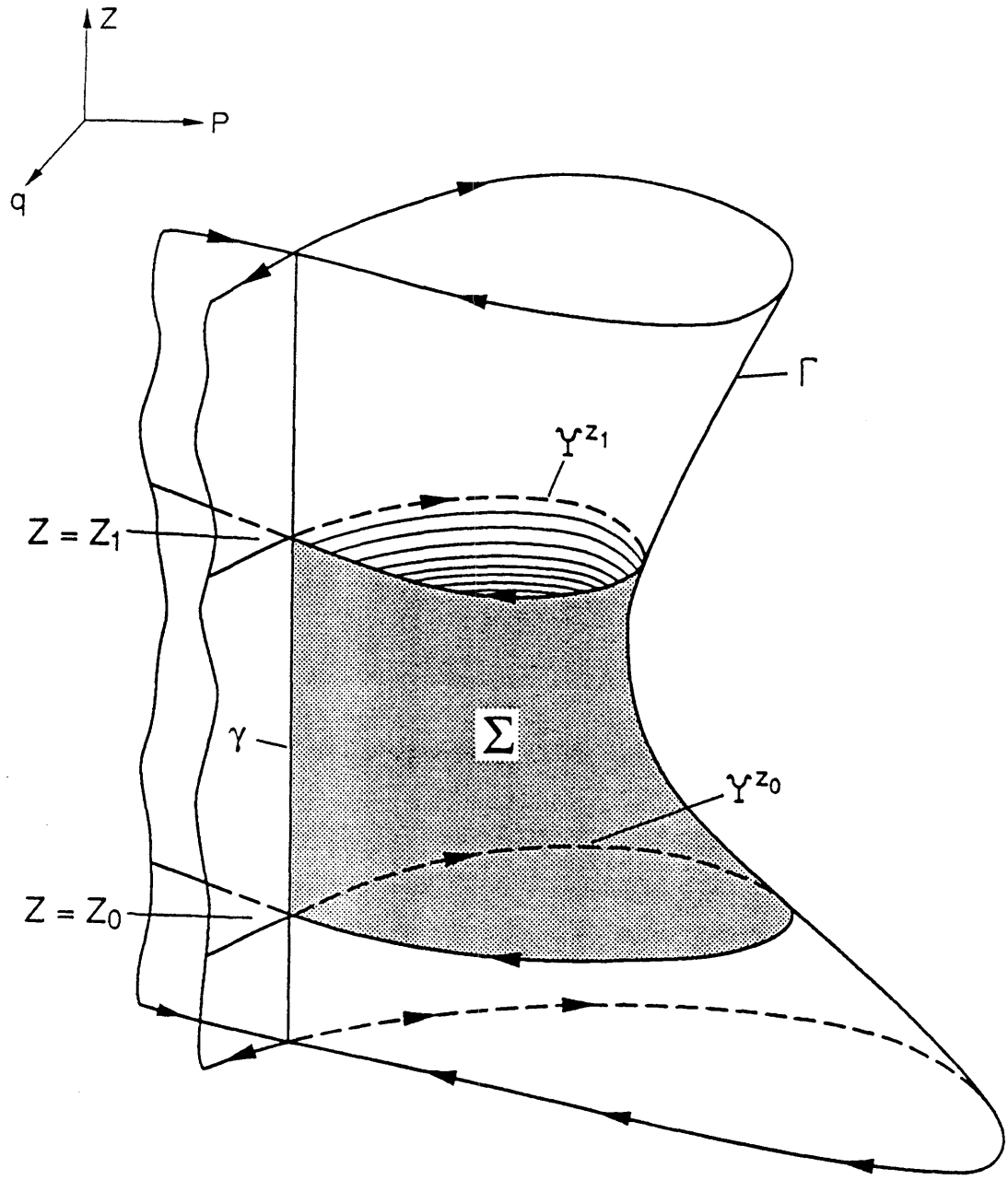

Fig. 3.4. The surface Σ in the extended $p - q - z$ phase space. The sketch is misleading because Υ^{z_0} and Υ^{z_1} should be the local minimum and maximum instantaneous separatrices.

with γ, we can write equivalently:

$$A_0 = \int_{\Upsilon^{z_1}} (pdq - Hdt) - \int_{\Upsilon^{z_0}} (pdq - Hdt) = \int_{\mathcal{P}_0 - \mathcal{Q}_0} (pdq - Hdt),$$

where the second equality is a result of the fact that we just add and subtract the integral over finite pieces of γ, that is with $z \in [-Z, Z]$, a process which does not contribute to the integral, and then we let $Z \to \infty$. We remark that we have attached γ to both Υ^{Z_0} and Υ^{Z_1} so that the surfaces we will define in Section 3.3 have closed boundaries.

Finally, since Σ is a compact surface, we can use Stokes' Theorem to rewrite our integral for A_0 as a surface integral over Σ. Thus the approximate lobe area A_0 is defined by

$$A_0 = \int\int_{\Sigma} dp \wedge dq - dH \wedge dt\,. \tag{3.10}$$

We now show in Lemma 3.1 that (3.10) leads directly to a closed form expression for A_0 in terms of the adiabatic Melnikov function.

Lemma 3.1.

$$A_0 = \int_{Z_0}^{Z_1} M_A(z)\, dz\,, \tag{3.11}$$

where Z_0 and Z_1 are the two consecutive zeros of the adiabatic Melnikov function, $M_A(z)$, corresponding to the two adjacent pips defining the endpoints of the lobe in question.

Proof of Lemma 3.1: Throughout the following derivation we keep in mind that the integrand is evaluated on Σ, *i.e.*, p and q take their values on the the piece of the unperturbed homoclinic manifold Σ.

First we change variables from p, q to s, z:

$$\begin{aligned} dp \wedge dq &= \frac{\partial(p_0^z, q_0^z)}{\partial(s,z)} ds \wedge dz \\ &= \left(\frac{\partial p_0^z}{\partial s} \frac{\partial q_0^z}{\partial z} - \frac{\partial q_0^z}{\partial s} \frac{\partial p_0^z}{\partial z} \right) ds \wedge dz \\ &= -\left(\frac{\partial H}{\partial q} \frac{\partial q_0^z}{\partial z} + \frac{\partial H}{\partial p} \frac{\partial p_0^z}{\partial z} \right) ds \wedge dz \\ &= \left(-\frac{dH}{dz} + \frac{\partial H}{\partial z} \right) ds \wedge dz \,. \end{aligned} \tag{3.12}$$

For the second term in the integrand we change variables from H, t to s, z, noting that t is independent of s and that $z = \epsilon t$ is a fixed constant on every slice Π_z:

$$\begin{aligned} dH \wedge dt &= \frac{\partial(H,t)}{\partial(s,z)} ds \wedge dz \\ &= \left(\frac{\partial H}{\partial s} \frac{\partial t}{\partial z} - \frac{\partial H}{\partial z} \frac{\partial t}{\partial s} \right) ds \wedge dz \\ &= \left(\frac{\partial H}{\partial p} \frac{\partial p_0^z}{\partial s} + \frac{\partial H}{\partial q} \frac{\partial q_0^z}{\partial s} \right) \frac{1}{\epsilon} ds \wedge dz \\ &= \left(-\frac{\partial H}{\partial p} \frac{\partial H}{\partial q} + \frac{\partial H}{\partial q} \frac{\partial H}{\partial p} \right) \frac{1}{\epsilon} ds \wedge dz \\ &= 0. \end{aligned} \tag{3.13}$$

Inserting (3.12) and (3.13) into (3.10), we get

$$A_0 = \int \int_\Sigma \left[-\frac{dH}{dz} + \frac{\partial H}{\partial z} \right] ds \wedge dz \,, \tag{3.14}$$

which can be rewritten as the iterated integral

$$A_0 = \int_{Z_0}^{Z_1} \left(\int_{-\infty}^{\infty} \left[-\frac{dH}{dz} + \frac{\partial H}{\partial z} \right] (p_0^z(s - s_0), q_0^z(s - s_0), z)\, ds \right) dz \,, \tag{3.15}$$

where the variable z is held constant in the inner integral over s.

We remark that neither the integral of $\frac{dH}{dz}$ nor that of $\frac{\partial H}{\partial z}$ over s need exist individually (because H may have different values on Υ^{z_0} and Υ^{z_1} and because $\frac{\partial H}{\partial z}$

need not asymptote to zero as $s \to \pm\infty$). However, the entire integral is finite because Σ is compact and the sum $\frac{dH}{dz} - \frac{\partial H}{\partial z}$ is uniformly bounded. See Remark 6 after this proof.

Since $\frac{dH}{dz} = \frac{\partial H}{\partial z}$ at the fixed points (X_0^z, z) (because $\frac{\partial H}{\partial q}$ and $\frac{\partial H}{\partial p}$ vanish at (X_0^z, z)), we can add and subtract these terms from the integrand in (3.15) and then the two total derivative terms cancel each other (because H is constant on the entire separatrix for each value of z):

$$\begin{aligned} A_0 &= \int_{Z_0}^{Z_1} \left(\int_{-\infty}^{\infty} - \left[\frac{dH}{dz}(p_0^z(s-s_0), q_0^z(s-s_0), z) - \frac{dH}{dz}(X_0^z, z) \right] \right. \\ &\qquad \left. + \left[\frac{\partial H}{\partial z}(p_0^z(s-s_0), q_0^z(s-s_0), z) - \frac{\partial H}{\partial z}(X_0^z, z) \right] ds \right) dz \\ &= \int_{Z_0}^{Z_1} \left(\int_{-\infty}^{\infty} \left[\frac{\partial H}{\partial z}(p_0^z(s-s_0), q_0^z(s-s_0), z) - \frac{\partial H}{\partial z}(X_0^z, z) \right] ds \right) dz \\ &= \int_{Z_0}^{Z_1} M_A(z)\, dz\,, \end{aligned} \tag{3.16}$$

because the inner integral over s in the middle line of (3.16) becomes the adiabatic Melnikov function, $M_A(z)$, upon sending s to $s + s_0$. Hence we arrive at our closed form expression (3.11), and we have completed the proof of Lemma 3.1 and also the first half of the proof of Theorem 1.

To conclude this section, we make several remarks about the content of Lemma 3.1:

Remark 1. We can find a more convenient form for $M_A(z)$ as follows. We observe that upon using integration by parts with respect to s on the definition of $M_A(z)$, the boundary terms vanish (because

$$\left. \frac{\partial H}{\partial z} \right|_{(X_0^z, z)}^{(p_0^z(s), q_0^z(s), z)} \to 0 \tag{3.17}$$

as $t \to \pm\infty$) and the term $\frac{d}{ds}\frac{\partial H}{\partial z}(X_0^z, z)$ vanishes because it is independent of s. Thus, we are left with

$$A_0 = -\int_{Z_0}^{Z_1} \left(\int_{-\infty}^{\infty} s \frac{d}{ds} \frac{\partial H}{\partial z}(p_0^z(s), q_0^z(s), z)\, ds \right) dz\,. \tag{3.18}$$

Now, the mixed second partial of H by s and z is identically zero because H is a constant on any orbit on Γ. Therefore,

$$\begin{aligned} A_0 &= -\int_{Z_0}^{Z_1} \left(\int_{-\infty}^{\infty} s \left[\frac{\partial^2 H}{\partial p \partial z} \frac{\partial p_0^z}{\partial s} + \frac{\partial^2 H}{\partial q \partial z} \frac{\partial q_0^z}{\partial s} \right] ds \right) dz \\ &= \int_{Z_0}^{Z_1} \left(\int_{-\infty}^{\infty} s \left[\frac{\partial^2 H}{\partial p \partial z} \frac{\partial H}{\partial q} - \frac{\partial^2 H}{\partial q \partial z} \frac{\partial H}{\partial p} \right] ds \right) dz \\ &= \int_{Z_0}^{Z_1} \left(\int_{-\infty}^{\infty} s \{H, \frac{\partial H}{\partial z}\}\, ds \right) dz, \end{aligned} \tag{3.19}$$

where the inner integral in the middle line of (3.19) represents a more convenient way to compute $M_A(z)$ and is the form of $M_A(z)$ found in the references. Here $\{H, \frac{\partial H}{\partial z}\}$ denotes the Poisson bracket of H and $\frac{\partial H}{\partial z}$ with respect to (q, p).

Remark 2. The result of Lemma 3.1 is a striking one. In the limit of $\epsilon = 0$, the lobe area is an $\mathcal{O}(1)$ quantity. The collapse onto the autonomous system as $\epsilon \to 0$ is a discontinuous process, because slowly-modulated oscillators are singular perturbation problems. For every non-zero value of ϵ orbits evolve upward along the z-axis in $U \times \mathbb{R}$, and the smaller ϵ gets the more slowly they evolve. However, as soon as ϵ vanishes identically orbits are constrained to lie on one slice with z fixed and the rich structure of the tangling manifolds and the lobes no longer exists.

Remark 3. At first glance, (3.11) seems identical to the result for Hamiltonian systems subject to small-amplitude perturbations, see Rom-Kedar and Wiggins [1990a], MacKay and Meiss [1988] and Kovacic [1991]. However, whereas both the integrals of $M(s)$ and $M_A(z)$ are $\mathcal{O}(1)$ quantities, the integral of $M(s)$ is multiplied by ϵ in the regular perturbation case and the integral of $M_A(z)$ is not. Thus A_0

is an $\mathcal{O}(1)$ quantity to leading order for systems $(1.1)_\epsilon$ as opposed to the $\mathcal{O}(\epsilon)$ quantity it is for Hamiltonians subject to weak perturbations. This is because $Z_1 - Z_0 = \mathcal{O}(1)$ and $M_A(z)$ is of $\mathcal{O}(1)$ throughout the interval $[Z_0, Z_1]$. In turn the previous statement implies that for ϵ sufficiently small, all except possibly one of the pips may lie exponentially close to the point $\gamma_\epsilon \cap \Pi_z$, because the time of flight along the separatrix between adjacent intersection points is $\mathcal{O}(\frac{1}{\epsilon})$. See Figure 4.2 in Chapter 4 for an example in which this phenomenon occurs.

Remark 4. The integrands of the regular Melnikov function (for regularly-perturbed systems with $H = H_0(p,q) + \epsilon H_1(p,q,t)$) and the adiabatic Melnikov function (which as we have seen in Chapter 2 is for the singularly-perturbed systems we study with $H = H(p,q,z=\epsilon t)$) may be written in terms of a single Poisson Bracket, as follows

$$\begin{aligned}\{H, \frac{\partial H}{\partial \epsilon}\} &= \{H_0, H_1\} \\ &= t\{H, \frac{\partial H}{\partial z}\},\end{aligned}$$

respectively.

Remark 5. A_0 is determined entirely by the integral of $dp \wedge dq$ over Σ.

Remark 6. A straight forward computation shows that neither the integral of $\frac{dH}{dz}$ nor that of $\frac{\partial H}{\partial z}$ in (3.15) need exist individually. We begin with the first term in the integrand:

$$\begin{aligned}\int_{Z_0}^{Z_1}\int_{-\infty}^{\infty}\frac{dH}{dz}dsdz &= \int_{-\infty}^{\infty}\int_{Z_0}^{Z_1}\frac{dH}{dz}dzds \\ &= \int_{-\infty}^{\infty} H|_{Z_0}^{Z_1} ds \\ &= H|_{Z_0}^{Z_1}\int_{-\infty}^{\infty} ds \\ &= \Big(H(q_0^{Z_1}(s), p_0^{Z_1}(s), Z_1) - H(q_0^{Z_0}(s), p_0^{Z_0}(s), Z_0)\Big)\int_{-\infty}^{\infty} ds\end{aligned}$$

which is infinite in general because $H(q_0^{Z_0}, p_0^{Z_0}, Z_0) \neq H(q_0^{Z_1}, p_0^{Z_1}, Z_1)$ in general. For the second term in the integrand of (3.15), we find that $\frac{\partial H}{\partial z}(p_0^z(s), q_0^z(s), z)$ need not asymptote to zero as $s \to \pm\infty$. In fact in the pendulum example of Chapter 4 we find $\frac{\partial H}{\partial z}(p_0^z(s), q_0^z(s), z) \to -1$ as $s \to \pm\infty$. Thus the integral

$$\int_{-\infty}^{\infty} \frac{\partial H}{\partial z}(p_0^z(s), q_0^z(s), z)ds$$

is infinite in general and hence so is the integral

$$\int_{Z_0}^{Z_1} \int_{-\infty}^{\infty} \frac{\partial H}{\partial z}(p_0^z(s), q_0^z(s), z)dsdz.$$

However, the integral in (3.14) is finite because Σ is compact and the sum $-\frac{dH}{dz} + \frac{\partial H}{\partial z}$ is uniformly bounded. The integral in (3.15) exists as well because the first integral cancels out the infinite piece of the second integral.

3.3 Asymptotic Accuracy of the Approximation.

In this section we complete the proof of Theorem 1. We establish the expression for the difference $A - A_0$ between the exact and approximate lobe area formulas in Lemma 3.2, and in Lemma 3.3 we prove that $|A - A_0| = \mathcal{O}(\epsilon)$.

We first establish the homotopies which we use throughout the remainder of this section. We look at biasymptotic orbits of the vector fields

$$\begin{aligned} q' &= \frac{\partial H}{\partial p}(p, q, z) \\ p' &= -\frac{\partial H}{\partial q}(p, q, z) \\ z' &= \mu\epsilon \end{aligned} \tag{3.20}$$

with r as the time variable which is related by $\mu\epsilon r = \epsilon t$ to the time t of $(1.1)_\epsilon$, and $'$ indicates the derivative with respect to r. Here $\mu \in [0, 1]$ is the parameter of our

homotopies. We remark that $\mu = 0$ and $\mu = 1$ correspond to the unperturbed and perturbed vector fields $(1.1)_0$ and $(1.1)_\epsilon$, respectively. We refer to the vector fields with $\mu \in (0,1)$ as the intermediate vector fields. Finally, we remark that we use r to indicate the time variable of the intermediate vector fields.

Let Z_0 and Z_1 be two adjacent zeroes of the adiabatic Melnikov function whose existence is guaranteed by Assumption A3. The theory of the adiabatic Melnikov function states that there exist two orbits, $\mathcal{P}$ and $\mathcal{Q}$, in $(1.1)_\epsilon$, which correspond to the above zeroes of $M_A(z)$ and lie in the intersection of $W^S(\gamma_\epsilon)$ and $W^U(\gamma_\epsilon)$. These two orbits define the lobe whose area we measure. The theory of the adiabatic Melnikov function further guarantees that every intermediate vector field for $\mu \in (0,1)$ has a pair of intersection orbits as well. We label these intermediate intersection orbits by $\mathcal{P}_\mu$ and $\mathcal{Q}_\mu$. Then the Implicit Function Theorem can be used to show that, as μ is varied in the interval $(0,1]$, $\mathcal{P}_\mu$ and $\mathcal{Q}_\mu$ vary smoothly. In the limit of $\mu \to 0$, outside of the small tubular neighborhood, V_ρ, with radius ρ of γ, $\mathcal{P}_\mu$ and $\mathcal{Q}_\mu$ tend to the orbits Υ^{Z_1} and Υ^{Z_0}, respectively. However, as curves, $\mathcal{P}_\mu$ and $\mathcal{Q}_\mu$ limit on $\mathcal{P}_0$ and $\mathcal{Q}_0$ as $\mu \to 0$.

The homotopies define two smooth surfaces

$$\Omega^{\mathcal{P}} = (\cup_{\mu\in(0,1]}\mathcal{P}_\mu)\bigcup\gamma\bigcup\Upsilon^{Z_1} = (\cup_{\mu\in(0,1]}\mathcal{P}_\mu)\bigcup\mathcal{P}_0$$

and

$$\Omega^{\mathcal{Q}} = (\cup_{\mu\in(0,1]}\mathcal{Q}_\mu)\bigcup\gamma\bigcup\Upsilon^{Z_0} = (\cup_{\mu\in(0,1]}\mathcal{Q}_\mu)\bigcup\mathcal{Q}_0.$$

$\Omega^{\mathcal{P}}$ is spanned between $\mathcal{P}$ and $\mathcal{P}_0$, and $\Omega^{\mathcal{Q}}$ is spanned between $\mathcal{Q}$ and $\mathcal{Q}_0$. See Figure 3.5 for the three-dimensional visualization of $\Omega^{\mathcal{P}}$ and $\Omega^{\mathcal{Q}}$.

We now introduce the the solutions which uniquely parametrize $\mathcal{P}_\mu$ and $\mathcal{Q}_\mu$ by taking $z = \mu\epsilon r$, just as we took $z = \epsilon t$ for $(1.1)_\epsilon$ at the beginning of this section. We let $\mathbf{x}^{\mathcal{P}}_{\mu\epsilon}(r)$ and $\mathbf{x}^{\mathcal{Q}}_{\mu\epsilon}(r)$ denote the solutions which parametrize $\mathcal{P}_\mu$ and $\mathcal{Q}_\mu$,

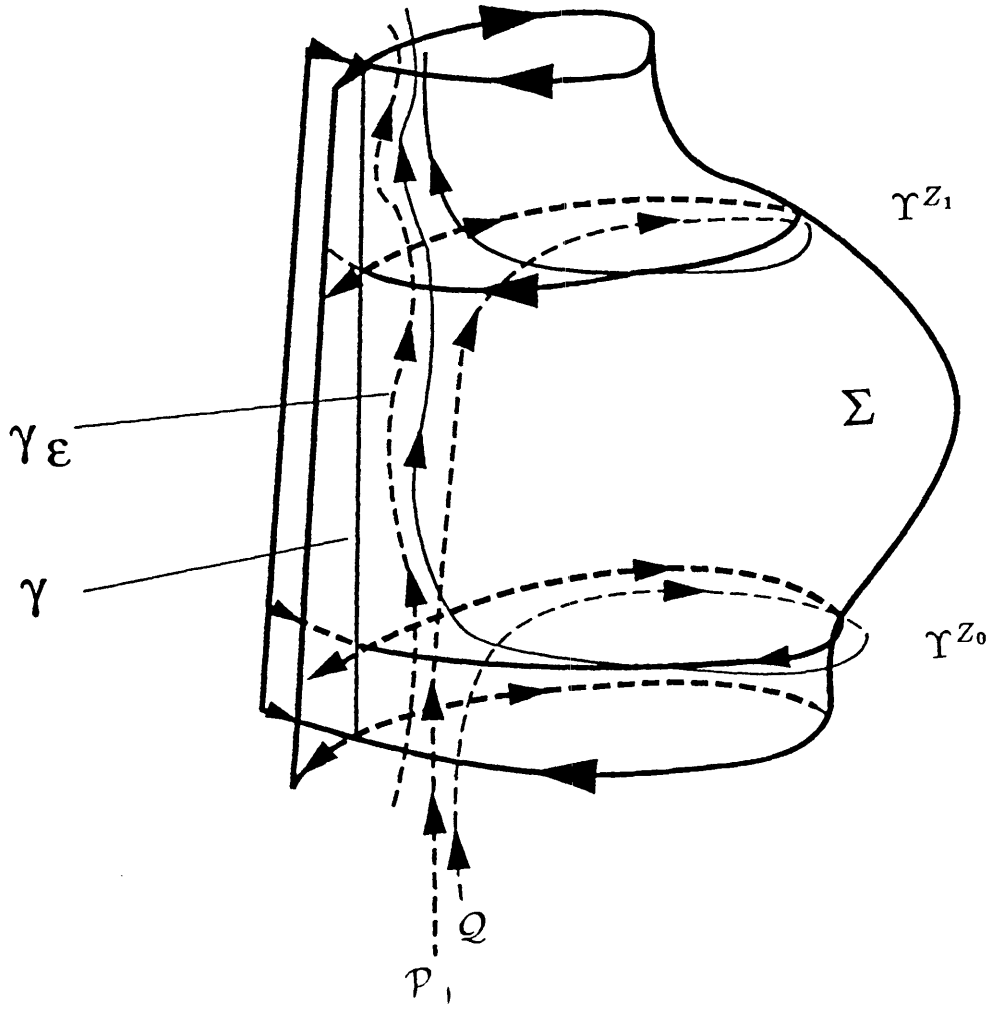

Fig. 3.5. The surfaces $\Omega^{\mathcal{P}}$ and $\Omega^{\mathcal{Q}}$.

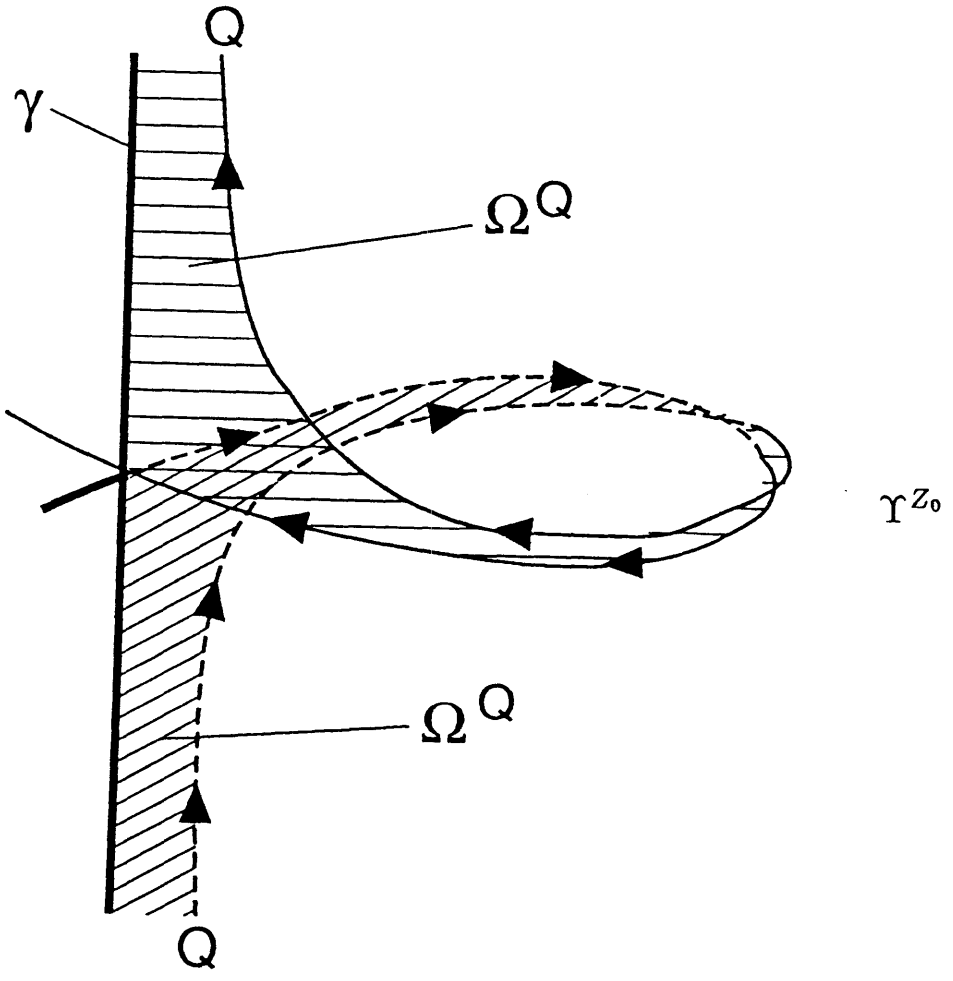

Fig. 3.5.b Detail of the surface $\Omega^{\mathcal{Q}}$.

respectively. We remark, however, that this parametrization does not include the $(\mu \to 0)$ limiting orbits Υ^{Z_0} and Υ^{Z_1} because of the discontinuity in the evolution of the z variable when $\mu = 0$. This discontinuity does not pose any difficulties in our calculations and is the reason why we defined the surfaces $\Omega^{\mathcal{P}}$ and $\Omega^{\mathcal{Q}}$ as unions of $\mathcal{P}_\mu$ and $\mathcal{Q}_\mu$, respectively, over $\mu \in (0, 1]$ with γ.

Lemma 3.2. *The difference between the exact lobe area, A, and the approximate area, A_0, is given by:*

$$A - A_0 = \int\int_{\Omega^{\mathcal{P}} - \Omega^{\mathcal{Q}}} dp \wedge dq - dH \wedge dt\,. \tag{3.21}$$

This integral must be performed over the difference of the two surfaces so that it is finite.

Proof of Lemma 3.2: Starting from the definitions of A and A_0, we know that

$$\begin{aligned} A - A_0 &= \int_{\mathcal{P}-\mathcal{Q}} (pdq - Hdt) - \int_{\mathcal{P}_0-\mathcal{Q}_0} (pdq - Hdt) \\ &= \lim_{Z\to\infty} \left\{ \int_{\mathcal{P}^Z-\mathcal{Q}^Z} (pdq - Hdt) - \int_{\mathcal{P}_0^Z-\mathcal{Q}_0^Z} (pdq - Hdt) \right\}, \end{aligned}$$

where $\mathcal{P}^Z$, $\mathcal{Q}^Z$, $\mathcal{P}_0^Z$, and $\mathcal{Q}_0^Z$ are the intervals of the curves for $z \in [z_2 - Z, z_2 + Z]$, where $z_2 \in \mathbb{R}$ chosen such that Z_0 and Z_1 lie in the interval and Z is sufficiently large. We remark that in all of the estimates in this proof the value of Z is fixed at the sufficiently large value used here. Furthermore, when we need r or t to be large, say R and T, respectively, the values of R and T are explicitly related to Z via $R = \frac{Z}{\mu\epsilon}$ and $T = \frac{Z}{\epsilon}$, respectively.

We will rewrite these integrals over the closed intervals of the curves $\mathcal{P}$, $\mathcal{Q}$, $\mathcal{P}_0$, and $\mathcal{Q}_0$ as integrals over compact pieces of the surfaces $\Omega^{\mathcal{P}}$ and $\Omega^{\mathcal{Q}}$ using Stokes'

Theorem. We will then show that the improper integrals obtained in taking the limit $Z \to \infty$ exist.

We define $\Omega_Z^{\mathcal{P}}$ to be the compact section of the side surface $\Omega^{\mathcal{P}}$ truncated by the slices Π_{z_2+Z} and Π_{z_2-Z}. $\Omega_Z^{\mathcal{Q}}$ is defined similarly. Let $\beta_Z^{\mathcal{P}}$, $\beta_Z^{\mathcal{Q}}$, $\beta_{-Z}^{\mathcal{P}}$ and $\beta_{-Z}^{\mathcal{Q}}$ be the intersections of the surfaces $\Omega^{\mathcal{P}}$ and $\Omega^{\mathcal{Q}}$ with the slices $\Pi_{z=z_2+Z}$ and $\Pi_{z=z_2-Z}$, respectively. We recall that $\mathbf{x}_{\mu\epsilon}^{\mathcal{P}}(r)$ and $\mathbf{x}_{\mu\epsilon}^{\mathcal{Q}}(r)$ denote the solutions we chose to parametrize $\mathcal{P}_\mu$ and $\mathcal{Q}_\mu$, respectively. The curves $\beta_Z^{\mathcal{P}}$ and $\beta_Z^{\mathcal{Q}}$ are formed by the solutions $\mathbf{x}_{\mu\epsilon}^{\mathcal{P}}(r)$ and $\mathbf{x}_{\mu\epsilon}^{\mathcal{Q}}(r)$ for $z = Z$ fixed (*i.e.*, $r = R = \frac{Z}{\mu\epsilon}$) and letting μ vary between 0 and 1. The other two curves are formed in a similar fashion. These curves will be referred to as the top and bottom pieces of the side surfaces $\Omega_Z^{\mathcal{P}}$ and $\Omega_Z^{\mathcal{Q}}$ and are are illustrated in Figure 3.5.

We now apply Stokes' Theorem to recast the integral over the compact surface $\Omega_Z^{\mathcal{P}} - \Omega_Z^{\mathcal{Q}}$ as a line integral around its boundary:

$$\int\int_{\Omega_Z^{\mathcal{P}}-\Omega_Z^{\mathcal{Q}}} dp \wedge dq - dH \wedge dt = \left(\int_{\mathcal{P}^Z - \mathcal{Q}^Z} - \int_{\mathcal{P}_0^Z - \mathcal{Q}_0^Z} + \int_{\beta_Z^{\mathcal{P}} - \beta_Z^{\mathcal{Q}}} - \int_{\beta_{-Z}^{\mathcal{P}} - \beta_{-Z}^{\mathcal{Q}}} \right) (pdq - Hdt)$$

The contributions from the integrals along the curves $\mathcal{P}^Z$, $\mathcal{Q}^Z$, ${\mathcal{P}_0}^Z$, and ${\mathcal{Q}_0}^Z$ as $Z \to \infty$ are exactly the pieces inside the limit in our original expression for $A - A_0$. Thus to establish (3.21), we only need to show that the contributions to $A - A_0$ from the top and bottom pieces of $\Omega_Z^{\mathcal{P}}$ and $\Omega_Z^{\mathcal{Q}}$ vanish in the limit $Z \to \infty$.

We evaluate the contribution from the top piece:

$$\int_{\beta_Z^{\mathcal{P}} - \beta_Z^{\mathcal{Q}}} (pdq - Hdt),$$

as that from the bottom piece in norm is bounded by the same term. First, we observe that, since we are on a slice of constant z, $dz = \epsilon dt = 0$. Hence,

$$\int_{\beta_Z^{\mathcal{P}} - \beta_Z^{\mathcal{Q}}} (pdq - Hdt) = \int_{\beta_Z^{\mathcal{P}} - \beta_Z^{\mathcal{Q}}} pdq.$$

Next, noting that $q = q_{\mu\epsilon}(r)$, $dz = 0 = \epsilon(\mu dr + r d\mu)$, and that R is dependent on μ in the way specified above so that Z is fixed for all $\mu \in (0,1]$, we can express the right hand side of the above expression as:

$$\begin{aligned}
\int_{\beta_Z^{\mathcal{P}} - \beta_Z^{\mathcal{Q}}} p dq &= \int_{\beta_Z^{\mathcal{P}} - \beta_Z^{\mathcal{Q}}} p \left[\frac{\partial q}{\partial r}\frac{\partial r}{\partial \mu} + \frac{\partial q}{\partial \mu}\right] d\mu \\
&= \int_0^1 \left(p\left[\frac{\partial q}{\partial r}\frac{\partial r}{\partial \mu} + \frac{\partial q}{\partial \mu}\right]\right)(\mathbf{x}_{\mu\epsilon}^{\mathcal{P}}(R))d\mu \\
&- \int_0^1 \left(p\left[\frac{\partial q}{\partial r}\frac{\partial r}{\partial \mu} + \frac{\partial q}{\partial \mu}\right]\right)(\mathbf{x}_{\mu\epsilon}^{\mathcal{Q}}(R))d\mu \qquad (3.22) \\
&= \int_0^1 \left(p\left[-\frac{\partial q}{\partial r}\frac{R}{\mu} + \frac{\partial q}{\partial \mu}\right]\right)\Big|_{\mathbf{x}_{\mu\epsilon}^{\mathcal{Q}}(R)}^{\mathbf{x}_{\mu\epsilon}^{\mathcal{P}}(R)} d\mu \\
&= \int_0^1 \left(p\left[\frac{\partial H}{\partial p}\frac{T}{\mu^2} + \frac{\partial q}{\partial \mu}\right]\right)\Big|_{\mathbf{x}_{\mu\epsilon}^{\mathcal{Q}}(R)}^{\mathbf{x}_{\mu\epsilon}^{\mathcal{P}}(R)} d\mu.
\end{aligned}$$

We rewrite the integrand in (3.22) in the usual way:

$$\begin{aligned}
\left(p\left[\frac{\partial H}{\partial p}\frac{T}{\mu^2} + \frac{\partial q}{\partial \mu}\right]\right)\Big|_{\mathbf{x}_{\mu\epsilon}^{\mathcal{Q}}(R)}^{\mathbf{x}_{\mu\epsilon}^{\mathcal{P}}(R)} &= p\Big|^{\mathbf{x}_{\mu\epsilon}^{\mathcal{P}}(R)} \cdot \left[\frac{\partial H}{\partial p}\frac{T}{\mu^2} + \frac{\partial q}{\partial \mu}\right]\Big|_{\mathbf{x}_{\mu\epsilon}^{\mathcal{Q}}(R)}^{\mathbf{x}_{\mu\epsilon}^{\mathcal{P}}(R)} \\
&+ p\Big|_{\mathbf{x}_{\mu\epsilon}^{\mathcal{Q}}(R)}^{\mathbf{x}_{\mu\epsilon}^{\mathcal{P}}(R)} \cdot \left[\frac{\partial H}{\partial p}\frac{T}{\mu^2} + \frac{\partial q}{\partial \mu}\right]\Big|^{\mathbf{x}_{\mu\epsilon}^{\mathcal{Q}}(R)}.
\end{aligned} \qquad (3.23)$$

We now find explicit bounds on each of the terms on the right hand side of the above expression: First, p asymptotes to $\pi_p \gamma_\epsilon$, where π_p denotes the projection of a point (p,q,z) onto its first component. Second, the (p,q) components of orbits on γ_ϵ are bounded in time by Assumption A2 and the persistence theory of Chapter 2. From these two facts we can conservatively estimate that for T sufficiently large,

$$|p\Big|^{\mathbf{x}_{\mu\epsilon}^{\mathcal{P}}(R)}| \leq K_1 R = K_1 \frac{T}{\mu},$$

for $Z = \epsilon T$ sufficiently large. Second, due to exponential contraction of the intersection orbits lying on $W^S(\gamma_\epsilon)$ and $W^U(\gamma_\epsilon)$ to γ_ϵ,

$$|p\Big|_{\mathbf{x}_{\mu\epsilon}^{\mathcal{Q}}(R)}^{\mathbf{x}_{\mu\epsilon}^{\mathcal{P}}(R)}| \leq K_2 R e^{-cR} = K_2 (\frac{T}{\mu}) e^{-\frac{cT}{\mu}},$$

for T sufficiently large. Furthermore, by Assumption A1, there exists a constant K_3 such that

$$|\frac{\partial H}{\partial p}(p,q;\epsilon\mu r)| \leq K_3$$

for all $r \in \mathbb{R}$. Finally, from Lemma 2.1, we know

$$|\frac{\partial q}{\partial \mu}\Big|_{\mathbf{x}^{\mathcal{Q}}_{\mu\epsilon}(R)}| \leq K_4 R = K_4(\frac{T}{\mu}),$$

for $Z = \epsilon T$ sufficiently large. Putting all of these estimates together, we arrive at:

$$|\left(p\left[\frac{\partial H}{\partial p}\frac{T}{\mu^2} + \frac{\partial q}{\partial \mu}\right]\right)\Big|_{\mathbf{x}^{\mathcal{Q}}_{\mu\epsilon}(R)}^{\mathbf{x}^{\mathcal{P}}_{\mu\epsilon}(R)}| \leq K_5 R e^{-cR} = K_5(\frac{T}{\mu})e^{-\frac{cT}{\mu}}, \tag{3.24}$$

for T sufficiently large.

Using (3.24) to estimate (3.23), we immediately have:

$$|\int_{\beta^{\mathcal{P}}_Z - \beta^{\mathcal{Q}}_Z}(pdq - Hdt)| \leq \frac{K_6}{c}Te^{-cT},$$

for T sufficiently large. We remark that one gets the same result for the contribution of the bottom end.

Therefore, combining the contributions from the top and bottom ends and letting $Z \to \infty$, *i.e.*, $T \to \infty$, establishes (3.21) and the existence of the improper integral as follows:

$$\begin{aligned}
&\int\int_{\Omega^{\mathcal{P}} - \Omega^{\mathcal{Q}}}(dp \wedge dq - dH \wedge dt) = \lim_{Z\to\infty}\left[\int\int_{\Omega^{\mathcal{P}^Z} - \Omega^{\mathcal{Q}^Z}}(dp \wedge dq - dH \wedge dt)\right] \\
&= \lim_{Z\to\infty}\left[\int_{\mathcal{P}^Z - \mathcal{Q}^Z} - \int_{\mathcal{P}^Z_0 - \mathcal{Q}^Z_0} + \int_{\beta^{\mathcal{P}}_Z - \beta^{\mathcal{Q}}_Z} - \int_{\beta^{\mathcal{P}}_{-Z} - \beta^{\mathcal{Q}}_{-Z}}\right](pda - Hdt) \\
&= \int_{\mathcal{P}-\mathcal{Q}}(pdq - Hdt) - \int_{\mathcal{P}_0 - \mathcal{Q}_0}(pdq - Hdt) \\
&= A - A_0.
\end{aligned}$$

Hence the proof of Lemma 3.2 is complete.

The above lemma again made strong use of hyperbolicity and its consequence that the orbits with the same μ on $\Omega^{\mathcal{P}}$ and $\Omega^{\mathcal{Q}}$ approach each other exponentially as $t \to \pm\infty$. In order to complete the second step of the proof we still need the estimate:

Lemma 3.3. $|A - A_0| = \mathcal{O}(\epsilon)$.

Proof of Lemma 3.3: We start with the expression (3.21) for the difference $A - A_0$ derived in the previous lemma:

$$A - A_0 = \int\int_{\Omega^{\mathcal{P}} - \Omega^{\mathcal{Q}}} dp \wedge dq - dH \wedge dt\,.$$

We change coordinates to μ and r as follows:

$$\begin{aligned} dp \wedge dq &= \frac{\partial(p,q)}{\partial(\mu,r)} d\mu \wedge dr \\ &= \left(\frac{\partial p_{\mu\epsilon}}{\partial \mu} \frac{\partial q_{\mu\epsilon}}{\partial r} - \frac{\partial p_{\mu\epsilon}}{\partial r} \frac{\partial q_{\mu\epsilon}}{\partial \mu} \right) d\mu \wedge dr \\ &= \left(\frac{\partial H}{\partial p} \frac{\partial p_{\mu\epsilon}}{\partial \mu} + \frac{\partial H}{\partial q} \frac{\partial q_{\mu\epsilon}}{\partial \mu} \right) d\mu \wedge dr. \end{aligned} \tag{3.25}$$

$$\begin{aligned} dH \wedge dt &= \frac{\partial(H,t)}{\partial(\mu,r)} d\mu \wedge dr \\ &= \left(\frac{\partial H}{\partial \mu} \frac{\partial t}{\partial r} - \frac{\partial H}{\partial r} \frac{\partial t}{\partial \mu} \right) d\mu \wedge dr \\ &= \left[\left(\frac{\partial H}{\partial p} \frac{\partial p_{\mu\epsilon}}{\partial \mu} + \frac{\partial H}{\partial q} \frac{\partial q_{\mu\epsilon}}{\partial \mu} + \frac{\partial H}{\partial z} \frac{\partial z}{\partial \mu} \right) \mu \right. \\ &\quad \left. - \left(\frac{\partial H}{\partial p} \frac{\partial p_{\mu\epsilon}}{\partial r} + \frac{\partial H}{\partial q} \frac{\partial q_{\mu\epsilon}}{\partial r} + \frac{\partial H}{\partial z} \frac{\partial z}{\partial r} \right) r \right] d\mu \wedge dr \\ &= \left[\left(\frac{\partial H}{\partial p} \frac{\partial p_{\mu\epsilon}}{\partial \mu} + \frac{\partial H}{\partial q} \frac{\partial q_{\mu\epsilon}}{\partial \mu} + \frac{\partial H}{\partial z} \epsilon r \right) \mu \right. \\ &\quad \left. - \left(\frac{\partial H}{\partial p} \frac{\partial p_{\mu\epsilon}}{\partial r} + \frac{\partial H}{\partial q} \frac{\partial q_{\mu\epsilon}}{\partial r} + \frac{\partial H}{\partial z} \cdot \mu\epsilon \right) r \right] d\mu \wedge dr \\ &= \mu \left(\frac{\partial H}{\partial p} \frac{\partial p_{\mu\epsilon}}{\partial \mu} + \frac{\partial H}{\partial q} \frac{\partial q_{\mu\epsilon}}{\partial \mu} \right) d\mu \wedge dr. \end{aligned} \tag{3.26}$$

Next, we observe that:

$$\frac{\partial p_{\mu\epsilon}}{\partial \mu} = \epsilon \frac{\partial p_{\mu\epsilon}}{\partial(\mu\epsilon)}$$
$$\frac{\partial q_{\mu\epsilon}}{\partial \mu} = \epsilon \frac{\partial q_{\mu\epsilon}}{\partial(\mu\epsilon)}.$$

Thus, the integrand in (3.21) can be rewritten as:

$$dp \wedge dq - dH \wedge dt = \epsilon(1-\mu)\left(\frac{\partial H}{\partial p}\frac{\partial p_{\mu\epsilon}}{\partial(\mu\epsilon)} + \frac{\partial H}{\partial q}\frac{\partial q_{\mu\epsilon}}{\partial(\mu\epsilon)}\right) d\mu \wedge dr. \tag{3.27}$$

Now we rewrite each of the two terms in (3.27) evaluated on the difference of the two surfaces in the usual way, ignoring the common factors out front. We rewrite only the first term here, because the second term can be handled in exactly the same fashion, to obtain:

$$\begin{aligned}\left(\frac{\partial H}{\partial p}\frac{\partial p_{\mu\epsilon}}{\partial(\mu\epsilon)}\right)\Big|_{x^{Q}_{\mu\epsilon}(r)}^{x^{P}_{\mu\epsilon}(r)} &= \left(\frac{\partial p_{\mu\epsilon}}{\partial(\mu\epsilon)}\right)\Big|^{x^{P}_{\mu\epsilon}(r)}\left(\frac{\partial H}{\partial p}\right)\Big|_{x^{Q}_{\mu\epsilon}(r)}^{x^{P}_{\mu\epsilon}(r)} \\ &+ \left(\frac{\partial p_{\mu\epsilon}}{\partial(\mu\epsilon)}\right)\Big|_{x^{Q}_{\mu\epsilon}(r)}^{x^{P}_{\mu\epsilon}(r)}\left(\frac{\partial H}{\partial p}\right)\Big|^{x^{Q}_{\mu\epsilon}(r)}.\end{aligned} \tag{3.28}$$

For the first term, we observe that $\left(\frac{\partial p_{\mu\epsilon}}{\partial(\mu\epsilon)}\right)\Big|^{x^{P}_{\mu\epsilon}(r)}$ grows at worst linearly in r by Lemma 2.1 in Chapter 2 and also that $\left(\frac{\partial H}{\partial p}\right)\Big|_{x^{Q}_{\mu\epsilon}(r)}^{x^{P}_{\mu\epsilon}(r)}$ decays exponentially for sufficiently large $|r|$ because of the exponential contraction of the intersection orbits to γ_ϵ. Switching variables from r to t (see the remark in the first paragraph of the proof of the previous lemma), we find that for $t = T$ sufficiently large

$$\left|\left(\frac{\partial p_{\mu\epsilon}}{\partial(\mu\epsilon)}\right)\Big|^{x^{P}_{\mu\epsilon}(\frac{T}{\mu})} \cdot \left(\frac{\partial H}{\partial p}\right)\Big|_{x^{Q}_{\mu\epsilon}(\frac{T}{\mu})}^{x^{P}_{\mu\epsilon}(\frac{T}{\mu})}\right| \leq K_1\left(\frac{T}{\mu}\right)e^{-\frac{cT}{\mu}}.$$

For the second term in (3.28), we observe that $\left(\frac{\partial p_{\mu\epsilon}}{\partial(\mu\epsilon)}\right)\Big|_{x^{Q}_{\mu\epsilon}(r)}^{x^{P}_{\mu\epsilon}(r)}$ decays exponentially for $|r| = R$ sufficiently large by Lemma 2.1. Furthermore, $\left(\frac{\partial H}{\partial p}\right)\Big|^{x^{Q}_{\mu\epsilon}(r)}$ is bounded by Assumption A1 for all $r \in \mathbb{R}$. Thus upon changing variables from r to t, we see

that the second term in (3.28) can be bounded by exactly the same expression as the first term, with a different constant of course. Therefore, we conclude that

$$\left|\left(\frac{\partial H}{\partial p}\frac{\partial p_{\mu\epsilon}}{\partial(\mu\epsilon)}\right)\Big|_{x^{Q}_{\mu\epsilon}(r)}^{x^{P}_{\mu\epsilon}(r)}\right| \leq K\left(\frac{T}{\mu}\right)e^{-\frac{cT}{\mu}}, \tag{3.29}$$

for $r = \frac{T}{\mu}$ and T sufficiently large. As remarked above, we get the same estimate for the second term in (3.27).

Now we rewrite the integral of (3.21) as an iterated integral on μ from 0 to 1 and on r from $-\infty$ to $+\infty$, change the variable on which the inner integration is performed from r to t so that the inner integral can be done uniformly in μ, and use (3.29) to estimate the integrand. The integrand of the inner integral vanishes exponentially as $t \to \pm\infty$ for all $\mu \in (0,1]$ because of the bound given in (3.29). Hence the inner integral converges uniformly in μ. Finally, we bound the absolute value of the outer integral by the maximum value of the inner integral:

$$\begin{aligned}
&\left|\int_0^1\int_{-\infty}^{+\infty}\left(\frac{\partial H}{\partial p}\frac{\partial p_{\mu\epsilon}}{\partial(\mu\epsilon)}\right)\Big|_{x^{P}_{\mu\epsilon}(\frac{t}{\mu})}^{x^{Q}_{\mu\epsilon}(\frac{t}{\mu})}+\left(\frac{\partial H}{\partial q}\frac{\partial q_{\mu\epsilon}}{\partial(\mu\epsilon)}\right)\Big|_{x^{P}_{\mu\epsilon}(\frac{t}{\mu})}^{x^{Q}_{\mu\epsilon}(\frac{t}{\mu})}dtd\mu\right| \\
&\leq \max_{\mu\in[0,1]}\left|\int_{-\infty}^{+\infty}\left(\frac{\partial H}{\partial p}\frac{\partial p_{\mu\epsilon}}{\partial(\mu\epsilon)}\right)\Big|_{x^{P}_{\mu\epsilon}(\frac{t}{\mu})}^{x^{Q}_{\mu\epsilon}(\frac{t}{\mu})}+\left(\frac{\partial H}{\partial q}\frac{\partial q_{\mu\epsilon}}{\partial(\mu\epsilon)}\right)\Big|_{x^{P}_{\mu\epsilon}(\frac{t}{\mu})}^{x^{Q}_{\mu\epsilon}(\frac{t}{\mu})}dt\right|,
\end{aligned}$$

which is finite because the convergence of the integral is uniform in μ. Therefore,

$$|A - A_0| \leq K\epsilon. \tag{3.30}$$

Thus we have completed the proof of Lemma 3.3 and also that of Theorem 1. Furthermore, we have established the rigorous connection between the theory of actions for adiabatic systems from the field of classical mechanics and the theory of the adiabatic Melnikov function from the field of global bifurcations.

3.4 A Maximum Property for the Lobe Area.

In this section we state Proposition 3.1, a maximum property for the lobe area in systems $(1.1)_\epsilon$, which we published in Kaper and Wiggins [1991a]. In particular, we show that the zeroes of the adiabatic Melnikov function occur in such a way that the area A_0 (determined by the separatrices Υ^{Z_0} and Υ^{Z_1}) is locally the largest possible. We remark that unless stated otherwise the notation used for and the assumptions made on the equations of this section are identical to those used in the previous sections.

We take $\Sigma(z_i, z)$ to be the piece of Γ with the variable z restricted to the interval $[z_i, z]$, where z_i is a constant. Second, we define the function:

$$A(z_i, z) = \int\int_{\Sigma(z_i,z)} dp \wedge dq, \tag{3.31}$$

which is the area of the projection of $\Sigma(z_i, z)$ on a slice Π_z. A proof identical to the one of Lemma 3.1 shows that the function A can also be written as:

$$A(z_i, z) = \int_{z_i}^{z} \Big[\int_{-\infty}^{\infty} s\{H, \frac{\partial H}{\partial z}\} ds \Big] dz, \tag{3.32}$$

which is the integral of $M_A(z)$ over $\Sigma(z_i, z)$.

We establish:

Proposition 3.1. *The adjacent zeroes, Z_0 and Z_1, of $M_A(z)$ choose the separatrices Υ^{Z_0} and Υ^{Z_1} in such a way that $A(Z_0, Z_1)$ is a local maximum of $A(z_i, z)$.*

Proof of Proposition 3.1 Clearly,

$$\frac{dA}{dz}(z_i, \bar{z}) = \int_{-\infty}^{\infty} s\{H, \frac{\partial H}{\partial z}\}\Big|_{z=\bar{z}} ds = M_A(\bar{z}). \tag{3.33}$$

Thus we know that Z_0 and Z_1 are simple zeroes of $\frac{dA}{dz}(z_i, \bar{z})$, because Z_0 and Z_1 are simple zeroes of $M_A(z)$. Now we remark that because $\frac{dM_A}{dz}(z)$ has different signs

at Z_0 and Z_1,

$$\frac{d^2A}{dz^2}(z_i, Z_0) \quad \text{and} \quad \frac{d^2A}{dz^2}(z_i, Z_1) \tag{3.34}$$

are of opposite signs, as well. Thus the adiabatic Melnikov function picks out in a natural fashion a pair of adjacent local extremas, one minimum and one maximum, of $A(z_i, z)$ and the minimal and maximal separatrices Υ^{Z_0} and Υ^{Z_1}, respectively.

Finally, we know that

$$A(Z_1, Z_0) = A(z_i, Z_1) - A(z_i, Z_0). \tag{3.35}$$

Hence $A(Z_0, Z_1)$ is a local maximum of $A(z_i, z)$, and the proposition is proven.

As a corollary to the above proposition, we have:

Corollary 3.2. *If H is periodic in z such that there is one value of z, say Z_0, per period such that the area enclosed by the separatrix of $(5.1)_0^z$ is a maximum and such that there is one value of z, say Z_1, per period such that the area enclosed by the separatrix of $(5.1)_0^z$ is a minimum and if in between Z_0 and Z_1, the area enclosed by the separatrix of $(5.1)_0^z$ is a monotone function of z with nonvanishing derivatives with respect to z, then to leading order A is the area between the separatrices which enclose the maximum and minimum areas.*

We remark that the result of this corollary is exactly what we find in the adiabatic pendulum example below.

3.5. Action-Minimizing and Minimax Homoclinic Orbits.

We conclude this chapter with a few observations about the nature of the two biasymptotic orbits defining a lobe. The homoclinic orbits of $(1.1)_\epsilon$ are of two types. One corresponds to a minimum of the action and the other type corresponds

to a minimax (*i.e.*, local maximum) of the action, see MacKay *et al.*, [1984]. The observations we made about $M_A(z)$ in the previous section determines this correspondence.

As $\epsilon \to 0$, the homoclinic orbit $\mathcal{Q}$ limits on the separatrix Γ^{Z_1}. Therefore, because Γ^{Z_1} is a local minimum of $A(z_i, z)$, $\mathcal{Q}$ is a local minimum of the action. Similarly, as $\epsilon \to 0$, the homoclinic orbit $\mathcal{P}$ limits on the separatrix Γ^{Z_0}. Therefore, because Γ^{Z_0} is a local maximum of $A(z_i, z)$, $\mathcal{P}$ is a local maximum of the action. In other words, the homoclinic orbit corresponding to $\bar{z}$ such that $\frac{dM_A}{dz}(\bar{z}) > 0$ and $M_A(\bar{z}) = 0$ is a local minimum, and the homoclinic orbit corresponding to $\bar{z}$ such that $\frac{dM_A}{dz}(\bar{z}) < 0$ and $M_A(\bar{z}) = 0$ is a local maximum. We remark that a similar correspondence, between the well-known Melnikov function for small-amplitude perturbations (see MacKay and Meiss [1986]) and the type (either action-minimizing or minimax) of the homoclinic orbit, must also apply in the case of small amplitude perturbations where the geometric identification of the minimum and the minimax homoclinic orbits is not as clear as it is for adiabatic problems. Finally, we remark that the action-minimizing homoclinic orbits can only be the accumulation points of action-minimizing periodic orbits; and the action-minimax homoclinic orbits can be the accumulation points of both action-minimizing and action-minimax periodic orbits.

CHAPTER 4. TWO PARADIGM PROBLEMS IN ADIABATIC CHAOS.

In this chapter we study two paradigm problems in adiabatic chaos: a pendulum whose base support is oscillated vertically, slowly, and periodically in time, see Chapter 1, Kaper and Wiggins [1991a], Elskens and Escande [1991], and Wiggins [1988a, 1988b], and a model equation due to Hastings and McLeod involving a slowly-varying cubic potential, see Hastings and McLeod [1991] and Kaper and Wiggins [1991c]. These two problems illustrate the result of Theorem 1 and the Corollary. Furthermore, on the second example we show for the first time in the literature on slowly-modulated systems that a horseshoe map can be created in only one iteration of the Poincaré map. A similar construction exists for the pendulum example. We remark that we study a third example, namely the fluid mechanics problem analyzed in Part II of this thesis, in great detail there.

4.1. The Adiabatic Pendulum.

The results of Chapter 3 are nicely illustrated on the adiabatic pendulum. As discussed in the introductory chapter, this is a pendulum with slowly varying base support governed by the Hamiltonian

$$H = \frac{p^2}{2} - (1 - \gamma \cos(z = \epsilon t)) \cos q \,, \tag{4.1}$$

where $\gamma \in (0,1)$. For every value of $z \in [0, 2\pi)$, the autonomous system, (4.1) with $\epsilon = 0$, has hyperbolic fixed points at $(k\pi, 0)$, for all $k \in \mathbf{Z}$. These points are all the same point due to the periodicity of the vector field in q. We only look at $(-\pi, 0)$ and $(\pi, 0)$. These two points are connected to each other by upper and

lower separatrices parametrized by

$$(p_0^z(s), q_0^z(s))$$
$$= (\pm 2\sqrt{1-\gamma\cos z}\,\mathrm{sech}(\sqrt{1-\gamma\cos z}s), \pm 2\arcsin(\tanh\sqrt{1-\gamma\cos z}s)),$$

where we use s as the time variable of the unperturbed system just as in Chapters 2 and 3. For convenience we consider only the upper half plane $p > 0$. The picture for the lower half plane is obtained by a 180^0 rotation. From the definition, we compute

$$\begin{aligned} M_A(z) &= \gamma \int_{-\infty}^{+\infty} s p_0^z(s) \sin(q_0^z(s)) \sin z ds \\ &= \frac{4\gamma \sin z}{\sqrt{1-\gamma\cos z}}. \end{aligned} \tag{4.2}$$

Thus we see that M_A has an infinite number of simple zeroes, and we know that the stable and unstable manifolds of γ_ϵ intersect transversely in an infinite sequence of pips for ϵ sufficiently small. The Poincaré maps for $s_0 = 0, \gamma = 0.75$, and various values of ϵ are shown in Figure 4.2.

From (4.2) we compute

$$\begin{aligned} A_0 &= 4\gamma \int_0^{\pi} \frac{\sin z}{\sqrt{1-\gamma\cos z}}\, dz \\ &= 8(\sqrt{1+\gamma} - \sqrt{1-\gamma}) \\ &= A_S\,, \end{aligned} \tag{4.3}$$

where A_S is precisely the difference in the areas enclosed by the separatrices of the unperturbed system in the upper half plane corresponding to $z = \pi$ and $z = 0$, respectively. See Figure 4.1 and Table 4.1. Thus by Theorem 1, $A = A_S + \mathcal{O}(\epsilon)$.

We discuss some transport issues about how the lobes are mapped for the adiabatic pendulum later in this subsection. The simplest way to untangle the two entwined heteroclinic tangles is to write down the Birkhoff signatures for each and then nest them. A further study of transport via the wildly-shaped lobes of adiabatic

	epsilon	lobe area
$\gamma = 0.5$	$2\pi/15$	3.74
$\gamma = 0.5$	$2\pi/18$	3.84
$\gamma = 0.5$	$2\pi/20$	3.88
$\gamma = 0.5$	$2\pi/25$	3.94
$\gamma = 0.5$	$2\pi/30$	3.97
$\gamma = 0.5$	0	$A_0 = A_s = 4.14$

Table 1: Lobe area vs. ϵ based on a numerical trapezoidal rule sum integration.
The lobe area increases as ϵ decreases.
Numerical solution of $(5.1)_\epsilon$ done using a fourth order symplectic integrator.

Table 4.1.

systems is presented in Part II of this thesis. Also, one can readily construct Smale horseshoes in one iteration of the Poincaré map.

Smale Horseshoes in the Adiabatic Pendulum.

The existence of orbits homoclinic to hyperbolic periodic orbits in systems of the form $(1.1)_\epsilon$ has interesting dynamical consequences. From the Smale-Birkhoff Theorem (see Smale [1963], Guckenheimer and Holmes [1983], and Wiggins [1988]), we know that some iterate of the Poincaré map, *i.e.*, that T^n for some $n \in \mathbf{N}$ and $n \geq 1$, has an invariant Cantor set, Λ, on which it is topologically conjugate to a Bernoulli shift on the space of sequences of a countable number of symbols. From this it follows that $T|_\Lambda$ has:

1. a countable infinity of periodic orbits of all periods;
2. an uncountable infinity of (bounded) nonperiodic orbits; and
3. an orbit that is dense in Λ.

Moreover, all of the orbits of Λ are of saddle stability type.

4.1.1. The Homoclinic Tangles of Adiabatic Systems.

To conclude this section, we make a few remarks about the homoclinic tangles in slowly-modulated oscillators, and the implications this knowledge of the homoclinic tangles has on orbits crossing the pseudo-separatrices and on the study of transport, which we study in Part II of this thesis.

The lobes of the tangles in time-periodic adiabatic systems are nested in a complex manner. The geometry of the lobes in the tangles is given by the intersection of two Birkhoff signatures, see Abraham and Shaw [1984], one signature for each of the two broken heteroclinic orbits. For the pendulum, see Figure 4.3, one lobe from each turnstile $L_{I,II}(1)$ from the upper tangle lying at at the pip $h_0^+(0)$ near the reference

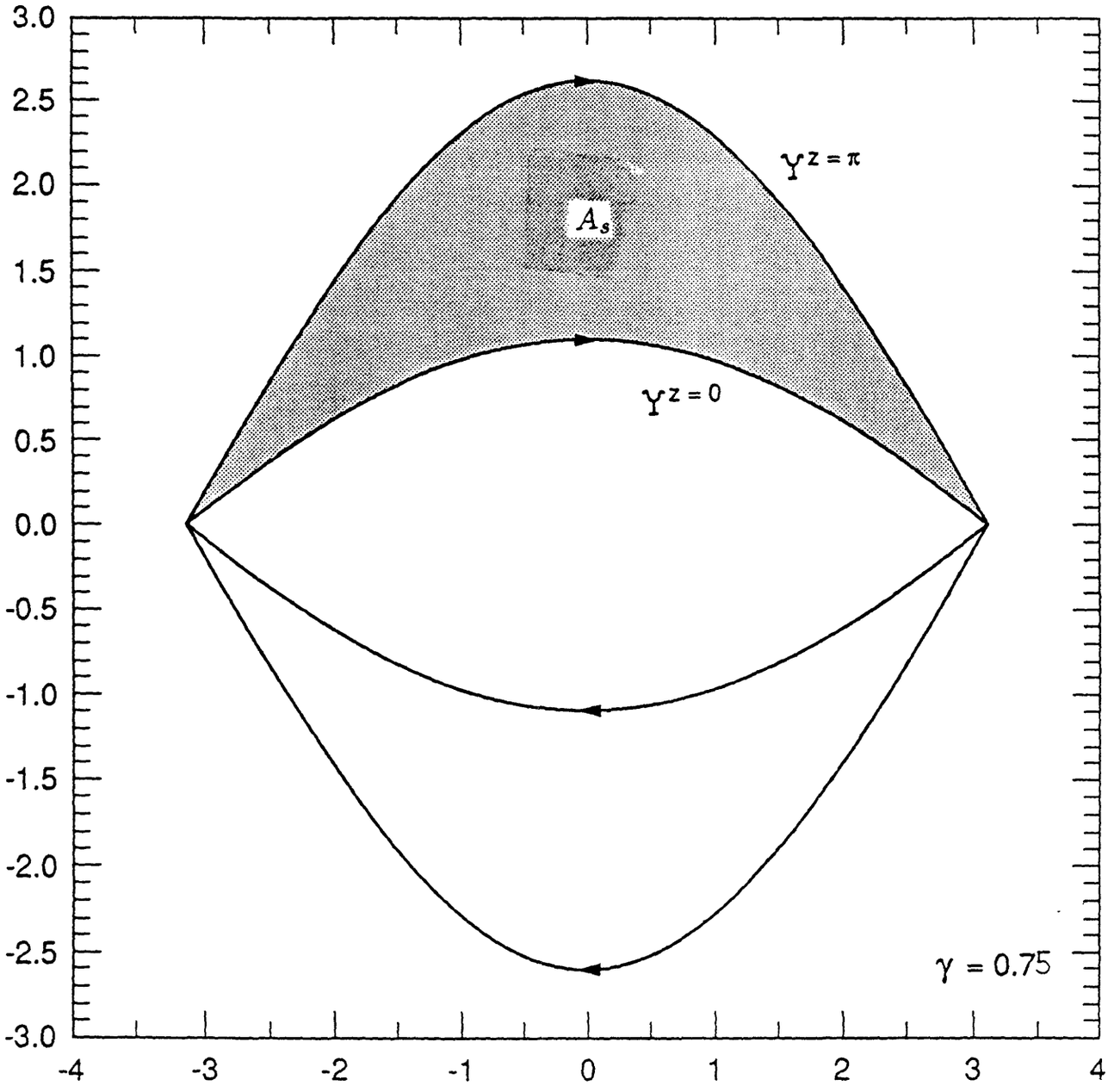

Fig. 4.1. The region A_S between the maximum and minimum instantaneous separatrices $\Upsilon^{z=\pi}$ and $\Upsilon^{z=0}$, respectively.

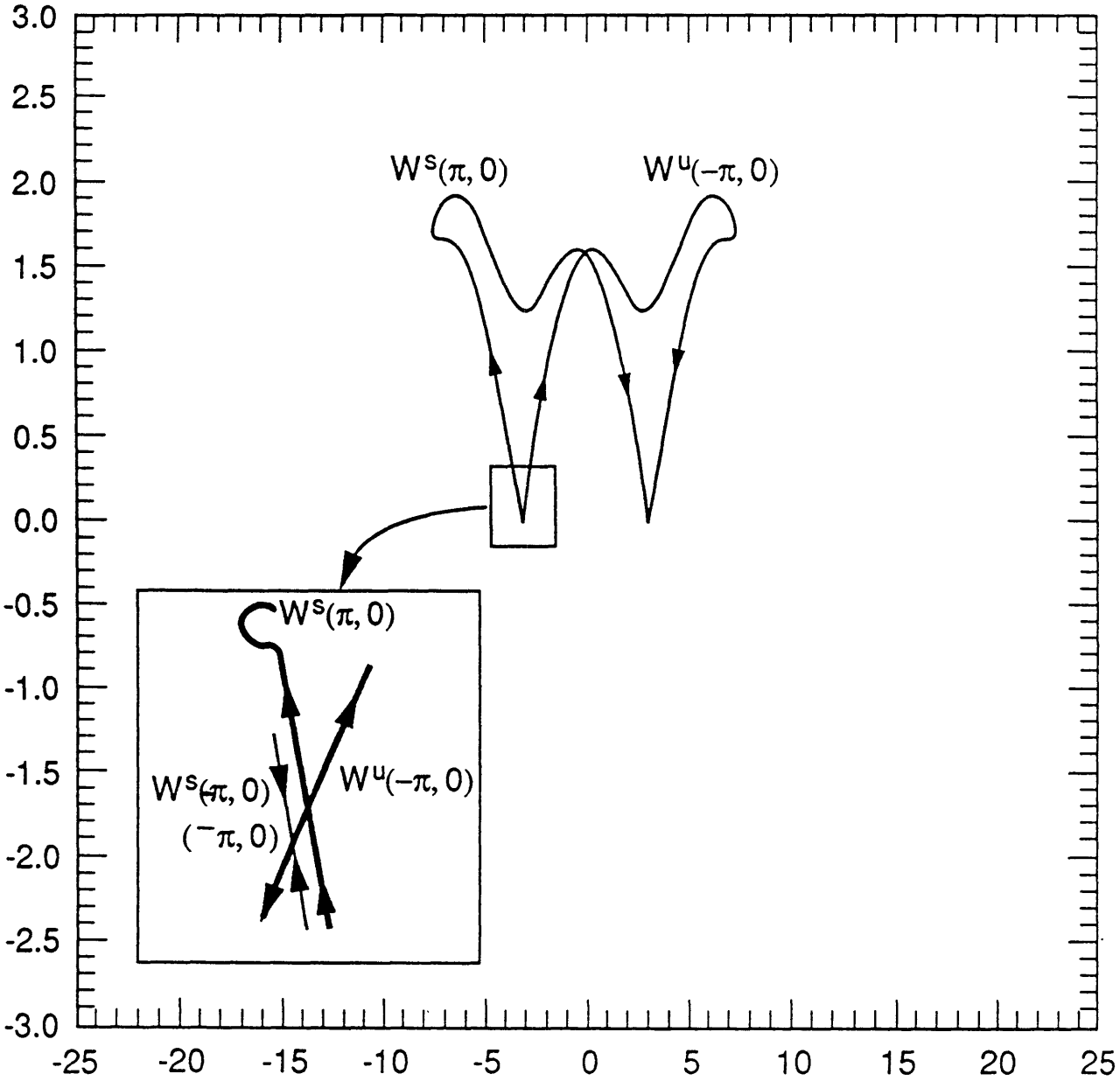

Fig. 4.2.a. The Poincaré map showing the main turnstile lobe $L_{I,II}(1)$ for $\epsilon = \frac{2\pi}{12}$.

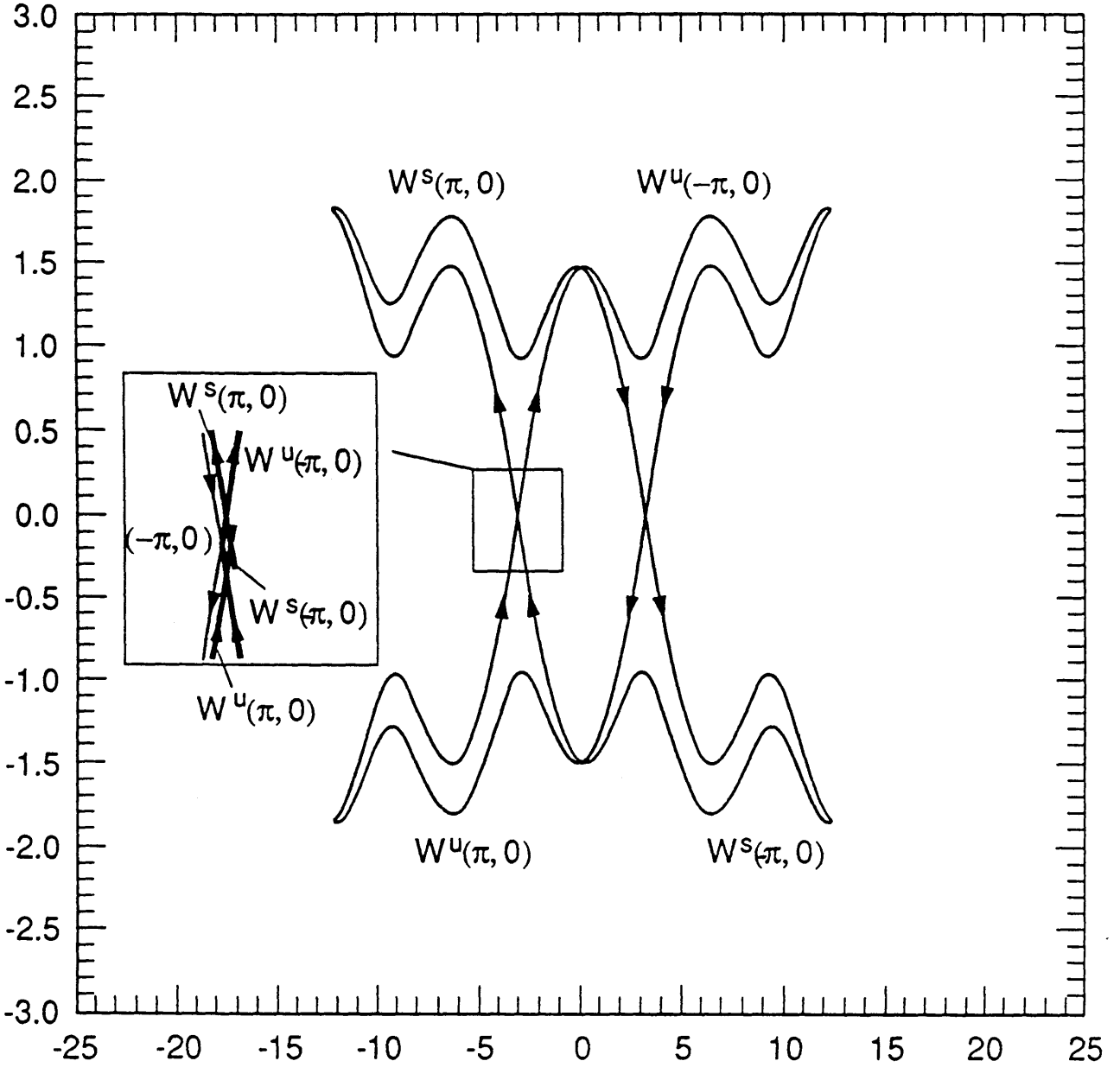

Fig. 4.2.b. The Poincaré map showing the main turnstile lobe $L_{I,II}(1)$ for $\epsilon = \frac{2\pi}{20}$.

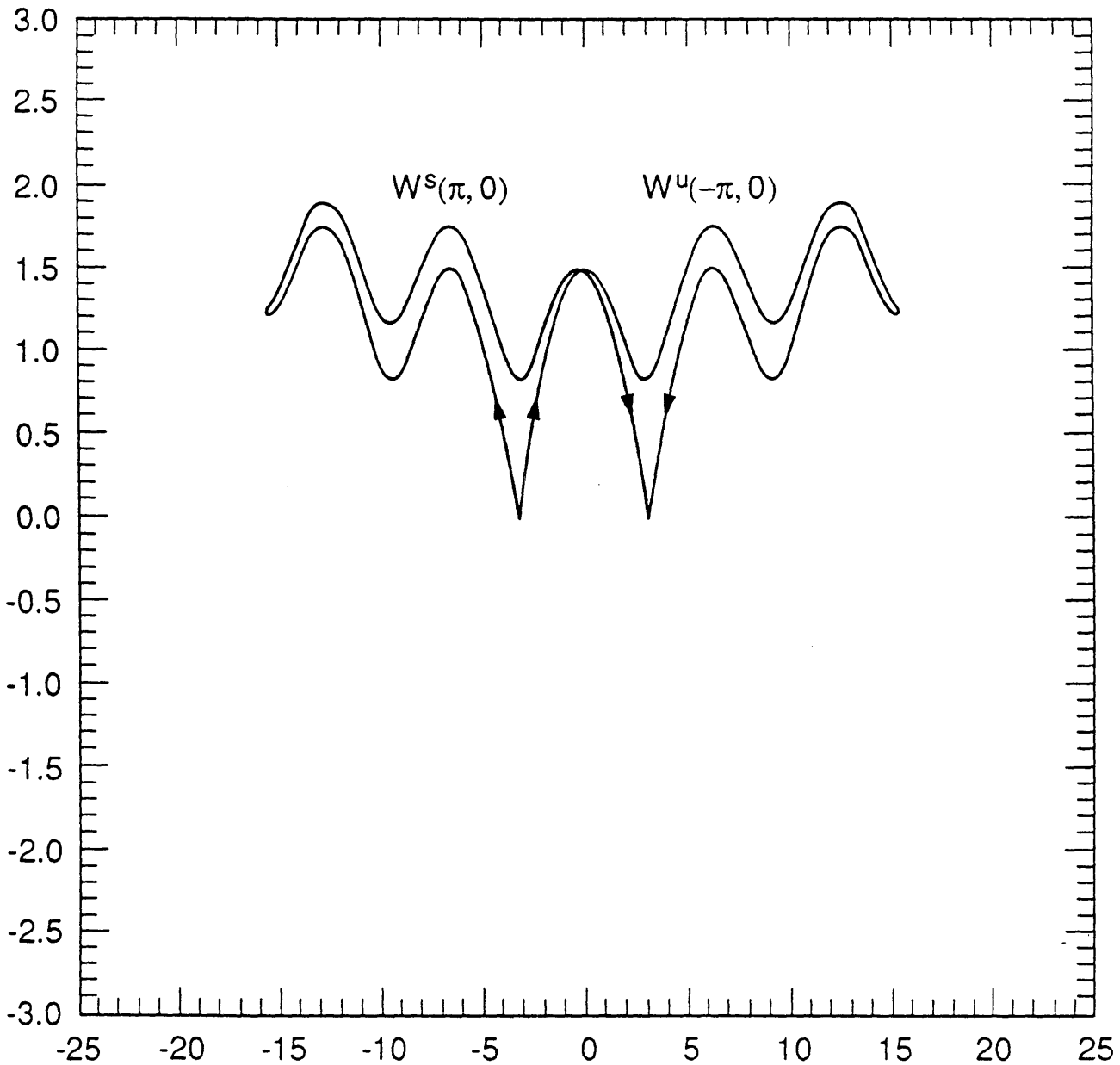

Fig. 4.2.c. The Poincaré map showing the main turnstile lobe $L_{I,II}(1)$ for $\epsilon = \frac{2\pi}{25}$.

point, and $L_{III,II}(1)$ from the lower tangle (equivalent to $L_{I,II}(1)$ under 180^o rotation in the $p-q$ plane) lying at the pip $h_0^-(0)$ lie completely in the rotating regions at the z time for which the minimum separatrix occurs. Most of the area contained inside the other lobe from each turnstile pair lies nested in these first two turnstile lobes in the rotating regions I and III, respectively. The other turnstile lobes have only thin slivers in the oscillating region. For example, the images of $L_{I,II}(1)$ and $L_{III,II}(1)$, labeled as $TL_{I,II}(1)$ and $TL_{III,II}(1)$, respectively, have extremely thin slivers in region II but most of their content lies in regions I and III. Thus, there is a mechanism for an orbit to get transported from one rotating region into the other rotating region in one period of the vector field, and this type of transport should occur much more frequently than that between the middle (oscillating) region and either of the rotating regions I or III. This may have consequences for schemes which use asymptotic approximations for describing the rate of change of the adiabatic invariant near separatrices. Much more work using the detailed knowledge of the tangles and lobe dynamics to answer the pseudo-separatrix crossing and transport questions for adiabatic Hamiltonians needs to be done.

4.2. The Example of Hastings and Mcleod.

The system studied by Hastings and McLeod [1991] is:

$$\begin{aligned} \dot{q} &= p \\ \dot{p} &= q^2 - (1 + c + \cos z) \\ \dot{z} &= \epsilon \end{aligned} \tag{4.4}$$

where $0 < \epsilon \ll 1$.

The Hamiltonian is given by:

$$H(p, q, z) = \frac{p^2}{2} - \frac{q^3}{3} + q(1 + c + \cos z).$$

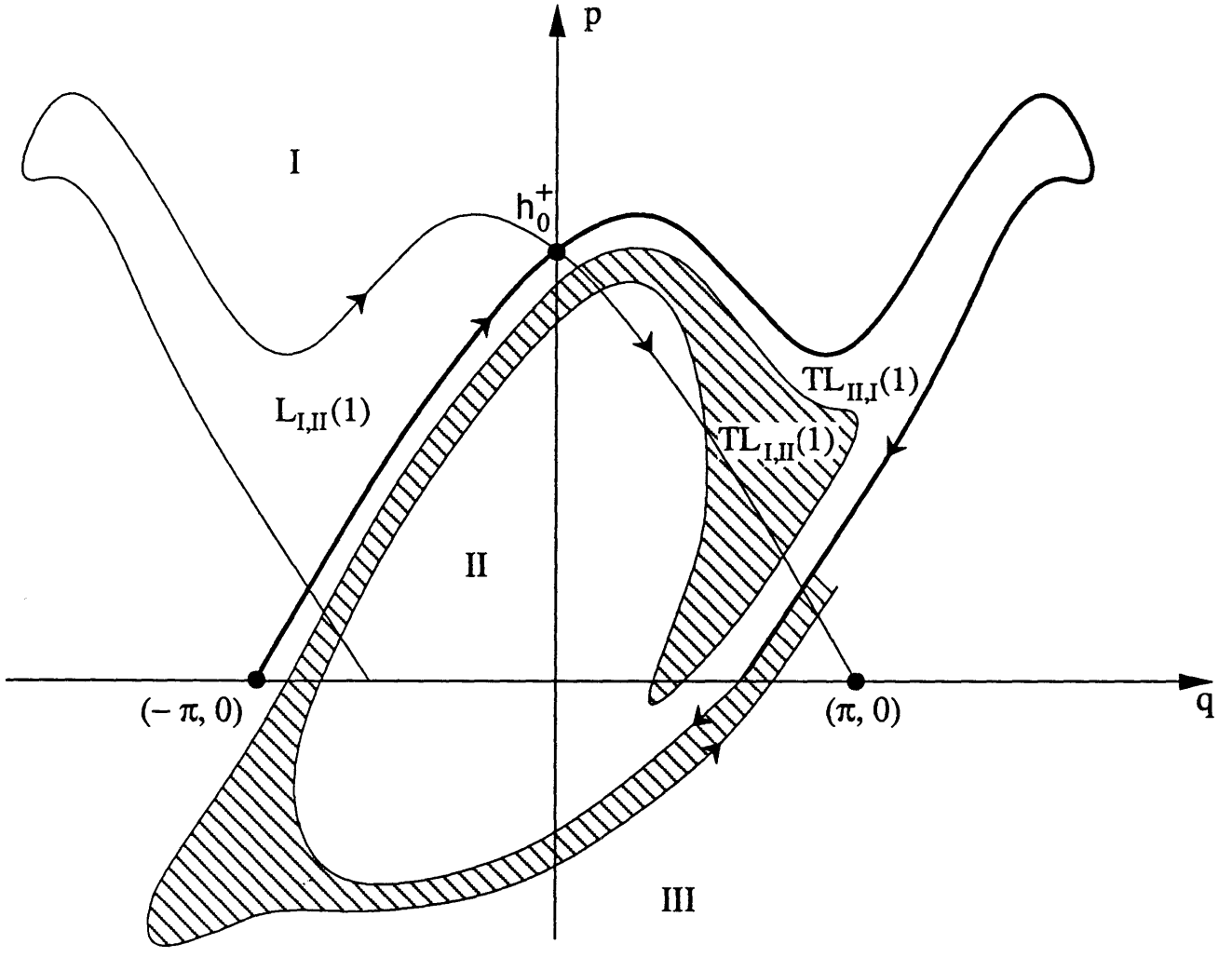

Fig. 4.3. Turnstile lobes and their images in the pendulum.

For every $z \in [0, 2\pi)$ and for $c > 0$, (4.4) has fixed points at $(\pm\sqrt{1+c+\cos z}, 0)$. The point $(\sqrt{1+c+\cos z}, 0)$ is a hyperbolic fixed point connected to itself by a homoclinic orbit

$$(p_0^z(s), q_0^z(s)) = \left(F^{\frac{1}{2}}(z)\left[1 - 3\mathrm{sech}^2(\frac{F^{\frac{1}{4}}(z)}{\sqrt{2}}s)\right], 3\sqrt{2}F^{\frac{3}{4}}(z)\mathrm{sech}^2(\frac{F^{\frac{1}{4}}(z)}{\sqrt{2}}s)\cdot\tanh(\frac{F^{\frac{1}{4}}(z)}{\sqrt{2}}s)\right), \tag{4.5}$$

where $F(z) \equiv 1 + c + \cos z$.

Using (4.5), we compute the adiabatic Melnikov function:

$$M_A(z) = 6\sqrt{2}F^{\frac{1}{4}}(z)\sin z. \tag{4.6}$$

Hence, $M_A(z)$ has simple zeroes at $z = k\pi$, $W^U(\gamma_\epsilon(z))$ and $W^S(\gamma_\epsilon(z))$ intersect transversely, and (4.4) possesses a Smale horseshoe. We sketch the domain of the Poincaré map for $z = \pi$ in the figures. Just as for the adiabatic pendulum, we find that at most one of the pips lies outside of an (arbitrarily) small neighborhood of X_ϵ. The existence of transverse intersections and the Smale horseshoe implies that some iterate of the Poincaré map T, say T^n for some $n \geq 1$, has an invariant Cantor set, Λ, on which it is topologically conjugate to a Bernoulli shift on sequences of a countable number of symbols. In the figures we sketch a horseshoe with $n = 1$.

We remark that

$$\frac{dM_A}{dz}(\pi) = -6\sqrt{2}c^{\frac{1}{4}} < 0. \tag{4.8}$$

Hence, the relative orientation of $W^U(\gamma_\epsilon(z))$ and $W^S(\gamma_\epsilon(z))$ at h_0 is as illustrated. Also, the homoclinic orbit through h_0 is a local minimum of the action, due to the results of Chapter 3.5.

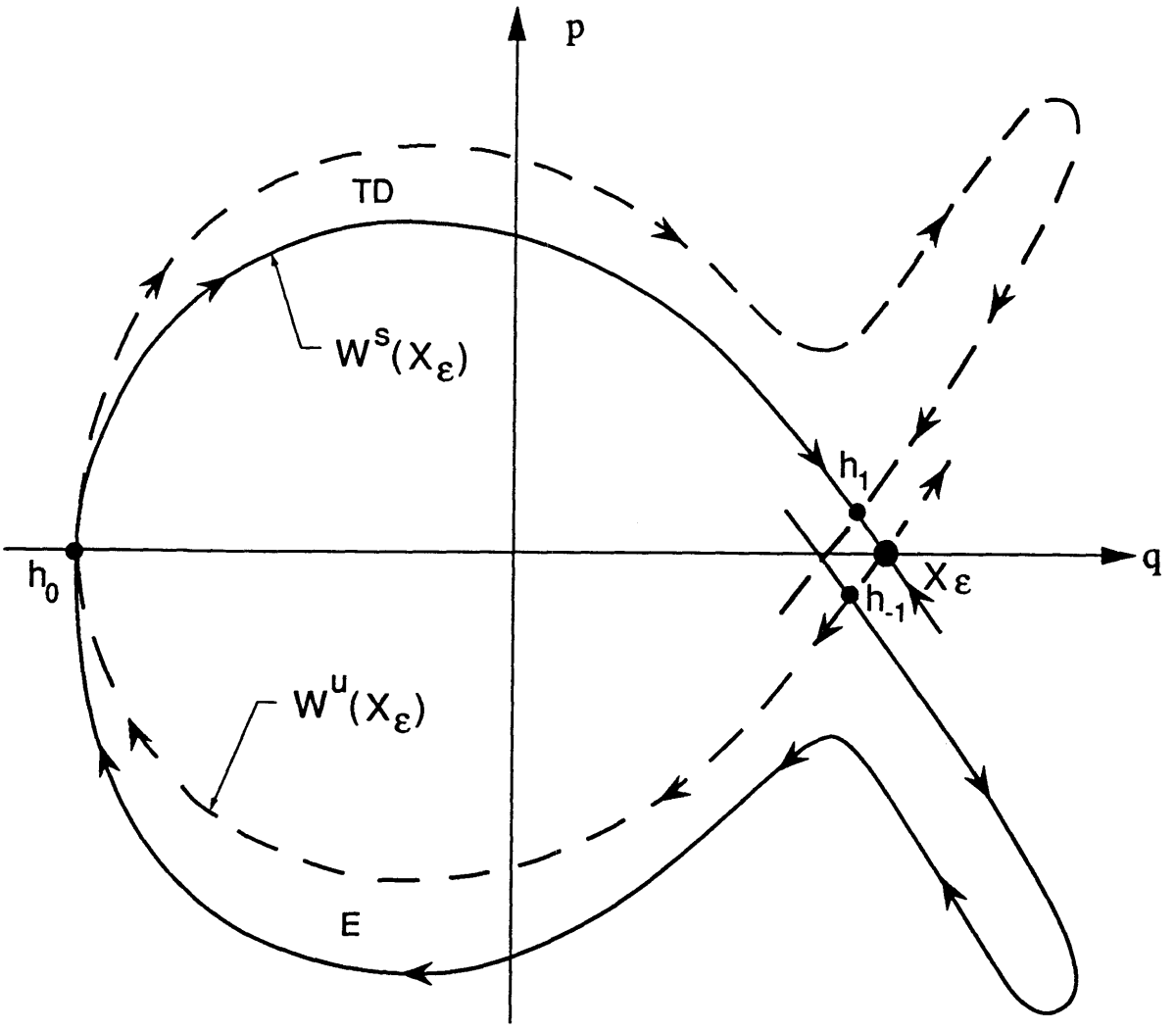

Fig. 4.4.a. A sketch of the basic structure of the tangle in the example of Hastings and McLeod.

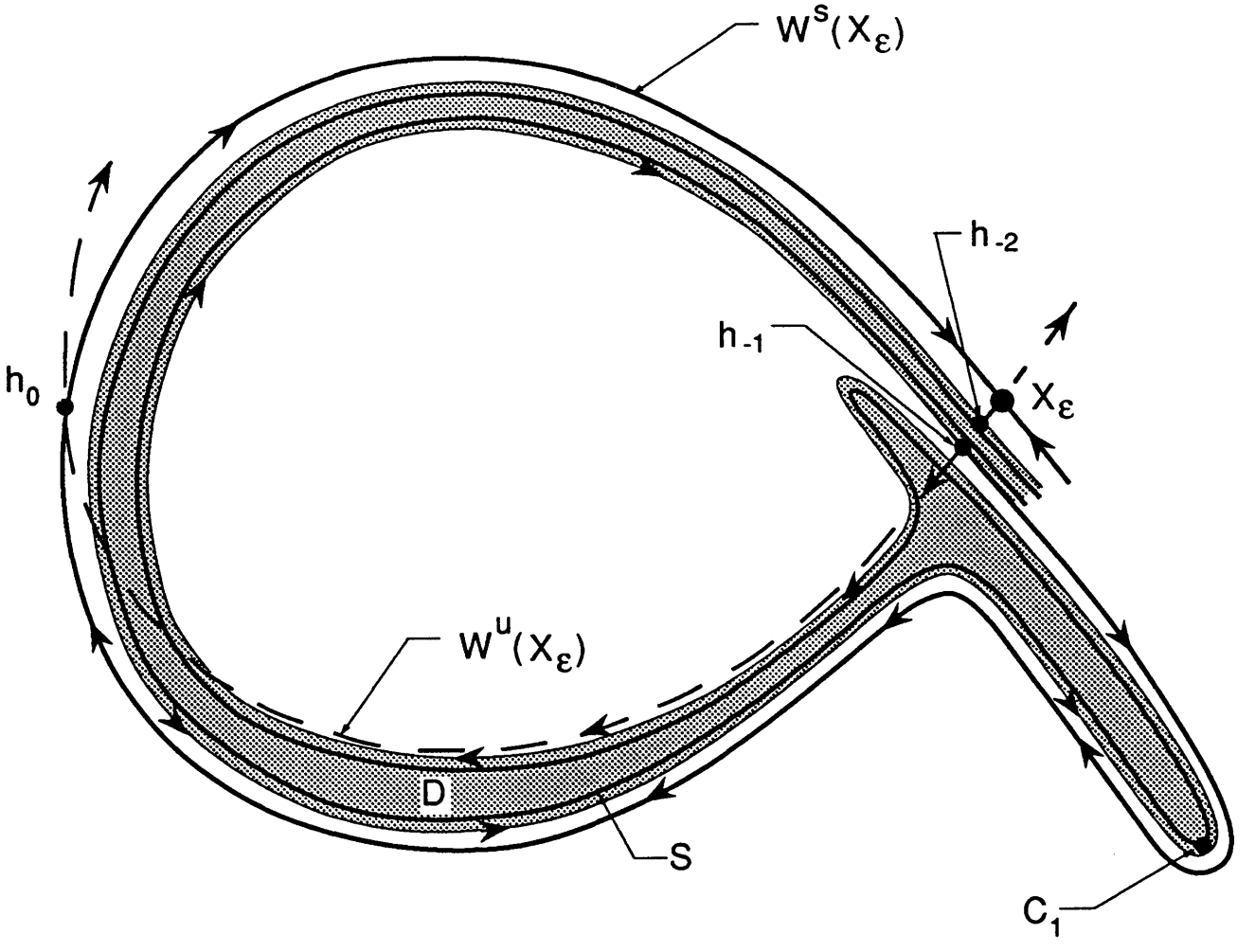

Fig. 4.4.b. The domain S of the horseshoe map is shaded.

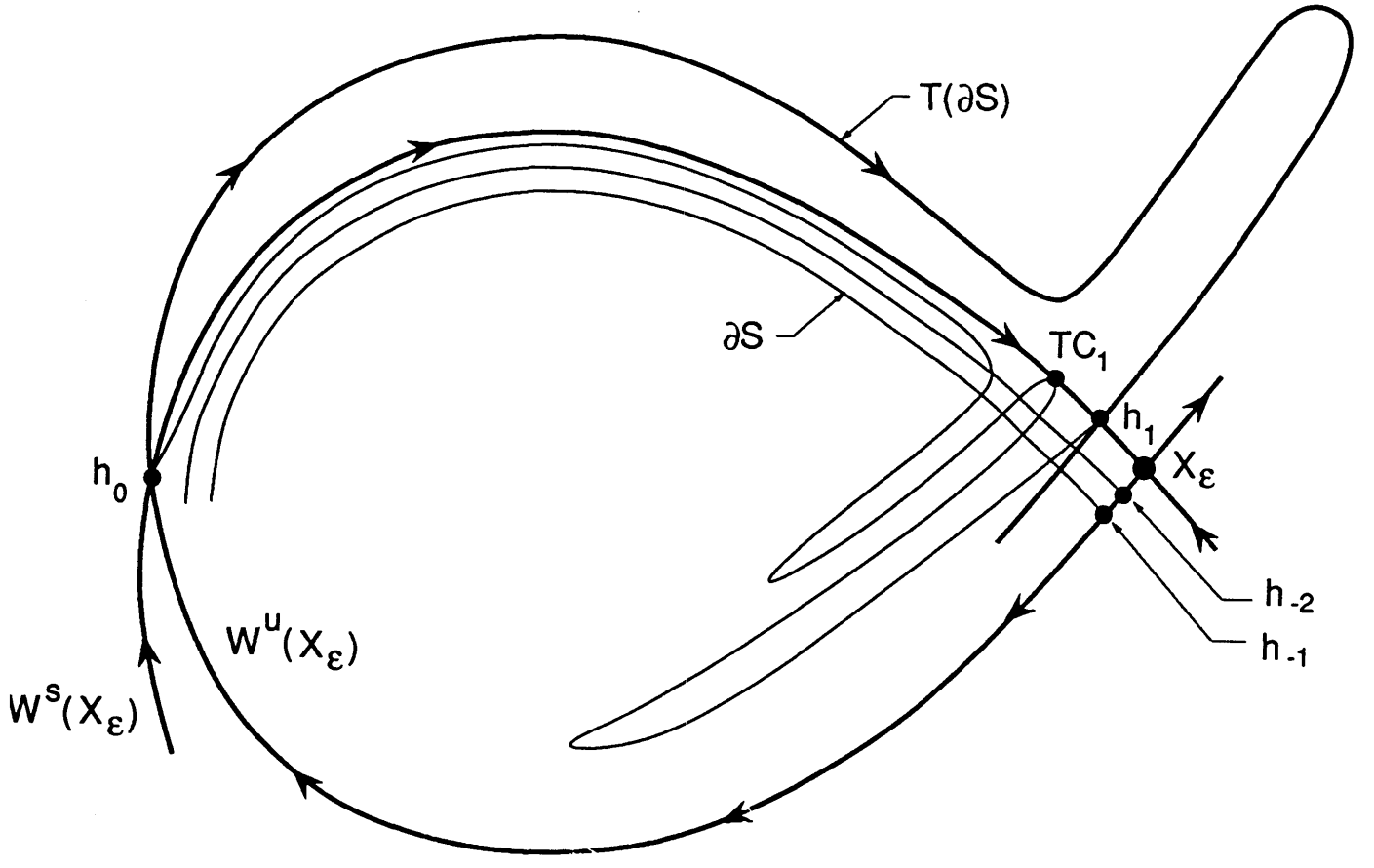

Fig. 4.4.c. The image, $T\partial S$, of the boundary of S, which we denote by ∂S.

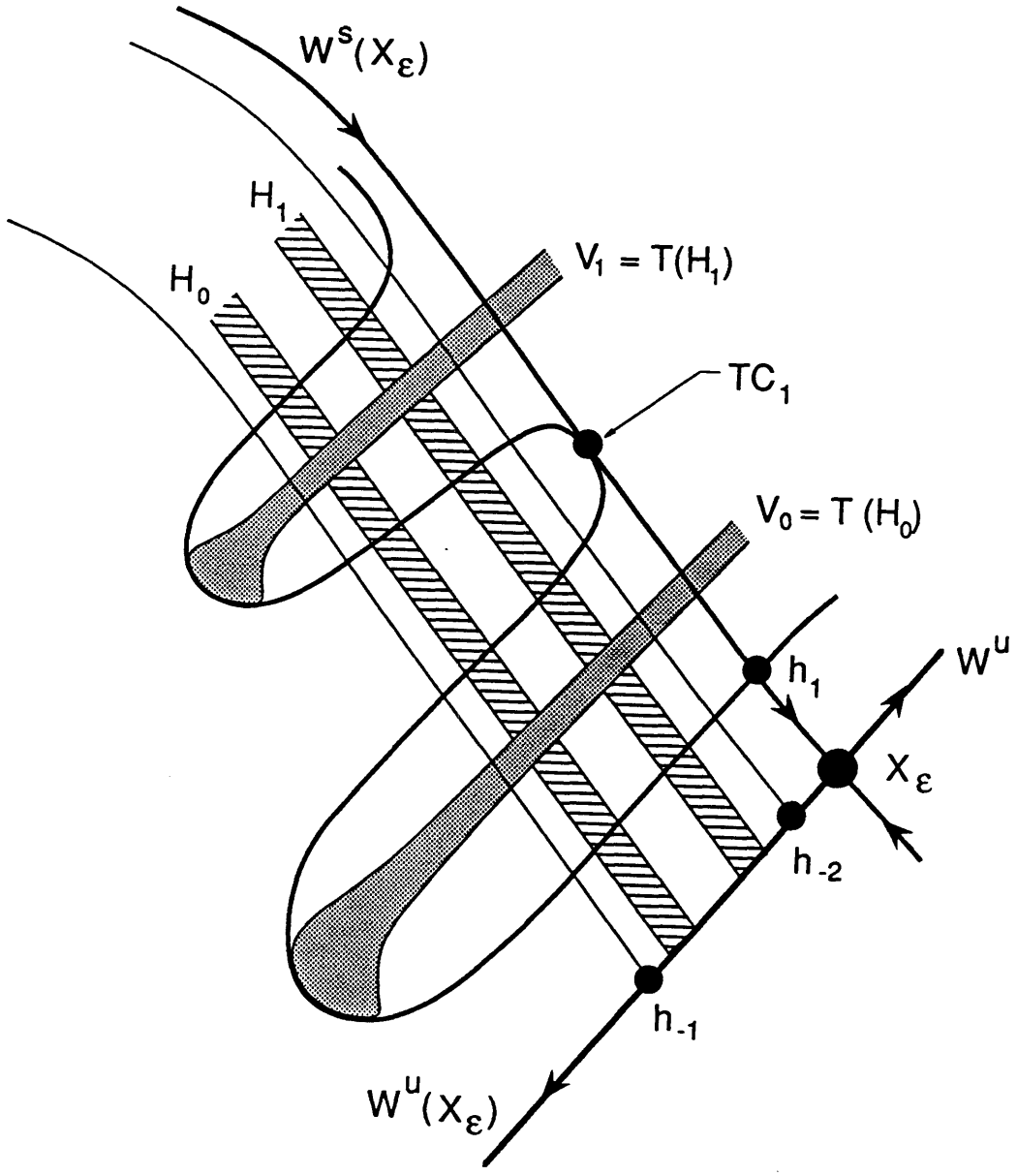

Fig. 4.4.d. Formation of the horseshoe in one iterate of the Poincaré map. The "horizontal" rectangles H_0 and H_1 get mapped over themselves as the "vertical" rectangles V_0 and V_1.

CHAPTER 5. ISLANDS.

In this extremely brief chapter, we summarize a new result for the size of islands in systems which are modulated periodically in time. We will publish the full presentation of this result elsewhere in the next several months.

On slices of constant time in the extended phase space, as for example on a Poincaré map, islands are cross-sections of invariant tori, which are created in bifurcations at $\epsilon = 0$ around stable resonant periodic orbits. The orbits on these tori are quasiperiodic. Now, for slowly-modulated systems, the stochastic-appearing separatrix-swept regions contain only small invariant regions. Because Elskens and Escande [1991] have shown that islands lie in the regions of the separatrix-swept regime that are complementary to the lobes, we know that islands occupy at most an area of $\mathcal{O}(\epsilon)$ in the limit as $\epsilon \to 0$, because lobe area limits on a special $\mathcal{O}(1)$ quantity.

Since numerical simulations we have run indicate that many of the islands are much smaller than $\mathcal{O}(\epsilon)$, we address the question of whether or not one can obtain sharper bounds. We now show that many of the islands occupy at most an area of $\mathcal{O}(\epsilon^2)$ as $\epsilon \to 0$. In particular, we focus on the islands about the $m : 1$ stable resonant subharmonics, for $m \geq 1$. Each of these islands lies in the resonance zone formed by the stable and unstable manifolds of the hyperbolic $m : 1$ resonant periodic orbit. Now, using action theory, MacKay *et al.*, [1987] derive an exact (although not computable in closed form as it stands) formula for the area enclosed in these resonance zones. This result states that the area is given by the sum of the actions of two orbits homoclinic to the hyperbolic periodic orbit (one along each branch) minus twice the action of the hyperbolic orbit itself. We refer the reader to MacKay *et al.* [1987] for the derivation of this formula.

In the forthcoming work, we show how to construct matched asymptotic expansions for the $m:1$ hyperbolic periodic orbits and how to use these to approximate the exact resonance area formula. The $m:1$ hyperbolic resonant subharmonic makes one near-separatrix excursion every m periods of the modulation, and it does so near the value of z such that the instantaneous separatrix encloses a minimal area. We simply match the inner expansion obtained from this near-separatrix excursion to the outer expansion, which corresponds to the (long) time intervals when the orbit is near the instantaneous saddle.

Next, we approximate the action of the two orbits homoclinic to the hyperbolic periodic orbit. These orbits execute almost exactly the same trajectories as the hyperbolic periodic orbit, with one important exception. The homoclinic orbit which is slightly further away from the saddle, *i.e.*, slightly deeper inside the potential well, picks one period of the modulation to make an extra near-separatrix excursion; whereas the the homoclinic orbit closer to the saddle selects one modulation period not to make a near-separatrix excursion.

Using our matched asymptotic expansions, we find that the leading order term for the area inside the resonance zones for $m \geq 2$ is $\mathcal{O}(\epsilon^2)$. We conclude by remarking that it seems possible to devise a procedure similar to that of Chapter 3 in order to determine the error made in this approximation.

APPENDIX A. New Technique for Generating the Unstable Manifolds in Singularly-Perturbed Systems.

In this appendix, we describe the numerical methods we use on the examples of Chapter 4, as well as for the equations of Part II. In particular, we outline the procedure by which we generate the stable and unstable manifolds of the hyperbolic fixed points of the Poincaré maps for these problems. Although we only treat z-periodic examples (and report the numerical procedures in the context of this special case), the techniques we use are applicable to more general time-dependent problems once a good representation of the hyperbolic orbit $\gamma_\epsilon(z)$ is at hand.

The process we use in order to generate the stable and unstable manifolds in each of the problems we studied is split into three parts. First, we use numerical shooting to determine the location of the hyperbolic fixed point, $\mathbf{X}_\epsilon^z$, of the Poincaré map. Second, we generate the "base" segments of both of its unstable manifolds. This part is where we needed to develop a new technique because of the slowness of the modulation. Finally, we proceed "segment by segment" to obtain more and more of the manifold. We now describe each of these steps in more detail.

For the Poincaré maps we study, except that of the pendulum in Chapter 4 (where we know the position of the fixed point is $(q = \pi, p = 0)$ for all times), we find their hyperbolic fixed points using numerical shooting. The accuracy to which they are found uniformly in z is determined by the requirements of the manifold plotting routine, described below. In all cases, the accuracy is at least eight significant figures, and for the smallest values of the modulation frequency ϵ considered, we obtain an accuracy of 18 significant digits using double precision arithmetic on the CRAY. We remark that we have also written an integer arithmetic routine to obtain however many significant figures are desired, although the code is slow at present,

which can be remedied by putting it on a parallel computer. Also, for the Hastings and McLeod example, we verified the accuracy of the numerically obtained fixed point by computing the asymptotic expansion for it and using Padé approximation.

Having found the hyperbolic fixed points, we generate the base segments of their unstable manifolds in the following fashion. At every time step, starting with $z = z_0$ and ending after one full period when z reaches $z_0 + 2\pi$, we drop one initial condition a distance of 10^{-n} out from the hyperbolic periodic orbit $\gamma_\epsilon(z)$ of $(1.1)_\epsilon$ along the instantaneous unstable eigendirection on Π_z. Each of the initial conditions which are dropped in during the previous time steps are simultaneously iterated forward. Thus, when z reaches $z_0 + 2\pi$, these points formed the base segment of the unstable manifold, see figure A.1. Therefore, the last point of the base segment (*i.e.*, the last initial condition dropped in) is the image after one period of the first point in the base segment, to within the tolerance we solved for. For the case of the pendulum, we verified the accuracy of our numerically generated base segment using a WKB calculation.

We also generated approximate base segments – a straight line segment between $\mathbf{X}_\epsilon^{z_0}$ and $\mathbf{X}_\epsilon^{z_0+2\pi}$ on which the points are distributed using a Gauss-Lobato distribution densest near $\mathbf{X}_\epsilon^z$ – in a few cases (only with the largest values of ϵ), and the results are similar to those obtained by the more accurate method just described.

The manifolds are then found segment by segment starting from the base segments. Points from the base segment, taken one at a time in the order they are encountered moving away from $\mathbf{X}_\epsilon^z$, are iterated forward one period. The distance between the image of a base point and the image of the previous base point is required to a specified tolerance. This tolerance is determined so that the manifold has a minimum degree of smoothness. If the tolerance is met, the next base point

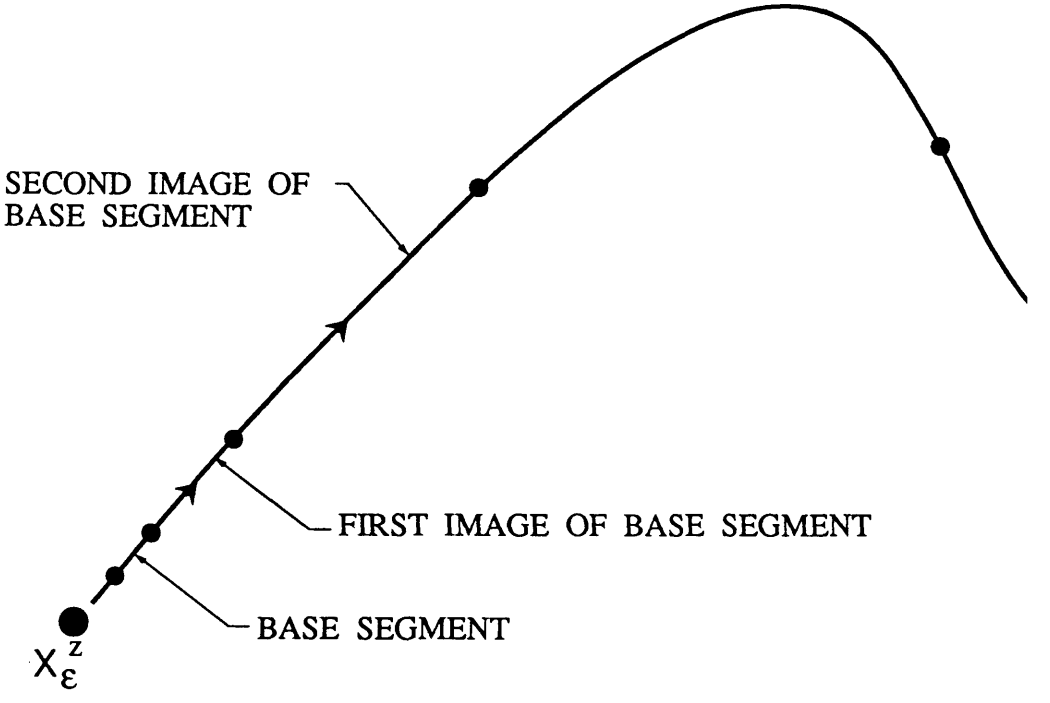

Fig. A.1. The segments of the unstable manifold are generated segment by segment.

is taken. However, if the tolerance is not met, then a point is inserted in the base segment in between the current and the previous base points. Then the procedure is repeated until either the tolerance is met or the pre-determined maximum number of divisions of the troublesome part of the base segment have been made, in which case the routine signaled the lack of smoothness and proceeded to the next base point.

In this way, the second segment of the manifold is generated from the base segment, then the third segment is generated using the second one as the base segment, and so forth...

Finally, for the problems we studied, we used the symmetry properties of the Poincaré map to get the stable manifolds. Although in general, one can also find these by simply reversing time and applying the above process.

APPENDIX B. On the Use of Symplectic Integration Schemes in Stiff, Non-Autonomous Systems.

In this appendix, we briefly discuss the two main symplectic integration algorithms we used: a Gauss-Legendre Runge-Kutta scheme and a scheme based on generating functions. The philosophy underlying these is to enforce that the integration step is a canonical map and hence preserves the symplectic invariants of a Hamiltonian vector field. The advantage of using the first one over the second is that it requires only function evaluations and not the first n derivatives of the vector field components, as well, where n is the order of the scheme. For discussions of the second scheme, we refer the reader to Channell and Scovel [1989].

The algorithm for an s-order implicit Gauss-Legendre Runge-Kutta scheme is:

$$\mathbf{y}_{n+1} = \mathbf{y}_n + \tau \sum_{i=1}^{s} b_i \mathbf{f}(t_n + c_i\tau, \mathbf{Y}_i) \qquad (*)$$

where for $1 \leq i \leq s$

$$\mathbf{Y}_i = \mathbf{y}_n + \tau \sum_{j=1}^{s} a_{ij} \mathbf{f}(t_n + c_j\tau, \mathbf{Y}_j), \qquad (**)$$

$\mathbf{y} \equiv (q,p)$, $\mathbf{f} \equiv \left(\frac{\partial H}{\partial p}, -\frac{\partial H}{\partial q}\right)$, a_{ij} are the entries of the $s \times s$ matrix A of constants and b and c are s-dimensional column vectors given by the Butcher tableau:

$$\begin{array}{c|c} c & A \\ \hline & b^T \end{array}$$

and τ is the time-step, see Dekker and Verwer [1984]. We implemented this scheme with $s = 4$ and $s = 5$. As it would take a page to write down all of the constants needed for the tableau, we refer the reader to pp.56-57 of Butcher [1964] for them.

The proof that this scheme is symplectic is interesting. The simplest proof I can give entails first rewriting the nonautonomous system $(1.1)_\epsilon$ as a degenerate two-degree-of-freedom system (which has the benefit that we deal with an autonomous

system), in which the second coordinate-like variable is z and its conjugate momentum is $-H$. Then $\mathbf{y}$ and $\mathbf{Y}$ in $(*)$ and $(**)$ are four-dimensional column vectors, and so is the now autonomous $\mathbf{f}$. Let $\mathbf{y}_n = (\mathbf{q}, \mathbf{p})$, $\mathbf{y}_{n+1} = (\mathbf{Q}, \mathbf{P})$, $\mathbf{Y}_i = (\mathbf{Y}_i, \mathbf{Z}_i)$. and $\mathbf{f} = (\mathbf{g}, \mathbf{h})$, where $\mathbf{g}_1 = \frac{\partial H}{\partial p_1}$, $\mathbf{g}_2 = \frac{\partial H}{\partial p_2}$, $\mathbf{h}_1 = -\frac{\partial H}{\partial q_1}$, $\mathbf{h}_2 = -\frac{\partial H}{\partial q_2}$. Therefore, to show that $(*)$ is symplectic we need to prove that $d\mathbf{Q} \wedge d\mathbf{P} = d\mathbf{q} \wedge d\mathbf{p}$. Calculating the differential ofs $(*)$ and $(**)$, we get:

$$\begin{aligned} d\mathbf{Q} &= d\mathbf{q} + \tau \Sigma_{i=1}^{s} b_i d\mathbf{g}(\mathbf{Y}_i, \mathbf{Z}_i) \\ d\mathbf{P} &= d\mathbf{p} + \tau \Sigma_{i=1}^{s} b_i d\mathbf{h}(\mathbf{Y}_i, \mathbf{Z}_i) \end{aligned} \tag{B.1}$$

$$\begin{aligned} d\mathbf{Y}_i &= d\mathbf{p} + \tau \Sigma_{j=1}^{s} a_{ij} d\mathbf{h}(\mathbf{Y}_j, \mathbf{Z}_j) \\ d\mathbf{Z}_i &= d\mathbf{q} + \tau \Sigma_{j=1}^{s} a_{ij} d\mathbf{g}(\mathbf{Y}_j, \mathbf{Z}_j) \end{aligned} \tag{B.2}$$

Then, taking the wedge product of $(B.2.a)$ and $d\mathbf{g}(\mathbf{Y}_i, \mathbf{Z}_i)$ and that of $d\mathbf{h}(\mathbf{Y}_i, \mathbf{Z}_i)$ and $(B.2.b)$, respectively, and plugging these expressions into $d\mathbf{Q} \wedge d\mathbf{P}$, we get

$$\begin{aligned} d\mathbf{Q} \wedge d\mathbf{P} = d\mathbf{p} \wedge d\mathbf{q} &+ \tau \Sigma_{i=1}^{s} b_i \left[d\mathbf{Y}_i \wedge d\mathbf{g}_i + d\mathbf{h}_j \wedge d\mathbf{Z}_i \right] \\ &+ \tau^2 \Sigma_{j=1}^{s} \left[b_i b_j - b_i a_{ij} - b_j a_{ji} \right] d\mathbf{h}_i \wedge d\mathbf{g}_j. \end{aligned} \tag{B.3}$$

Finally, the second term in the above expression vanishes because a Hamiltonian vector field is divergence free and the wedge product is a skew-symmetric operation. Therefore, since $m_{ij} \equiv a_{ij} b_i + a_{ji} b_j - b_i b_j = 0$, for all i and j, for Gauss-Legendre RK schemes, the last term in (B.3) also vanishes, and we arrive at the desired conclusion that these schemes are symplectic.

APPENDIX C. Derivation of $M_A(z)$.

In this appendix, we present a derivation of the adiabatic Melnikov function, using the result of Lemma 2.1. As we stated in Chapter 2.2, the signed distance between $\mathbf{q}_\epsilon^S(0,z;0)$ and $\mathbf{q}_\epsilon^U(0,z;0)$ is given by

$$d(z;\epsilon) = \frac{\mathbf{f}(\mathbf{q}_0^z(0),z) \wedge \left(\mathbf{q}_\epsilon^U(0,z;0) - \mathbf{q}_\epsilon^S(0,z;0)\right)}{\|\mathbf{f}(\mathbf{q}_0^z(0),z)\|}. \tag{C.1}$$

Asymptotically as $\epsilon \to 0$:

$$\begin{aligned} d(z;\epsilon) &= \epsilon \frac{\mathbf{f}(\mathbf{q}_0^z(0),z) \wedge \left(\frac{\partial \mathbf{q}_\epsilon^U}{\partial \epsilon}(0,z;0)|_{\epsilon=0} - \frac{\partial \mathbf{q}_\epsilon^S}{\partial \epsilon}(0,z;0)|_{\epsilon=0}\right)}{\|\mathbf{f}(\mathbf{q}_0^z(0),z)\|} + \mathcal{O}(\epsilon^2) \\ &\equiv \epsilon \frac{M_A(z)}{\|\mathbf{f}(\mathbf{q}_0^z(0),z)\|} + \mathcal{O}(\epsilon^2) \end{aligned} \tag{C.2}$$

Our goal is to derive the following computable expression for $M_A(z)$.

$$M_A(z) = \int_{-\infty}^{\infty} t\{H, \frac{\partial H}{\partial z}\}(\mathbf{q}_0^z(t))\, dt. \tag{C.3}$$

We begin by defining a time-dependent version of (C.2), which we label $d(t,z;\epsilon)$, and write a differential equation for $d(t,z;\epsilon)$, which can then be solved to yield (C.3).

The time-dependent distance is:

$$d(t,z;\epsilon) \equiv \epsilon \frac{\mathbf{f}(\mathbf{q}_0^z(t),z) \wedge \left(\frac{\partial \mathbf{q}_\epsilon^U}{\partial \epsilon}(t,z;0)|_{\epsilon=0} - \frac{\partial \mathbf{q}_\epsilon^S}{\partial \epsilon}(t,z;0)|_{\epsilon=0}\right)}{\|\mathbf{f}(\mathbf{q}_0^z(t),z)\|} + \mathcal{O}(\epsilon^2) \tag{C.4}$$

For convenience, we rewrite (C.4) as

$$d(t,z;\epsilon) = \epsilon \frac{\left(\Delta^U(t,z;0) - \Delta^S(t,z;0)\right)}{\|\mathbf{f}(\mathbf{q}_0^z(t),z)\|} + \mathcal{O}(\epsilon^2), \tag{C.5}$$

where

$$\begin{aligned}\Delta^U(t,z;\epsilon) &\equiv \mathbf{f}(\mathbf{q}_0^z(t),z) \wedge \frac{\partial \mathbf{q}_\epsilon^U}{\partial \epsilon}(t,z;0)|_{\epsilon=0} \\ \Delta^S(t,z;\epsilon) &\equiv \mathbf{f}(\mathbf{q}_0^z(t),z) \wedge \cdot \frac{\partial \mathbf{q}_\epsilon^S}{\partial \epsilon}(t,z;0)|_{\epsilon=0}\end{aligned} \tag{C.6}$$

We first work on Δ^U. The equation and its solution for Δ^S are similar. Letting $D_{\mathbf{q}}\mathbf{f}$ denote the Jacobian of $\mathbf{f}$ with respect to $\mathbf{q}$, suppressing the arguments at $\epsilon = 0$ of all of the functions, using the relation $\dot{\mathbf{q}}_0^z(t) = \mathbf{f}$, we compute:

$$\dot{\Delta}^U(t,z;0) = (D_{\mathbf{q}}\mathbf{f} \cdot \mathbf{f}) \wedge \frac{\partial \mathbf{q}_\epsilon^U}{\partial \epsilon} + \mathbf{f} \wedge \frac{d}{dt}\left(\frac{\partial \mathbf{q}_\epsilon^U}{\partial \epsilon}\right) \tag{C.7}$$

The first variational equation yields the last the term in the above expression:

$$\frac{d}{dt}\left(\frac{\partial \mathbf{q}_\epsilon^U}{\partial \epsilon}\right) = D_{\mathbf{q}}\mathbf{f} \cdot \frac{\partial \mathbf{q}_\epsilon^U}{\partial \epsilon} + \frac{\partial \mathbf{f}}{\partial z}\frac{dz}{d\epsilon} = D_{\mathbf{q}}\mathbf{f} \cdot \frac{\partial \mathbf{q}_\epsilon^U}{\partial \epsilon} + t\frac{\partial \mathbf{f}}{\partial z}.$$

We recall that all terms are evaluated at $\epsilon = 0$ and remark that the latter term is responsible for the slow t-growth in $\frac{\partial \mathbf{q}_\epsilon^U}{\partial \epsilon}$. Thus,

$$\begin{aligned}\dot{\Delta}^U(t,z;0) &= (D_{\mathbf{q}}\mathbf{f} \cdot \mathbf{f}) \wedge \frac{\partial \mathbf{q}_\epsilon^U}{\partial \epsilon} + \mathbf{f} \wedge \left(D_{\mathbf{q}}\mathbf{f} \cdot \frac{\partial \mathbf{q}_\epsilon^U}{\partial \epsilon}\right) + t\mathbf{f} \wedge \frac{\partial \mathbf{f}}{\partial z} \\ &= \mathrm{Tr}(D_{\mathbf{q}}\mathbf{f})\left[\mathbf{f} \wedge \frac{\partial \mathbf{q}_\epsilon^U}{\partial \epsilon}\right] + t\mathbf{f} \wedge \frac{\partial \mathbf{f}}{\partial z} \\ &= t\mathbf{f} \wedge \frac{\partial \mathbf{f}}{\partial z} \\ &= t\{H, \frac{\partial H}{\partial z}\}\end{aligned} \tag{C.8}$$

since a Hamiltonian vector field is divergence free.

Integrating the result in (C.8), we get:

$$\Delta^U(0,z;0) - \Delta^U(T_U,z;0) = \int_{T_U}^{0} t\{H, \frac{\partial H}{\partial z}\}(\mathbf{q}_0^z(t),z)dt, \tag{C.9}$$

where $T_U < 0$. Performing the same steps on Δ^S, we also get:

$$\Delta^S(T_S,z;0) - \Delta^S(0,z;0) = \int_{0}^{T_S} t\{H, \frac{\partial H}{\partial z}\}(\mathbf{q}_0^z(t),z)dt, \tag{C.10}$$

where $T_S > 0$. Now, at the end of this section, we show that

$$\lim_{T_U \to -\infty} \Delta^U(T_U, z; 0) = 0$$
$$\lim_{T_S \to \infty} \Delta^S(T_S, z; 0) = 0.$$

Therefore, adding (C.10) and (C.9) together and taking the limits on T_U and T_S, we get:

$$M_A(z) \equiv \Delta^U(0, z; 0) - \Delta^S(0, z; 0) = \int_{-\infty}^{\infty} t\{H, \frac{\partial H}{\partial z}\}(\mathbf{q}_0^z(t), z)dt, \qquad (C.11)$$

Thus, we have completed the derivation of the adiabatic Melnikov function. We remark that

$$M_A(z) = \int_{-\infty}^{\infty} \{H, \frac{\partial H}{\partial \epsilon}\}(\mathbf{q}_0^z(t), z)dt$$

because $\frac{\partial H}{\partial \epsilon} = t\frac{\partial H}{\partial z}$. This observation allows us to write both the adiabatic Melnikov function and the usual Melnikov function (for weakly-perturbed systems) $M(t_0) = \int_{-\infty}^{\infty} \{H_0, H_1\}(\mathbf{q}_0(t), t + t_0)dt$ in terms of one expression, because $\{H, \frac{\partial H}{\partial \epsilon}\} = \{H_0, H_1\}$.

As mentioned above, we conclude this appendix by proving

$$\begin{aligned} \lim_{T_U \to -\infty} \Delta^U(T_U, z; 0) &= 0 \\ \lim_{T_S \to \infty} \Delta^S(T_S, z; 0) &= 0 \end{aligned} \qquad (C.12)$$

Our proof consists of two observations. First,

$$\begin{aligned} \mathbf{f}(\mathbf{q}_0^z(T_U), z) &\to 0 \\ \mathbf{f}(\mathbf{q}_0^z(T_S), z) &\to 0 \end{aligned} \qquad (C.13)$$

exponentially fast as $T_U \to -\infty$ and $T_S \to \infty$, respectively. Second,

$$\begin{aligned} |\frac{\partial \mathbf{q}_\epsilon^U}{\partial \epsilon}(T_U, z; 0)| &< K_1|T_U| \\ |\frac{\partial \mathbf{q}_\epsilon^S}{\partial \epsilon}(T_S, z; 0)| &< K_2 T_S \end{aligned} \qquad (C.14)$$

as $T_U \to -\infty$ and $T_S \to \infty$, respectively. This follows from the proof of Lemma 2.1 of paper. Therefore, combining (C.13) and (C.14), we have proven (C.12).

APPENDIX D. Brief Review of Adiabatic Invariance Theory.

In this appendix, we review some aspects of adiabatic invariance theory as it applies to systems of the form $(1.1)_\epsilon$. As a preliminary step, we transform $(1.1)_\epsilon$ to action-angle coordinates, a realization of Kruskal's "more appropriate variables." The action of an orbit which lies on the closed contour $H(q,p,z) = h$ with $p = P(q,h,z)$ is:

$$I(h,z) \equiv \frac{1}{2\pi} \oint P(q,h,z)dq.$$

For $\epsilon \neq 0$, the time-dependent canonical transformation from (p,q) to action-angle variables (I,θ) is determined by the mixed-type generating function

$$F(q,I,z) = \int_{q_0(I,z)}^{q} P(\bar{q},H(I,z),z)d\bar{q}$$

which satisfies the Hamilton-Jacobi equation

$$H(\frac{\partial F}{\partial q},q,z) = h,$$

where $h = h(I,z)$. The solutions of the equations $p = \frac{\partial F}{\partial q}$ and $\theta = \frac{\partial F}{\partial I}$ implicitly determine the relations $p = p(I,\theta,z)$ and $q = q(I,\theta,z)$. The periodic orbits of $(1.1)_0$ are now curves of constant action I parametrized by $\theta \in [0,2\pi)$ with frequency $\omega_0(I,z) \equiv \frac{\partial H_0}{\partial I}(I,z)$. Furthermore, the new Hamiltonian is simply the old one augmented by the time-derivative of F:

$$K(I,\theta,z) = H_0(I,z) + \epsilon\frac{\partial F}{\partial z}(q(I,\theta,z),I,z) \equiv H_0(I,z) + \epsilon H_1(I,\theta,z),$$

where H_1 is 2π-periodic in θ. Thus, the equations for $(1.1)_\epsilon$ may now be written as:

$$\begin{aligned} \dot{I} &= -\epsilon\frac{\partial H_1}{\partial \theta}(I,\theta,z) \\ \dot{\theta} &= \omega_0(I,z) + \epsilon\frac{\partial H_1}{\partial I}(I,\theta,z) \end{aligned} \tag{D.1}$$

Clearly, $|I(t) - I(0)| < K$ for $t \in (0, \frac{K_1}{\epsilon})$ because H_1 and its derivative with respect to θ are $\mathcal{O}(1)$. We recall that a function $J(p,q,z)$ is an n-th order adiabatic invariant if $|J(t) - J(0)| < K\epsilon^n$ for $t \in (0, \frac{K_1}{\epsilon})$, where $J(t) = J(p(t), q(t), z(t))$ and $n \in \mathbb{N}$. Therefore, I is a zeroeth order adiabatic invariant. With a little more work, one can show that the action of an orbit in $(1.1)_\epsilon$ is a first order adiabatic invariant if $\omega_0(I,z)$ is nowhere zero. We refer the reader to Percival and Richards [1984] Section 9.4 or Arnol'd [1978] Section 52.E for an exposition.

The action is the leading term of a series for the adiabatic invariant. Kruskal showed (assuming H is C^∞) that "nice variables" J and ϕ exist, and may be found in the form of a perturbation series in the small parameter ϵ:

$$\begin{aligned} J &\equiv I + \epsilon J_1(I,\theta,z) + \epsilon^2 J_2(I,\theta,z) + \cdots \\ \phi &\equiv \theta + \epsilon\theta_1(I,\theta,z) + \epsilon^2\theta_2(I,\theta,z) + \cdots \end{aligned} \tag{D.2}$$

They are termed "nice" because

$$\begin{aligned} \dot{J} &= 0 \quad \text{toallordersin}\epsilon \\ \dot{\phi} &= \omega_0(I,z) + \epsilon G_1(I,z) + \epsilon^2 G_2(I,z) + \cdots, \end{aligned} \tag{D.3}$$

i.e., J is an infinite-order adiabatic invariant.

The functions J_i and θ_i, for $i \in \mathbb{N}$, are determined pairwise in i using near-identity transformations. The prescription is that J_i and θ_i depend on I, θ, and z in such a way that the new Hamiltonian only depends on θ in the terms of $\mathcal{O}(\epsilon^{i+1})$ and higher. Hence, the time rate of change of $I + \epsilon J_1 + \cdots + \epsilon^i J_i$ is $\mathcal{O}(\epsilon^{i+1})$ and the time rate of change of $\theta + \epsilon\theta_1 + \cdots + \epsilon^i\theta_i$ is independent of θ up to and including the $\mathcal{O}(\epsilon^i)$ terms. The first term is:

$$J_1(I,z) = \frac{1}{2\omega_0(I,z)}\frac{\partial I}{\partial z} - \oint \frac{\partial P}{\partial h}(\bar{q},h,z) \cdot \int_q^{\bar{q}} \frac{\partial P}{\partial z}(q',h,z)dq'd\bar{q} \tag{D.4}$$

The next term, J_2, is proportional $\frac{1}{\omega_0^2}$. We refer the reader to Henrard [1989] for further terms in J and a general review.

The ratio of successive terms in the series for J is: $\frac{\epsilon}{\omega_0}$, which is $\ll 1$ if $\omega_0(I,z)$ is bounded away from zero uniformly in I and z. Therefore, when an orbit gets too near an instantaneous separatrix, *i.e.* when $\omega_0(I,z)$ is of the same order as ϵ for some z, then adiabatic invariance theory breaks down. We recall that ω_0 decays logarithmically to zero as the separatrix is approached.

References

Abraham, R.H., Shaw, C.D., 1984, *Dynamics - The Geometry of Behavior, Part Three: Global Behavior*, Aerial Press, Inc.: Santa Cruz.

Arnol'd, V.I., 1962, On the Behavior of the Adiabatic Invariant Under Slow Periodic Variation of the Hamiltonian, *Sov Math Dokl*, **3**, 136-140.

Arnol'd, V.I., 1963, Small Denominators and Problems of Stability of Motion in Classical and Celestial Mechanics, *Russ Math Surv*, **18**, no.6, 85-192.

Arnol'd, V.I., 1978, *Mathematical Methods of Classical Mechanics*, Springer Verlag: New York.

Bruhwiler, D.L., 1990, University of Colorado, Boulder, Ph.D. Thesis.

Butcher, J.C.,1964, Implicit Runge-Kutta Processes, *Mathematics of Computation*, **18**, 50-64.

Camassa, R., Wiggins, S., 1991, Chaotic Advection in a Rayleigh-Benard Flow, *Phys Rev A*.

Cary, J.R., Escande, D.F., Tennyson, J.L., 1986, Change of the Adiabatic Invariant Due to Separatrix Crossing, *Phys Rev A*, **34**, no.5, Nov., 4256-4275.

Cary, J.R., and Skodje, R.T., 1989, *Physica D*, **36**, 287.

Channell, P.J., and Scovel, C., 1989, LA-UR No. 89-1828, Los Alamos Technical Report.

Coddington, E.A., Levinson, N., 1987, *Theory of Ordinary Differential Equations*, Krieger: Florida, reprinted edition.

Coppel, W.A., 1978, *Dichotomies in Stability Theory*, Springer Verlag: New York, Lecture Notes in Mathematics Series, no.629.

Dekker and Verwer, 1984, *Stability of Runge-Kutta Methods for Stiff Nonlinear Differential Equations*, North-Holland, Chapter 3.

Elskens, Y., Escande, D.F., 1991, to appear in *Nonlinearity.*

Escande, D.F., 1988, Proc. Int'l. Workshop Kiev, April 13-25, Hamiltonian Chaos and Adiabaticity, World Scientific Press.

Fenichel, N., 1971, Persistence and Smoothness of Invariant Manifolds for Flows, *Ind Univ Math Jl* , **21**, no.3, 193-225; 1974 and 1977, Asymptotic Stability with Rate Conditions I and II, **23**, no.12, 1109-1137, and **26**, no. 1, 81-93; 1979, Geometric Singular Perturbation Theory for ODE's, *JDE*, **31**, 53-98.

Guckenheimer, J., Holmes, P.J., 1983, *Nonlinear Oscillations, Dynamical Systems, and Bifurcations of Vector Fields*, Springer Verlag: New York.

Hastings, S. and McLeod, J.B., 1991, to appear in *Journal of Nonlinear Science.*

Henrard, J., 1989, to appear in *Dynamics Reported.*

Hirsch, M.W., Pugh, C.C., Shub, M., 1983, *Invariant Manifolds*, Springer Verlag: New York, Lecture Notes in Mathematics Series, no.583.

Holmes, P.J., 1984, Some Remarks on Chaotic Particle Paths in Time-Periodic Three-Dimensional Swirling Flows, *Cont Math*, **28**, 393-403.

Kaper, T.J., Wiggins, S., 1989, Transport, Mixing, and Stretching in Chaotic Stokes' Flow: The Two-Roll Mill, paper presented at the 3rd Joint ASME ASCE Mech. Conf. La Jolla, CA, July. Available as a Los Alamos Technical Report.

Kaper, T.J. and Wiggins. S., 1991a, Lobe Area in Adiabatic Hamiltonian Systems, to appear in *Physica D.*

Kaper, T.J. and Wiggins. S., 1991b, On the Structure of the Separatrix-Swept Regions in Slowly-Modulated Hamiltonian Systems, submitted to *Differential and Integral Equations.*

Kaper, T.J. and Wiggins. S., 1991c, to appear in *Journal of Nonlinear Science.*

Katok, A., Hasselblatt, B., 1990, *Introduction to the Modern Theory of Dynamical Systems*, manuscript.

Kevorkian, J., and Cole, J.D., 1981, *Perturbation Methods in Applied Mathematics*, Springer, New York.

Kovacic, G., 1991, to appear in *Physica D.*

Kruskal, M., 1962, *Journal of Mathematical Physics*, **3**, no.4, 806.

MacKay, R.S., Meiss, J.D., and Percival, I.C., 1984, Transport in Hamiltonian Systems, *Physica13D*, 55-81.

MacKay R.S., Meiss, J.D., 1986, Flux and Differences in Action for Continuous Time Hamiltonian Systems, *Jl Phys A: Math Gen*, **19**, L225-L229.

MacKay, R.S., Meiss, J.D., Percival, I.C., 1987, Resonances in Area-Preserving Maps, *Physica D*, **27**, 1-20.

MacKay R.S., Meiss, J.D., 1988, The Relation Between Quantum and Classical Thresholds in Multiphoton Ionization of Excited Atoms, *Phys Rev A*, **37**, 4702-4706.

Martens, C.C., Davis, M.J., Ezra, G.S., 1987, Local Frequency Analysis of Chaotic Motion In Multi-Dimensional Systems: Energy Transport and Bottlenecks in Planar OCS, *Chemical Physics Letters*, **142**, no.6, Dec 25, 519-528

Melnikov, V.K., 1963, On the Stability of the Center in Time-periodic Perturbations, *Trans Moscow Math*, **12**, 1-57.

Meyer, K.R., Sell, G., 1989, Melnikov Transforms, Bernoulli Bundles, and Almost Periodic Perturbations, *Trans AMS*, July, **314**, no.1, 63-105.

Neishtadt, A.I., 1975, *PMM*, **39** , no. 4, 621-632.

Neishtadt, A.I., 1986, Change in Adiabatic Invariant at a Separatrix, *Sov Jl of Plasma Physics*, **12** , no. 8, 568-573.

Ockendon, J., Ockendon, H., Johnson, A.D., 1986, Resonant Sloshing in Shallow Water, *JFM*, **167**, 465-479.

Palmer, K., 1986, Transversal Homoclinic Points and Cherry's Example of a Non-integrable Hamiltonian System, *JDE*, **65**, 321-360.

Percival, I. and Richards, D., *Introduction to Dynamics*, 1982, Cambridge U. Press.

Robinson, C., 1983, Sustained Resonance for a Nonlinear System with Slowly Varying Coefficients, *SIAM J Math Anal*, **14**, no.5, Sept., 847-860.

Rom-Kedar, V., Leonard, A., Wiggins, S., 1987, Jan.11-14,*Nucl Phys B*, Proc. Int'l Conf. on Chaos and Physics of Systems Far from Equilibrium.

Rom-Kedar, V., Leonard, A., Wiggins, S., 1990a, An Analytical Study of Transport Mixing, and Chaos in an Unsteady Vortical Flow, *JFM*, **214**, 347-394.

Rom-Kedar, V., Wiggins, S., 1990b, Transport in Two-Dimensional Maps, *Arch Rat Mech and Analysis*, **109**, no.3, 239-298.

Sakamoto, K., 1990, to appear in *Proc Roy Soc of Edin.*

Sanz-Serna, J.M.,1988, Runge-Kutta Schemes for Hamiltonian Systems, *BIT*, **28**, 877-883.

Sell, G., 1978, The Structure of the Flow in the Vicinity of an Almost Periodic Motion, *JDE*,**27**, no. 3, 359-393.

Wiggins, S., 1988a, *Global Bifurcations and Chaos*, Springer Verlag: New York.

Smale, S., 1963, in *Differential and Combinatorial Topology*, S.S. Cairns, *ed*, 63-80, Princeton U. Press.

Wiggins, S., 1988b, On the Detection and Dynamical Consequences of Orbits Homoclinic to Hyperbolic Periodic Orbits and Normally Hyperbolic Invariant Tori in a Class of Ordinary Differential Equations, *SIAM Jl Appl Math*, April, **48**, no.2, 262-285.

Wiggins, S., 1988c, Adiabatic Chaos, *Physics Letters A*, April 11, **128**, no.6,7, 339-342.

PART II: ON THE QUANTIFICATION OF MIXING IN CHAOTIC STOKES' FLOWS: THE ECCENTRIC JOURNAL BEARING

CHAPTER 1. INTRODUCTION.

The distinction between the eulerian and the lagrangian approach to fluid mechanics is one of the first things one learns in a fluid mechanics class at Caltech. In the eulerian approach, the equations of motion are derived by applying the principles of conservation of mass, momentum, and energy to the fluid flowing through a fixed control volume. The particular fluid particles inside the control volume are continually changing. In contrast, in the lagrangian approach, the equations of motion are derived by applying the same conservation principles to a patch of "labeled" fluid particles and following the patch as it evolves and deforms in time. Now, in experiments, a dye that does not alter the density of the fluid and has a small molecular diffusivity is usually used as the "label." Thus, theoretical and numerical results obtained using the lagrangian approach may be compared to experimental results in a natural fashion.

Although the eulerian approach is the one in greater use, the lagrangian description has advantages for a number of problems. Among the topics well-suited to the lagrangian approach is mass transport, which can be a highly complicated problem even for simple velocity fields, as has been shown in recent experimental and numerical work (see Ottino [1989] for an overview). Although the flows in these studies are laminar, they simultaneously possess chaotic particle paths and large-scale structures, such as whorls, tendrils, periodic points, Smale horseshoes, and islands.

Dynamical systems theory is ideally suited to analyzing these flows and the problems of mass transport in them. Setting aside the more complicated case of three-dimensional flows, we limit our discussion to the use of dynamical systems theory in two-dimensional problems. The two-dimensional flows which have been

studied using dynamical systems theory are from both ends of the Reynolds number range, including inviscid flows such as the blinking vortex flow (Aref [1984]), the oscillating vortex pair flow (Rom-Kedar *et al.* [1990a]), Rayleigh Benard convection (Camassa and Wiggins [1991]), and scattering of point vortices, as well as low Reynolds number flows such as the two-dimensional cavity flows, the eccentric journal bearing, the two-roll mill, geophysical flows, and others (see Ottino [1989] and the references). They are often referred to collectively as problems in chaotic advection or lagrangian turbulence.

Furthermore, most of the flows that have been studied are time-periodic. Indeed, it is precisely the unsteadiness of these flows which is responsible for breaking the integrability of the steady-state flow and for creating the chaotic particle paths and large-scale structures identified above. These flows have been analyzed using the maps that are the common currency of dynamical systems theory, such as non-integrable, area-preserving twist maps and Poincaré return maps of near-integrable, one-degree-of-freedom Hamiltonian systems. In the Lagrangian formulation of these flows, the equations of motion for fluid particles are Hamiltonian with the stream function serving as the Hamiltonian, and the fluid domain as the domain of the map, because the two Cartesian coordinates x and y are the canonically conjugate variables.

In addition to its having been fruitful for identifying the structures mentioned above, dynamical systems theory has led to progress toward the goal of determining various transport quantities in these flows. We discuss this progress in the following paragraphs. As the transport literature is vast (see for example Rom-Kedar *et al.* [1990a] and Ottino [1989] for references), however, we narrow the focus of this work and discussion to the study of low Reynolds number two-dimensional flows. The large amount of literature on these flows and the initial successes of dynamical

systems theory in understanding them attests to their fundamental importance.

However, as has been observed by Ottino and Swanson [1989], existing dynamical systems theory is inadequate to study the large chaotic regions in these flows. Experimentally and numerically, it was discovered that a patch of tracer fluid in a periodically-blinking Stokes' flow rapidly develops into a highly-striated lamellar structure as it gets stretched exponentially and folded and covers a large area in the flow domain, see Aref and Balachandar [1986] and Chaiken, et al. [1986]. We remark that, for the eccentric journal bearing, for example, blinking implies that the cylinders each rotate with a constant angular velocity for half of the period and are stationary during the other half period while the other one rotates. Since then, these discoveries have been pursued in the different geometries listed above. In the study of reacting species in a cavity flow, to name just one example, this exponential stretching is highly desirable because it can be used to create a large interface between two reacting species.

The main tool for quantifying this stretching and transport has been the concept of Lyapunov characteristic exponents (LCEs) from dynamical systems theory. LCEs have been computed for some of these flows with different geometries and with stirring protocols of the blinking type. First the existence of positive Lyapunov exponents implies that nearby trajectories separate exponentially in time in these flows. Second, there typically exists a spatially non-uniform distribution for the LCE's in the fluid domain that depends in a nonlinear way on the flow parameters.

This work is also directed toward the goal of quantifying transport and mixing. Rather than rely on LCEs, which are *a posteriori* measures of stretching and mixing, however, we develop for the first time a theory for quasi-steady Stokes' flows which predicts many important stretching and transport quantities before any ex-

perimental or numerical simulations are performed. In fact, the main techniques we use are new tools (developed largely in Part I of this thesis) for slowly-modulated dynamical systems that are ideally suited for describing fluid motion in large ($\mathcal{O}(1)$) chaotic regions. In the process of demonstrating their suitability, we will show how our results are markedly different from those of the usual (small-amplitude) perturbations usually studied in dynamical systems theory and how these new tools these results provide us with enable us to overcome the inadequacies of the usual dynamical systems theory.

In particular, we study transport of tracer dye in a low Reynolds number flow in the two-dimensional, annular domain between two nonconcentric counterrotating cylinders. This geometry, known as the eccentric journal bearing, is widely used in the study of mixing. The inner cylinder is referred to as the shaft, and the outer cylinder as the casing. Modulation of the angular velocities of the cylinders continuously, slowly, and periodically in time causes the integrable steady-state flow to become nonintegrable. As a result the tracer particles exhibit many of the features characteristic of chaotic advection or lagrangian turbulence discussed above. In stark contrast to the flows usually studied with dynamical systems (in which the perturbation on the integrable flow is of small amplitude and with $\mathcal{O}(1)$ frequency), however, these slowly-varying systems are singular-perturbation problems in which the nonintegrability is due to the slow $\mathcal{O}(1)$ modulation of the position of the saddle stagnation point and the two streamlines stagnating on it.

We may summarize the difference between our modulation protocols and the "stirring" protocols used in the literature as follows. The protocols used in the literature prescribe the angular velocities of the two cylinders Ω_1 and Ω_2, where the subscripts 1 and 2 refer to the casing and the shaft, respectively, either as a

small-amplitude modulation:

$$\Omega_1(t,\epsilon) = \Omega_1 + \epsilon\cos\omega t$$

$$\Omega_2(t,\epsilon) = \Omega_2 + \epsilon\sin\omega t$$

where $0 < \epsilon \ll 1$ and ω and $\Omega_i = \mathcal{O}(1)$, and $\Omega_1(t)\cdot\Omega_2(t) < 0$ for all t, or as a blinking modulation:

$$\Omega_1(t) = \begin{cases} \Omega_1 & 0 \le t < T/2 \\ 0 & T/2 \le t < T \end{cases}$$

$$\Omega_2(t) = \begin{cases} 0 & 0 \le t < T/2 \\ \Omega_2 & T/2 \le t < T \end{cases}$$

where $\Omega_1 \neq \Omega_2$, $\Omega_1\cdot\Omega_2 < 0$, and the period, T, is long compared to the characteristic time of the steady state flow. In contrast, our modulation protocols prescribe a slow, large-amplitude modulation:

$$\Omega_1(t,\epsilon) = \Omega_1 + \gamma\cos\epsilon t$$

$$\Omega_2(t,\epsilon) = \Omega_2 + \gamma\sin\epsilon t$$

where $0 < \epsilon \ll 1$, and $\Omega_2 < -\gamma < 0 < \gamma < \Omega_1$. This fundamental difference forces us to look at the transport problem in a new way. We discuss these details of the modulation protocols in Chapter 2.1. Furthermore, as we prove rigorously in Chapter 4.4, the requirement on the Strouhal number, $St \equiv \frac{\omega L}{U} \ll 1$, where L and U are characteristic lengths and velocities, and ω is the modulation frequency, shows that our slow modulation is the natural way to study these flows, because we take $\omega = \epsilon$. We remark that we denote the slow time by $z = \epsilon t$ and the ratio of the two angular velocities by $\bar{\Omega}(z) \equiv \frac{\Omega_2(z)}{\Omega_1(z)}$.

We remark that the Fourier series for the blinking protocols in the counterrotating case are infinite sums of higher harmonics of the periodic modulation (whose amplitudes decrease linearly with the order of the harmonic); just write the Fourier expansion for a square wave. Thus, one may get the results for the blinking case by

looking at the trend in a sequence of results obtained from continuous modulation protocols with more and more harmonics added.

We establish an analytical technique to determine the location and size of the region in which mixing occurs, a region we call the *mixing zone*. We show that the mixing zone is, to leading order, the region swept out by the instantaneous separatrices during the period of the modulation. It is precisely the zone in which a patch of tracer develops into a highly-striated lamellar structure, the vector field is nonintegrable, the exponential separation of nearby trajectories occurs, orbits are chaotic, and the islands lie. We discuss the mathematical definition of mixing later in this work.

In the course of showing how each of the three independent flow parameters: the eccentricity of the bearing $\bar{e}$, the time-dependent ratio of the angular velocities of the cylinders $\bar{\Omega}(z)$, and the modulation frequency ϵ, influences the location and size of the mixing zone, we determine the choice of parameters for which the mixing zone occupies the entire fluid domain. The same reasoning used for this determination can also be used to achieve mixing zones at other desired locations and sizes. Thus, our techniques offer a new manner in which mixing can be controlled.

After determining the location and size of the mixing zone, we develop a transport theory based on the regions, or lobes, formed by the segments of stable and unstable manifolds of the fixed points of the Poincaré map, which are responsible for the transport of tracer in the mixing zone. In particular, we show that the radically different shape of these lobes, as compared to the shape of the lobes studied in the usual flows, readily makes them identifiable as the mechanism by which the modulation causes the patches of tracer to develop into elaborately striated and folded lamellar structures. We are therefore able to refine the notion commonly expressed in the literature that tracer evolves along unstable manifolds. Furthermore,

we analytically derive exponentially growing lower bounds on the rate of stretching of the manifolds defining the lobes and use these to get similar bounds on the rate at which patches of tracer fluid stretch.

The results described so far are obtained independently of how small the modulation frequency, ϵ, is. When ϵ is small (we find $\epsilon < 0.3$ is small enough in practice) we show rigorously that these flows constitute adiabatic dynamical systems. This fact enables us to use recently developed tools (see Part I of this thesis, Kaper and Wiggins [1991a] and Elskens and Escande [1991]) from that field to analytically predict several important quantities associated with the lobes and transport theory. The ability to predict these quantities theoretically is very important, not just because their determination has hitherto depended on experimental data or the calculation of Lyapunov exponents, but also because it leads to a practical way in which our definition of mixing can be verified, as we will show in Chapter 3.

From the measurement of these quantities, we determine theoretically (and confirm with numerical simulation) the combination of the parameters $\bar{e}$, $\bar{\Omega}(z)$, and ϵ, with which one achieves the most efficient mixing possible. This optimal combination, which also maximizes the size of the mixing zone, consists of chosing $\bar{e}$ to be fairly small, so that the bearing is nearly concentric, $\bar{\Omega}(z)$ to vary in a large, negative interval so that the instantaneous saddle stagnation point moves across most of the narrow gap between the two cylinders of the bearing, and ϵ to be moderately small, but not too small. In the process of finding this optimal combination, we show how our theory makes it possible to control the rate and various other aspects of the mixing process with these parameters largely from theoretical considerations.

Having established our transport theory, we turn to the objects which obstruct mixing, and show how, for these objects as well, adiabatic dynamical systems theory

constitutes a useful framework. Using an extension of KAM theory, we show for the first time that the theory of adiabatic dynamical systems predicts the size of the regions, or "islands," in which the flow looks integrable and which obstruct mixing. Through our choice of ϵ, this theory gives us the ability to control, and hence to minimize, the area of islands. As in the analytical determination of the efficient mixing geometry, we find that a moderately small, but not too small, value of ϵ achieves the aim of minimizing the regular zones. Furthermore, we also use this extension of the KAM theory to explain the highly-regular appearance of islands in quasi-steady Stokes' flows, which is in contrast to the behavior of islands seen in weakly-perturbed flows, for the first time.

Finally, in studying the influence of diffusion on the evolution of tracer in these flows, we identify the mechanism of diffusion-enhanced stretching, which has not been studied systematically in the context of chaotic flows. We also discuss the robustness of our model by analyzing the influence of the inertial terms. In the last section, we compare our results to those obtained experimentally using so-called blinking protocols, and show how our results apply to other quasi-steady Stokes' flows, such as the cavity flow, the two-roll mill, and a geophysical flow.

Part II of the thesis is organized as follows. In Chapter 2, we discuss the steady state flow and the prescriptions for making them time-periodic which we use. We show how these prescriptions give us control over the location and size of the mixing zone. Then, the presentation of the transport theory is split into four sections, one on each of the structures governing the stretching and transport, the half-period and full-period inter-regional transport formulae, and the computation of an exponentially-growing lower bound on the rate of stretching of material interfaces. Chapter 3 is devoted to the application of adiabatic dynamical systems theory, including the ideas developed in Part I of this thesis, to this modulated

Stokes' flow. In particular, we obtain analytical results in the limit of slow modulation. We also discuss the issues of chaos, highly-regular zones, and islands in the context of the eccentric journal bearing and other quasi-steady Stokes' flows. In Chapter 4 we study the robustness of the purely-convective model presented in Chapter 2. The quantitative effects of molecular diffusivity are measured, and we identify the mechanism by which diffusion leads to enhanced stretching of tracer patches. We also include the effects of inertia and compare results from the continuous modulation protocols we use to those obtained in experiments on blinking flows. Finally, we show that in general quasi-steady Stokes flows are adiabatic dynamical systems and how the results of our study apply to other flows such as the cavity flow, the flow in the two-roll mill, and a geophysical application. The two appendices contain the derivations of some results quoted in Chapter 2.

CHAPTER 2. TRANSPORT THEORY.

In this chapter, we state the equations of motion for the evolution of tracer particles in the counterrotating eccentric journal bearing and introduce the modulation protocols we use to make the two-dimensional flow time-periodic. In addition, we study the mixing zone and show how the three flow parameters may be used to control its location and size. Finally, by identifying the structures which govern the transport of tracer in the time-periodic flow, we develop a transport theory which analytically predicts important mixing quantities.

2.1 Governing Equations and Modulation Protocols.

The geometry of the eccentric journal bearing is clearly illustrated using the bipolar coordinate system, an orthogonal curvilinear system which is related to Cartesian coordinates (x, y) by the following transformations:

$$\begin{aligned} x &= -b\frac{\sinh\xi}{\cosh\xi - \cos\eta} \\ y &= b\frac{\sin\eta}{\cosh\xi - \cos\eta} \end{aligned} \tag{2.1}$$

$$\begin{aligned} \xi &= \frac{1}{2}\ln\left(\frac{(x-b)^2+y^2}{(x+b)^2+y^2}\right) \\ \eta &= \frac{i}{2}\ln\left(\frac{x^2+(y-ib)^2}{x^2+(y+ib)^2}\right) \end{aligned} \tag{2.2}$$

The curves of constant ξ and η are exhibited in Figure 2.2. The two poles are at $(x, y) = (\pm b, 0)$, which correspond to $\xi = \mp\infty$, respectively. η is the angle made by the two segments connecting the point (x, y) to the poles, and e^{ξ} is the ratio of the lengths of these two segments, *i.e.*, of the polar radii. We remark that both ξ and η are real numbers.

The casing and the shaft of the bearing correspond, respectively, to the level curves $\xi = \xi_1$ and $\xi = \xi_2$, where $\xi_2 < \xi_1 < 0$ so that the shaft lies inside the casing

in the open half plane $x > 0$. We remark that although the level curves of ξ are circles, they are not concentric. Hence, this is a natural coordinate system to use in studying the eccentric journal bearing.

The radii of the casing and shaft are R_1 and R_2, respectively, where $R_1 > R_2$, and Ω_1 and Ω_2 are the angular velocities. We define the Reynolds number in terms of these and the kinematic viscosity ν:

$$\mathrm{Re} \equiv \frac{\left[R_1^2\Omega_1^2 + R_2^2\Omega_2^2\right]^{\frac{1}{2}} R_2}{\nu}.$$

Since we are interested in studying the evolution of tracer particles in Stokes' flow, we require $0 < \mathrm{Re} \ll 1$ so that the inertial terms in the Navier-Stokes equations may be neglected. The integrable, unperturbed flow between the shaft and the casing is governed by the stream function, ψ, which is the solution of the biharmonic equation $\nabla^4\psi = 0$ subject to no-slip boundary conditions on the two cylinders, see Ballal and Rivlin [1976]. Hence, the equations of motion for a tracer particle are:

$$\begin{aligned}\psi = &\frac{b}{\cosh\xi - \cos\eta}\left[(A_0 + C_0\xi)\cosh\xi + (B_0 + D_0\xi)\sinh\xi\right] \\ &+ \frac{b}{\cosh\xi - \cos\eta}\left[A_1\cosh 2\xi + B_1\sinh 2\xi + C_1\xi + D_1\right]\cos\eta.\end{aligned} \tag{2.3}$$

The constants $A_0, B_0, C_0, D_0, A_1, B_1, C_1$, and D_1 are given in terms of the radii and angular velocities of the cylinders, and the constants $f_i, i = 1 - 14$, (which depend only on the location and eccentricity of the two cylinders and which may be found in Appendix A):

$$\begin{aligned}(A_0, B_0, C_0, D_0) &= (f_1, f_3, f_5, f_7)\Omega_1 R_1 + (f_2, f_4, f_6, f_8)\Omega_2 R_2 \\ (A_1, B_1, C_1, D_1) &= (f_9, f_{11}, -f_5, f_{13})\Omega_1 R_1 + (f_{10}, f_{12}, -f_6, f_{14})\Omega_2 R_2.\end{aligned} \tag{2.4}$$

We remark that since ψ is linear in Ω_1 and Ω_2, it effectively depends only on the ratio of the two.

Using the inverse transformation (2.2), we put the streamfunction in Cartesian coordinates, which is the form of ψ we use in our study so that our results may be directly compared to those of experiments. The unperturbed equations of motion are:

$$\begin{aligned} \dot{x} &= \frac{\partial \psi}{\partial y}(x, y; \Omega_1, \Omega_2) \\ \dot{y} &= -\frac{\partial \psi}{\partial x}(x, y; \Omega_1, \Omega_2). \end{aligned} \tag{2.5}$$

We remark that, in contrast to the case for Hamiltonian systems in mechanics, the phase space of these Hamiltonian systems (2.5) is the fluid domain, and the two Cartesian coordinates x and y are the canonically conjugate coordinates.

We concentrate on the counterrotating ($\Omega_1 \cdot \Omega_2 < 0$) case. In Chapter 4.2, we discuss the remaining cases: corotating, and the two cases in which a cylinder is stationary.

In the counterrotating case, there is precisely one saddle stagnation point (hyperbolic fixed point) on the x-axis in the narrow gap for all values of $\bar{e}$, $\bar{r}$, Ω_1 and Ω_2, which is attached to itself by two stagnation streamlines (orbits homoclinic to the hyperbolic fixed point). We denote the fixed point by X_0, and we denote the inner and outer stagnation streamlines by Γ and Λ, respectively. The two stagnation streamlines separate the fluid domain into three regions: region A is the area adjacent to the shaft; region B is the backflow region; and region C is the annular piece adjacent to the casing. In Tables 2.1-2.3, we give the area of each of these three regions for various values of $\bar{e}$ and the ratio $\bar{\Omega} \equiv \frac{\Omega_2}{\Omega_1}$. The streamlines (integrable flow field) for a typical case in Figure 2.1, where $\Omega_1 = 1, \Omega_2 = -4, \xi_1 = -0.9397, \xi_2 = -1.9966, b = 1.0843, R_1 = 1.0, R_2 = 0.3, \bar{e} = 0.5$.

We remark that we first specify R_1, $\bar{r} \equiv \frac{R_2}{R_1}$, and $\bar{e}$, which determine the cylinder geometry uniquely, and then determine the parameter b and the level curves, $\xi = \xi_1$ and $\xi = \xi_2$, on which the cylinders lie from this choice. Although this choice, which

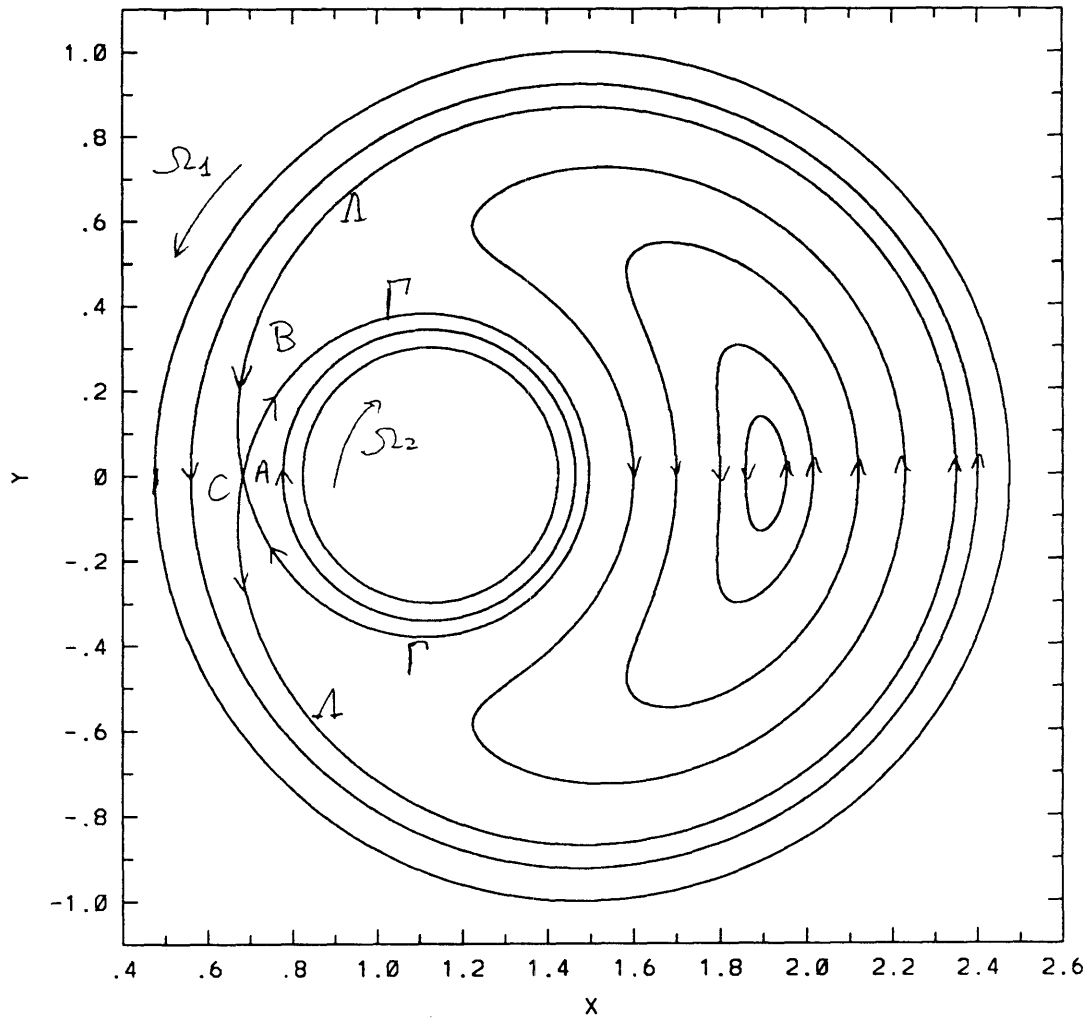

Fig. 2.1. Steady state flow in the counterrotating eccentric journal bearing with $\bar{r} = 0.3, \bar{e} = 0.5, \Omega_1 = 1.0, \Omega_2 = -4.0$.

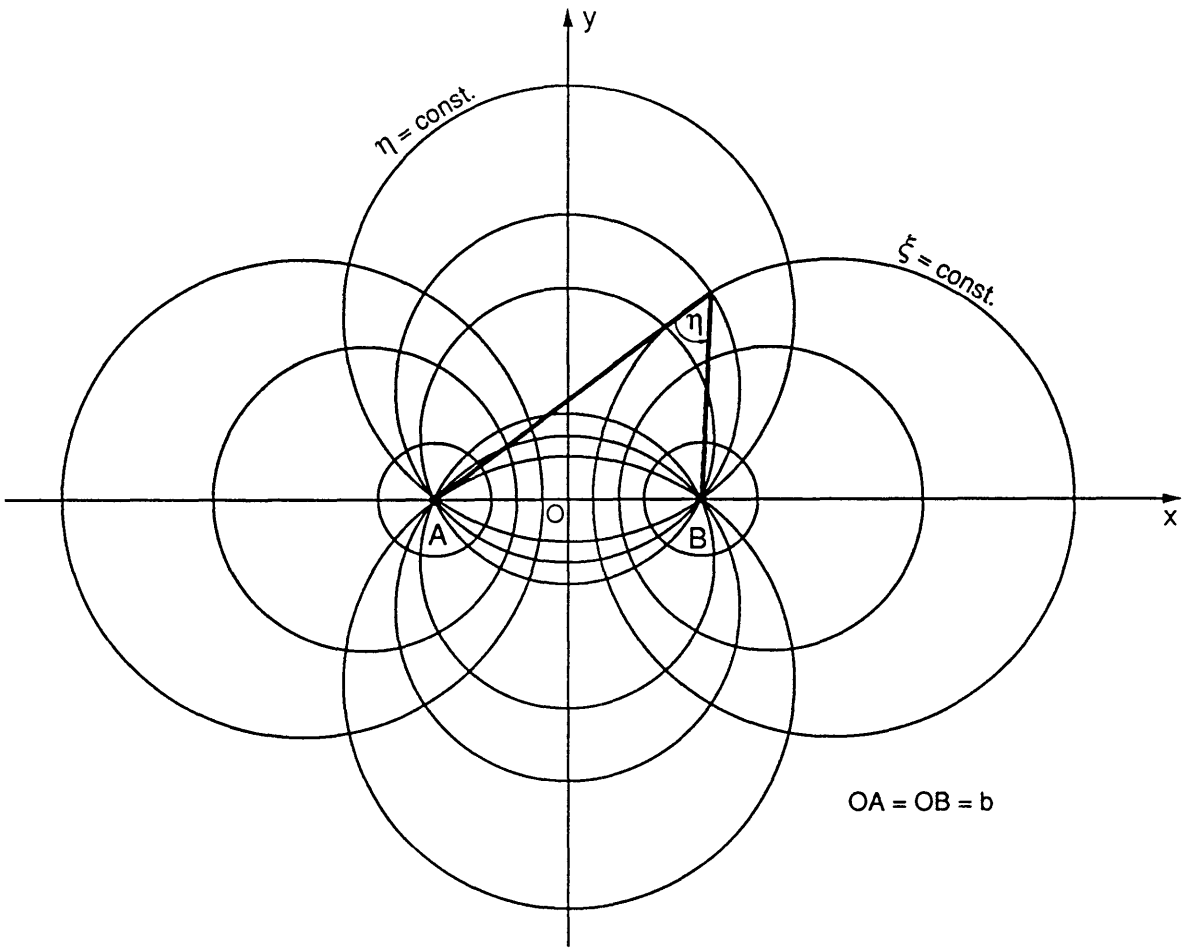

Fig. 2.2. Geometry of the bipolar coordinate system.

is made without loss of generality, means that b and hence the absolute bipolar coordinate system we use depends on the value of $\bar{e}$ we specify, this choice makes everything easier to implement numerically. The appropriate formulae and a more complete catalog of streamline plots, including ones for the corotating case, may be found in Ballal and Rivlin [1976], whose notation we use throughout this work.

Modulation Protocols.

As discussed in the introduction, we are interested in studying the system when the angular velocities of the cylinders change slowly and periodically in time. We refer to the prescription for these variations as modulation protocols, and we present results from simulations for three of them in this work:

$$\begin{aligned} \Omega_1(t,\epsilon) &= 1 \\ \Omega_2(t,\epsilon) &= -6 + 4\cos(\epsilon t) \end{aligned} \tag{MP1}$$

$$\begin{aligned} \Omega_1(t,\epsilon) &= 1 \\ \Omega_2(t,\epsilon) &= -11 + 9\cos(\epsilon t) \end{aligned} \tag{MP2}$$

$$\begin{aligned} \Omega_1(t,\epsilon) &= 1 \\ \Omega_2(t,\epsilon) &= -30.5 + 29.5\cos(\epsilon t) \end{aligned} \tag{MP3}$$

Here the modulation frequency ϵ satisfies $0 < \epsilon \ll 1$. This choice guarantees that the modulation occurs on a time-scale much larger than the characteristic time of the unperturbed system and satisfies the requirement on the Strouhal number given in the introduction.

Furthermore, we have three intervals in which $\bar{\Omega}$ varies: $[-2,-10]$ with (MP1), $[-2,-20]$ with (MP2), and $[-1,-60]$ with (MP3), so that we may study the influence of the parameter $\bar{\Omega}$ on the mixing process. In particular, since the ratio of Ω_2

to Ω_1 determines the location of X_0, we can study the dependence of the mixing results on the size of the interval in which the saddle point oscillates. For (MP1) that interval is small and near the middle of the narrow gap, whereas for (MP3) that interval is almost as wide as the narrow gap itself. Finally, (MP2) yields an intermediate interval.

(MP1) - (MP3) have been chosen so that their implementation is the simplest experimentally. The experimental set-up of Swanson and Ottino [1990] may be used, for example, replacing their motor to drive the shaft with a computer-controlled stepping-motor, so that the angular velocity may be changed many times per period of the modulation, Leal, private communication [1989]. We remark that our techniques are valid for general, small frequency, time-periodic modulation protocols. We have chosen (MP1) - (MP3) as representative examples. The choice of $\Omega_1(t) \equiv 1$ for all t in both modulation protocols is made with out loss of generality because the equations are linear in the angular velocities. Finally, using (MP1) - (MP3), we operate well within the range of angular velocities for which Ballal and Rivlin [1976] report their results.

The introduction of the modulation protocols (MP1) - (MP3) makes the equations of motion for the tracer particles, (2.5), nonintegrable and puts their perturbed equations in the form of an adiabatic dynamical system (see Introduction):

$$\begin{aligned} \dot{x} &= \frac{\partial \psi}{\partial y}(x, y; z) \\ \dot{y} &= -\frac{\partial \psi}{\partial x}(x, y; z) \\ \dot{z} &= \epsilon, \end{aligned} \tag{2.6}$$

where the dependence of ψ on z is through the time-dependent functions Ω_1 and Ω_2 as given by (MP1), (MP2), or (MP3). Since the modulation protocols are periodic

in $z = \epsilon t$, we use the Poincaré map

$$T_{z_0}\begin{pmatrix} x(z_0) \\ y(z_0) \end{pmatrix} \equiv \begin{pmatrix} x(z_0 + 2\pi) \\ y(z_0 + 2\pi) \end{pmatrix}$$

with $z_0 \in [0, 2\pi)$, which gives a stroboscopic picture of the fluid domain and enables us to isolate the main features of the nonintegrable flow in the next sections. We remark that T_{z_0} is area-preserving. As for the notation in this work, z always denotes the time-dependent value: $z = \epsilon t$, and z_0 denotes some fixed value of z.

One other concept we will use often in the remainder of this work is that of an *instantaneous streamline*. The instantaneous streamline is the closed trajectory the particle would execute if the system evolves with the value of z frozen at its instantaneous value. Thus, it coincides with the orbit one would obtain in the steady state flow with the constants Ω_1 and Ω_2 equal to their value at the instantaneous value of the slow time variable z that passes through the particle's instantaneous position. Of course, since particle paths in the modulated flow no longer coincide with streamlines, this concept is a fictitious one; nevertheless it is widely used in the literature on adiabatic dynamical systems, and we will find it helpful in our discussions.

2.2. Location and Size of the Mixing Zone.

In this section, we isolate the region in the fluid domain in which mixing occurs and discuss how its location and size can be optimized and controlled. We use the term mixing loosely now, and remark that we discuss mixing from the mathematical point of view further on. We also remark that, although we give numerical results here for one particle over long time periods, the good mixing for patches of tracer in the flows begins in the very first period, as we will see in the next sections. The purpose of this section is to show how one can control the size and location of the mixing zone.

The three independent parameters which determine the location and size of the mixing zone are the eccentricity of the bearing, $\bar{e}$, the interval in which the time-dependent ratio of the angular velocities of the shaft and the casing, $\bar{\Omega}(z) \equiv \frac{\Omega_2(z)}{\Omega_1(z)}$ varies, recalling that $z = \epsilon t$, and the modulation frequency, ϵ. In the counterrotating regime, we show that the largest possible mixing zone is obtained when these three parameters are chosen such that: $\bar{e} \approx 0.1$; $\bar{\Omega}(z)$ varies in an interval which is finite, negative, and as large as possible, on the order of [-1,-60], as in (MP3); and ϵ is moderately small, but not too small. With this choice of parameters the mixing zone occupies virtually the entire fluid domain. We remark that islands in this zone are negligibly small for this optimal choice of parameters and that we discuss them in Chapter 3. Also, our $\bar{e}$ is the identical to the variable $\bar{\epsilon}$ in Ballal and Rivlin [1976].

Although $\bar{e}$, $\bar{\Omega}(z)$, and ϵ are mutually independent parameters, the search for the combination of these three parameters which maximizes the size of the mixing zone requires that we study their effects simultaneously. For clarity, we begin by considering the influence of the first two parameters, and maximizing the potential area for mixing. Then we add to these considerations the influence of ϵ, which determines how much of the area potentially available for mixing is actually used. We remark that this optimal combination of the three parameters can be determined without any knowledge of the invariant structures in the mixing zone and with only a minimal amount of numerical simulation.

Finally, we present the results of our numerical simulations for a geometry with $\frac{R_2}{R_1} \equiv \bar{r} = 0.3$ at the end of this section. These results support the claims we made above.

In the course of our discussion, we shall observe that the use of continuous modulation protocols gives us explicit control over the location and size of the

mixing zone. Thus, although we focus on how to optimize the size of the mixing zone, the theory we present and the type of data we collect also enable one to chose a modulation protocol which achieves an alternatively specified location and size for the mixing zone. In this sense, we provide a new tool for control over this aspect of chaotic mixing.

Optimizing the choice of $\bar{e}$ and of the interval in which $\bar{\Omega}(z)$ varies.

As we mentioned in the introduction of this chapter, the (fictitious) instantaneous stagnation streamlines sweep out a predetermined $\mathcal{O}(1)$ area in the fluid domain during one period of the modulation protocol as $\bar{\Omega}(z)$ varies over a chosen interval, *e.g.*, the interval $[-10, -2]$ with choice of (MP1). In the mixing zone, the theory of adiabatic invariance and the extension of the KAM theorem are not applicable because the assumption that those theories rely on, namely that the frequency of the instantaneous steady state orbits be one order of magnitude larger, *i.e.*, $\mathcal{O}(1)$, than the modulation frequency ϵ, ceases to be valid on and near stagnation streamlines, which are zero frequency orbits. In fact, observations collected from theoretical and numerical work on various model problems, see the discussion in the introduction and the references cited there, suggest that tracer particles can explore most of this region because there are very few barriers to their transport in this region. Hence this is the region in which mixing can be expected to occur.

For (MP1) – (MP3), the region swept out may be specified exactly as:

$$\left(\bigcup_{z\in[0,\pi]} \Gamma^z\right) \cup \left(\bigcup_{z\in[0,\pi]} \Lambda^z\right). \tag{2.7}$$

Because the area of the set (2.7) is to leading order the area potentially available for mixing, we label region (2.7) as the *potential mixing zone.* We refer the reader to Figure 2.3 for illustrations showing this zone.

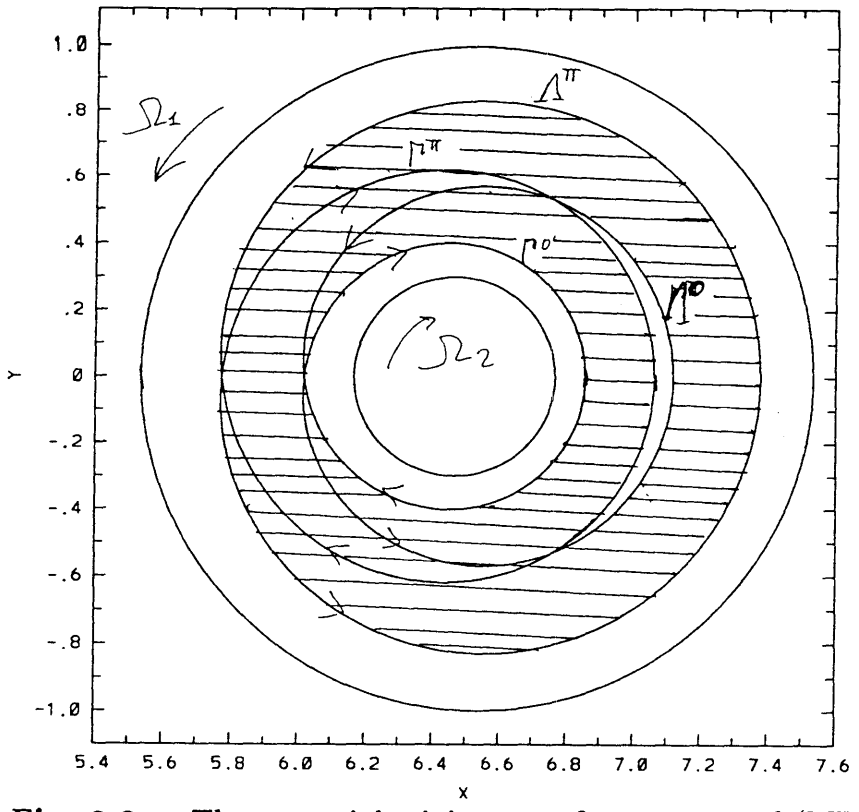

Fig. 2.3.a. The potential mixing zone for $\bar{e} = 0.1$ and (MP1).

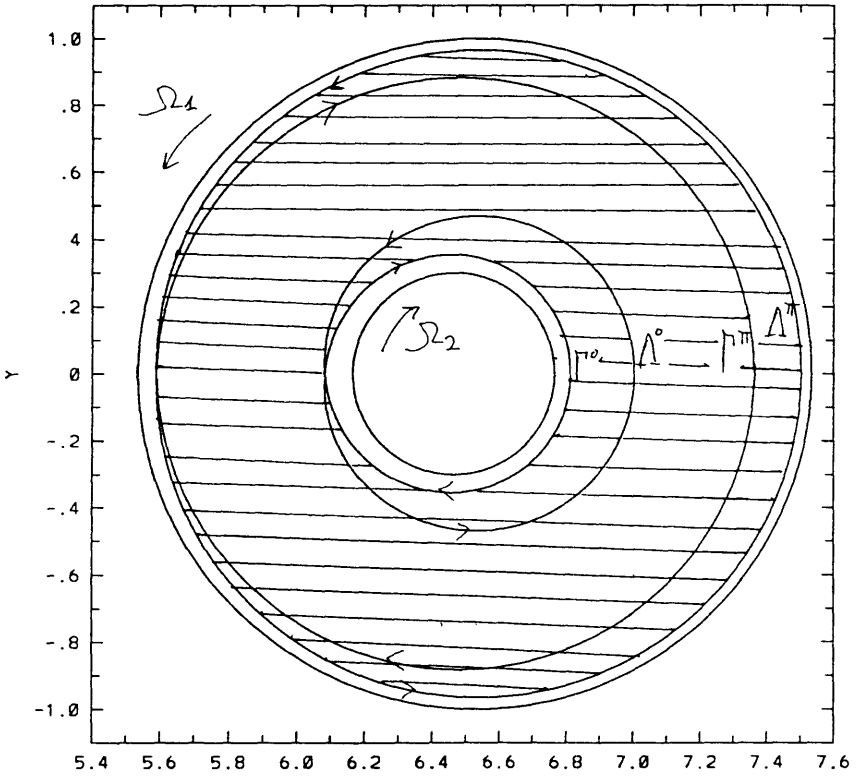

Fig. 2.3.b. The potential mixing zone for $\bar{e} = 0.1$ and (MP3).

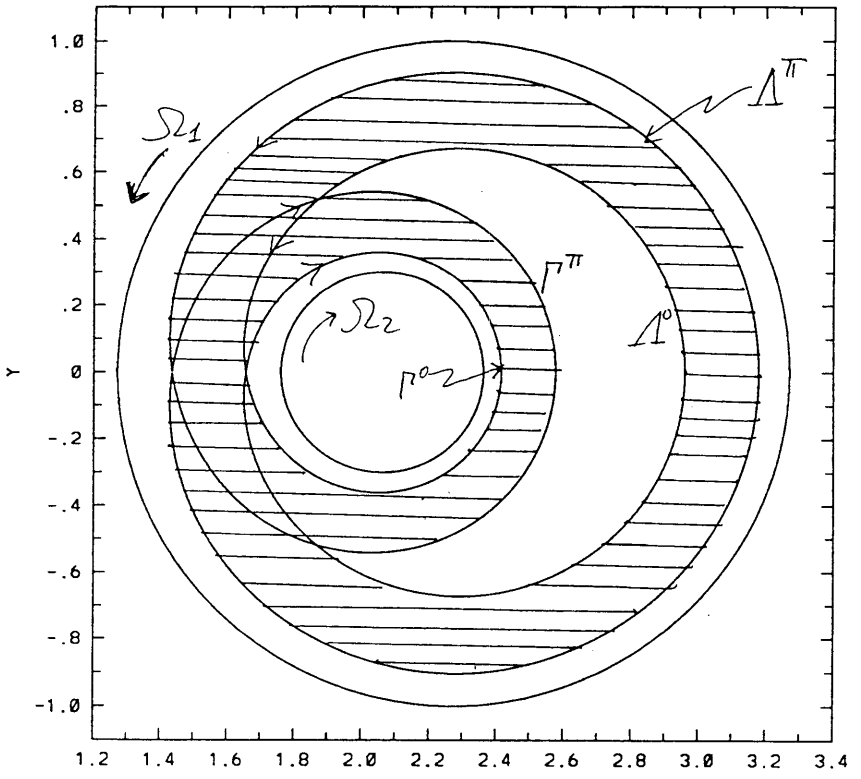

Fig. 2.3.c. The potential mixing zone for $\bar{e} = 0.3$ and (MP1).

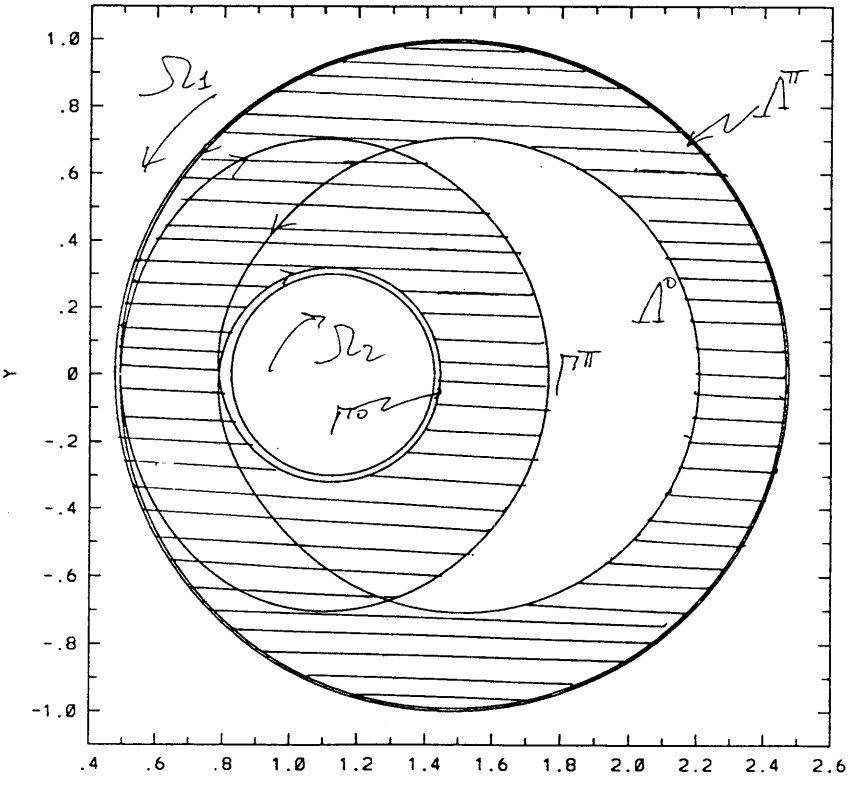

Fig. 2.3.d. The potential mixing zone for $\bar{e} = 0.5$ and (MP1).

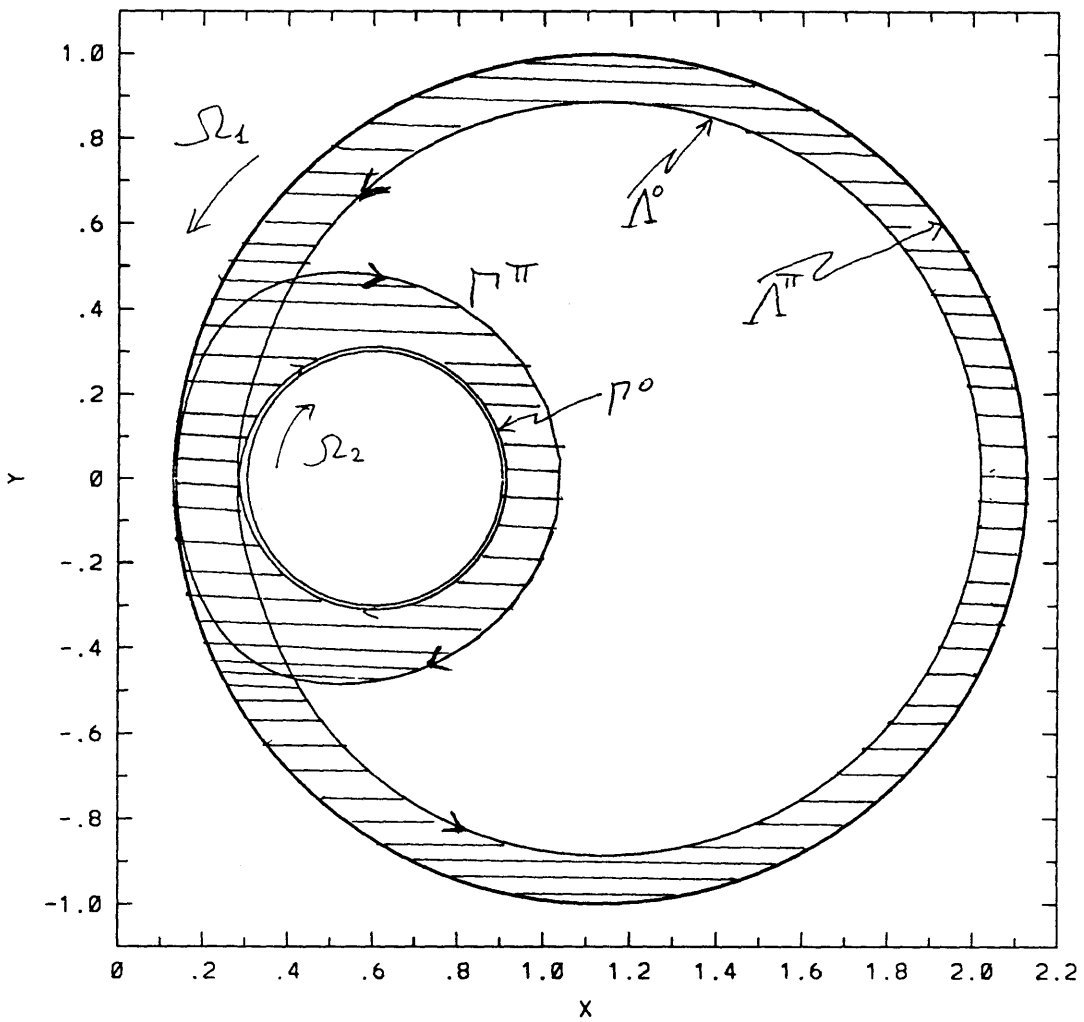

Fig. 2.3.e. The potential mixing zone for $\bar{e} = 0.75$ with (MP3).

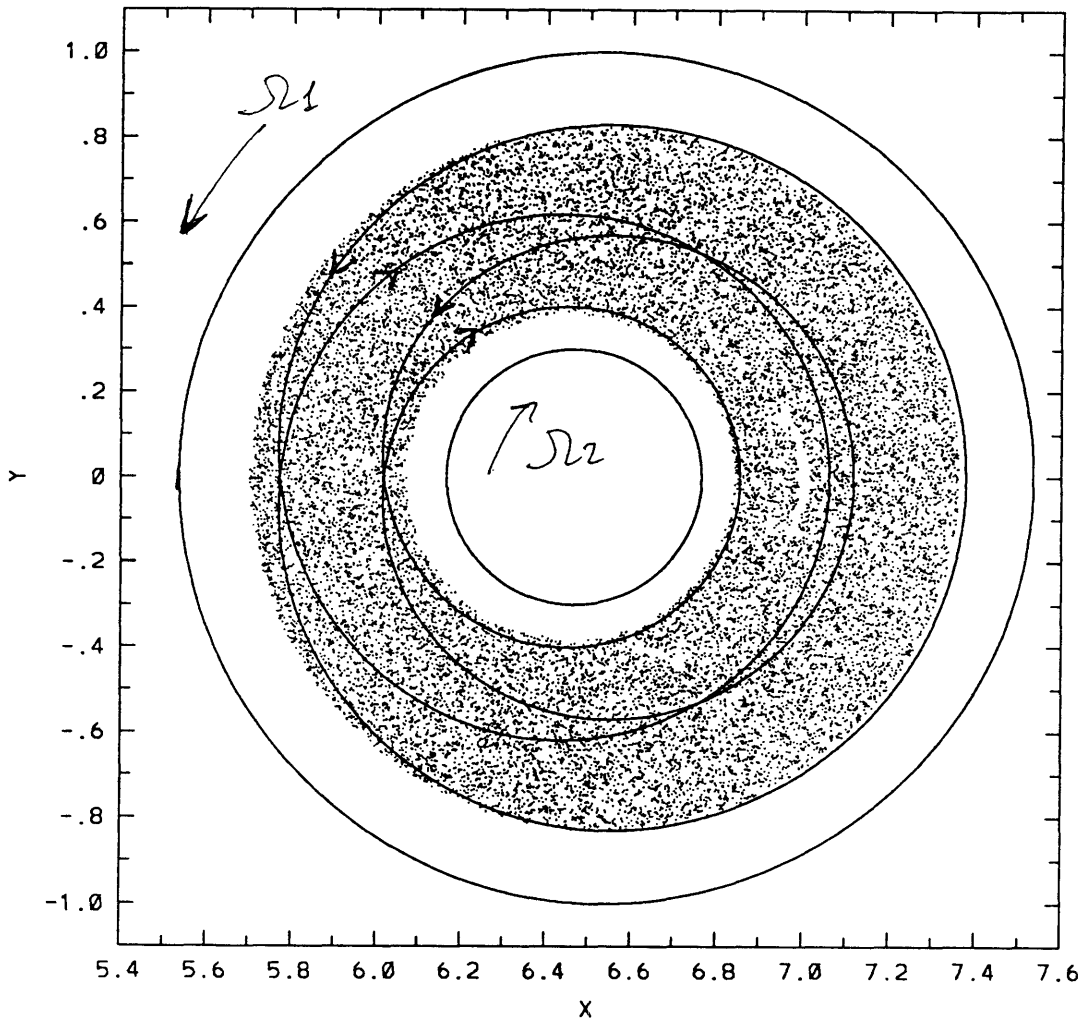

Fig. 2.4. Actual mixing zone for $\bar{e} = 0.1$, $\bar{r} = 0.3$, (MP1), $\epsilon = \frac{2\pi}{50}$. One initial condition integrated for 20,000 modulation periods. We emphasize that we only use these pictures to illustrate what area a fluid particle can sample; the results of Chapters 2-4 concern mixing for all times especially the very short time intervals (on the order of a few periods) which are of most interest in mixing studies.

We tabulate the area of this zone as a function of both the parameter $\bar{e}$ and the range over which the parameter $\bar{\Omega}(z)$ varies in Table 2.4. The determination of the area can be made analytically once one has found a numerical representation of the instantaneous stagnation streamlines. As may be seen from the data, the choice of $\bar{e} \leq 0.1$ combined with prescribing $\bar{\Omega}(z)$ to vary in the largest possible finite, negative interval during one modulation period maximizes the size of the potential mixing zone.

We remark that symmetry in (MP1) - (MP3) about $z = \pi$, namely $\bar{\Omega}(z_0) = \bar{\Omega}(2\pi - z_0)$ for $z_0 \in (\pi, 2\pi]$, implies that we only need to take the unions over $z_0 \in [0, \pi]$ in (2.7). For more general protocols, the unions are taken over all z_0 between the two values of z_0 corresponding to an instantaneous separatrix which locally (*i.e.*, compared to the instantaneous separatrices for nearby values of z_0) encloses a maximum area and an instantaneous separatrix which locally encloses a minimum area, see Kaper and Wiggins [1991a]. Also the analysis for more general protocols is most readily performed after one has found a canonical transformation which brings the systems in a form such that the instantaneous saddle lies at one point for all z. Furthermore, we remark that when we measure the area of this region, we must be careful not to count the overlapping pieces in (2.7) twice.

Influence of the parameter ϵ.

Until now, our considerations have only involved the parameters $\bar{e}$ and the time-dependent ratio of the angular velocities $\bar{\Omega}(z = \epsilon t)$. In the remainder of this subsection, fixing $\bar{e} = 0.1$ and using (MP1), we show how the modulation frequency, ϵ, influences the size and location of the actual mixing zone. In particular, we show that there exist two qualitatively different regimes - one, corresponding to small values of ϵ, *i.e.*, $\epsilon < 0.1$, in which the actual mixing zone is considerably smaller

than the potential mixing zone, and the other regime, corresponding to moderate values of ϵ, *i.e.*, $0.14 \leq \epsilon \leq 0.34$, in which the actual mixing zone is as big as the potential mixing zone. We find a similar dependence on ϵ using (MP2) and (MP3), although the lower bound on the range of "moderate" ϵ is smaller for (MP3) than it is for either (MP1) or (MP2) in the same geometry, see Figure 2.13 for an example. We show how the value of this lower bound can be obtained analytically before experiments or numerical simulations are performed from knowing the thickness of the minimal backflow region in the course of our analysis of the regime corresponding to moderate values of ϵ. Furthermore, we illustrate what the transition, corresponding to ϵ increasing from being less than 0.1 to being approximately 0.14 in this case, between the two regimes looks like. We discuss the regime of small ϵ first, describe the transition, and then present the results for the regime corresponding to moderate values of ϵ.

For small values of ϵ and $z_0 = 0 \bmod 2\pi$, the theory of adiabatic invariance and an extension of the KAM Theorem (see Kruskal [1962] and Arnold [1963], resp.) state that many orbits in the backflow region (region II on the Poincaré section Π_{z_0}) will remain in the region II for all times. In particular, many orbits have a perpetually conserved adiabatic invariant and lie on invariant tori. Hence a large part of the backflow region appears to be a regular zone, and since region II is a part of the potential mixing zone, the actual mixing zone is smaller than the potential zone (2.7).

These theories, along with some numerical results, enable us to justify and quantify the above statements as follows. The leading order term of the perturbation series in the small parameter ϵ for the adiabatic invariant of an orbit in the instantaneous backflow region is exactly the area enclosed by the instantaneous periodic streamline it is on. For example, if one starts an orbit in the backflow region

at a given value of the slow time z, say z_1, then the leading order term of its adiabatic invariant is the area $A_{\rm po}(z_1)$ enclosed by the instantaneous periodic streamline $s_{\rm po}$ that it starts out on. However, as we discussed in the previous section, because the backflow region grows and decreases in size periodically during the modulation, only those orbits for which $A_{\rm po}(z_1)$ is sufficiently less than the minimum size of the backflow region over all z (see Table 2.2 for an example with $\bar{\rm e} = 0.1$ and (MP1) in which the area is 0.4716) stay in region II for all times and have an adiabatic invariant. We can use Arnold's extension of the KAM theorem to get slightly more information since the modulation is periodic in z. In particular, the theory states that most of the orbits for which $A_{\rm po}(z_1)$ is sufficiently less than the size of the minimal backflow region lie on invariant tori which fill all but some exponentially vanishing, $\mathcal{O}(e^{-\frac{c}{\epsilon}})$ where c is a positive constant, part of the interior of the backflow region.

Observing that the backflow region is at its smallest for $z = 0 \bmod 2\pi$ with the choice of any of (MP1) – (MP3), we conclude that most of the orbits which are in the minimal backflow region at the slow time $z = 0$ lie on invariant tori and have a perpetually conserved adiabatic invariant. We also conclude that the minimum backflow region is what we have referred to as a regular zone since the irregular or stochastic part of it is at most $\mathcal{O}(e^{-\frac{c}{\epsilon}})$, see Arnold [1988].

Therefore, no mixing occurs in the interior of the $\mathcal{O}(1)$–sized minimal backflow region, and we exclude it from the actual mixing zone. We show a case in which the minimum backflow region contains a large regular zone in Figure 2.6. We remark that we discuss regular zones in detail in the section with the same name, *i.e.* Chapter 3.3.

Finally, as we discussed in the previous section, most of the orbits for which A_z is larger than the minimal size of the backflow region may be expected to cross an

instantaneous stagnation streamline for some z. The adiabatic invariants of these orbits change after each crossing, and they cannot lie on invariant tori. These orbits lie in a layer, Σ_ϵ, just inside the minimal backflow region. The thickness of Σ_ϵ, see Figures 2.5 and 2.6, which cannot be obtained from the theories cited above, is exactly what we need in order to completely determine the location and size of the mixing zone for small ϵ.

Σ_ϵ has an annular shape. Its inner boundary is the outermost (or last) Arnold torus in the minimal backflow region, and on the outside it is adjacent to the potential mixing zone. Thus, as we see in the figures, it forms part of the actual mixing zone. We report the values for the thickness of Σ_ϵ, as measured along the x-axis in the wide part of the gap between the shaft and the casing, obtained from our numerical simulations for various of the canonical cases in Table 2.5. The data indicate that the width of Σ_ϵ is $\mathcal{O}(\epsilon)$ as $\epsilon \to 0$.

While a general theory is not yet available to give the asymptotic scaling of Σ_ϵ for $\epsilon \to 0$, Neishtadt and coworkers, private communication [1990], have extended their work and that of Cary, *et al.* [1986], and shown for a model problem that the layer which corresponds to Σ_ϵ in this problem is $\mathcal{O}(\epsilon^2 |\ln \frac{1}{\epsilon}|^2)$ as $\epsilon \to 0$. One can try to fit the data from one case ($\bar{e} = 0.1$, $\bar{r} = 0.3$, (MP1) with various values of ϵ for $\epsilon < 0.14$) - see Table 2.5 - to this functional dependence on ϵ, however, the fit is not good. This completes our discussion of the location and size of the mixing zone in the first regime, that corresponding to $\epsilon < 0.1$.

Now, we study what happens in the transition regime, *i.e.*, as ϵ increases to approximately 0.14 in the case we consider. We observe that because the minimal backflow region has a kidney-like shape and the layer Σ_ϵ is inside its boundary, there exists some critical value of ϵ at which the Σ_ϵ is as thick as the half-width of the backflow region. The plots and data show that the regular-appearing backflow

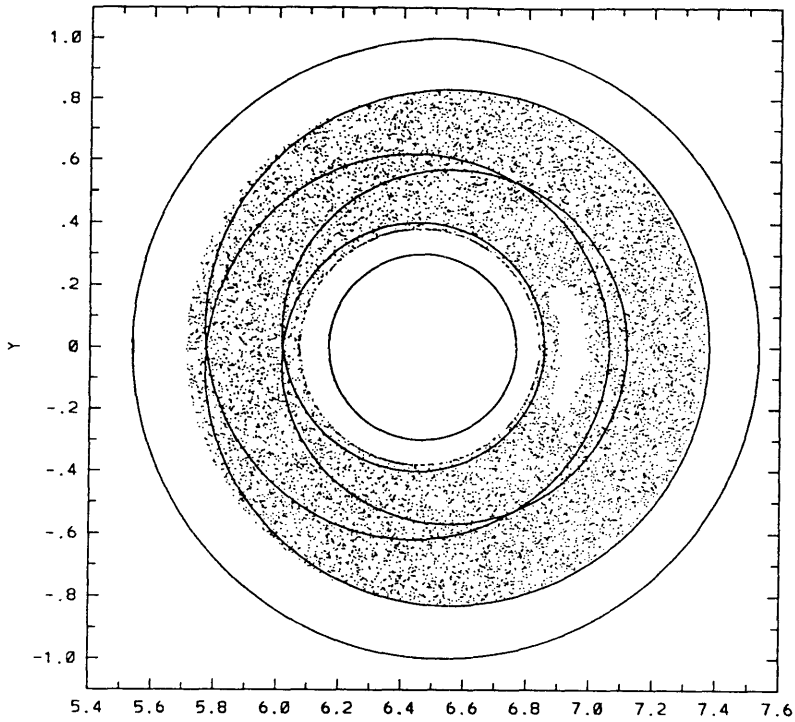

Fig. 2.5. Actual mixing zone for $\bar{e} = 0.1$, $\bar{r} = 0.3$, (MP1), $\epsilon = \frac{2\pi}{60}$. One initial condition integrated for 10,000 periods.

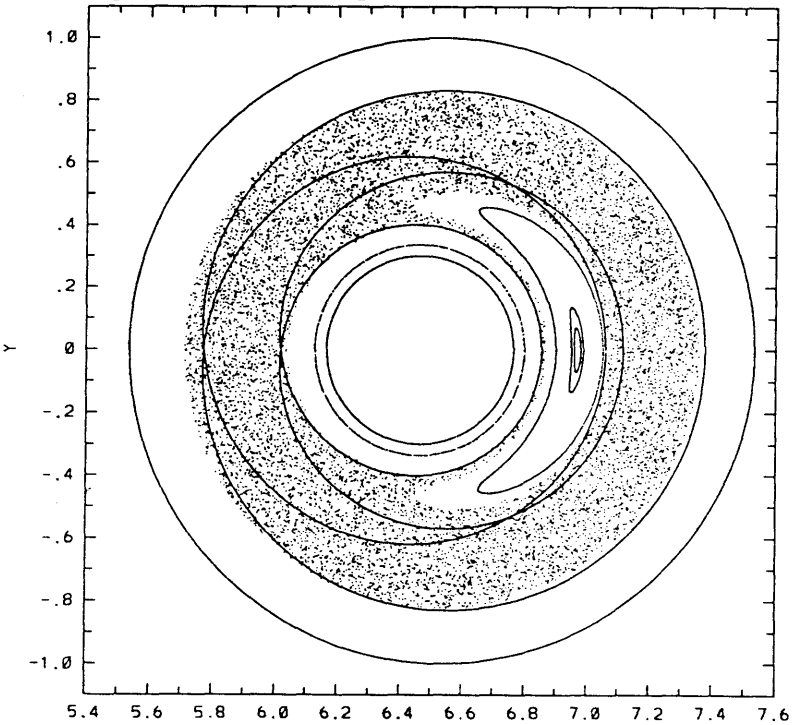

Fig. 2.6. Actual mixing zone for $\bar{e} = 0.1$, $\bar{r} = 0.3$, (MP1), $\epsilon = \frac{2\pi}{120}$. One initial condition integrated for 10,000 periods. Also see invariant tori.

region becomes smaller as ϵ grows from being very small (less than 0.03), looks like a tiny island for $\epsilon \approx 0.13$ (see the plot for $\frac{2\pi}{50}$ in the figures), and ceases to exist altogether for $\epsilon \geq 0.14$. Thus, this critical value is approximately $\epsilon = 0.14$. Furthermore, we remark that the transition appears to be smooth.

In the second regime the actual mixing zone is at least as big as the potential mixing zone. For $0.14 \leq \epsilon \leq 0.34$, our numerical simulations show that the entire backflow region belongs to the mixing zone. We illustrate the results of two typical cases in Figures 2.7 and 2.8. Furthermore, we remark that if one uses (MP3), the lower bound on this interval of "moderate values" of ϵ is smaller than that obtained for either (MP1) or (MP2). This is because the smallest value of ϵ for which Σ_ϵ is wider than the minimal backflow region using (MP3) is less than that when using (MP1) or (MP2). From Figure 2.13, we can see that the lower bound for (MP3) with the given values of $\bar{e}$ and $\bar{r}$ is less than 0.14.

We round off our discussion of the parameter ϵ by showing, for the optimal choice of parameters, that the actual mixing zone is slightly bigger than the potential one. Of course, the conclusions made in the above discussion of the layer Σ_ϵ apply with suitable modifications to the layers around the inner and outer boundaries of the mixing zone. As we discuss in Chapter 3.3, most orbits in the regular zones adjacent to either the shaft or the casing, *i.e.*, in region I or III, lie on invariant tori (since the modulation is time-periodic) and have adiabatic invariants (which is true for all slow-time modulation protocols). However those which lie within some layer (of width $\mathcal{O}(\epsilon)$) just inside and outside, respectively, of the extremal instantaneous stagnation streamlines Γ^0 and Λ^π, which form the inner and outer boundaries of the potential mixing zone (2.7), are part of the mixing zone. So in fact, the actual mixing zone is slightly larger than the set (2.7). We refer the reader to Figure 2.7 for a representative Poincaré section.

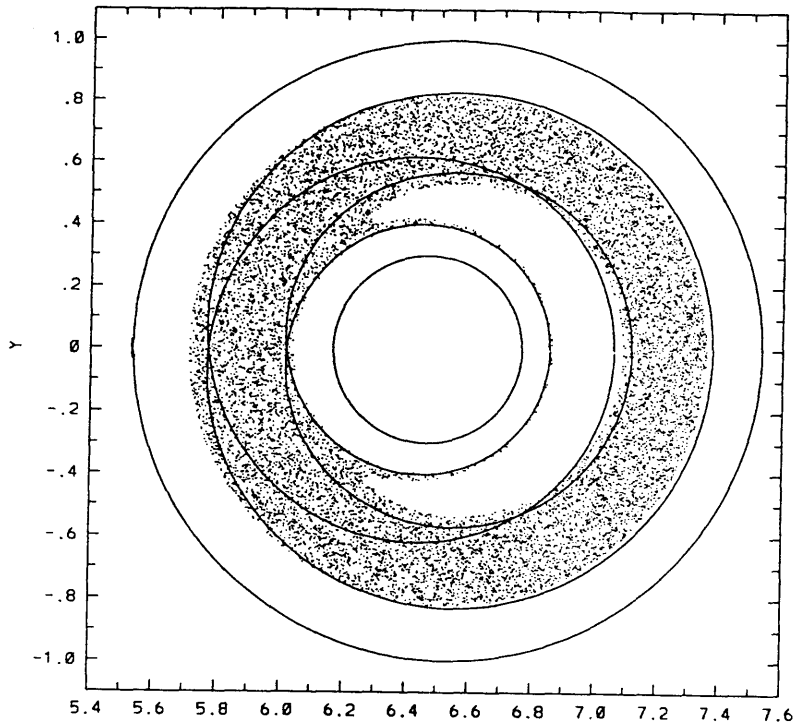

Fig. 2.7. Actual mixing zone for $\bar{e} = 0.1$, $\bar{r} = 0.3$, (MP1), $\epsilon = \frac{2\pi}{180}$. One initial condition integrated for 12,000 periods.

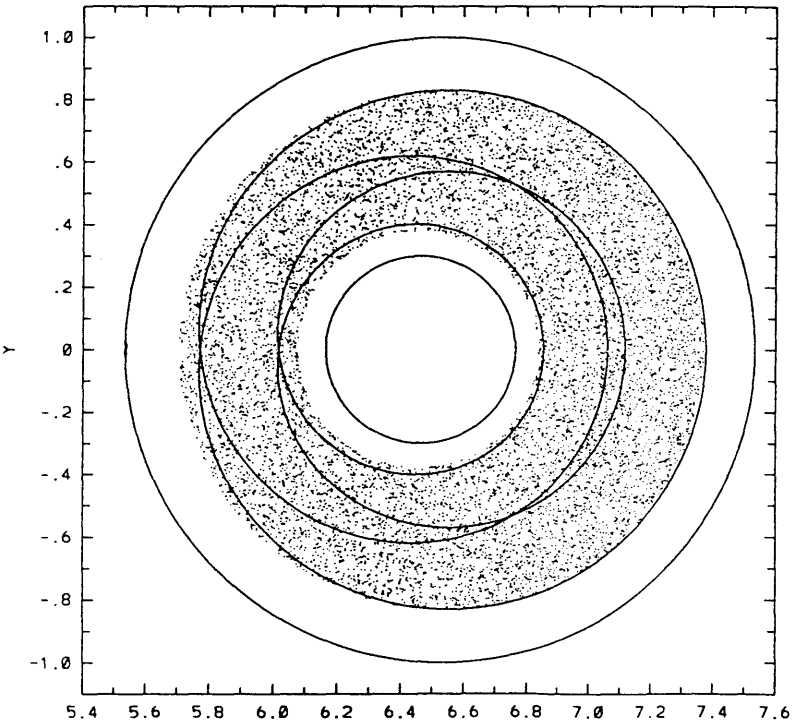

Fig. 2.8. Actual mixing zone for $\bar{e} = 0.1$, $\bar{r} = 0.3$, (MP1), $\epsilon = \frac{2\pi}{40}$. One initial condition integrated for 10,000 periods.

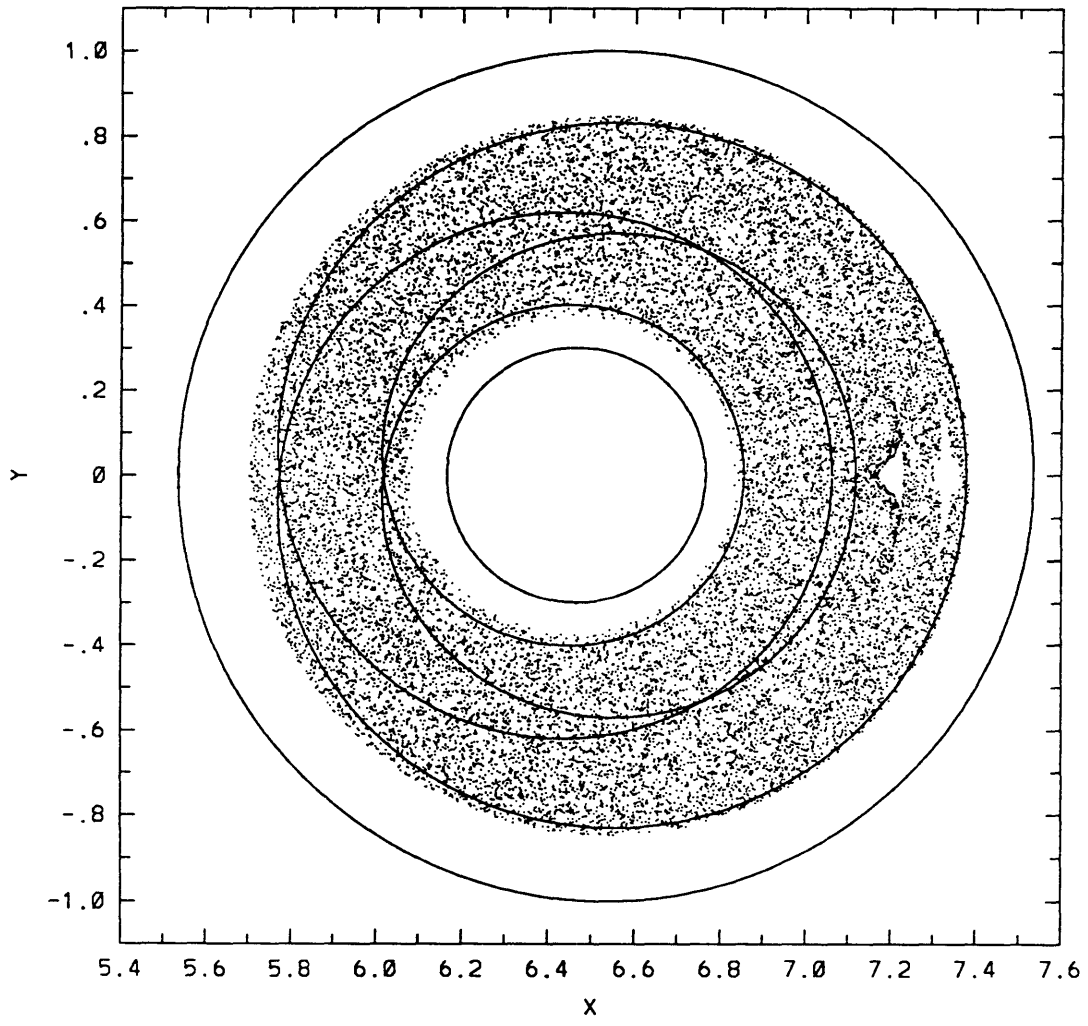

Fig. 2.9. Actual mixing zone for $\bar{e} = 0.1$, $\bar{r} = 0.3$, (MP1), $\epsilon = \frac{2\pi}{20}$. One initial condition integrated for 20,000 periods.

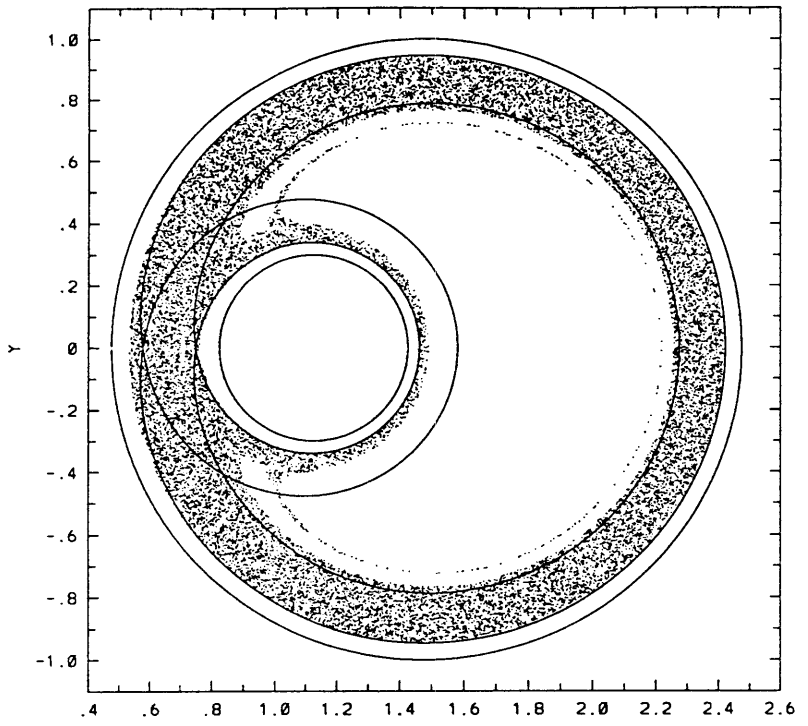

Fig. 2.10. Actual mixing zone for $\bar{e} = 0.5$, $\bar{r} = 0.3$, (MP1), $\epsilon = \frac{2\pi}{60}$. One initial condition integrated for 20,000 periods.

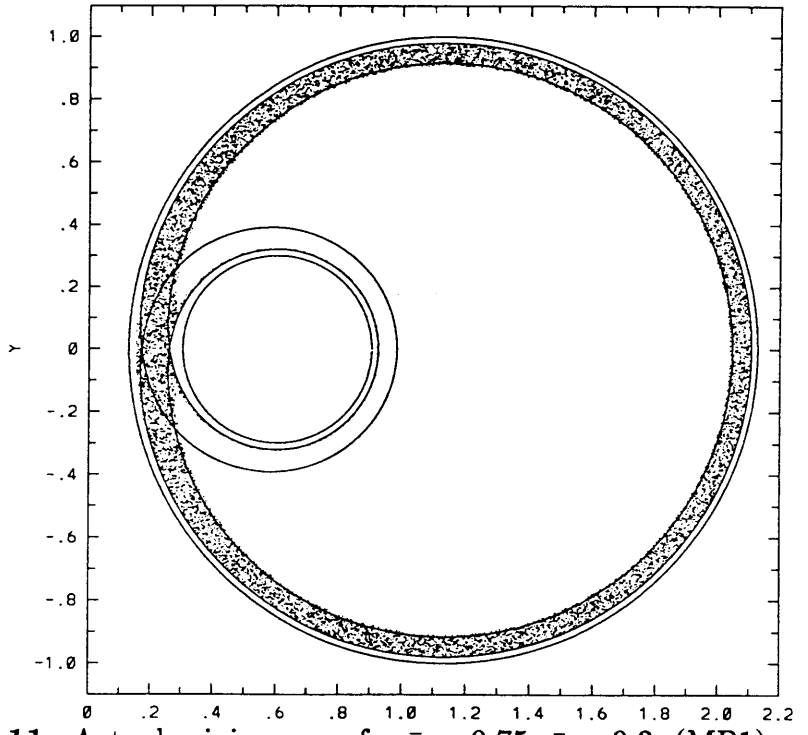

Fig. 2.11. Actual mixing zone for $\bar{e} = 0.75$, $\bar{r} = 0.3$, (MP1), $\epsilon = \frac{2\pi}{60}$. One initial condition integrated for 10,000 periods.

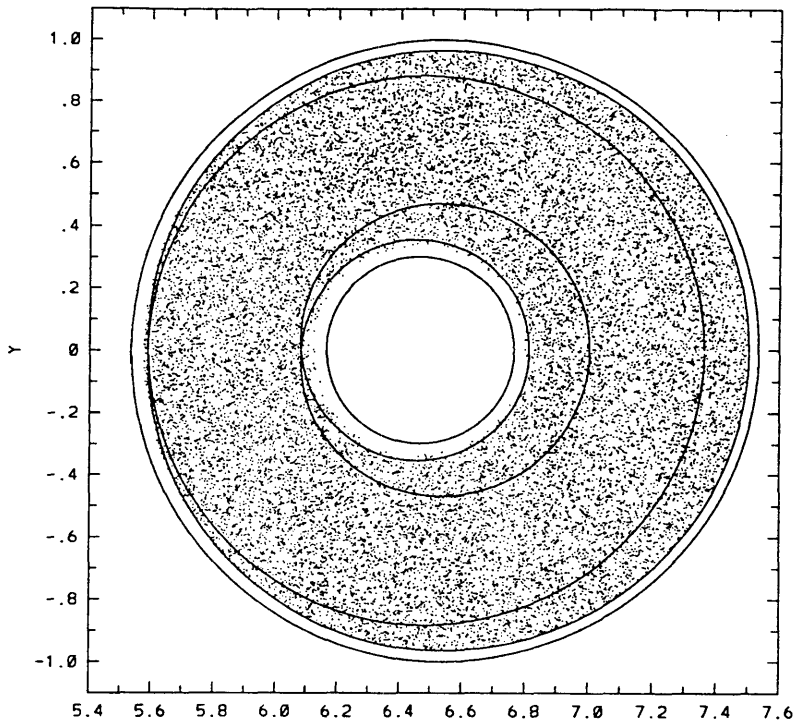

Fig. 2.12. Actual mixing zone for $\bar{e} = 0.1$, $\bar{r} = 0.3$, (MP3), $\epsilon = \frac{2\pi}{40}$. One initial condition integrated for 20,000 periods.

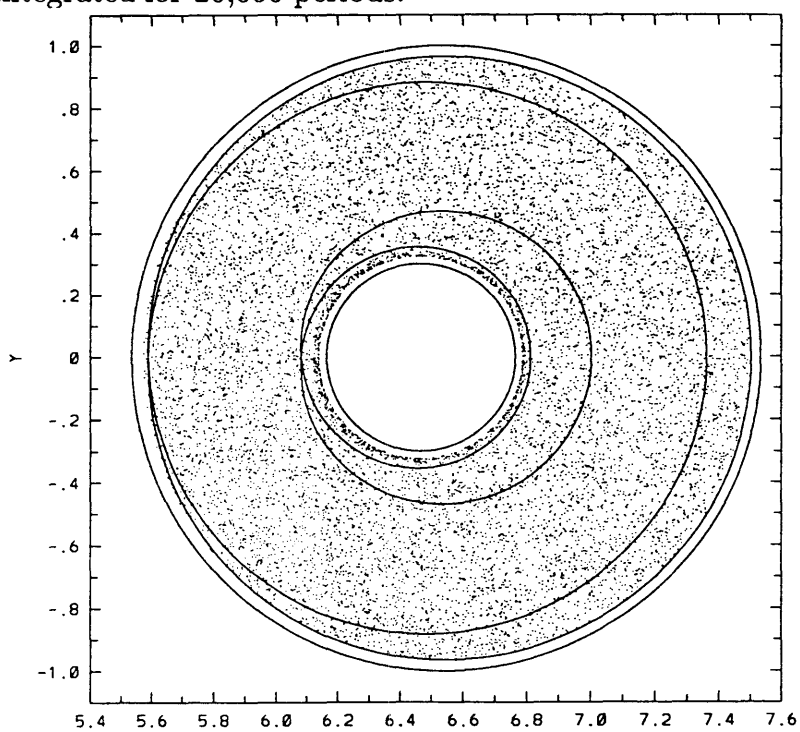

Fig. 2.13. Actual mixing zone for $\bar{e} = 0.1$, $\bar{r} = 0.3$, (MP3), $\epsilon = \frac{2\pi}{120}$. One initial condition integrated for 20,000 periods.

The theory and data therefore establish the claims we made at the beginning of this section. By chosing a small value of the eccentricity, $\bar{e} \leq 0.1$, by prescribing that $\bar{\Omega}(z)$ vary over a large negative interval such as the one in (MP3), and by using a moderate, but not too small, modulation frequency, we can obtain a mixing zone which is as large as possible for the counterrotating eccentric journal bearing. From our steady state measurements we saw how to optimize the potential mixing zone so that it occupies virtually the entire fluid domain, see Figure 2.3b, and from adding the considerations involving the parameter ϵ, we have shown that the actual mixing zone is slightly bigger than the potential one with this optimal choice of parameters, see Figure 2.12.

We remark that the results for geometries with different values of $\bar{r} \in (0,1)$ can be treated in exactly the same fashion we have treated the case of $\bar{r} = 0.3$ here, and the results should be qualitatively similar. We also remark that we deal with the question of efficiency of mixing within the mixing zone in Chapter 3.1.

2.3. Transport theory.

In the time-modulated system, the amounts of fluid which are in the various regions (which we define shortly) of the mixing zone oscillate periodically and, as a result of incompressibility, many fluid particles are forced to cross the instantaneous stagnation streamlines Γ^z and Λ^z. For example, as we see from Figure 2.3 and Table 2.1, the area enclosed by Γ^z increases as Γ^z sweeps outward away from the shaft for z increasing from 0 to π, and then that area decreases for the second half of the modulation period as Γ^z sweeps back inward toward the shaft. Thus, a group of fluid particles, which are initially outside of $\Gamma^{z=0}$ and which account for an area equal to the difference between the maximum and the minimum areas enclosed, are ingested during the first half of the modulation, and an equal amount (although

by no means the same particles necessarily) are ejected from it as z increases from π to 2π. Similarly the amount of fluid in the other regions oscillates periodically, and fluid is transported into and out of them across the instantaneous stagnation streamlines in each period of the modulation. Of course, since the flow is time-dependent, particle paths do not coincide with streamlines anymore, but we shall show that the instantaneous stagnation streamlines guide us in determining the natural boundaries between the regions in the mixing zone.

In this section, we discuss the structures upon which the transport theory is built, such as the fixed point and the homoclinic tangles of the Poincaré map, define three special regions in the mixing zone, identify the mechanism – turnstile lobes – by which the transport between these regions occurs, show how the intertwined tangles form the template from which quantitative information about this transport can be obtained, and show that material interfaces are stretched at least exponentially in time.

The tangles one observes in slowly-modulated (singularly-perturbed) systems, such as ours, are both qualitatively and quantitatively very different from those studied in weakly-perturbed systems, *i.e.*, systems to which the usual Melnikov theory applies and about which much has been written (see Wiggins [1991] and the literature cited there for examples). Furthermore, the structure of the tangles in slowly-modulated systems has only recently been understood (see Kaper and Wiggins [1991a] and Elskens and Escande [1991]). Therefore, we describe the relevant structure in detail in this and the following sections. The differences between the tangles in the two types of systems are especially striking in the measurements of the stretching and transport quantities which we give in these sections.

Chief among the differences, we remark that the turnstile lobes are very long and thin – of length $\mathcal{O}(\frac{1}{\epsilon})$ and area $\mathcal{O}(1)$ so that their average width is $\mathcal{O}(\epsilon)$ asymp-

totically as $\epsilon \to 0$, as we show in Chapter 3.1, and as we shall demonstrate each successive image (both forward and backward) of a turnstile lobe is longer and thinner than the preceding image, while having the same area due to the area-preservation property of the Poincaré map. This stands in stark contrast with the usual (regular-perturbation) systems in which the lobe area is $\mathcal{O}(\epsilon)$. Thus, besides giving us the results listed in the previous paragraph, these features enable us to refine the notions in the literature that transport occurs along unstable manifolds. As we see in our numerical simulations and in the experiments and numerical simulations with blinking protocols, tracer fluid appears to follow the unstable manifolds, deforming itself into a kind of fattened-up unstable manifold, *i.e.*, a strip of tracer is thicker than the corresponding segment of the unstable manifold (at least for finite times). In the following sections, we show that these fattened-up regions are lobes for continuous modulation protocols and measure their thickness using the transport theory and the special features of homoclinic tangles in adiabatic dynamical systems.

In addition, the singular-perturbation nature of these modulated flows implies that lobe area is the inter-regional flux per half period, and, as a result, the transport in these flows is more complicated than in the usual case in which transport is studied every full period only. Finally, although these three major differences do not exhaust all of them, we mention the fact that the turnstiles permeate the entire mixing zone, causing the tangle to function as its "backbone," because the tangle sweeps out the entire, $\mathcal{O}(1)$ separatrix-swept area, which is also in marked contrast with the usual, regular-perturbation case where the turnstile lobes only cover some $\mathcal{O}(\epsilon)$ fraction of the stochastic layer.

We identify the relevant structures in section 2.3.1 and present the transport theory in sections 2.3.2 and 2.3.3. Section 2.3.4 contains our results on the stretching

of interfaces. In Chapter 3.1 we develop analytical estimates for the dimensions – areas, lengths, and average widths – of these features using newly-developed asymptotic theory (see Kaper and Wiggins [1991a] and Elskens and Escande [1991]) which applies when ϵ is sufficiently small.

2.3.1. Structures governing stretching and transport.

The saddle stagnation point of the steady flow with $z = z_0$ persists as the saddle stagnation point $X_\epsilon(z_0)$ of the Poincaré map T_{z_0}, *i.e.*, as a periodic point of the flow, see Wiggins [1988] for an exposition of the theory. Since $X_\epsilon(z_0)$ lies near $X_0(z_0)$, one can construct an asymptotic expansion in powers of ϵ for its position as a function of z. We perform this expansion in Appendix B. From the calculations presented there, we know that the leading order term is $X_0(z_0)$ and that the first correction term is $\mathcal{O}(\epsilon)$ in the y-component and $\mathcal{O}(\epsilon^2)$ in the x-component. From symmetry considerations (or, alternatively from the asymptotic expansion in the appendix), we know that $X_\epsilon(z_0)$ lies on the x–axis for $z_0 = 0 \mod 2\pi$ and for $z_0 = \pi \mod 2\pi$. We identify the stagnation point of T_{z_0} on a Poincaré section with $z_0 = 0 \mod 2\pi$ in Figure 2.14. We remark that when we refer to time, we refer to the discrete time, n, of the Poincaré map.

If one were to watch the experiment continuously as z increases from z_0 to $z_0 + 2\pi$, instead of sampling it stroboscopically with the Poincaré map, one would see that the saddle executes a periodic orbit $\gamma_\epsilon(z)$. This closed path lies in the fluid domain inside a strip of width $\mathcal{O}(\epsilon)$ around the segment $[X_0(z_0 = \pi), X_0(z_0 = 0)]$ on the x-axis in the narrow gap between the shaft and the casing in the mixing zone. We show the closed path the saddle executes for several values of ϵ in a representative geometry in Figure 2.15.

Introduction of the time modulation breaks the coincidental stable and unsta-

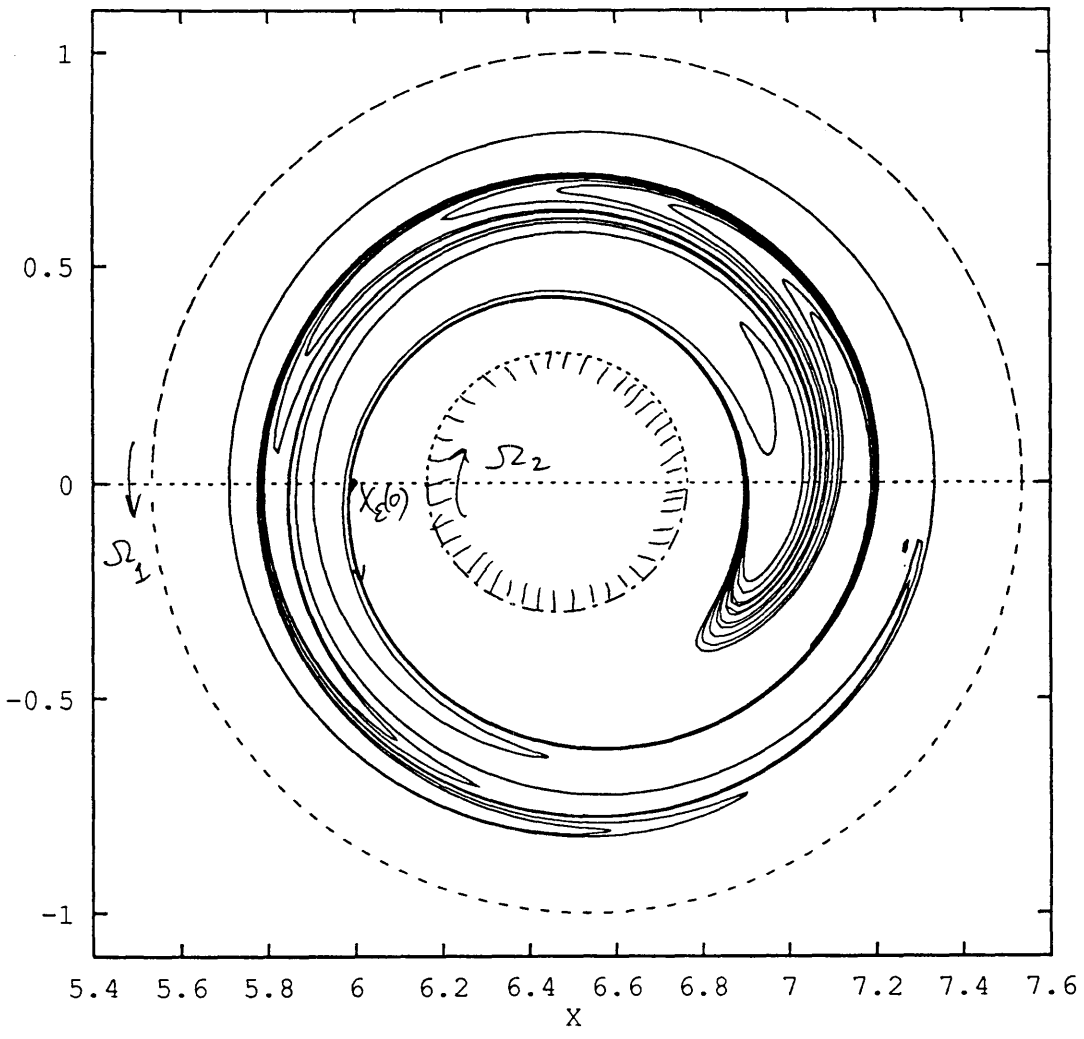

Fig. 2.14.a. The unstable manifold $\Gamma^U(\mathbf{X}_\epsilon(0))$ for the flow with $\epsilon = \frac{2\pi}{40}$, $\bar{e} = 0.1$, $\bar{r} = 0.3$ and (MP1).

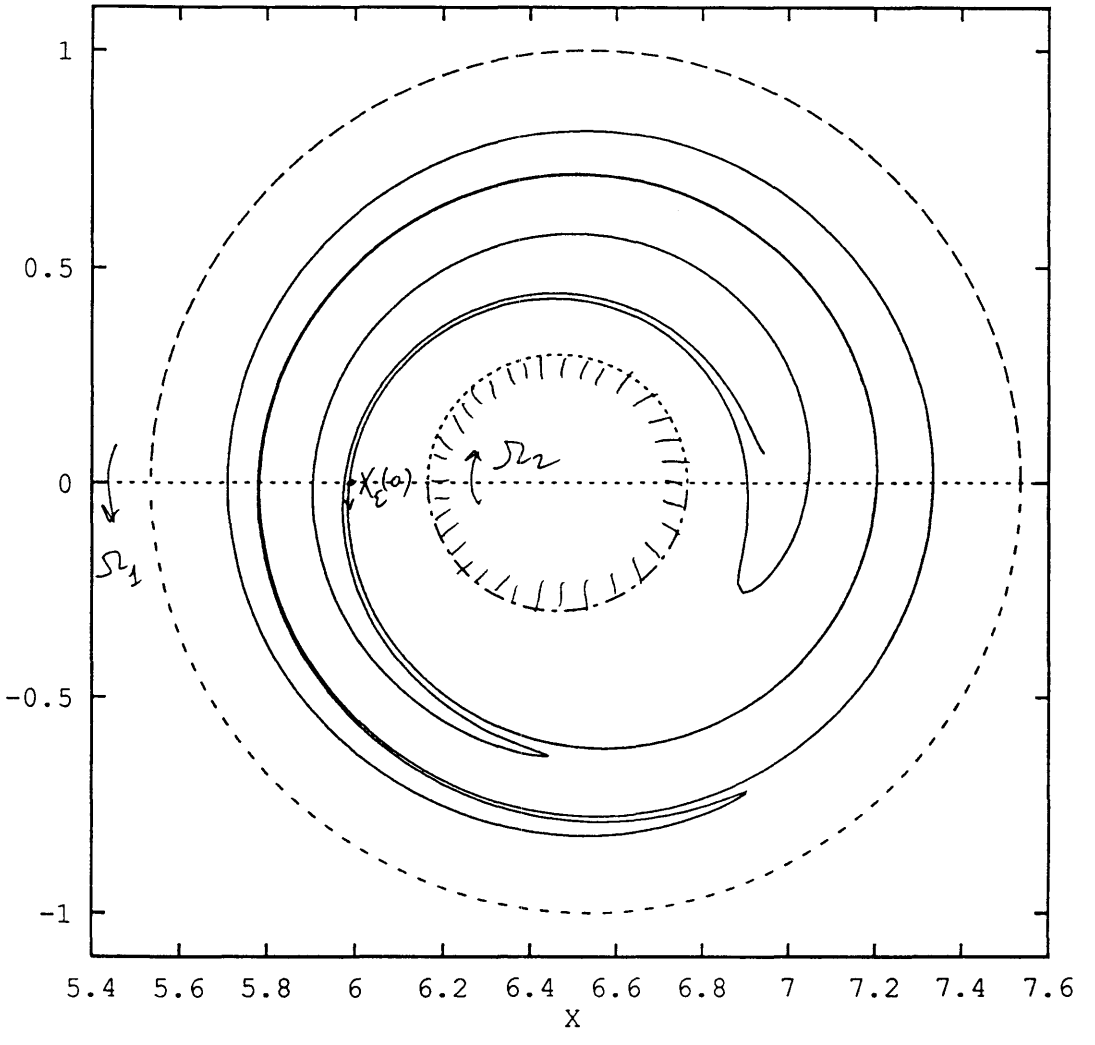

Fig. 2.14.b. The unstable manifold $\Lambda^U(\mathbf{X}_\epsilon(0))$ for the flow with $\epsilon = \frac{2\pi}{40}$, $\bar{e} = 0.1$, $\bar{r} = 0.3$ and (MP1).

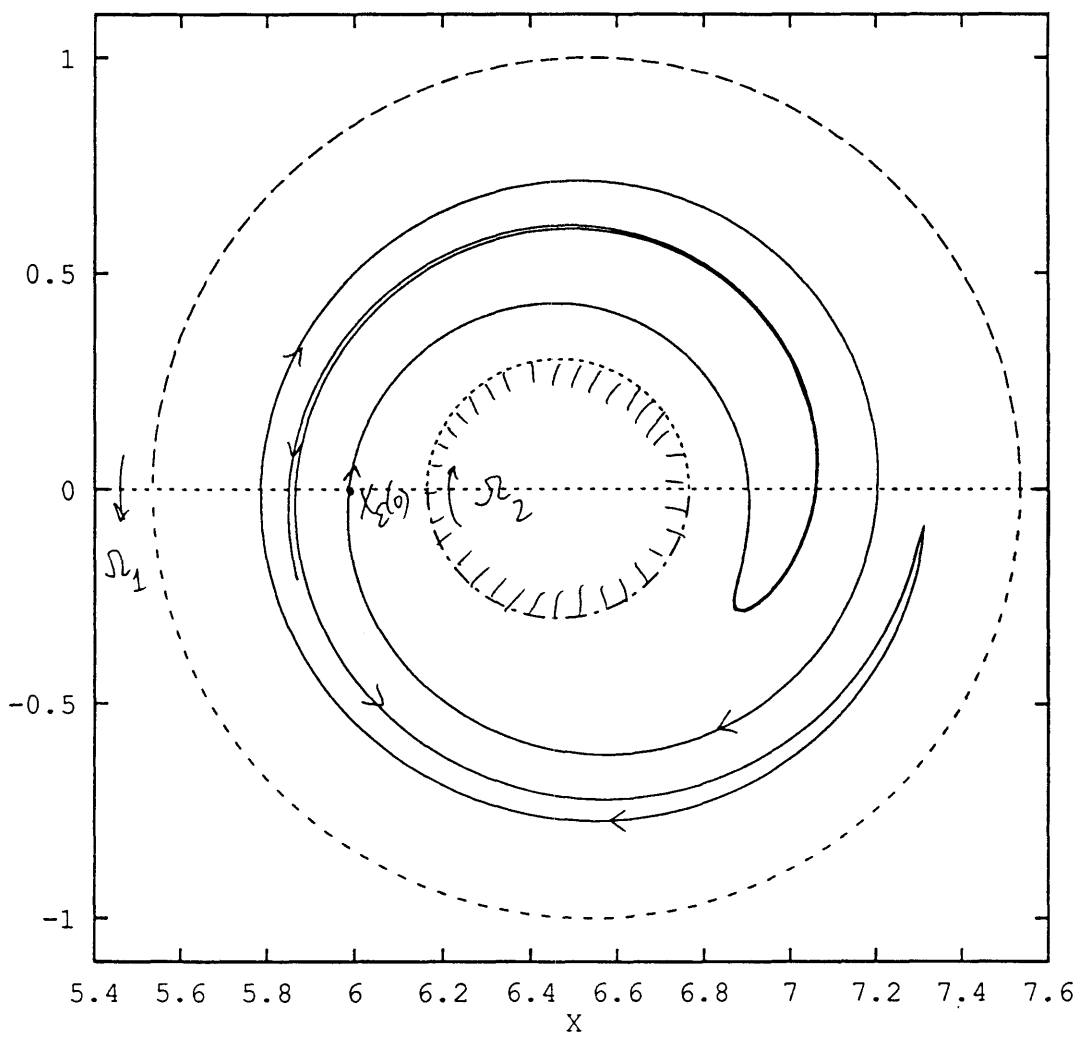

Fig. 2.14.c The first piece of $\mathcal{W}^U(\mathbf{X}_\epsilon(0))$.

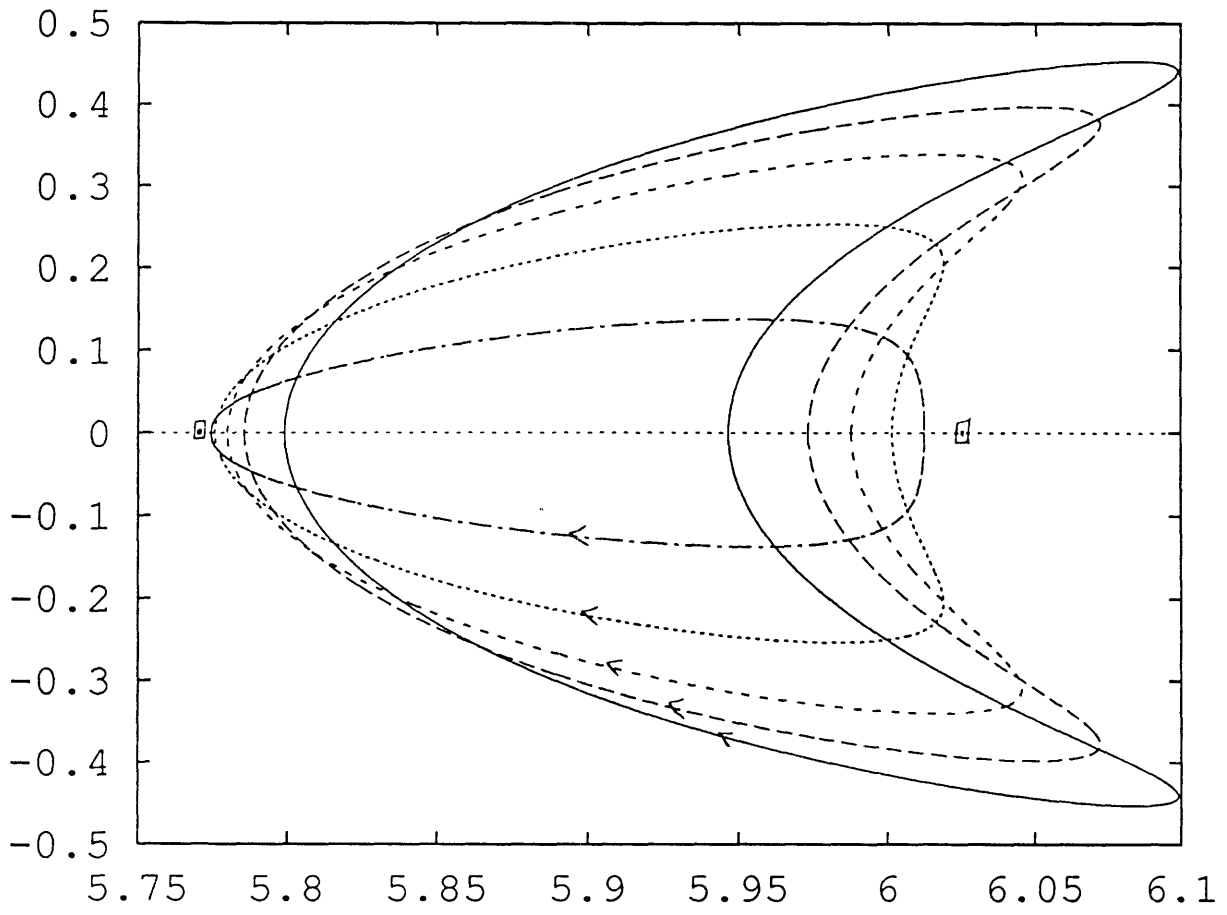

Fig. 2.15. The orbit $\gamma_\epsilon(z)$ for various values of ϵ with $\bar{e} = 0.1$ and $\bar{r} = 0.3$ and (MP1). The curve with the largest maximum value of y is for $\epsilon = \frac{2\pi}{20}$ and those with a maximum lower than that are for $\epsilon = \frac{2\pi}{30}, \frac{2\pi}{40}, \frac{2\pi}{60}, \frac{2\pi}{120}$, successively.

ble manifolds (stagnation streamlines) Λ^{z_0} and Γ^{z_0} and causes them to intersect transversely. To be precise, there exist four infinitely long distinguished streaklines (manifolds) which intersect in two intertwined homoclinic tangles. Two of these consist of all of the points in the fluid domain which are forward ($n \to +\infty$) asymptotic to $X_\epsilon(z_0)$. We label these $\Gamma^S(X_\epsilon(z_0))$ and $\Lambda^S(X_\epsilon(z_0))$ to remind ourselves that that they are the stable manifolds of $X_\epsilon(z_0)$ and remnants of the branches of the stable manifolds of $X_0(z_0)$ which coincide with Γ^{z_0} and Λ^{z_0}, respectively. The other two are backward ($n \to -\infty$) asymptotic in time to $X_\epsilon(z_0)$. We denote these last two by $\Gamma^U(X_\epsilon(z_0))$ and $\Lambda^U(X_\epsilon(z_0))$, because they are the unstable manifolds of $X_\epsilon(z_0)$. Although one only observes the unstable manifolds in experiments, one can obtain the stable manifolds from symmetry considerations for special z_0 ($z_0 = 0, \pi$ mod 2π for (MP1)-(MP3)) and in general by performing a second experiment in which the directions of the rotation of the two cylinders are reversed.

Going outward on $\Gamma^U(X_\epsilon(z_0))$ from $X_\epsilon(z_0)$ there is a point h_0 at which $\Gamma^U(X_\epsilon(z_0))$ first intersects $\Gamma^S(X_\epsilon(z_0))$. Similarly, leaving from $X_\epsilon(z_0)$ along the manifold $\Lambda^U(X_\epsilon(z_0))$, we see that $\Lambda^U(X_\epsilon(z_0))$ first intersects $\Lambda^S(X_\epsilon(z_0))$ at a point on the x–axis which we label k_0. We label the segment of $\Gamma^U(X_\epsilon(z_0))$ between $X_\epsilon(z_0)$ and h_0 by $U[X_\epsilon(z_0), h_0]$ and that of $\Gamma^S(X_\epsilon(z_0))$ between $X_\epsilon(z_0)$ and h_0 by $S[X_\epsilon(z_0), h_0]$. Similarly, $U[X_\epsilon(z_0), k_0]$ denotes the segment of $\Gamma^U(X_\epsilon(z_0))$ between $X_\epsilon(z_0)$ and k_0, and $S[X_\epsilon(z_0), h_0]$ denotes that of $\Gamma^S(X_\epsilon(z_0))$ between $X_\epsilon(z_0)$ and k_0. See Figure 2.16. h_0 and k_0 are special, or *primary*, homoclinic points p in the sense that $U[X_\epsilon(z_0), p]$ and $S[X_\epsilon(z_0), p]$ intersect only in the point p.

With the choice of $z_0 = 0$ or 0 mod 2π, the symmetry of the Poincaré map:

$$n \to -n$$

$$x \to x$$

$$y \to -y$$

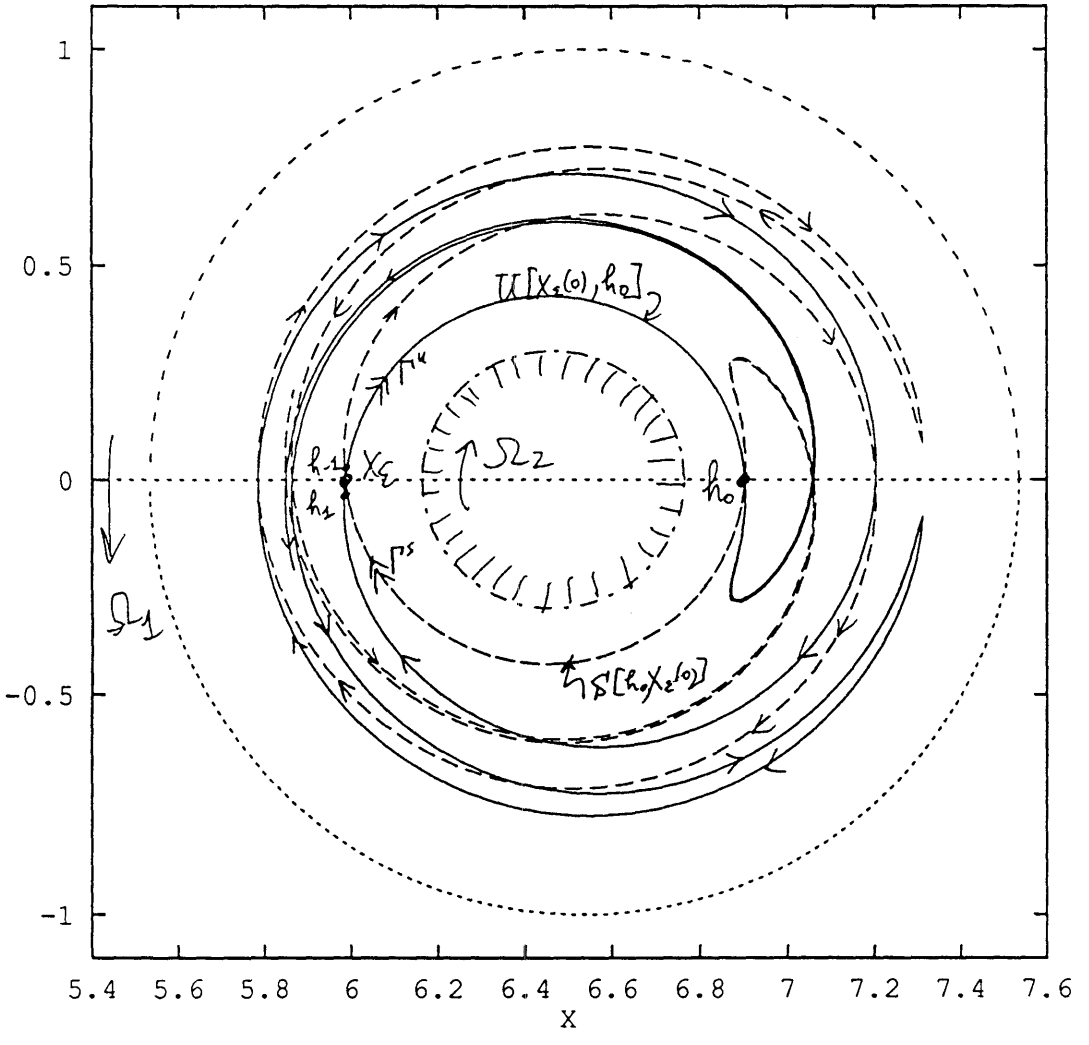

Fig. 2.16. The segments of the unstable manifolds, the pips h_i for $i = -1, 0, 1$, and the region boundaries with $\bar{e} = 0.1$, $\bar{r} = 0.3$, $\epsilon = \frac{2\pi}{40}$, and (MP1).

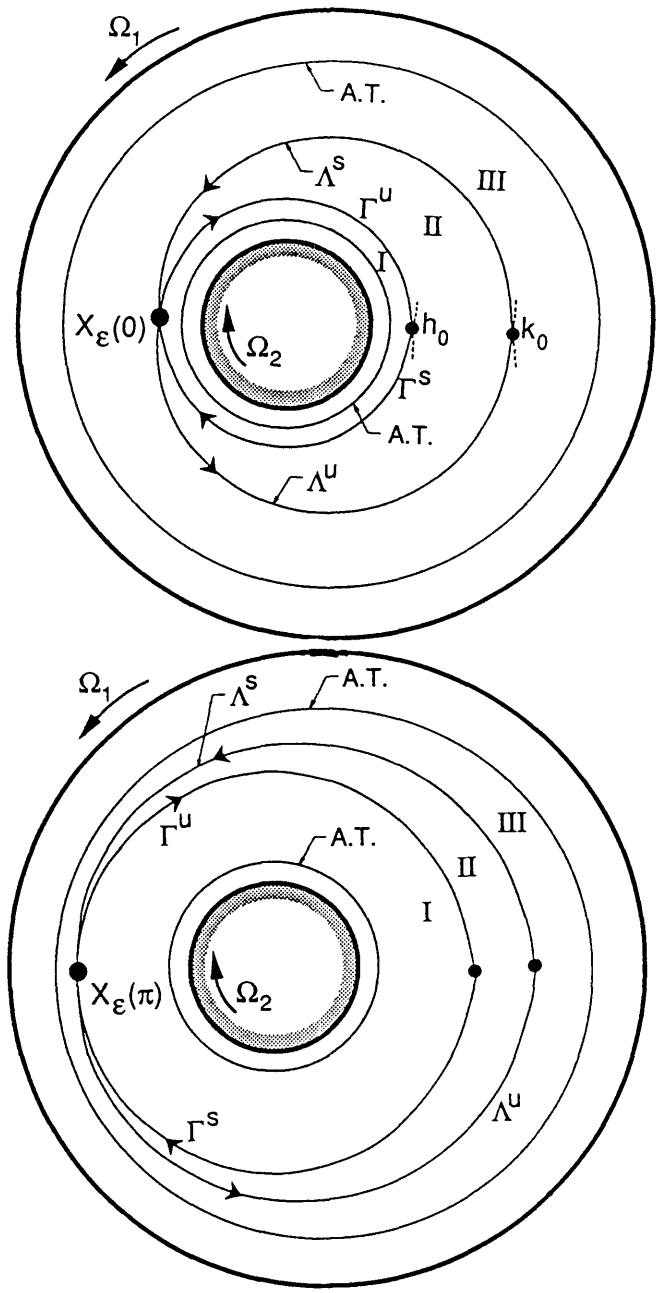

Fig. 2.16.b. A sketch to show how the area inside R1 increases as z increases from 0 to π.

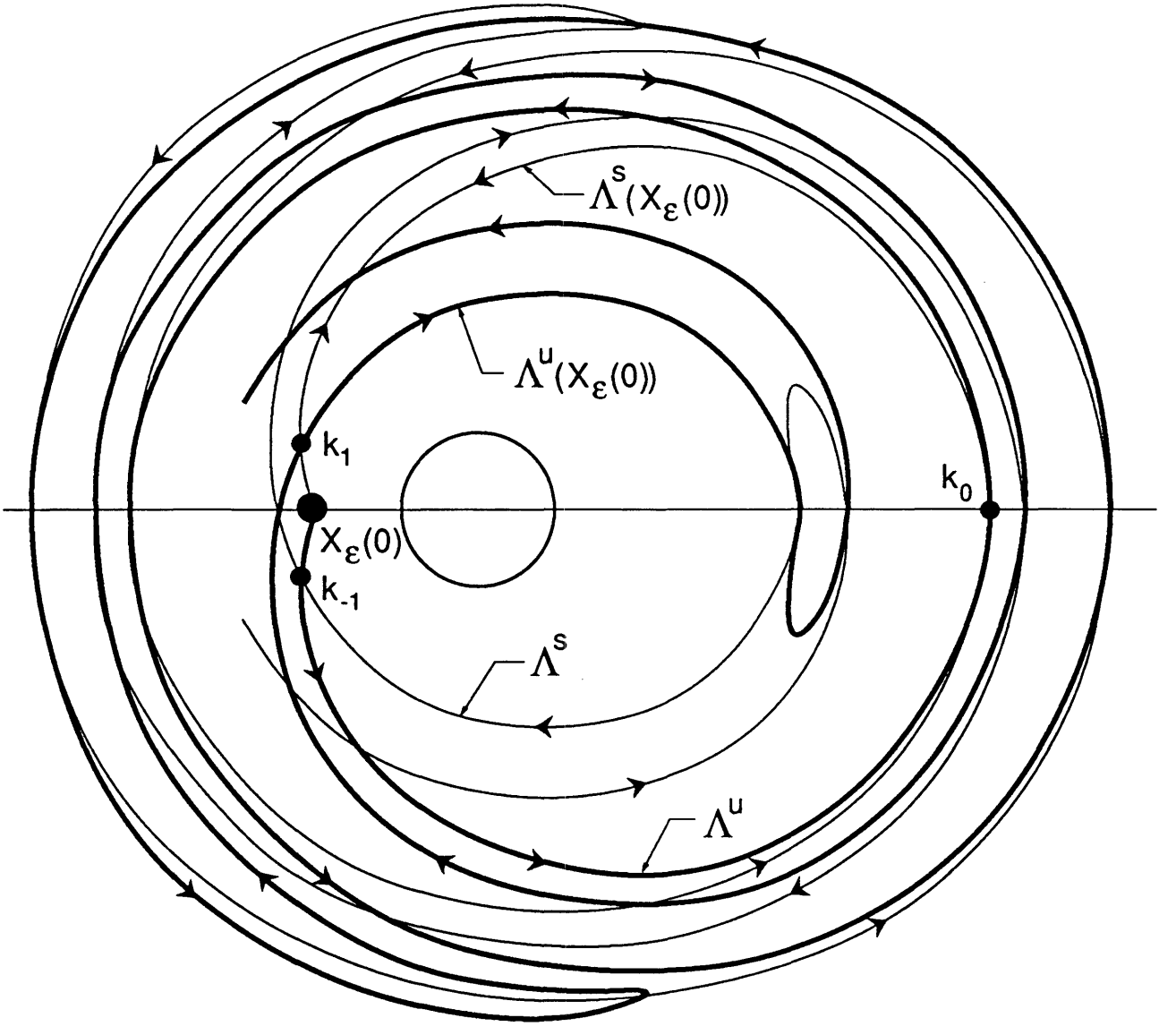

Fig. 2.16.c. A schematic sketch of the homoclinic tangle formed by the Λ pair.

or 0 mod 2π, the symmetry of the Poincaré map:

$$n \to -n$$

$$x \to x$$

$$y \to -y$$

is such that the unions

$$\begin{aligned} B_{1,2} &\equiv U[X_\epsilon(z_0), h_0] \bigcup S[X_\epsilon(z_0), h_0] \\ B_{2,3} &\equiv U[X_\epsilon(z_0), k_0] \bigcup S[X_\epsilon(z_0), k_0] \end{aligned} \tag{2.8}$$

naturally divide the mixing zone into three regions in the time-periodic flow. Region 1 is the annular domain bounded on the inside by the outermost Arnold torus of the family of tori which make up the regular zone adjacent to the shaft and on the outside by $B_{1,2}$. The kidney-shaped domain in the middle of the mixing zone bounded on the outside by $B_{1,2}$ and $B_{2,3}$ is region 2. To completely define it, however, we recall from the previous section that there are two possibilities. Either ϵ is large enough, *e.g.*, $\epsilon \geq 0.14$ in the case when $\bar{e} = 0.1$, $\bar{r} = 0.3$, and one uses (MP3), such that the entire domain between $B_{1,2}$ and $B_{2,3}$ is part of the actual mixing zone, or ϵ is small and there exists a regular region occupying part of the minimal backflow region. In the former case, the entire kidney-shaped domain is region 2, and in the latter case, region 2 is an annular domain and the inner boundary is the outermost Arnold torus in the family of tori which make up the regular zone. Finally, region 3 is also an annular domain bounded on the inside by $B_{2,3}$ and on the outside by the smallest Arnold torus in the family of tori in the regular zone adjacent to the casing. Thus, the boundaries $B_{1,2}$ and $B_{2,3}$ act as the watershed between the three regions. We refer the reader to Figure 2.16 in which these regions, which we label R1, R2, and R3, are identified. One can identify three regions and their natural boundaries for every value of z_0 in $[0, 2\pi)$, but for simplicity, we focus only on these two choices of z_0.

These regions are remnants of those from the steady flow identified in section 2. In contrast to the situation in the steady state, however, transport between the three regions is possible in the time-modulated case. Before showing how the structures we have just identified form a template from which we can determine stretching and transport quantities, we introduce one final concept, that of a turnstile lobe.

Invariance of the manifolds implies that homoclinic points are mapped to homoclinic points under T_{z_0} and its inverse $T_{z_0}^{-1}$. In particular, principal homoclinic points are mapped to principal homoclinic points, see Rom-Kedar and Wiggins [1990b], and thus, the streaklines $\Gamma^S(X_\epsilon(z_0))$ and $\Gamma^U(X_\epsilon(z_0))$ intersect each other infinitely many times as $X_\epsilon(z_0)$ is approached from both sides along the stable manifolds, forming a homoclinic tangle, as do the streaklines $\Lambda^S(X_\epsilon(z_0))$ and $\Lambda^U(X_\epsilon(z_0))$. The segments of $\Gamma^S(X_\epsilon(z_0))$ and $\Gamma^U(X_\epsilon(z_0))$, which we label $S[h_i, h_{i+1}]$ and $U[h_i, h_{i+1}]$, between any two adjacent principal intersection points h_i and h_{i+1}, where $i \in \mathbf{Z}$, bound an area on the Poincaré section which is called a lobe. Similarly, the segments $S[k_i, k_{i+1}]$ and $U[k_i, k_{i+1}]$ of $\Lambda^S(X_\epsilon(z_0))$ and $\Lambda^U(X_\epsilon(z_0))$ form a lobe. Now, because the system is Hamiltonian, T_{z_0} is an area-preserving diffeomorphism of the fluid domain to itself. Thus, one can show that all of the lobes of a given tangle, *i.e.*, of the Γ–tangle or of the Λ-tangle, have the same area. We give the area of the lobes in both tangles in Chapter 3.1.

The lobes which are defined by the segments between h_{-1} and h_0 and those between h_{-2} and h_{-1}, as well as the corresponding ones between k_{-1} and k_0 and between k_{-2} and k_{-1} of the Λ–tangle, play a special role in the stretching and transport of fluid. We refer to them as turnstile lobes, see Figure 2.17.

2.3.2. Transport in Half Period Intervals.

The mechanisms convecting particles from one region to another are the turnstile

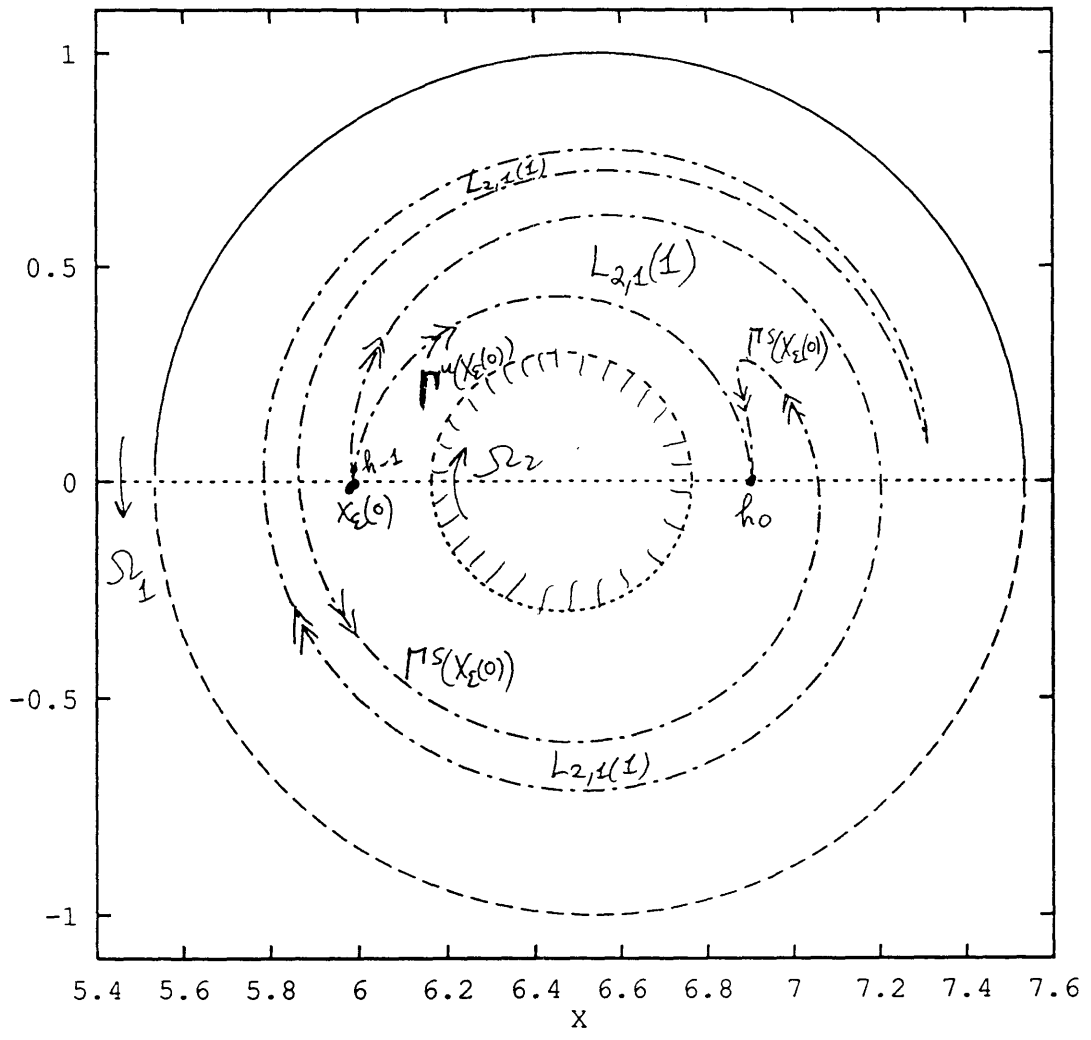

Fig. 2.17.a. The turnstile lobes and their intersections with $\bar{e} = 0.1$, $\bar{r} = 0.3$, $\epsilon = \frac{2\pi}{40}$ and (MP1).

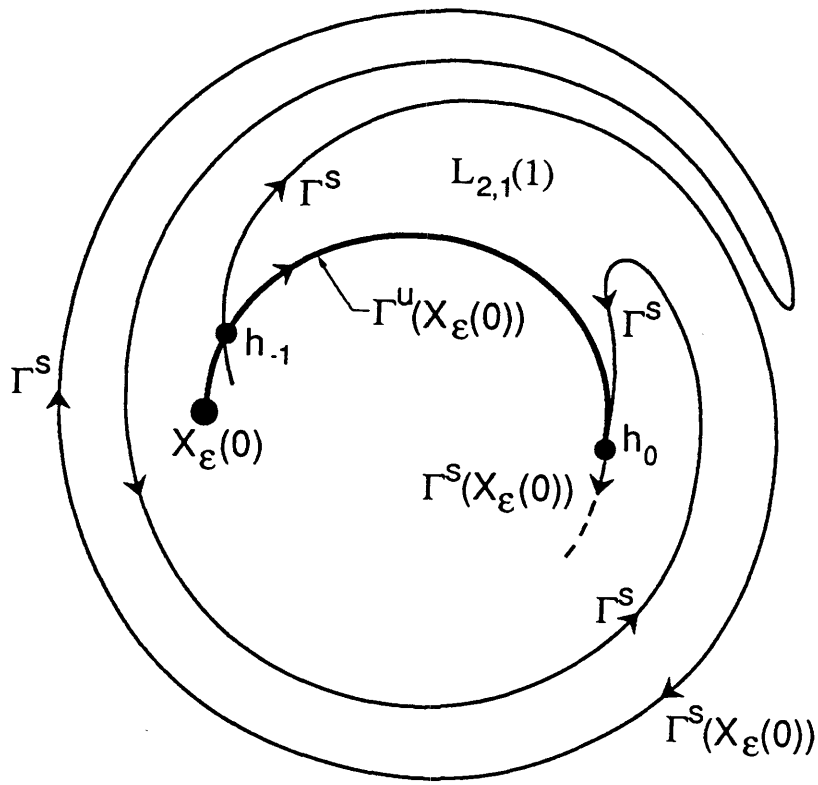

A schematic sketch of Figure 2.17.a.

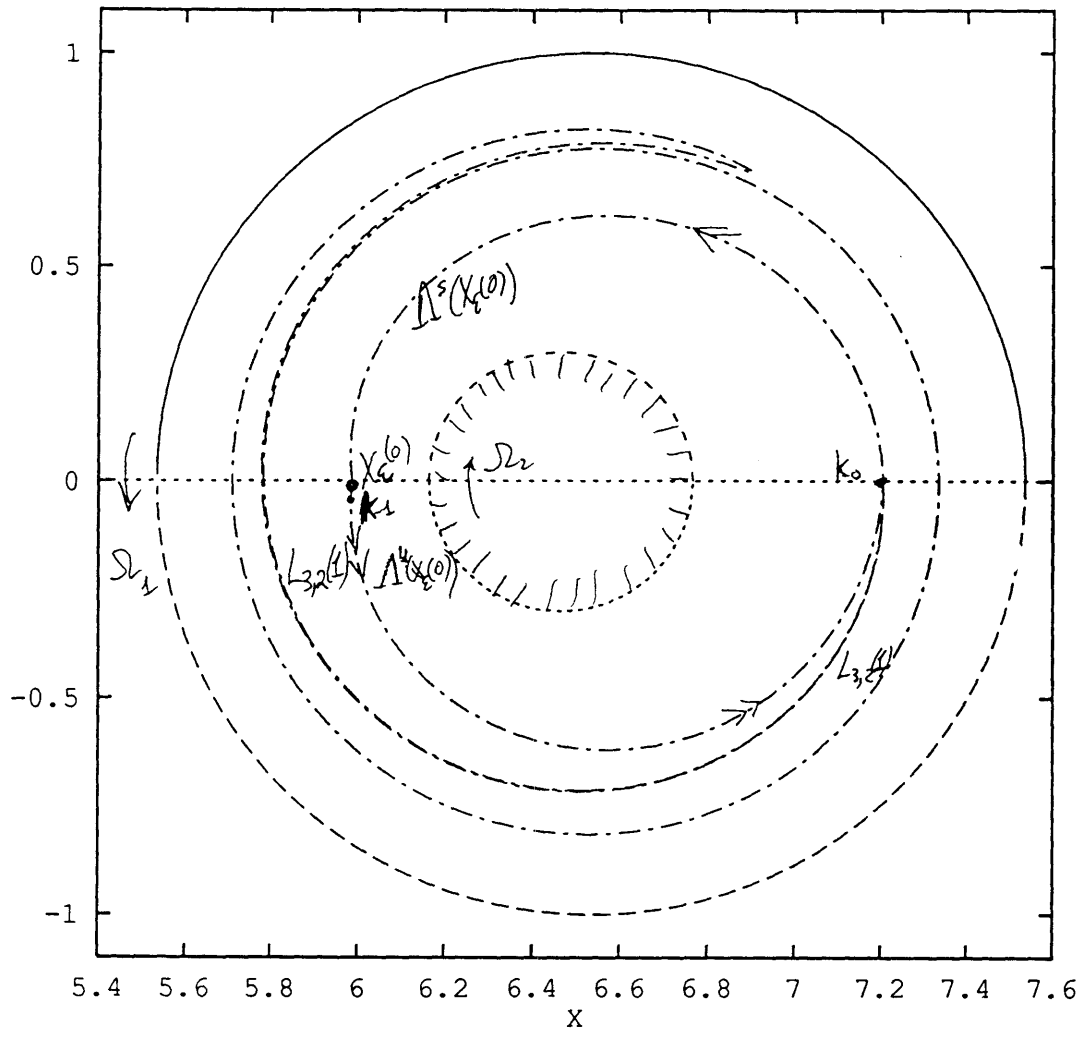

Fig. 2.17.b The turnstile lobes and their intersections with $\bar{e} = 0.1$, $\bar{r} = 0.3$, $\epsilon = \frac{2\pi}{40}$ and (MP1).

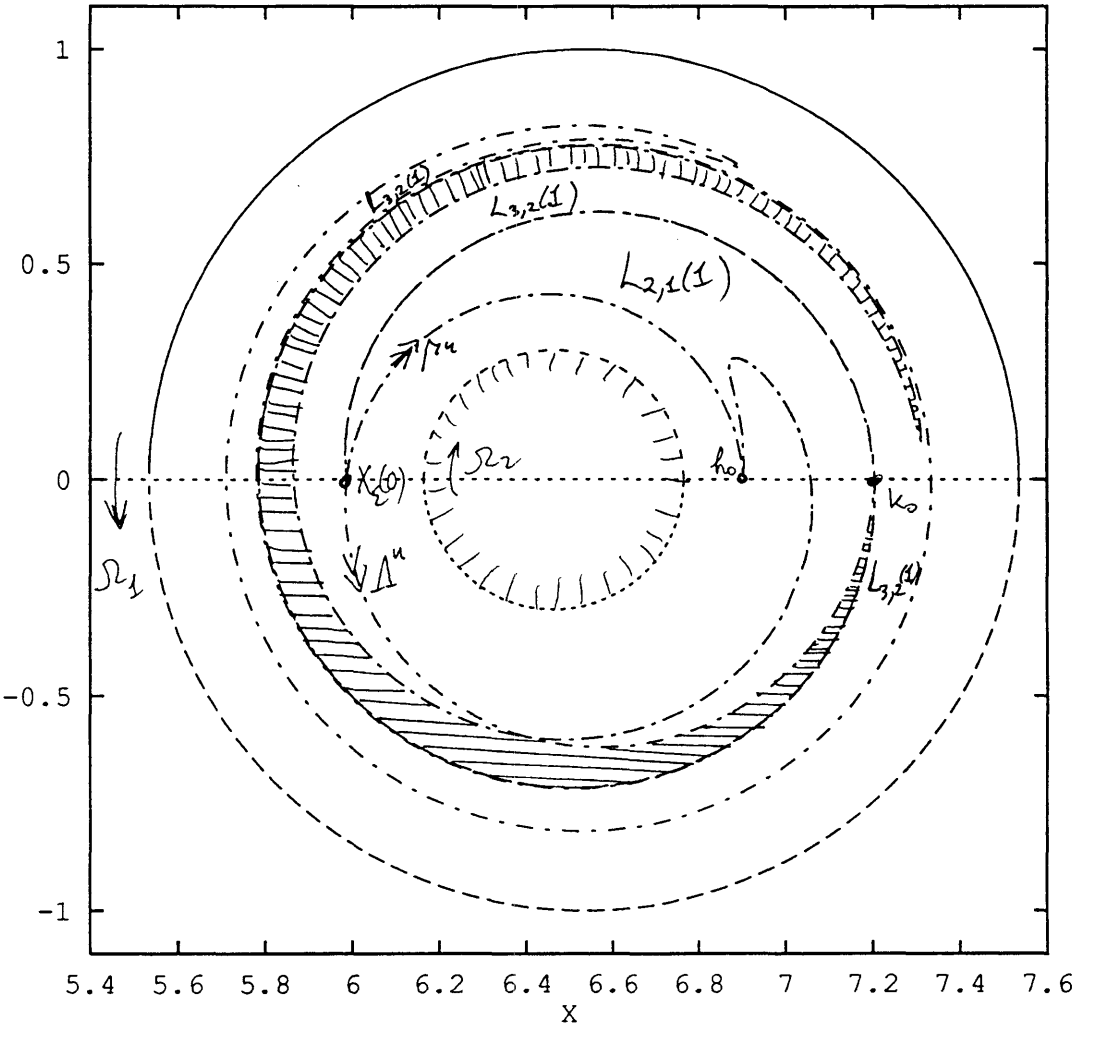

Fig. 2.17.c The turnstile lobes and their intersections with $\bar{e} = 0.1$, $\bar{r} = 0.3$, $\epsilon = \frac{2\pi}{40}$ and (MP1).

lobes. As we stated in the previous subsection both the Γ– and the Λ–tangles have a pair of turnstile lobes. Now, in this and the next section, we prove that the pair of lobes $L_{1,2}(1)$, defined by h_{-2} and h_{-1}, and $L_{2,1}(1)$, defined by h_{-1} and h_0, govern the transport out of and into R1, and the pair of lobes $L_{2,3}(1)$ and $L_{3,2}(1)$, defined by the pairs k_{-2} with k_{-1} and k_{-1} with k_0, govern the transport into and out of R3.

The usual way to proceed, as is done in the transport studies for weakly-perturbed systems (see, for example, the review in Wiggins [1991]), is to compute inter-regional transport every unit period of the flow. However, in order to completely determine the dynamics of separatrix-crossing orbits in slowly-modulated systems, one must analyze the mechanism for inter-regional transport on a half-period basis.

Indeed, we find that the flux across the inter-regional boundaries per half period is given by the turnstile lobes. Furthermore, upon examining the turnstile lobes every half period, we readily see that the continuous modulation causes the turnstile lobes to be the mechanism by which tracer patches deform into long, thin spirals and elaborate lamellar structures. Thus, the singular perturbation case is markedly different from that usually studied in which full period transport is the only quantity of interest. This work represents the first time analysis from adiabatic dynamical systems theory is brought to bear on a fluid mechanical problem, except in the conference proceedings Kaper and Wiggins [1988]. In this section, we show that half-period transport is a natural technique to quantify stretching and mixing in quasi-steady Stokes' flows. We remark that the half-period analysis we present here is an extension of the methods developed in Elskens and Escande [1991] and Kaper and Wiggins [1991a] for general slowly-varying planar Hamiltonian systems.

Before giving the details of this transport, we note that uniqueness of solutions

implies that initial conditions on stable and unstable manifolds can not jump ahead of each other. This orientation preservation implies that the ordering of points on them as the system evolves is fixed by their initial ordering. Thus, the segments of manifold in between the adjacent homoclinic points defining the lobe always remain between the two intersection points as the system evolves, *i.e.*, the boundaries of the lobes are invariant. This result enables us to give the following description of the transport process:

During the first half of the modulation period, the areas of R1 and R2 increase, while that of R3 decreases. In particular, only those tracer particles which are in lobe $L_{2,1}(1)$ (which is a subset of R2 and R3) at time $z = 0 \bmod 2\pi$ enter into R1 in one half of a period. Similarly, only those particles which are in lobe $L_{3,2}(1)$ (which is a subset of R3) at time $z = 0 \bmod 2\pi$ will be in R2 and R1 at time $z = \pi \bmod 2\pi$.

An analogous result is true for the remainder of the modulation period. During the second half of the period, the above is reversed, because the areas of R1 and R2 decrease, while that of R3 increases. The mechanisms by which fluid must exit these regions are turnstile lobes. In particular, only those tracer particles which are in lobe $L_{1,2}(1)$ (which is a subset of R1) at time $z = \pi \bmod 2\pi$ enter into R2 and R3 during the second half of the modulation period and lie entirely in those regions at time $z = 0 \bmod 2\pi$. Similarly, only those particles which are in lobe $L_{2,3}(1)$ (which is a subset of R2 and R1) at time $z = \pi \bmod 2\pi$ will lie completely in R3 at time $z = 0 \bmod 2\pi$.

To illustrate the above statements, we examine the case in which $\bar{e} = 0.1$, $\bar{r} = 0.3$, $\epsilon = \frac{2\pi}{40}$, and (MP1) is used. We cover the lobe $L_{2,1}(1)$ in R2 (and partially in R3) with a uniform grid of points (spacing= see data in folder) at time $z = 0$, as shown in Figure 2.17a. We then show in Figure 2.17b that the tracer lies inside

R1, exactly in the spiral-shaped turnstile lobe $T_0^{\frac{1}{2}} L_{2,1}(1)$, at time $z = \pi$. In Figure 2.18, we blow up the region marked in Figure 2.17b so that the boundaries of the thin, lamellar striations are clearly visible.

Furthermore, we remark that two cases are possible, one in which $L_{2,1}(1) \cap L_{3,2}(1) \neq \emptyset$, as shown in Figure 2.17, and the other in which $L_{2,1}(1) \cap L_{3,2}(1) = \emptyset$. However, for $\epsilon < 0.3$ in all of the cases we analyzed the former holds true. This explains why we said above that $L_{2,1}(1)$ is a subset of R2 and R3, among other things. The results we present in the remainder of this paper apply in both cases; one need only be slightly careful about justifying the formulae we use in the former case, as we show in the next section.

2.3.3. Transport in Intervals of Unit Periods.

In this section, we look at the inter-regional transport process from the usual, per-unit-period point of view and obtain results giving the probability that an orbit initially in one region can be found in another region after any period of the modulation. Rather than treat this problem in its full generality immediately, however, we first consider the particular problem of what fraction of tracer initially in R3 gets transported to R1 in each period of the modulation. One may then compute the other eight quantities $T_{i,j}(n)$ for $i, j = 1, 2, 3$, which can be used to give all of the other probabilities, using the same procedure as we do here for $T_{3,1}(n)$ and the conservation equations. These equations, five in all for the nine independent quantities $T_{i,j}(n)$ for $i, j = 1, 2, 3$, express the conservation of tracer

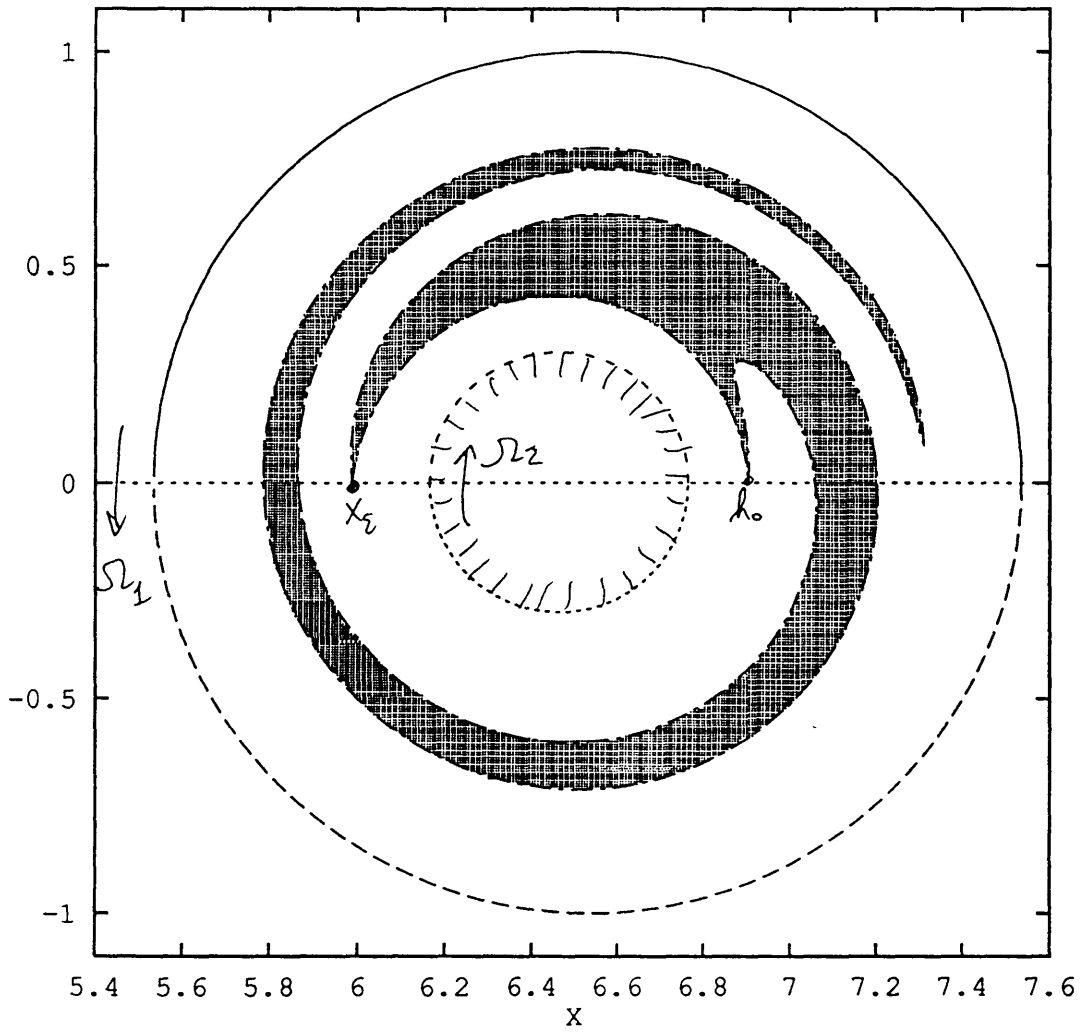

Fig. 2.18.a Transport in half-period intervals. At $z = 0$, turnstile lobe in the case $\bar{e} = 0.1$, $\bar{r} = 0.3$, $\epsilon = \frac{2\pi}{40}$, with (MP1).

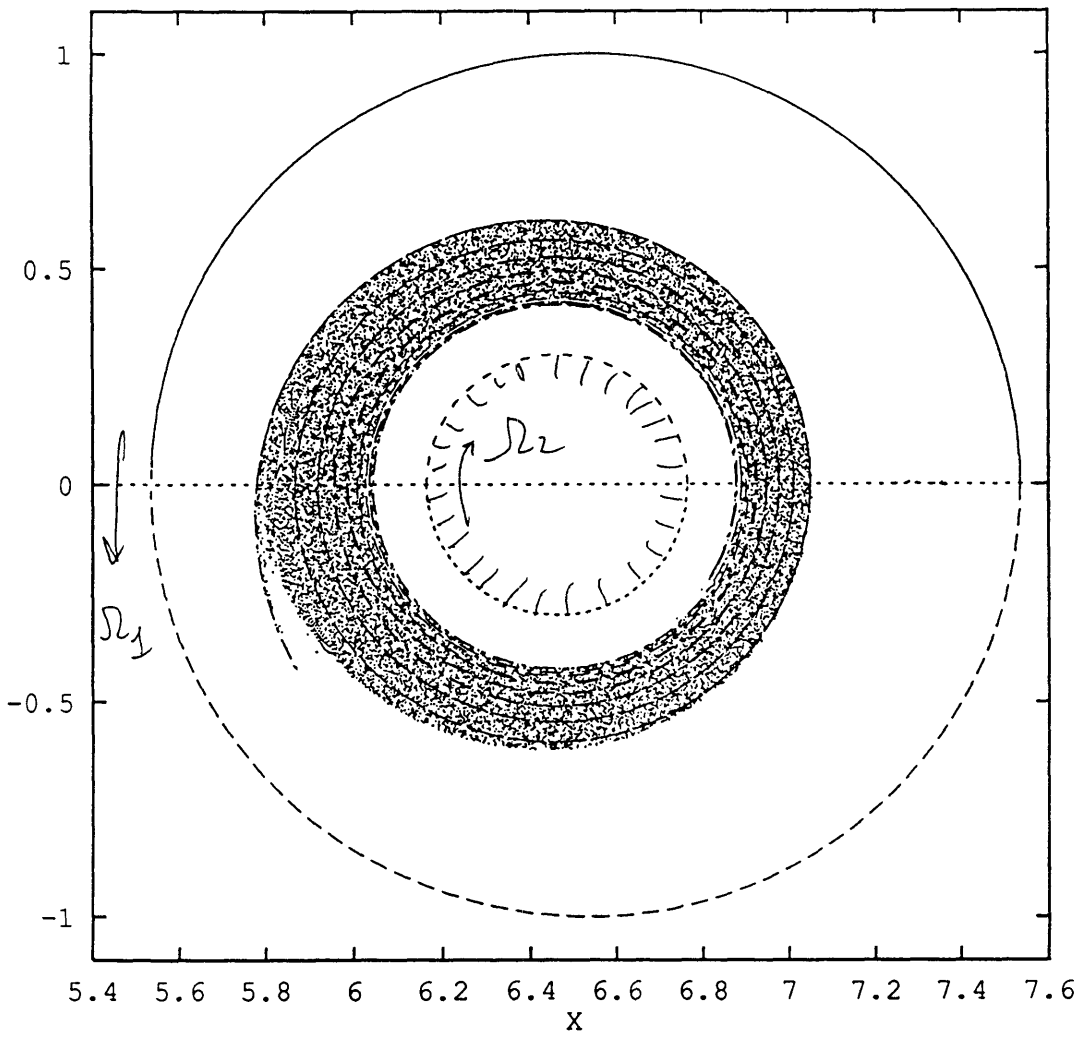

Fig. 2.18.b. Image of above turnstile lobe at $z = \pi$ showing that all of the fluid is in R1.

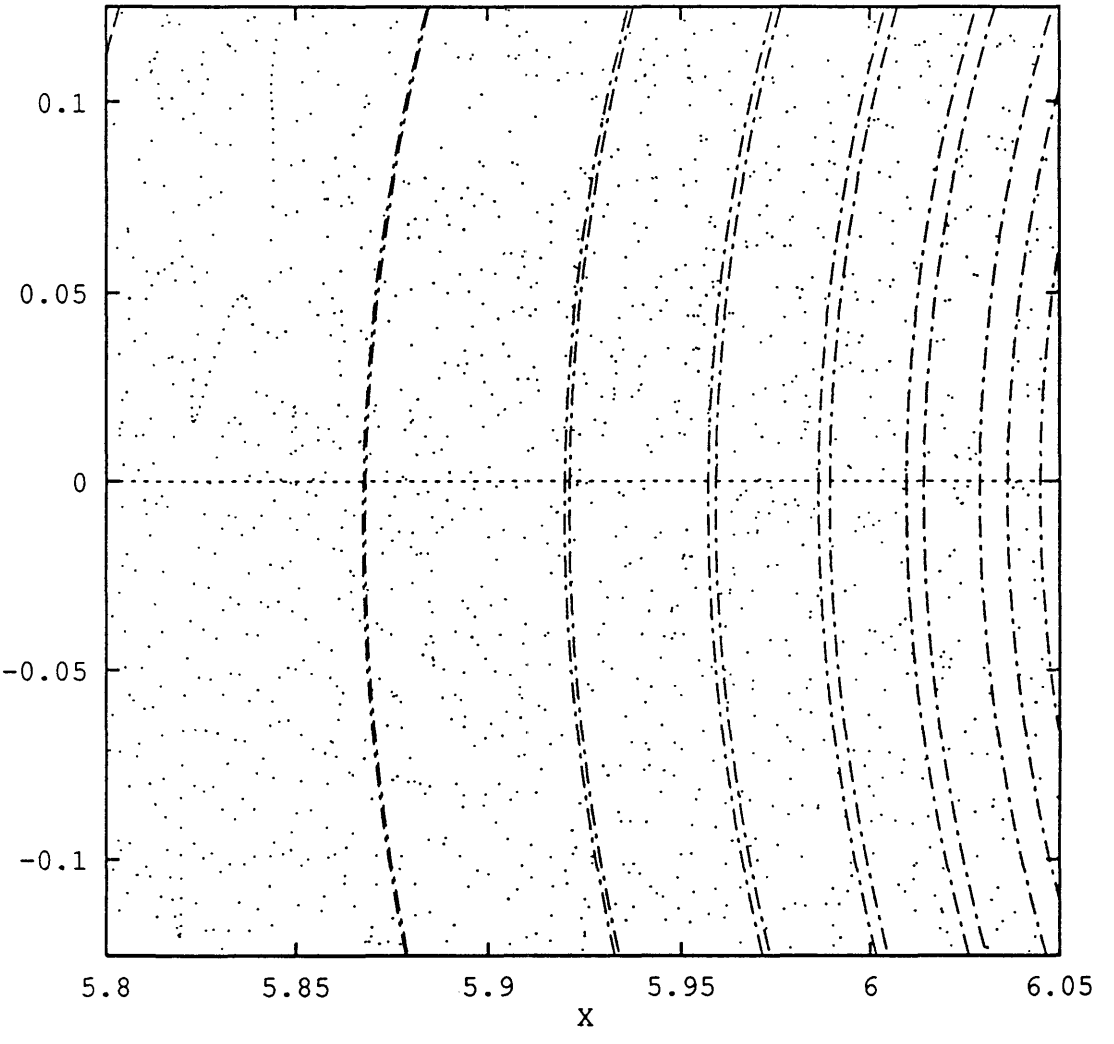

Fig. 2.18.c. Blowup of Fig. 2.18.b to show that all of the points are inside the image of the turnstile lobe at $z = \pi$.

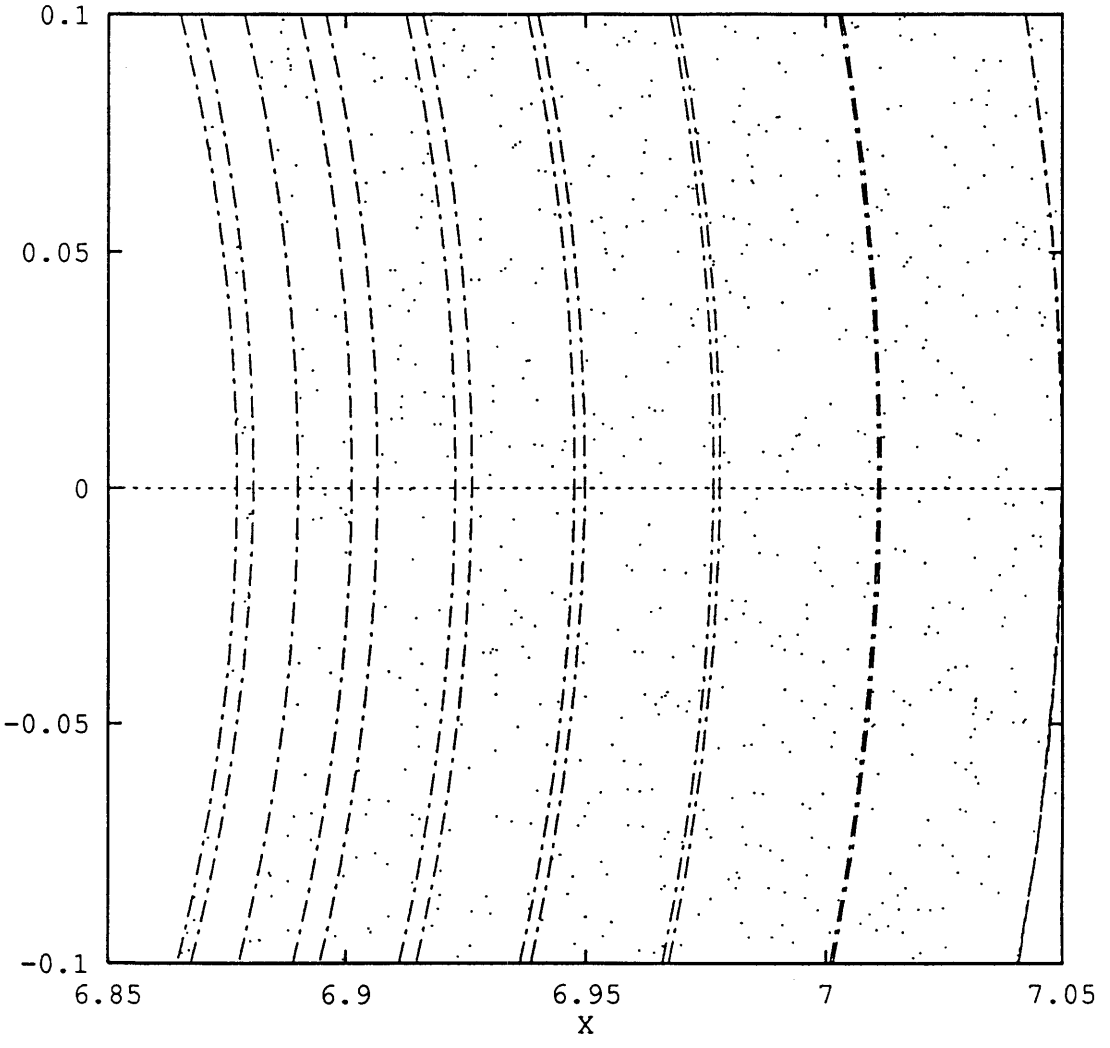

Fig. 2.18. Same as Fig.2.18.c.

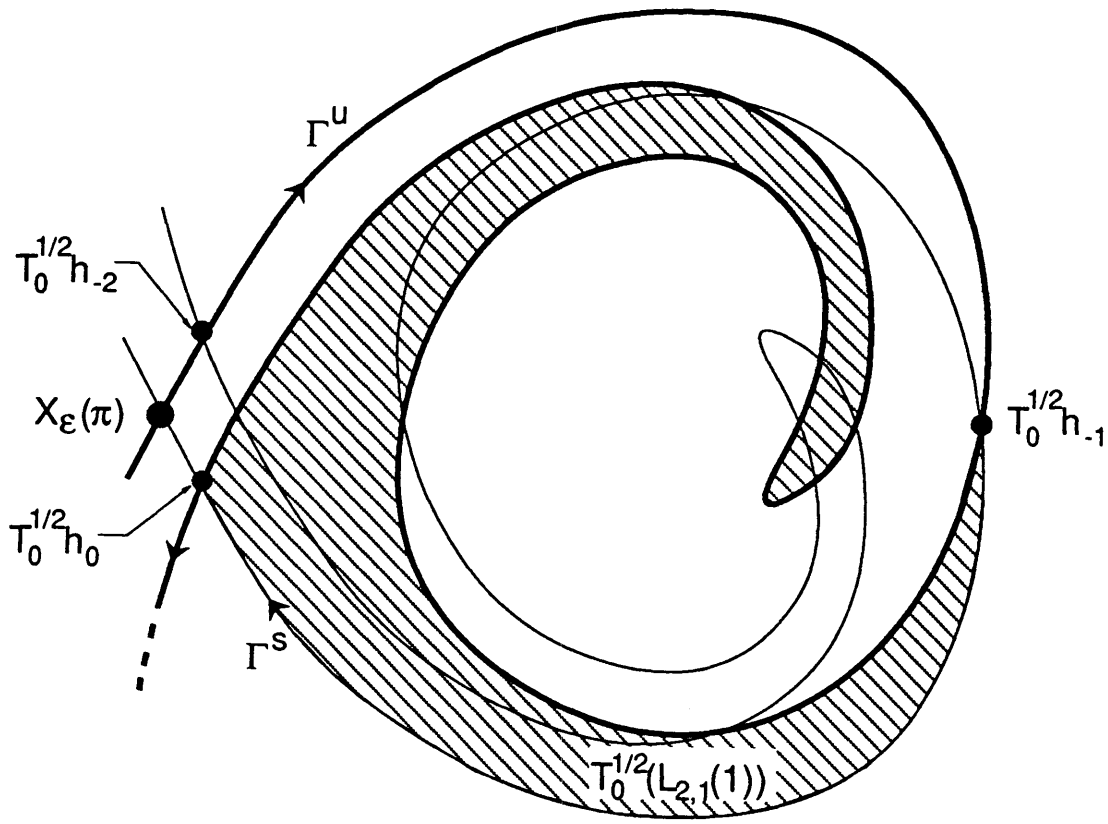

Fig. 2.18.e. Schematic of Fig. 2.18.b. We only show one of the eight spirals inward for clarity.

and the conservation of the areas $\mu(R_i)$ for $i = 1,2,3$:

$$\begin{aligned} \sum_{j=1}^{3} (T_{i,j}(n) - T_{i,j}(n-1)) &= 0 \qquad & i &= 1,2,3 \\ \sum_{i=1}^{3} (T_{i,j}(n) - T_{i,j}(n-1)) &= 0 \qquad & j &= 1,2,3 \end{aligned} \tag{2.9}$$

Illustrating another way in which the structures identified in the previous sections can be used and extending the analysis of the mechanism by which patches of tracer are stretched and folded, the solution to this problem represents the probability that an orbit, initially rotating in the same sense as the casing, changes the direction it is flowing in as a function of the modulation period. To define the problem precisely, we assume that the tracer is uniformly concentrated in R3 initially, *i.e.*, at the slow time $z = 0$. The question we answer, then, is: how much tracer is in R1 at time $z = 2n\pi$ for $n = 1,2,...$? We label this quantity as $T_{3,1}(n)$.

Before proceeding, we must redefine the turnstile lobes to eliminate the intra-turnstile overlap areas $L_{1,2}(1) \cap L_{2,1}(1)$ and $L_{2,3}(1) \cap L_{3,2}(1)$. In particular, we set:

$$\begin{aligned} \tilde{L}_{1,2}(1) &\equiv L_{1,2}(1) \cap \mathrm{R1} \\ \tilde{L}_{2,1}(1) &\equiv L_{2,1}(1) - L_{2,1}(1) \cap L_{1,2}(1) \\ \tilde{L}_{2,3}(1) &\equiv L_{2,3}(1) \cap (\mathrm{R2} \cup \mathrm{R1}) \\ \tilde{L}_{3,2}(1) &\equiv L_{3,2}(1) - L_{3,2}(1) \cap L_{2,3}(1) \end{aligned} \tag{2.10}$$

The excluded parts of the original turnstile lobes, although they get mapped across the inter-regional boundaries during the first half of the modulation period, get mapped back across before the end of the period to the region they were in at the beginning of the period. For example, during every period the fluid in $L_{2,1}(1) \cap L_{1,2}(1)$ gets mapped from R2 into R1 and back again. Therefore, the orbits in these overlapping regions change their orbit type (*i.e.*, rotate in the same sense as the

shaft or the casing, or are in the instantaneous backflow region) an even number of times in each period, and the parts in the redefined lobes do so an odd number of times.

Now, the fact that Γ^S cannot self-intersect implies that $L_{1,2}(1)$ must lie in $L_{2,1}(1)$ and R1, because as soon as it crosses Γ^U between $\mathbf{X}_\epsilon(z_0)$ and h_1 it does so at the pip which defines the boundary of $L_{1,2}(1)$. Thus, the overlap region is large, in fact complete in the limit of $\epsilon \to 0$ as we will see in the next chapter.

In addition, exclusion of the intra-turnstile overlap, which may characterized by saying that we exclude, for example, from $L_{2,1}(1)$ the (large) piece of the lobe $L_{1,2}(1)$ "nested" inside $L_{2,1}(1)$, isolates the long, thin, folded structure of $\tilde{L}_{2,1}(1)$ that gets transported into R1 at the end of each cycle. We now show that it is responsible for continuing the stretching and folding of the lamellar tracer structure discussed in the previous section as z increases from $z = \pi$ to $z = 2\pi$ and in each subsequent period.

$\tilde{L}_{2,1}(1)$ directly transports an amount of fluid equal to $\mu(\tilde{L}_{2,1}(1) \cap \tilde{L}_{3,2}(1))$ from R3 into R1 during each period, where $\mu(L)$ denotes the area of the planar set L. In fact, only the tracer contained in the intersections of $\tilde{L}_{2,1}(1)$ with $T_0^{n-k}\tilde{L}_{3,2}(1)$, for $k = 1, 2, ..., n-1, n$, can enter R1 at the n-th iteration.

However, the intersection $\tilde{L}_{2,1}(1) \cap \tilde{L}_{3,2}(1)$ is only uniformly filled with tracer fluid initially. At later times, the concentration of tracer is not uniform. Furthermore, although the fluid in this and the other intersections is exactly what we need, not all of it is tracer fluid. Thus, the problem requires us not only to identify the flux mechanism, as we have done so far, but also to find a way to determine the content of the lobes.

Fortunately, having redefined the turnstile lobes, we can directly use the transport theory presented in Rom-Kedar and Wiggins [1990b] to determine the lobe

content. The two main quantities we need are the amount of tracer which is in the lobes $\tilde{L}_{2,1}(n)$ and $\tilde{L}_{1,2}(n)$, which we denote by $\tilde{L}^3_{2,1}(n)$ and $\tilde{L}^3_{1,2}(n)$ following the notation of Rom-Kedar and Wiggins [1990a], where the superscript 3 indicates that we are following the tracer which was initially uniformly distributed in R3. For $n > 1$, we find:

$$\begin{aligned}
\mu\left(\tilde{L}^3_{2,1}(n)\right) &= \mu\left(\tilde{L}_{2,1}(1) \cap \tilde{L}_{3,2}(1)\right) \\
&\quad + \sum_{k=1}^{n-1} \left\{ \mu\left(T_0^{k-n} \tilde{L}_{2,1}(1) \cap L_{3,2}(1)\right) - \mu\left(T_0^{k-n} \tilde{L}_{2,1}(1) \cap \tilde{L}_{2,3}(1)\right) \right\} \\
\mu\left(\tilde{L}^3_{1,2}(n)\right) &= \mu\left(\tilde{L}_{1,2}(1) \cap \tilde{L}_{3,2}(1)\right) \\
&\quad + \sum_{k=1}^{n-1} \left\{ \mu\left(T_0^{k-n} \tilde{L}_{1,2}(1) \cap L_{3,2}(1)\right) - \mu\left(T_0^{k-n} \tilde{L}_{1,2}(1) \cap \tilde{L}_{2,3}(1)\right) \right\}
\end{aligned} \tag{2.11}$$

At first glance it may seem that, in addition to redefining the turnstile lobes as we did above, we also must modify the transport theory, because of the fact that part of $\tilde{L}_{2,1}(1)$ lies in R3 and part of $\tilde{L}_{2,3}(1)$ lies in R1. However, the above formulae are exactly the necessary ones because the intersections with $\tilde{L}_{3,2}(1)$ and $\tilde{L}_{2,3}(1)$ are accounted for from the first period onward.

Next, the change in the amount of tracer in R1 at the n-th cycle is

$$T_{3,1}(n) - T_{3,1}(n-1) = \mu\left(\tilde{L}^3_{2,1}(n)\right) - \mu\left(\tilde{L}^3_{1,2}(n)\right). \tag{2.12}$$

Using (2.11), we evaluate the right hand side. Finally, we write a (telescopically-collapsing) sum using the above difference formula to obtain $T_{3,1}(n)$ strictly as a

function of $T_{3,1}(0)$ and the lobe content expressions (2.11):

$$T_{3,1}(n) = T_{3,1}(0) + \sum_{m=1}^{n-1}(n-m)\left\{\mu\left(\tilde{L}_{2,1}(1)\cap T_0^m\tilde{L}_{3,2}(1)\right) - \mu\left(\tilde{L}_{2,1}(1)\cap T_0^m\tilde{L}_{2,3}(1)\right)\right\}. \tag{2.13}$$

Since by assumption all of the tracer is in R3 initially, $T_{3,1}(0)$ is identically zero, and (2.13) reduces to

$$T_{3,1}(n) = \sum_{m=1}^{n-1}(n-m)\left\{\mu\left(\tilde{L}_{2,1}(1)\cap T_0^m\tilde{L}_{3,2}(1)\right) - \mu\left(\tilde{L}_{2,1}(1)\cap T_0^m\tilde{L}_{2,3}(1)\right)\right\}. \tag{2.14}$$

2.3.4. Exponential Stretching of Material Interfaces and Lobes.

One of the most desirable features for good mixing is the creation of a large interface between the regions in which different species lie. In quasi-steady Stokes' flows, it has been shown that material interfaces can be stretched exponentially in time. The very recent work of Muzzio, *et al.*, [1991], for example, presents a systematically-collected set of data quantifying stretching rates for the eccentric journal bearing subject to blinking protocols. Further examples and references may be found in Ottino [1989]. The results reported in these works rely on experimental data and the numerical calculation of Lyapunov exponents. Although the stretching rates obtained from these techniques have been well-correlated to the flow parameters, no theory has been developed to date with the power to predict these rates before an experiment is run or before any Lyapunov exponents are calculated.

In this section we provide such a theory for the stretching of interfaces and lobes in the eccentric journal bearing subject to continuous modulation protocols. Using the notion of Birkhoff signatures and the lobe dynamics theory presented in the previous subsection, we obtain exponentially growing lower bounds on the

stretching rates for both interfaces and lobes. The numerical data we collected from simulations with $\mathcal{O}(10^5)$ points in typical cases agree with our analytical expressions and are reported in Chapter 3.1. Finally, we show theoretically that the rate at which a patch of tracer fluid is stretched asymptotes to some constant rate after the first several periods. The actual stretching rates predicted by our theory for patches in continuously-modulated flows appear to be similar to those reported in Muzzio, *et al.*, [1991] for blinking flows. We discuss reasons for this apparent similarity in Chapter 4. We begin our discussion with interfacial stretching and then derive from the results presented there further results for the rate at which lobes are stretched.

Birkhoff signatures are ideally suited to demonstrating that material interfaces stretch at exponential rates. Relying on the invariance of the stable and unstable manifolds, they represent a compact way to encode the relevant data about homoclinic tangles. We now show how they may be used to yield quantitative information in quasi-steady Stokes' flows.

We begin by illustrating schematically in Figure 2.19 on a simple example how the unstable manifold winds around the stable manifold, forming a homoclinic tangle, as the fixed point, X_ϵ, of the Poincaré map is approached. The segments between the principal intersection points h_0 and h_2 constitute the fundamental pattern, or "basic signature," which gets repeated every iteration of the Poincaré map in the following sense. As we stated in section 2.3.1, pip's get mapped to pip's. In particular, $T_0 h_i = h_{i+2}$ for all $i \in \mathbf{Z}$, where this lower bound is conservative, but rigorous. Now, as we saw in the previous section, the segments of the stable and unstable manifolds between pip's are mapped to the appropriate segments between the forward images of the pip's under the action of the Poincaré map in such a way that the relative ordering of initial conditions stays the same, due to uniqueness of solutions. Therefore, from the basic signature we can obtain a

sequence of signatures which schematically (and topologically) encode the entire tangle. In this example, as we go from h_1 to h_2 along $W^U(X_\epsilon(z_0))$, $U[h_1, h_2]$ arches back toward h_0 and intersects $S[h_0, h_1]$ in two secondary homoclinic points, s_1 and s_2. Because s_1 and s_2 lie on $S[h_0, h_1]$, we know that $s_3 \equiv T_0 s_1$ and $s_4 \equiv T_0 s_2$ are on the segment $S[h_2, h_3]$ and that $U[h_3, h_4]$ intersects $S[h_2, h_3]$ in those two points. Therefore, $U[h_3, h_4]$ must wind around $U[h_1, h_2]$ as sketched in Figure 2.19 because the unstable manifold cannot self-intersect. Following Abraham and Shaw [1989], we refer to the segments of $W^U(X_\epsilon(z_0))$ and $W^S(X_\epsilon(z_0))$ between h_0 and h_4 as the second signature. This fundamental process, *i.e.*, $U[H_{2i+1}, h_{2i+2}]$ intersecting $S[h_{2i}, h_{2i+1}]$ and winding back to h_0 around the previous segments of the unstable manifold (creating higher order homoclinic points), repeats itself for every $i \geq 1$. Furthermore, this process implies that the interface is stretched by a factor of at least twice the length of $U[h_1, h_2]$ each iteration because the pieces of the segments which wind back are at least as long as the "finger" of $U[h_1, h_2]$ arching back. Thus, denoting the length of a segment $U[h_1, h_{1+1}]$ by $l(U[h_1, h_{1+1}])$, we have:

$$l(U[h_{2i+1}, h_{2i+2}]) > 2^i l(U[h_1, h_2]),$$

for all $i \in \mathbf{Z}^+$.

Using the concepts illustrated on this simple example, we now analyze a typical case in the counterrotating eccentric journal bearing. For the parameters $\bar{e} = 0.1$, $\bar{r} = 0.3$, $\epsilon = \frac{2\pi}{40}$, and (MP1), we focus on the tangle formed by $\Lambda^S(X_\epsilon(z_0))$ and $\Lambda^U(X_\epsilon(z_0))$. The basic signature for this tangle shows that $U[h_1, h_2]$ and $S[h_0, h_1]$ intersect in many more (18) secondary homoclinic points. Thus, the long length of these segments gets stretched exponentially in time by the above inequality. This also implies that the length of a lobe (which we define carefully in the next chapter) grows exponentially in time.

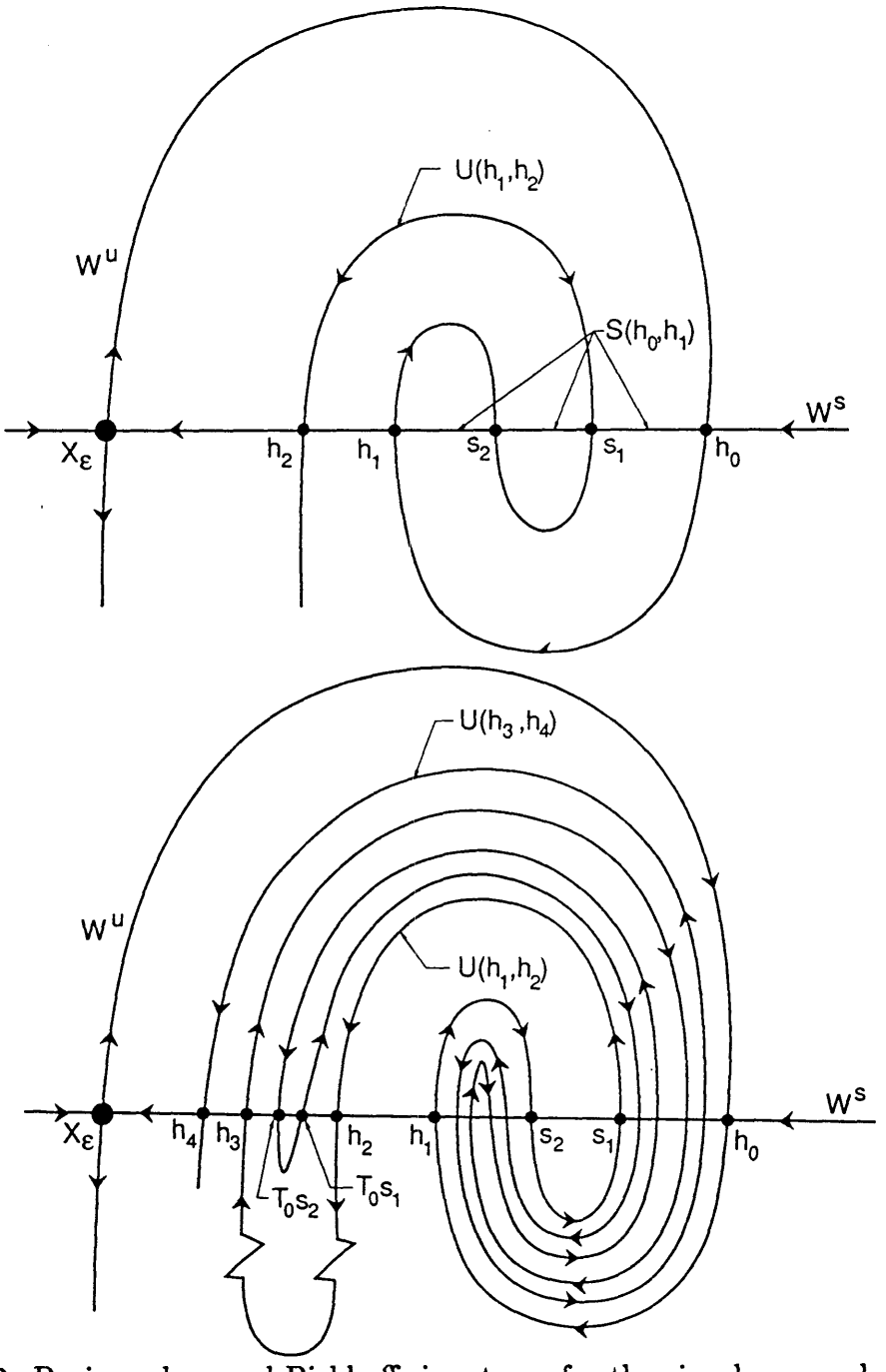

Fig. 2.19. Basic and second Birkhoff signatures for the simple example of section 2.3.4.

We conclude this chapter by observing that all of the results we have obtained about stretching are independent of how small ϵ is. We now turn our attention to further results which are asymptotic for $\epsilon \to 0$.

$\bar{e}$	$\bar{\Omega}$	area of A ($\pm$ 4 $\times 10^{-4}$)
0.1	-1	0.1231
0.1	-2	0.2404
0.1	-10	0.9586
0.1	-20	1.4563
0.1	-60	2.1725
0.3	-2	0.1406
0.3	-10	0.6778
0.5	-0.2	0.0253
0.5	-1	0.0492
0.5	-2	0.0924
0.5	-10	0.4614
0.5	-60	1.1297
0.75	-0.2	0.0121
0.75	-1	0.0261
0.75	-2	0.0497
0.75	-10	0.2205
0.75	-20	0.3205
0.75	-60	0.4483

Table 2.1: Area of region A in the steady state flow domain as a function of $\bar{e}$ and $\bar{\Omega}$. The total area inside the fluid domain is ≈ 2.8588.

$\bar{e}$	$\bar{\Omega}$	area of B ($\pm$ 4 $\times 10^{-4}$)
0.1	-1	0.2774
0.1	-2	0.4716
0.1	-10	0.8777
0.1	-20	0.7909
0.1	-60	0.4477
0.3	-2	0.9752
0.3	-10	1.5529
0.5	-0.2	0.8314
0.5	-1	1.2316
0.5	-2	1.5306
0.5	-10	2.0334
0.5	-60	1.6509
0.75	-0.2	1.8971
0.75	-1	2.0982
0.75	-2	2.2638
0.75	-10	2.5030
0.75	-20	2.4626
0.75	-60	2.3714

Table 2.2: Area of region B in the steady state flow domain as a function of $\bar{e}$ and $\bar{\Omega}$.

$\bar{e}$	$\bar{\Omega}$	area of C ($\pm$ 4 $\times 10^{-4}$)
0.1	-1	2.4584
0.1	-2	2.1468
0.1	-10	1.0225
0.1	-20	0.6117
0.1	-60	0.2386
0.3	-2	1.7431
0.3	-10	0.6282
0.5	-0.2	2.0021
0.5	-1	1.5780
0.5	-2	1.2358
0.5	-10	0.3641
0.5	-60	0.0783
0.75	-0.2	0.9496
0.75	-1	0.7346
0.75	-2	0.5453
0.75	-10	0.1353
0.75	-20	0.0757
0.75	-60	0.0392

Table 2.3: Area of region C in the steady state flow domain as a function of $\bar{e}$ and $\bar{\Omega}$.

$\bar{e}$	protocol	area ($\pm 10^{-3}$)	% of total area
0.1	MP1	1.643	57.5
0.1	MP2	2.007	70.2
0.1	MP3	2.497	87.3
0.3	MP1	1.514	53.0
0.5	MP1	1.150	40.2
0.5	MP3	2.170	75.9
0.75	MP1	0.541	18.9
0.75	MP2	0.656	22.9
0.75	MP3	0.957	33.5

Table 2.4: Area of the potential mixing zone as a function of $\bar{e}$ and the modulation protocol. The area is given both in absolute units and as a percentage of the total fluid domain.

ϵ and $\epsilon^2 \ln^2(1/\epsilon)$		Λ^z layer	Γ^z layer
0.105	0.056	0.050	0.126
0.052	0.024	0.016	0.037
0.035	0.014	0.005	0.027

Table 2.5: Thickness of the layer Σ_ϵ for $\bar{e} = 0.1$ and $\bar{r} = 0.3$, with (MP1).

CHAPTER 3. APPLICATIONS OF ADIABATIC DYNAMICAL SYSTEMS THEORY.

For sufficiently small ϵ, additional quantitative information beyond that which we presented in the previous chapter can be obtained from the theory of adiabatic dynamical systems about the invariant structures responsible for transport and stretching. In this chapter, we give asymptotic ($\epsilon \to 0$) formulae valid for all times (including the short times of most interest in mixing) for the areas and lengths of lobes, the average striation thickness of spiral-shaped tracer patches (which may be thought of as a convective length scale), and the length of material interfaces. The formulae we use are derived for a large class of adiabatic dynamical systems to which our flow belongs in Elskens and Escande [1991], Kaper and Wiggins [1991a] and [1991b], and in Part I of this thesis. In addition, we report the data we obtained from numerical simulations on six different cases. These cases have been chosen so that we can study the effects of all three parameters, $\bar{e}$, $\bar{\Omega}(z)$, and ϵ, on these quantities. We find that the asymptotic-scaling is as predicted in the theory and depends only on ϵ and that the constants in front depend on $\bar{e}$ and the modulation protocol through $\bar{\Omega}(z)$. Furthermore, the data from our numerical simulations show that these formulae are fairly accurate for a wide range of small ϵ, in fact up to $\epsilon = 0.3$ in most cases.

In the second and third parts of this chapter, we discuss the issues of chaos, large integrable looking regions, and islands in these flows.

3.1. Analytical Estimates of Lobe Areas, Lengths, Stretching, and the Average Striation Thickness.

The first tool we need is the adiabatic Melnikov function, $M_A(z)$. It is the coefficient

of the leading order term in an asymptotic series for the distance between the stable and unstable manifolds forming a "same pair" tangle as measured along the normal to the instantaneous stagnation streamlines, see Neishtadt [1975], Robinson [1983], Palmer [1986], and Wiggins [1988]. It is defined in terms of the following integral:

$$M_A(z) \equiv \int_{-\infty}^{\infty} t \cdot \left(\frac{\partial \psi}{\partial x} \frac{\partial^2 \psi}{\partial y \partial z} - \frac{\partial \psi}{\partial y} \frac{\partial^2 \psi}{\partial x \partial z} \right) (x_0^z(t), y_0^z(t); z) dt, \tag{3.1}$$

where $(x_0^z(t), y_0^z(t))$ is an orbit parametrizing the instantaneous stagnation streamline for which the function is being evaluated, either Γ^z or Λ^z. A simple zero of $M_A(z)$ implies that, for ϵ sufficiently small, the two manifolds, Γ^S and Γ^U if $M_A(z)$ is evaluated for Γ^z ($\equiv M_A^\Gamma(z)$) and Λ^S and Λ^U if $M_A(z)$ is evaluated for Λ^z ($\equiv M_A^\Lambda(z)$), intersect each other transversely. Furthermore, for periodic and quasiperiodic systems, one intersection of the manifolds implies that there are infinitely many others, because, as we stated in the previous section, invariance of the manifolds implies that a point on both manifolds must always be on both manifolds.

The theory presented in Kaper and Wiggins [1991a] shows that $M_A^\Gamma(z) = \frac{dA^\Gamma}{dz}(z, z_0)$, where A^Γ is the difference between the areas enclosed by the instantaneous separatrices Γ^z and Γ^{z_0} and z_0 is the zero of $M_A^\Gamma(z)$ corresponding to the nearest intersection and extremal instantaneous separatrix. A similar result holds for $M_A^\Lambda(z)$. Thus, since $\frac{dA}{dz}$ changes sign at the extremal values of z, we know that both $M_A^\Gamma(z)$ and $M_A^\Lambda(z)$ have have periodically spaced simple zeroes for our modulation protocols at $z = 0, \pi \bmod 2\pi$, and hence the intersecting stagnation streaklines form two homoclinic tangles as shown in the figures of the previous chapter. Thus, we have rigorously established the existence of the intersections of the manifolds we obtained numerically in the previous section. We refer the reader to either Wiggins [1988] or Part I of this thesis for an exposition of the adiabatic Melnikov function.

Furthermore, the theory of the adiabatic Melnikov function enables us to show

that all of the pip's h_i and k_i, for $i \in \mathbf{Z}$ except $i = 0$, lie in a small neighborhood, $\mathcal{N}_\epsilon$, whose size depends on ϵ, of $\mathbf{X}_\epsilon(z)$ on the Poincaré section. Since the z–distance between adjacent zeroes of both $M_A^\Gamma(z)$ and $M_A^\Lambda(z)$ is equal to π, we know that in the fast time t, two adjacent pip's are separated from each other by a time-of-flight of $\Delta t = \frac{\pi}{\epsilon}$ along Γ^z and Λ^z, respectively. Thus, on the Poincaré section with $z = 0$, all of the pip's h_i and k_i, for $i \in \mathbf{Z}$, except h_0 and k_0 which lie near the respective reference points on Γ^z and Λ^z, lie exponentially close in time to $\mathbf{X}_\epsilon(z)$ and, hence, in $\mathcal{N}_\epsilon$. This, in turn, implies that the tangles are as shown in the figures from the previous section and that they are very difficult to obtain accurately numerically. We remark that even for values of ϵ as large as $\epsilon = \frac{2\pi}{20} \approx 0.314$, the time-of-flight is large enough so that all of the pip's but h_0 and k_0 lie in $\mathcal{N}_\epsilon$.

Finally, *a propos* the first result we use, we remark that one can rewrite (3.1) in a computationally more convenient manner, as is shown in Kaper and Wiggins [1991], as

$$M_A(z) = \int_{-\infty}^{\infty} \left(\frac{\partial H}{\partial z}|_{\Gamma}(z) - \frac{\partial H}{\partial z}|_{\mathbf{x}_0^z} \right) dt. \tag{3.2}$$

Using this form, one can see that the adiabatic Melnikov functions for both separatrices have simple zeroes at $z = 0, \pi \mod 2\pi$, because the derivative on Ψ only contains terms proportional to $\sin z$ and hence vanishes there.

The second result we can use is a formula for lobe area. The formula derived in Elskens and Escande [1991] and Kaper and Wiggins [1991a] and [1991b] states that the area of a lobe is given to leading order by the difference between the areas enclosed by the maximum and minimum instantaneous stagnation streamlines that occur during the modulation period. Thus, to leading order the area is an $\mathcal{O}(1)$ quantity as $\epsilon \to 0$, which is strikingly different from the regular perturbation case in which the leading order term is $\mathcal{O}(\epsilon)$ asymptotically. Furthermore, we have shown that the remaining terms in the asymptotic expansion are $\mathcal{O}(\epsilon)$ in Kaper

and Wiggins [1991b].

The data required to determine the $\mathcal{O}(1)$ contributions to the lobe areas for our flows may be read off from the tables given in Chapter 2. To be precise, the leading order term in the asymptotic expansion for the area of $L_{2,1}(1)$ and all of the other lobes in the Γ-tangle is the difference between the maximum and minimum areas of region A attained during the given protocol, see Table 2.1. Similarly, the leading order term in the asymptotic expansion for the area of $L_{3,2}(1)$ and all of the other lobes in the Λ-tangle is the difference between the maximum and minimum areas of region C attained during the given protocol, see Table 2.3. In Kaper and Wiggins [1991a], we prove that the remaining terms in the asymptotic expansion for the lobe area are $\mathcal{O}(\epsilon)$.

We also computed the areas of the lobes in our numerical simulations. The data are reported in Table 3.1 for various values of ϵ in the case of a typical geometry and protocol. Finally, the integral of $M_A(z)$ between two of its adjacent simple zeroes gives the same result as the leading order term for the lobe area, see Kaper and Wiggins [1991a]. We have used this property to verify the correctness of our computations of $M_A^\Gamma(z)$ and $M_A^\Lambda(z)$.

Finally, our lobe area result leads to some thoughts about achieving mixing in the mathematical sense of the word. Let $\mu/\mu(R1 \cup R2 \cup R3)$ be the normalized invariant measure in the mixing zone. If

$$\lim_{n\to\infty} \frac{\mu(\mathcal{M} \cap F^n\mathcal{N})}{\mu(R1 \cup R2 \cup R3)} = \frac{\mu(\mathcal{M})\mu(\mathcal{N})}{\mu(R1 \cup R2 \cup R3)^2}$$

for any two sets $\mathcal{M}$ and $\mathcal{N}$ in this domain, then F is said to be strong-mixing. Although we cannot establish this for any $\mathcal{M}$ and $\mathcal{N}$, our lobe area result does let us establish it for the (trivial, as shall become apparent) case in which the only sets are the two pairs of turnstile lobes (or their images), one pair from each tangle.

This statement follows from the fact that in the limit of $\epsilon \to 0$, the union of one lobe from the Λ and Γ tangles has the same area as the mixing zone. That is, we have the right to set $\mu(R1 \cup R2 \cup R3) = 1$ and the quantities in the numerator are one as well so that the equality is satisfied. We remark that all quantities are computed in the limit $\epsilon \to 0$. Hence it is not necessary to interchange limits.

Shape of turnstile lobes.

Given that we know the lobe area, we now determine the shape of the first turnstile lobes and then those of all of their images. Independently of our lobe area result but essential in their own derivation of that result, Elskens and Escande [1991] derived a result for the lengths of turnstile lobes which in the context of our flows implies that the lengths of the two turnstile lobes $L_{2,1}(1)$ and $L_{3,2}(1)$ are $\mathcal{O}(\frac{1}{\epsilon})$ as $\epsilon \to 0$ to leading order. Here, we measure the length from the midpoint of the base segment, $U[\mathbf{X}_\epsilon(z), h_0]$ and $U[\mathbf{X}_\epsilon(z), k_0]$, repsectively, of the lobe along the circle intersecting the midpoint and centered in the middle of the casing to the (radial) projection of its "tip" on that circle. This constitutes the measurement of lobe length which corresponds to Elskens and Escande's use of length along the q-axis in the pendulum. The asymptotic scaling depends on ϵ, and the constants in front depend on $\bar{e}$ and the choice of protocol through $\bar{\Omega}(z)$. Thus, since our lobe area result is independent of this length calculation, we also know that the average width of the lobe is $\mathcal{O}(\epsilon)$, as measured along the normal to the segments of Γ^S and Λ^S that define it.

We report the lengths and average widths of the lobes $L_{2,1}(1)$ and $L_{3,2}(1)$ for the six different cases in Tables 3.2 and 3.3. We also see that the initial folds in the boundaries of these two lobes, marked by F^Γ and F^Λ in the figures, move toward $\mathbf{X}_\epsilon(z)$ as ϵ decreases. This behavior shows that the manifolds are making room

for the growing regular zone, which is made up of an increasingly larger number of persistent Arnold tori as $\epsilon \to 0$, in the instantaneous backflow region; see the next section.

Average striation thickness.

The evolution of an arbitrary patch of tracer fluid in the mixing zone is determined completely by the evolution of the set of lobes it is in. In general, any part of the patch in a turnstile lobe gets stretched, folded, and "thinned" by the same amount the lobe does. The same applies to those parts of the patch which are outside of the turnstile lobes. Furthermore, we see that the rates are equal for $n \geq 3$ in most cases.

Quantitatively, the theory predicts that the patch gets stretched by a factor of $\mathcal{O}(\frac{1}{\epsilon})$ in each period of the modulation. In fact, we have shown that the unstable manifold forming the boundary of the lobes grow exponentially in length. Thus, we may estimate that the average striation thickness, which is approximately the average width of the lobes, decreases with time as follows:

$$d_{\text{striation}}(z = 2n\pi + z_0; t = 2n\pi\epsilon) = \mathcal{O}(\epsilon^n) \tag{3.3}$$

for $n \in \mathbb{N}$. In Table 3.4, we report the data for the average striation thickness and the number of folds as a function of the modulation period for the first three-six periods for many (approx 12) cases.

3.2. Chaotic Fluid Particle Motion.

Although chaos is not the primary focus of our study since the stretching and folding in the flow responsible for it have already been quantified using the lobe dynamics and Birkhoff signatures in the previous sections, we state briefly in this section in

what sense the slowly-modulated counterrotating flows exhibit chaotic dynamics. The novel feature these flows possess which has been shown only in the context of a model flow for "whorl-tendril" flows, see Ottino, et al., is that the basic stretching and folding required in the horseshoe construction can occur in one iteration of the Poincaré map. Thus, a horseshoe in these flows can be created in the minimum possible number iterates.

Chaos has been shown to exist in several experimental and numerical studies of quasi-steady Stokes' flows. A partial list of the relevant work includes Aref and Balachandar [1986], Chaiken, *et al.* [1986], Ottino, *et al.* [1988], Ng [1989], as well as the references cited in Ottino [1989]. Subjecting the two-dimensional flow to so-called blinking protocols, these studies either point to the observation of stochastic regions characteristic of near-integrable systems or locate regions that get mapped over themselves as in a horseshoe construction to establish the existence of chaos. Since time-periodicity of the blinking protocols plays an essential facilitating role for chaos, the existence of chaos in continuously, periodically modulated flows, such as the one we study, does not come as a great surprise. However, we can show immediately the Smale horseshoe chaos also exists if the modulation protocols are quasi-periodic in time, because the instantaneous separatrices still sweep out large domains and the manifolds intersect in quasiperiodic flows. Thus, we broaden the class of flows which are chaotic to a wider class than just time-periodic flows.

Wiggins [1988] has established that, in general, the splitting of separatrices in adiabatic dynamical systems implies that the hypotheses of the Smale-Birkhoff Homoclinic Theorem are satisfied and, hence, that these systems, as well as quasiperiodic systems, possess Smale horseshoes. Since the flow in the counterrotating eccentric journal bearing subject to the modulation protocols (MP1) – (MP3) has two intertwined homoclinic tangles, we conclude directly from the Smale-Birkhoff Ho-

moclinic Theorem that horseshoes, *i.e.*, sets of initial conditions of measure zero on which the motion is chaotic, exist. Among the possible horseshoe constructions, we find that there are two types of horseshoes, one created by each of the tangles individually, *i.e.*, $\Gamma^S(X_\epsilon(z_0))$ with $\Gamma^U(X_\epsilon(z_0))$ and $\Lambda^S(X_\epsilon(z_0))$ with $\Lambda^U(X_\epsilon(z_0))$, which we refer to as "same pair" horseshoes, and the other by the transverse intersections of "mixed pairs" of manifolds, *i.e.*, $\Gamma^S(X_\epsilon(z_0))$ with $\Lambda^U(X_\epsilon(z_0))$ or $\Lambda^S(X_\epsilon(z_0))$ with $\Gamma^U(X_\epsilon(z_0))$, which are of particular interest. We discuss these briefly below. Figure 4.4 in Part I illustrates the formation of a horseshoe in one period of the Poincaré map. It applies to the "same pair" Γ-tangle, in addition to the Hastings and McLeod problem, because the set S used and the lobes it lies in are topologically equivalent.

The figure also illustrates how the stretching and folding required in order to have a horseshoe map occurs in one iterate of the Poincaré map. It was obtained by looking for a four-sided domain containing segments of Γ^S and Γ^U such that the forward image contains a long segment of Γ^U and overlaps the original domain in two disjoint regions due to the constraints placed on the evolution of the boundary of the region by its touching the manifolds.

The utility of chaos for quantitative purposes in the study of macroscopic transport properties is unclear, however, since we have already obtained quantitative information about the structures responsible for the stretching and transport from the lobe dynamics and the Birkhoff signature theory in the previous sections, and it is precisely that stretching and folding type transport which is responsible for the formation of the horseshoes. Certainly the existence of chaos indicates that time-periodic modulation enhances transport. For example, "same pair" horseshoes contain orbits which are transported between a pair of adjacent regions in the mixing zone, and "mixed pair" horseshoes have orbits which hop between R1 and R3. In addition, despite the fact that the set of initial conditions given by the

horseshoe construction which exhibit chaotic motion is of measure zero, this set appears to influence the dynamics of nearby initial conditions and causes them to exhibit chaotic-like behavior.

We conclude this section with two remarks. First, one can show that a single iterate of the Poincaré map suffices to create a horseshoe map in many adiabatic dynamical systems and hence also in different quasi-steady Stokes' flows, see Kaper and Wiggins [1991a]. Second, the theory presented in Wiggins [1988] also enables one to prove the existence of chaos in quasi-periodically modulated Stokes' flows.

3.3. Regular Zones and Islands.

In some areas of the fluid domain, the flow looks highly regular (or integrable). The main two regular zones lie adjacent to the cylinders, one attached to the inside of the casing and the other attached to the outside of the shaft, and as we have seen in Chapter 2.2, for ϵ small enough, there can be a regular zone inside the instantaneous backflow region, as well. The boundaries of these zones are the outermost invariant Arnold tori of the family of tori which make up these zones, so that together with the mixing zone, the regular zones account for the entire domain of the Poincaré map. In this section we report on some observations concerning regular zones in quasisteady Stokes' flows. We believe that these observations represent the first explanation of the highly-regular appearance of regular zones. At the end of this section, we discuss islands, which are families of invariant tori that look like regular zones, with one twist, the tori are created as resonant responses to the time-periodic modulation in global bifurcations instead of being tori which persist, as those of a regular zone.

Almost all fluid particles in the regular zones execute quasiperiodic orbits. On the Poincaré map, these quasiperiodic orbits lie on closed curves, each closed curve

being the cross-section of an Arnold torus. As we will see below, the exceptional orbits lie in transcendentally narrow, $\mathcal{O}(e^{-\frac{c}{\epsilon}})$ for sufficiently small ϵ (where the constant satisfies $c > 0$), annuli in between these closed curves. The total area occupied by these exceptional orbits is also transcendentally small. Thus, for ϵ small enough, a regular zone looks highly regular. In fact, in the singularly-perturbed case, a regular zone looks much more integrable than a regular zone in the regularly-perturbed case. This difference in appearance arises because in regularly-perturbed systems the regions in between any pair of invariant tori are $\mathcal{O}(\sqrt{\epsilon})$; whereas, as we have just stated, invariant tori occupy all but an area of $\mathcal{O}(e^{-\frac{c}{\epsilon}})$ in singularly-perturbed systems, Large laminar regions of apparently integrable flow have been observed experimentally, but not explained yet, in Stokes' flows subjected to blinking protocols. We predict such regions when continuous, periodic modulation protocols are used and have direct control over the size of these zones via the parameters in our protocols.

For ϵ sufficiently small, these observations about regular zones are direct consequences of adiabatic dynamical systems theory. The specific theory we need consists of Arnold's [1963] extension of the proof of the KAM theorem to adiabatic dynamical systems. The KAM Theorem applies to regularly-perturbed systems derived from a Hamiltonian $H = H_0(p,q) + \delta H_1(p,q,t)$, where $0 < \delta \ll 1$, for which the frequency of the unperturbed periodic orbits satisfies the nondegeneracy condition $\frac{d\omega}{dI}(I) \neq 0$, where ω is the frequency of the unperturbed orbit with action I. It states that many of the periodic orbits of the integrable unperturbed ($\delta = 0$) system persist for sufficiently small δ as tori on which orbits evolve quasiperiodically. Here many means those whose frequencies satisfy a Diophantine condition. The area not occupied by invariant tori is $\mathcal{O}(\sqrt{\epsilon})$. For an exposition of the theory see Arnold [1988].

Adiabatic dynamical systems derived from Hamiltonians of the form $H = H(p, q; z = \epsilon t)$, however, are singularly- perturbed systems. For the orbits which satisfy a nondegeneracy condition, $\frac{d\omega}{dI}(I, z) \neq 0$ for all z, where ω is the frequency of the unperturbed orbit with action I, Arnold introduced a sequence of transformations, including an averaging-based coordinate change, to bring the equations of motion of an adiabatic system into the standard form for KAM theory. Using this transformation, he proved that most of the unperturbed, nondegenerate periodic orbits survive as invariant tori on which orbits evolve quasiperiodically. He quantifies "most" by showing that that part of a regular zone in which there are no tori on the Poincaré section has a total size of $\mathcal{O}(e^{-\frac{c}{\epsilon}})$ as $\epsilon \to 0$ with c a constant satisfying $c > 0$. Since it is possible to carry out the transformations needed in the proof to all orders in the perturbation expansion in ϵ, as long as one stays sufficiently far away from instantaneous separatrices, the result is that exceptional orbits must lie in regions whose size is beyond all orders. We refer the reader to Arnold [1988] for an exposition of this theory.

In addition to the fact that the gaps between tori are exponentially small, the action of an orbit, which is the leading order term of the adiabatic invariant, stays within an $\mathcal{O}(\epsilon)$ interval of its initial value for infinitely long times, see Arnold [1988], and all orbits in regular regions have an adiabatic invariant which is conserved to all orders, Kruskal [1962], on a time scale of length $\mathcal{O}(\frac{1}{\epsilon})$.

Finally, we remark that besides guiding us in formulating the definition of the regular zones, Arnold's theory also motivated our definition of the mixing zone. To leading order, the mixing zone is exactly the part of the fluid domain in which Arnold's theory is not valid. The frequency, $\omega(I, z)$, of unperturbed periodic orbits approaches zero logarithmically as a stagnation streamline is neared. Thus, when the modulation frequency is very small (recall that we are interested in $\omega = \epsilon \ll 1$)

the separation of time scales on which his averaging-based coordinate change depends does not exist anywhere in the region swept out by the stagnation streamlines Γ^z and Λ^z during one period of the modulation, which is exactly the region we have defined as the mixing zone, see Chapter 2.2.

Islands.

We conclude this section with a brief discussion of the islands which exist around elliptic subharmonic periodic orbits. Islands are invariant regions in which fluid particles advect in a regular (integrable) sense. They obstruct the transport and mixing fluid cannot leave or enter them. We apply new results to obtain information about the location and size of islands in this section. Using our modulation protocols, we can chose the frequency of modulation so that we minimize the area in the mixing zone occupied by islands and hence maximize the area in which good stretching and mixing occurs.

Elskens and Escande [1991] have shown that these islands are no bigger than $\mathcal{O}(\epsilon)$. Using different means, we have been able to show that many of the islands are no bigger than $\mathcal{O}(\epsilon^2)$, see Chapter 5 of Part I of this thesis. Since the results presented there apply to this flow, we briefly discuss the relevant features.

From a typical plot of the periods of the steady-state orbits versus the point at which they intersect the x-axis in the wide part of the annular gap in the bearing, one sees that the period diverges logarithmically to infinity as the stagnation streamlines Γ and Λ are approached. We refer the reader to Figure 3.1 for such plots. Now, the frequency of the orbits is given by 2π divided by the period, so we see that it vanishes logarithmically near either separatrix. Finally, we recall that the modulation frequency satisfies $0 < \epsilon \ll 1$. Thus, the orbits which resonate with the modulation, *i.e.*, those whose natural frequency is some rational multiple

of ϵ, lie very close to the stagnation streamlines. As a result, one must construct matched asymptotic expansions for the resonant subharmonics, as we did in Part I. Then using the same action-theoretic arguments we present there, one can show that the islands about $n:1$ subharmonics are no bigger than $\mathcal{O}(\epsilon^2)$ for all $n \geq 2$. In fact, all of the numerical simulations we performed with $\epsilon < 0.2$ are consistent with this observation.

Finally, we remark that the islands are created in global bifurcations. In the case of $\bar{e} = 0.1$, $\bar{r} = 0.3$, (MP1), there is a global bifurcation between $\epsilon = \frac{2\pi}{30}$ and $\epsilon = \frac{2\pi}{20}$ in which the manifolds Γ^S and Γ^U lose their intersection at the point h_0, see Figure 3.2. This event is correlated with the fact that just below $\epsilon = \frac{2\pi}{20}$, the period of the modulation ($= 20$ in the units in Figure 3.1) first exceeds the minimum period of orbits in the backflow region, see Figure 3.1, and recall that $\Omega_2 = -2$ at $z = 0 \bmod 2\pi$. Now, for this same case, we first see the (small) $2:1$ island when ϵ reaches $\frac{2\pi}{20}$, see Figure 2.9.

Also, these results are asymptotic. For example the $1:1$ island in the case for which $\bar{e} = 0.5$ and (MP1) are used is big for as small an ϵ as $\epsilon = \frac{2\pi}{60}$, see Figure 2.10. Again, there is a global bifurcation below this value of ϵ in which, as one decreases ϵ, a new homoclinic point is created.

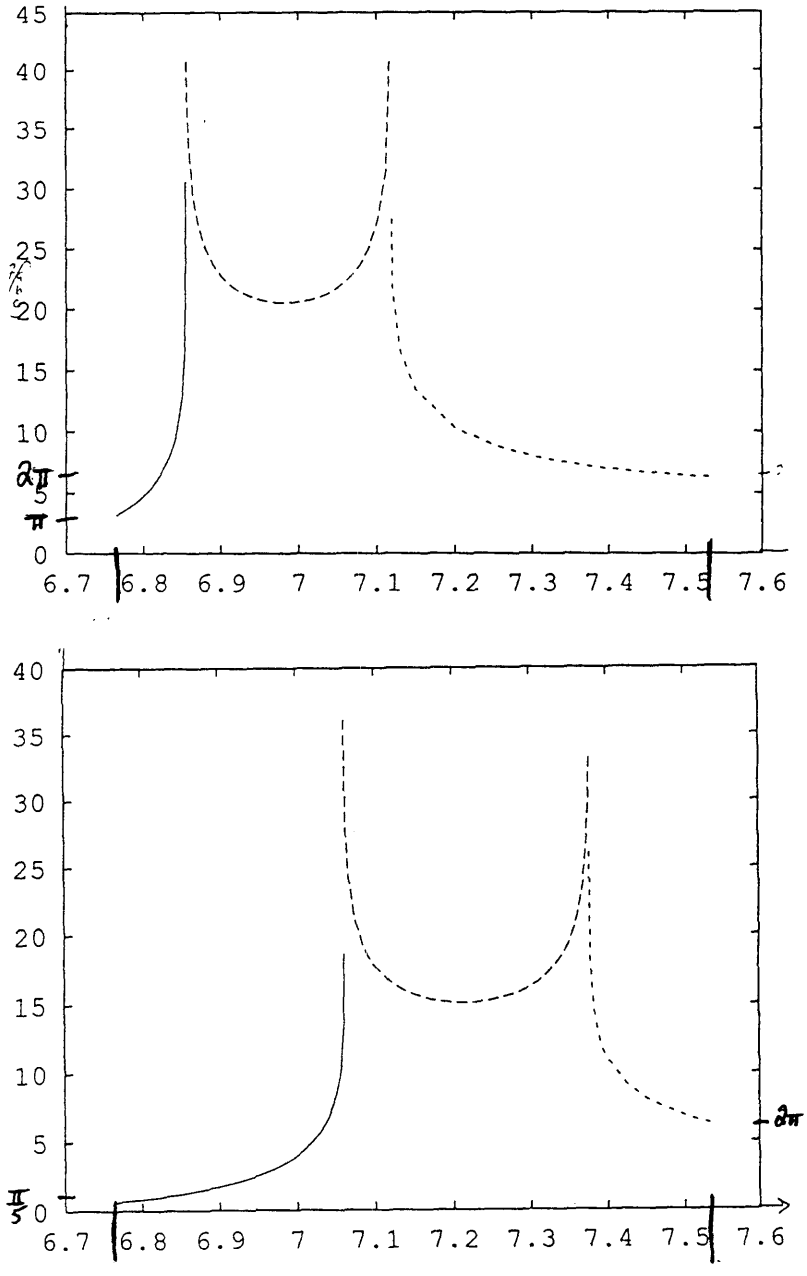

Fig. 3.1. Plots of the period of the steady state periodic orbits along the wide gap between the shaft and the casing. The period goes to infinity logarithmically as the stagnation streamlines Γ and Λ are approached. In Fig a, $\Omega_2 = -2$ and in Fig b, $\Omega_2 = -10$. In both figures, $\bar{e} = 0.1$, $\bar{r} = 0.3$.

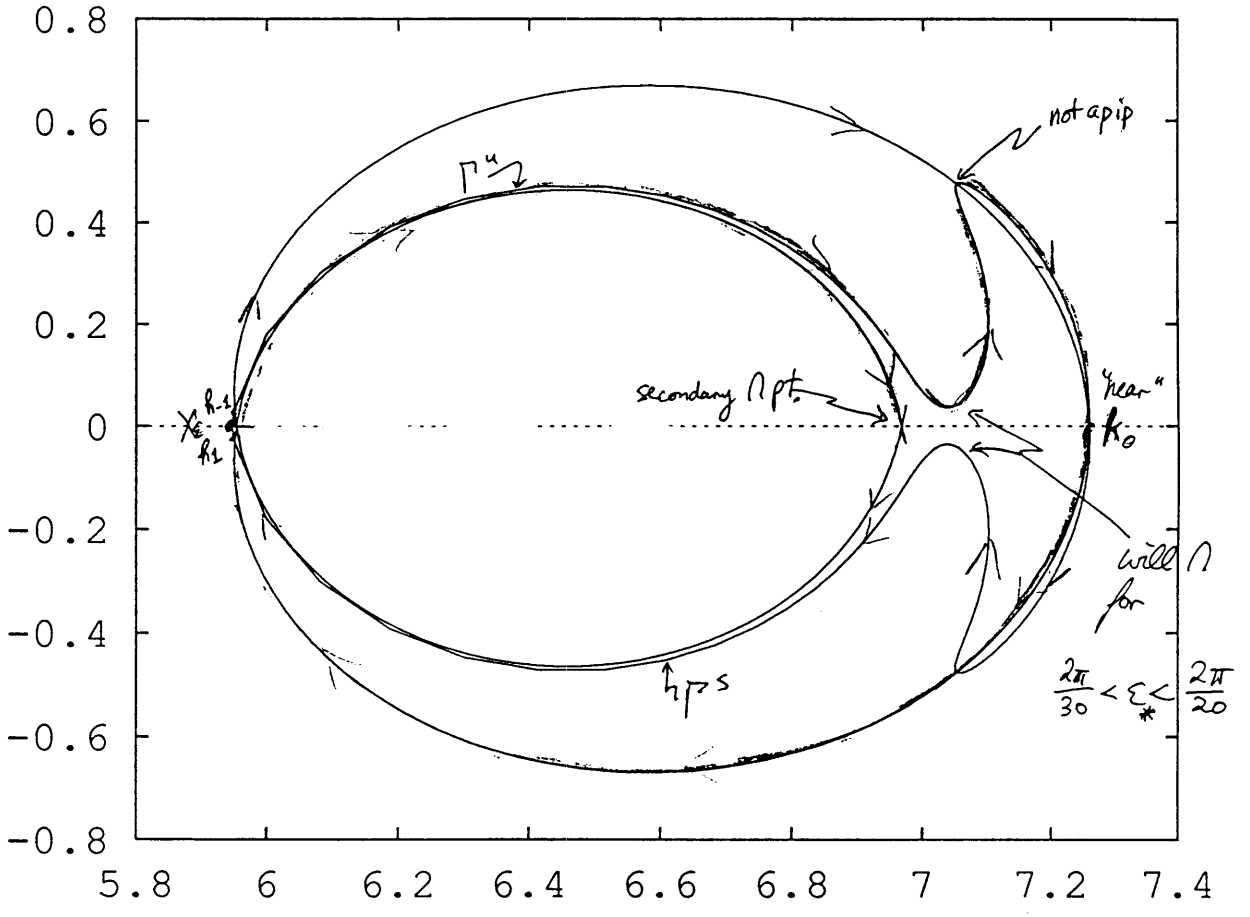

Fig. 3.2. The Γ branches of stable and unstable manifolds of $\mathbf{X}_\epsilon(0)$ for $\epsilon = \frac{2\pi}{20}$. This is just before the global bifurcation, where the modulation period is equal to the minimum backflow orbital period.

CHAPTER 4. ROBUSTNESS OF THE MODEL AND COMPARISON TO EXPERIMENT.

In this chapter, we study several other important topics related to the mixing process discussed in the previous chapters. First, we concentrate on the impact of molecular diffusivity on the results of the purely convective model introduced in Chapter 2. Second, we discuss the robustness of the model under the inclusion of inertial correction terms. Third, we compare our results to some obtained in blinking experiments. Fourth, we prove rigorously that quasi-steady Stokes' flows are adiabatic dynamical systems. Finally, we show how many of our results can be applied to other quasi-steady Stokes' flows of interest; in particular, we show why for many quantities it is not even necessary that we know the stream function for the problem.

4.1. Molecular Diffusion.

In the foregoing sections, we have restricted ourselves to simulating the ideal case in which the transport of tracer particles in the quasisteady Stokes' flow occurs only via convection. We now make our study more realistic and consider also the impact of molecular diffusion in the transport process. In particular, we identify the phenomenon of diffusion-enhanced stretching for the first time in quasi-steady Stokes' flows and explain the mechanism responsible for it. This effect, which may also be characterized as mechanical dispersion induced or facilitated by diffusion, shows that diffusion of tracer particles is important from the beginning of any experiment and has a macroscopic impact on the location of convectively-transported tracer particles, as well as on the rate at which patches of tracer fluid are stretched. The data we obtain from numerical simulations, for which the equations consist of

adding a term representing the Brownian motion a tracer particle experiences due to molecular diffusivity to the Lagrangian equations of motion, see (4.3), agree with the theory we present.

For the treatment of the full problem, we rely on the exposition of the convective-transport theory presented in the previous sections, as well as on a careful analysis of the mechanical dispersion induced by molecular diffusion. We begin, however, with a simple example – diffusion in a local shear flow – to illustrate the idea.

In the absence of diffusion, fluid particles in a local shear flow governed by the stream function $\Psi = \frac{G}{2}y^2$, where G is the magnitude of the shear, are constrained to evolve along the horizontal streamline they start on. Now, diffusion in the vertical, y, direction enables a particle to hop onto different streamlines. Hence, the distance between two tracer particles initially on the same streamline can grow linearly in time. In this way, diffusion induces a mechanical dispersion.

This example, though apparently trivial, illustrates the mechanism that is also at work in the modulated flows we study. To be precise, the diffusion-induced dispersion enhances the stretching that occurs due to convection in the full problem. At any given time, a particle at a point P may be expected to hop radially inward or outward from the instantaneous streamline, S_P, that it lies on with equal probability, because the tangent to S_P divides a local neighborhood, $\mathcal{N}$, of P in two, see Figure 4.1. Furthermore, at any given time, the particle is in a local shear flow, because the frequencies of all instantaneous streamlines satisfy a nondegeneracy condition; namely, the derivative of the frequency with respect to the action is negative along these orbits, so that the instantaneous velocity of particles on the instantaneous streamlines radially outward from S_P is less than that of P, and the instantaneous velocity of particles radially inward is greater than that of P. Thus,

diffusion induces the same type of mechanical dispersion in the full flow as it does in the simple example.

Of course, the details for the full flow are more complicated than we've discussed so far, and simultaneously the effect produced is much more dramatic in the full flow than it is in the regions of local shear. The complications arise due to the fact that the full flow is governed by a spatially non-uniform velocity field which oscillates periodically in time. In particular, oscillation of the instantaneous saddle and the streaklines stagnating on it imply that patches of tracer particles often pass in the vicinity of the instantaneous saddle point. Now, in a local extensional flow, the separation of nearby initial conditions is exponential. Thus, the mechanical dispersion induced by diffusion during the time intervals in which a patch is near the instantaneous saddle is much stronger than that which occurs in a local shear flow.

One may attempt to quantify this dispersion in the following way. Since the stretching of nearby particles is exponential, we know that in a local neighborhood of a point (which can be any point in the flow outside of an exponentially- small in ϵ neighborhood of the saddle) initial conditions on adjacent streamlines are separated exponentially in time at the rate determined by the difference in their individual exponential stretching rates. We study the diffusion normal to the instantaneous streamlines, observing that diffusion along them is less important. Furthermore, for particles in the interior of the patch is not as important as it is for those near the boundaries. Thus, we focus on particles near the spiral-shaped boundaries of the deformed patch we observed in the purely-convective model. Now, for a given time t, the distance a Brownian particle may reasonably be expected to randomly walk in the radial direction is $r_{\text{diff}}(t) = \sqrt{Dt}$. Using this expression and the rate of separation, one can determine the amount of enhanced stretching that a patch

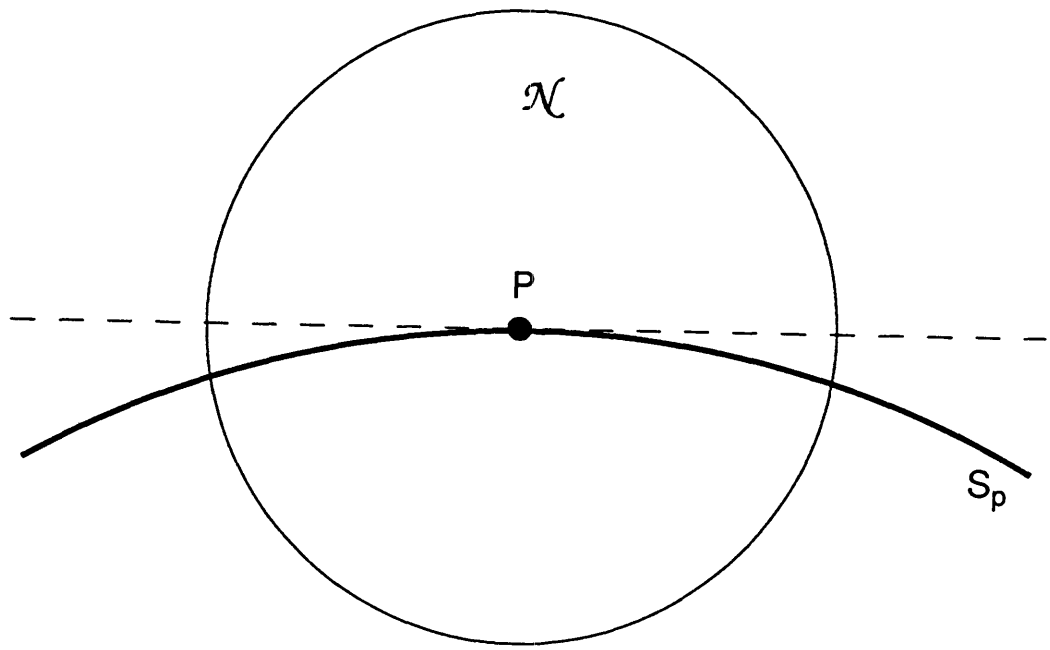

Fig. 4.1. The neighborhood $\mathcal{N}$ used in the diffusion example of Chapter 4.1.

experiences as it deforms due to the radial diffusion of some of the particles inward and outward beyond the spiral-shaped boundaries of the patch obtained from the purely convective model. Rather than develop the detailed expressions necessary for completing this analysis (since the relevant rate constants must be obtained on a case by case basis), however, we conclude this section by discussing the data from the numerical simulations we performed with $\mathcal{O}(10^5)$ points.

Numerical experiments.

In the simulations, we model the effects of molecular diffusivity by adding a term representing the Brownian motion a tracer particle experiences due to molecular diffusivity to the characteristic equations (the purely convective model) of the partial differential equation governing the advection and diffusion of tracer-concentration. In particular, we use a generalized Langevin equation:

$$\begin{aligned} \dot{x} &= \frac{\partial \Psi}{\partial y}(x, y, \epsilon t) + \zeta_1(t) \\ \dot{y} &= -\frac{\partial \Psi}{\partial x}(x, y, \epsilon t) + \zeta_2(t), \end{aligned} \tag{4.1}$$

where Ψ is the stream function given by (2.3) in section 2, and $\zeta_i(t), i = 1, 2$, are random variables drawn from a Gaussian probability distribution characterized by the following correlations:

$$\begin{aligned} &< \zeta_i(t)\zeta_i(t') > = 2D\delta(t - t') \\ &< \zeta_i(t)\zeta_j(t') > = 0. \end{aligned} \tag{4.2}$$

for $i, j = 1, 2$ and $i \neq j$. The factor of 2 arises due to the derivation of the Langevin equation from a Fokker-Planck formalism with coefficient of diffusion D. Furthermore, we refer the reader to Chandrasekhar [1943] for the justification of using a Gaussian for the position distribution of a Brownian particle.

As expected from the discussion in the first part of this section, we find that the amount by which patches are stretched is enhanced significantly due to diffusion. In particular, we find that the "tips" of patches are lengthened by amounts on the order of 5% of the length of the spiral-shaped patch in the first period alone. We report the data for various ϵ and D in a forthcoming paper. Although an effect of small magnitude may seem insignificant at first glance, it is dramatized in subsequent periods because as time goes on, convection will stretch also this extra piece of the deformed patch exponentially.

Furthermore, we find that most of the boundary of a deformed patch remains almost as sharp as they are in the purely convective case. Taking into account that each data point in our numerical simulations represents an infinitesimal area element that gets stretched during the modulation, we find that the deformed patch is as sharp (up to an amount less than ten percent of the width) as the convectively-stretched patch for runs we performed. The exceptions to this are the pieces of the boundary near the "tips" of the patch, which become slightly fuzzier than they are in the purely convective model.

Thus, we have shown that diffusion alters the macroscopic transport properties of the flows by actually increasing the quantities predicted by the purely convective model and that the effects of diffusion must be incorporated into the model from the beginning of the simulation.

4.2. Robustness of the model – Inertial effects.

In our model, we assume that the flow is determined exactly by the solution of the Stokes' equations. The stream function we use is the solution of the biharmonic equation which results from neglecting the inertial terms in the Navier-Stokes equations. We argue now that the results we obtained in the previous sections for the

mixing zone, the rate of stretching, *etc...* in the counterrotating case are the same to leading order for small Re. That is, one would get the same leading order results if one ran an experiment, solved the Navier-Stokes equations numerically, or used a stream function which incorporates inertial corrections as we do from the purely convective model given in Chapter 2.

The essential features of the steady counterrotating flow are the saddle stagnation point, the two streamlines which stagnate on it, and the three families of periodic streamlines bounded by them. We have found these structures in Chapter 2 using the equations of motion with $Re = 0$. For $0 < Re \ll 1$, the position of the saddle and the two stagnation streamlines changes by an amount of $\mathcal{O}(Re)$ from that which we use. The expansion for the position of the saddle taking account the first-order inertial terms performed in Ballal and Rivlin [1976] shows that the y–component of its position changes by an $\mathcal{O}(Re)$ amount whereas the x–component is unaltered from that of $X_0^{z_0}$. Furthermore, the saddle is still connected to itself by two stagnation streamlines (slightly tilted from the position of Γ^{z_0} and Λ^{z_0}) which are level curves of the enhanced stream function, *i.e.*, the stream function obtained when the first correction terms for inertial are included. We refer the reader to Figure 26 in Ballal and Rivlin [1976], for an illustration of the effect of the linear inertial corrections. Thus, although our steady state picture must be slightly tilted (where the direction of the tilt depends on the direction in which the cylinders are rotating), the essential features of the streamline pattern remain unaltered from those of our model, and all of the analysis we performed in the previous sections gives the correct leading order results.

Robustness of the streamline pattern is one of the main reasons we chose the counterrotating case. The flow in the corotating case is more delicate. If $\bar{\Omega} > \bar{\Omega}_{\text{crit}}$, Ballal and Rivlin [1976] showed that there exist two saddle stagnation points in

the corotating connected to each other by four stagnation streamlines (heteroclinic orbits). Although addition of the inertial effects only changes the locations of these two saddle points by an amount of $\mathcal{O}(Re)$ (just as in the counterrotating case), the topography of the level curves of the full streamfunction is changed drastically. In particular, the value of the enhanced streamfunction is no longer the same at the two stagnation points so that they cannot be connected to each other as they are in the $Re = 0$ limit. Instead of having four heteroclinic orbits, one has two homoclinic orbits, one to each saddle. Thus, although the time-periodic modulation should make the corotating flow exhibit good mixing because the two homoclinic orbits break and sweep out a large area, one cannot apply the results from the $Re = 0$ model to the full flow and one needs to perform a detailed analysis based on the enhanced streamfunction instead.

4.3. Comparison to Results from Blinking Experiments.

In the mixing zone, thin, highly stretched and folded ribbons of dyed fluid develop from initial clusters of dyed tracer particles. These ribbons appear to be similar to the whorls and tendrils described in experiments with Stokes' flows subjected to so-called blinking protocols, see Ottino [1989]. Indeed, the basic mechanism for the formation of a long, highly-striated lamellar structure is the fact that some fraction of the patch must pass to one side of the saddle and the remaining fraction must pass to the other side. The difference between these two paths then becomes exagerated due to the underlying convection, which in the case of the blinking protocols is the steady state convection (at all times except at the half-periods) and in the case of modulation protocols is the continuously changing steady state. We remark that one may succinctly summarize the difference between the two protocols by saying that the streamline map gets changed every half-period in the blinking

case whereas in ours it is continuously being changed but by tiny increments each time step.

In addition, many important differences hide behind this semblance of similarity. First and foremost, we take advantage of the fact that the theory of adiabatic dynamical systems gives us a great amount of control over the formation, size, and shape of ribbons when the flow is subjected to continuous modulation protocols. In contrast, it does not appear that the blinking protocols enable one to have *a priori* control over the formation, size, and shape of whorls and tendrils. Quantitative information about the whorls and tendrils seems to be obtainable only after collecting experimental or numerical data.

A more direct comparison (*e.g.* comparing LCEs) might be possible in the counterrotating blinking case. This can be done by considering the blinking protocol as the limit of a sequence of continuous modulation protocols. The Fourier series for a square wave is infinite, so by adding on higher and higher modes to the periodic modulation (with the correct amplitude) on can limit on the blinking case.

It does not appear possible to compare to the blinking case in which only one cylinder spins at a time. For one thing, in the eccentric journal bearing, the position of the stagnation point on the stationary cylinder depends only on the eccentricity of the bearing and is independent of the angular velocity of the spinning cylinder, at least to leading order ($Re = 0$). Since the corrections are $\mathcal{O}(Re)$, the area this creates for mixing is much smaller than that which we studied here.

4.4. Proof of the Statement that Quasi-steady Stokes' Flows Constitute Adiabatic Dynamical Systems.

In this section, we use the definition of an adiabatic dynamical system given in Part I to show rigorously that time-periodic, two-dimensional Stokes' flows constitute

adiabatic dynamical systems. We also make a brief comment about the use of Melnikov theory in these flows and state how the results we obtained in the previous sections for the eccentric journal bearing apply to other quasi-steady Stokes' flows, such as the cavity flow, the two-roll mill apparatus, and a few others.

Recall that we defined an adiabatic dynamical system as a planar Hamiltonian system which depends continuously and periodically on a slowly varying parameter. The Hamiltonian for these systems is $H = H(p, q; z = \epsilon t)$, where p and q are the canonically conjugate momentum and position variables, z is the time-dependent parameter, H depends periodically on z, and the modulation frequency ϵ satisfies $0 < \epsilon \ll 1$. The equations of motion are

$$\begin{aligned} \dot{q} &= \frac{\partial H}{\partial p}(p, q; z) \\ \dot{p} &= -\frac{\partial H}{\partial q}(p, q; z) \\ \dot{z} &= \epsilon . \end{aligned} \tag{4.8}$$

General time-periodic two-dimensional Stokes' flows are adiabatic dynamical systems because they are systems which are exactly of the form (4.8). We demonstrate the validity of this assertion as follows. First, the velocities of fluid particles in these Stokes' flows are given by the vector field

$$\begin{aligned} \dot{x} &= \frac{\partial \psi}{\partial y}(x, y; \omega t) \\ \dot{y} &= -\frac{\partial \psi}{\partial x}(x, y; \omega t), \end{aligned} \tag{4.9}$$

where ψ is the streamfunction (Hamiltonian) which depends periodically on time (with frequency ω), and the two spatial coordinates x and y are the canonically conjugate variables.

Next, we show that the frequency ω must be finite and small. In addition to satisfying the requirement on all Stokes' flows, *i.e.*, that $\mathrm{Re} \equiv \left(\frac{UL}{\nu}\right) \ll 1$, time-periodic

Stokes' flows must also satisfy the following criterion on the Strouhal number:

$$\mathrm{St} \equiv \left(\frac{\omega L}{U}\right) \ll 1, \tag{4.10}$$

where U and L are the characteristic velocity and length scale, respectively, of the flow and depend on the geometry of the flow field at hand. The Strouhal number is an extra dimensionless parameter which arises when U, L, and ω are independent, externally-imposed quantities, as they are in the eccentric journal bearing and many other quasisteady Stokes' flows that arise in practice. Note that the frequency ω is the rate at which the angular velocities, of the casing and the shaft, for example, are modulated and is imposed independently of the characteristic length and velocity in these flows. We refer the reader to Batchelor [1967] p.216 for a discussion of the Strouhal number. Therefore, in flows for which U and L are $\mathcal{O}(1)$ (as they are in the eccentric journal bearing and in the other Stokes' flows mentioned in the introduction), the criterion for the Strouhal number, (4.10), translates into the requirement $\omega \ll 1$. Introducing notation that reminds us of this requirement, we denote the frequency by ϵ so it is clear that we are considering $\epsilon \equiv \omega \ll 1$.

Finally, combining the above arguments, we rewrite (4.9) as:

$$\begin{aligned} \dot{x} &= \frac{\partial \psi}{\partial y}(x, y; z) \\ \dot{y} &= -\frac{\partial \psi}{\partial x}(x, y; z) \\ \dot{z} &= \epsilon, \end{aligned} \tag{4.11}$$

where we have replaced the quantity ϵt in the last slot of ψ by z and added an extra equation $\dot{z} = \epsilon$. Thus, our assertion is established. Once one accepts the validity of the quasisteady Stokes' approximation for describing these flows, adiabatic dynamical systems theory can be used to study them.

The above argument shows, for example, that in the case of the eccentric journal bearing we must modulate the angular velocities continuously and slowly

enough so that the system stays within the quasi-steady Stokes' approximation. When the angular velocities of the cylinders change periodically in time, ψ depends periodically on time. In fact, the angular velocities of the shaft and the casing are functions of the parameter z. We have exploited this formulation of the eccentric journal bearing problem in this work.

Before discussing some other quasi-steady Stokes flows to which our results may be applied, we make two remarks. First, as long as one stays in the quasisteady Stokes' regime, some of the results described in this paper apply also to Stokes' flows in which external parameters are varied nonperiodically in time. Instead of studying modulations in which ψ is forced to vary periodically in time with an $\mathcal{O}(\epsilon)$ frequency, one can consider (with methods similar to those used in this paper) a much more general class of modulations in which ψ is forced to vary merely slowly in time and not necessarily periodically, so that one speaks of the rate of change of z being $\mathcal{O}(\epsilon)$. Many of the techniques which exist for adiabatic systems apply to systems in which the Hamiltonian has general dependence on the parameter z, see Kaper and Wiggins [1991a].

Secondly, when its use can be justified, regular Melnikov function theory, see Guckenheimer and Holmes [1983] for an exposition, is of limited applicability in the study of quasisteady Stokes' flows. The requirement on the Strouhal number (4.10) implies that the modulation frequency must be small, *i.e.* $\mathcal{O}(\epsilon)$, and the interesting case is when the velocity field undergoes $\mathcal{O}(1)$-sized changes during each period of the modulation. Regular Melnikov theory, however, can only treat the case in which the perturbation amplitudes are $\mathcal{O}(\epsilon)$ and requires that the forcing be with $\mathcal{O}(1)$ frequency. In contrast, as we have shown in Chapter 3.1, the adiabatic Melnikov function is ideally suited to studying the interesting phenomena in Stokes' flows.

4.5. Application to Other Interesting Mixing Problems.

The above results may be applied to any system with features commonly found in adiabatic dynamical systems. During the time evolution of the system through one period of the modulation, or through some $\mathcal{O}(1)$ interval as measured in the slow time if the modulation has more general time dependence, $\mathcal{O}(1)$ changes can occur in the vector field. These $\mathcal{O}(1)$ changes include $\mathcal{O}(1)$ changes in the position of a saddle point, $\mathcal{O}(1)$ motions of the stable and unstable manifolds of a hyperbolic orbit, and $\mathcal{O}(1)$ changes in the areas in phase space of regions which are occupied by a given type of orbit.

The two-roll mill is one important application in chemical engineering see for example Ng [1989] and the references given there. In this device, there are two cylinders in a box external to each other. Again, the externally-modulated angular velocities of the two cylinders, both of which occur as terms in the appropriate streamfunction, are functions of the parameter z. The interesting case is when the saddle stagnation point moves back and forth along the entire gap between the two cylinders.

In addition, our method may be applied to systems for which the streamfunction is not known. One merely needs to look at a sequence of steady state flows and find a saddle stagnation point attached to itself or other points, even on a wall, by a stagnation streamline for each flow in the sequence. If the position of that stagnation streamline changes over an $\mathcal{O}(1)$ distance in this family of steady-states, then one can modulate the flow in time as we do, and one will know the leading order terms for the transport quantities just from knowing the peaks and valleys of the modulation protocol. Furthermore, recent work of Rand and Coppola indicates that it may even be possible to get the good mixing when the saddle stagnation

point disappears for part of the modulation, see Coppola and Rand [1991] to appear in *Nonlinear Dynamics.*

Thus, in the case of the cavity flow or geophysical applications, in which the stream function is not known, further analytical results may be possible.

Appendix A.

In this appendix we archive the geometry-dependent constants in the streamfunction Ψ, which are taken directly from Ballal and Rivlin [1976].

$$f_1 = \frac{1}{\Delta}\left(\frac{\bar{\Delta}}{\Delta^*}h_1 h_7 + h_3\right)$$

$$f_2 = \frac{1}{\Delta}\left(\frac{\bar{\Delta}}{\Delta^*}h_2 h_7 + h_4\right)$$

$$f_3 = \frac{1}{\Delta}\left(\frac{\bar{\Delta}}{\Delta^*}h_1 h_8 + h_5\right)$$

$$f_4 = \frac{1}{\Delta}\left(\frac{\bar{\Delta}}{\Delta^*}h_2 h_8 + h_6\right)$$

$$\frac{\Delta^* f_5}{h_1} = \frac{\Delta^* f_6}{h_2} = \cosh(\xi_1 - \xi_2)$$

$$\frac{\Delta^* f_7}{\sinh\xi_2} = \frac{\Delta^* f_8}{\sinh\xi_1} = -\sinh^2(\xi_1 - \xi_2)$$

$$\frac{2\Delta^* f_9}{h_1} = \frac{2\Delta^* f_{10}}{h_2} = -\sinh(\xi_1 + \xi_2)$$

$$\frac{2\Delta^* f_{11}}{h_1} = \frac{2\Delta^* f_{12}}{h_2} = \cosh(\xi_1 + \xi_2)$$

$$\frac{2\Delta^* f_{13}}{h_1} = \frac{2\Delta^* f_{14}}{h_2} = \sinh(\xi_1 - \xi_2) + 2\xi_2\cosh(\xi_1 - \xi_2)$$

Here the constants Δ, $\bar{\Delta}$, Δ^*, and h_i, $i = 1 - 8$ are given by:

$$\Delta = (\xi_1 - \xi_2)^2 - \sinh^2(\xi_1 - \xi_2) < 0$$

$$\bar{\Delta} = (\xi_1 - \xi_2)\cosh(\xi_1 - \xi_2) - \sinh(\xi_1 - \xi_2) > 0$$

$$\Delta^* = \sinh(\xi_1 - \xi_2)\left(2\sinh\xi_1\sinh\xi_2\sinh(\xi_1 - \xi_2) - (\xi_1 - \xi_2)(\sinh^2\xi_1 + \sinh^2\xi_2)\right)$$

$$h_1 = (\xi_1 - \xi_2)\sinh\xi_1 - \sinh\xi_2\sinh(\xi_1 - \xi_2) > 0$$

$$h_2 = -(\xi_1 - \xi_2)\sinh\xi_2 + \sinh\xi_1\sinh(\xi_1 - \xi_2) > 0$$

$$h_3 = \xi_1\sinh\xi_2\sinh(\xi_1 - \xi_2) - \xi_2(\xi_1 - \xi_2)\sinh\xi_1 > 0$$

$$h_4 = -\xi_2 \sinh\xi_1 \sinh(\xi_1 - \xi_2) + \xi_1(\xi_1 - \xi_2)\sinh\xi_2$$

$$h_5 = -\xi_1 \cosh\xi_2 \sinh(\xi_1 - \xi_2) + \xi_2(\xi_1 - \xi_2)\cosh\xi_1$$

$$h_6 = \xi_2 \cosh\xi_1 \sinh(\xi_1 - \xi_2) - \xi_1(\xi_1 - \xi_2)\cosh\xi_2$$

$$h_7 = \sinh\xi_2 \cosh\xi_1 \sinh(\xi_1 - \xi_2) + \frac{1}{2}\xi_1 \sinh 2\xi_2 - \frac{1}{2}\xi_2 \sinh 2\xi_1 - (\xi_1 - \xi_2)\xi_2 > 0$$

$$h_8 = -\cosh\xi_1 \cosh\xi_2 \sinh(\xi_1 - \xi_2) + \xi_2 \cosh^2\xi_1 - \xi_1 \cosh^2\xi_2$$

Appendix B. In this appendix we derive the asymptotic expansion of the position of the saddle fixed point on the Poincaré map. First, we rewrite the equations of motion for the fluid particles in terms of the slow time z:

$$\begin{aligned} \epsilon x' &= f_1(x,y,z) \\ \epsilon y' &= f_2(x,y,z), \end{aligned} \tag{B.1}$$

where $f_1 = \frac{\partial \psi}{\partial y}$, $f_2 = -\frac{\partial \psi}{\partial x}$, and $'$ denotes the derivative with respect to z. Next, we expand about the location of the saddle stagnation point in the steady state case, $(x_0(z), y_0(z))$:

$$\begin{aligned} x(z) &= x_0(z) + \epsilon x_1(z) + \cdots \\ y(z) &= y_0(z) + \epsilon y_1(z) + \cdots. \end{aligned} \tag{B.2}$$

Thus,

$$\begin{aligned} \epsilon x_0' + \epsilon^2 x_1' + \cdots &= f_1(x_0,y_0,z) + \epsilon \frac{df_1}{dx} x_1 + \epsilon \frac{df_1}{dy} y_1 + \mathcal{O}(\epsilon^2) \\ \epsilon y_0' + \epsilon^2 y_1' + \cdots &= f_2(x_0,y_0,z) + \epsilon \frac{df_2}{dx} x_1 + \epsilon \frac{df_2}{dy} y_1 + \mathcal{O}(\epsilon^2). \end{aligned}$$

Now, we equate the terms of like powers in ϵ. First, the $\mathcal{O}(1)$ terms give us the steady state stagnation point $(x_0(z), 0)$, because $f_i(x_0(z), 0, z) \equiv 0$ for $i = 1, 2$ and for all z. Balancing the $\mathcal{O}(\epsilon)$ terms leads to:

$$\begin{aligned} \frac{df_1}{dx}(x_0(z),0,z) + \frac{df_1}{dy}(x_0(z),0,z) y_1(z) &= x_0'(z) \\ \frac{df_2}{dx}(x_0(z),0,z) + \frac{df_2}{dy}(x_0(z),0,z) y_1(z) &= y_0'(z) \equiv 0. \end{aligned} \tag{B.3}$$

Thus, for all z, except $z = 0 \bmod \pi$, $y_1(z)$ is nonzero. In particular, we find $x_1(0) = 0$ because $x_0'(0) = 0$. Consequently, $y_1(0) = 0$. Further expanding the f_i and realizing that $x_1(0) = y_1(0) = 0$, the $\mathcal{O}(\epsilon^2)$ terms yield:

$$\begin{aligned} x_2 \frac{df_1}{dx} + y_2 \frac{df_1}{dy} &= x_1' \\ x_2 \frac{df_2}{dx} + y_2 \frac{df_2}{dy} &= y_1'. \end{aligned} \tag{B.4}$$

Inverting this system and computing x_1' and y_1' from the solution of (B.3) for general z, we get

$$\begin{aligned} x_2(0) &= \frac{x_0''}{[\det A]^2}\left(\frac{df_2}{dy}^2 + \frac{df_1}{dy}\frac{df_2}{dx}\right) \\ y_2(0) &= -\frac{df_2}{dx}\frac{x_0''}{[\det A]^2}\left(\frac{df_1}{dx} + \frac{df_2}{dy}\right), \end{aligned} \tag{B.5}$$

where A is the 2×2 matrix with entries $a_{11} = \frac{df_2}{dy}$, $a_{12} = -\frac{df_1}{dy}$, $a_{21} = -\frac{df_2}{dx}$, and $a_{22} = \frac{df_1}{dx}$. But, the vector field is divergence-free and hence $y_2(0) = 0$. Proceeding along these same lines, we get:

$$\begin{aligned} x(z) &= x_0(z) + \mathcal{O}(\epsilon^2) \\ y(z) &= 0. \end{aligned} \tag{B.6}$$

Thus one gets the result expected due to the symmetry.

REFERENCES.

Abraham, R.H., and Shaw, C.D., 1985, *Dynamics- The Geometry of Behavior*, Aerial Press, Santa Cruz.

Aref, H. 1984, Stirring by Chaotic Advection, *JFM*, **143**, 1-21.

Aref, H. and Balachandar,S., 1986, Chaotic Advection in a Stokes Flow, *Physics of Fluids*, **29**, no.11, 3515-3521.

Aref, H. and Jones,S., 1989, Enhanced separation of diffusing particles by chaotic advection, *Physics of Fluids A*, 1, no.3, 470-474.

Arnold,V.I., 1963, Small Denominators II. *Russian Math Surveys*, **18**, no.5, 9-35.

Arnold,V.I., 1988, Enc Math Sci, Vol. II *Dynamical Systems*, Springer.

Ballal, B.Y., and Rivlin, R.S., 1976, *Arch rat Mech Anal*, 237-294.

Batchelor, G.K., 1967, *An introduction to fluid dynamics*, Cambridge U. Press.

Camassa, R.A., and Wiggins, S., 1991, to appear in *Phys Rev A*.

Cary,J.R.,Escande,D.F., Tennyson,J., 1986, Adiabatic Invariant Change Due to Separatrix Crossing, *Physical Review A*, **34**, no.5, 4256-4275.

Cary,J.R., Skodje,R.T., 1989, *Physica D*, **39** 287.

Chaiken,J., et al, 1987, Lagrangian Turbulence and Spatial Complexity in a Stokes Flow,*Physics of Fluids*, **30**, no.3, 687-699.

Chaiken,J., *et al.*, 1986, Experimental Study of Lagrangian Turbulence in a Stokes Flow, *Proceedings of the Royal Society*, Series A, **408**, 165-174.

Chandrasekhar, S., 1943, Stochastic problems in physics and astronomy, *Rev Mod Phys*, **15**, no.1, 1-89.

Chien,W.-L., Rising,H., Ottino,J.M., 1986, Laminar Mixing and Chaotic Mixing in Several Cavity Flows, *JFM*, 170, 355-377.

Coppola, V.T., and Rand, R.H., 1991, to appear in *Nonlinear Dynamics*.

Elskens, Y. and Escande, D., 1991, to appear in *Nonlinearity.*

Kaper,T.J., and Wiggins,S., 1991a, Lobe Area in in Adiabatic Hamiltonian Systems, to appear in *Physica D.*

Kaper,T.J., and Wiggins,S., 1991b, *On the structure of separatrix-swept regions in slowly-modulated Hamiltonian systems*, submitted to *Differential and Integral Equations.*

Kaper,T.J., Leal,L.G., 1990, Steady Stokes' Flow External to Two Rotating Cylinders, in preparation.

Kaper,T.J., Wiggins, S., 1989, paper to appear in the Proceedings of the Annual ASME/ASCE Mechanics Conference, La Jolla.

Lichtenberg and Liebermann, *Regular and Stochastic Motion* 1st ed., Springer, 1983.

Meiss,J.D., MacKay,R.S., Percival,I.C., 1984, Transport in Hamiltonian Systems, *Physica D*,**13D** , 55-81.

Muzzio, F.J., Ottino, J.M., Swanson, P.D., 1991, *Physics of Fluids A*, **3**, no.5, 822-834.

Ng, Ricky, 1989, Caltech PhD Thesis.

Ottino,J.M., 1988, Chaos in Deterministic Systems: Strange Attractors, Turbulence, and Applications in Chemical Engineering, *Chem Eng Sci*, **43**, No.2, 1988, 139-183.

Ottino,J.M., 1989, *The kinematics of mixing: stretching, chaos, and transport*, Cambridge U. Press.

Rom-Kedar,V., Leonard,A., and Wiggins,S., 1990a An Analytical Study of the Transport, Mixing and Chaos in an Unsteady Vortical Flow, *Journal of Fluid Mechanics*, **214**, 347-394.

Rom-Kedar,V., Wiggins, S., 1990b, Transport in Two-Dimensional Maps, *Archive for Rational Mechanics and Analysis*, **109**, 239-298.

Swanson, P., Ottino, J.M., 1990, submitted to *JFM*.

Wiggins,S.,*Global Bifurcations and Chaos: Analytical Methods*, 1st ed., Springer Verlag, 1988a.

Wiggins,S., 1988b, On the Detection and Dynamical Consequences of Orbits Homoclinic to Hyperbolic Periodic Orbits and Normally Hyperbolic Invariant Tori in a Class of Ordinary Differential Equations, *SIAM Journal of Applied Math*, **48**,no. 2, 262-285.

Wiggins,S., 1988c, Adiabatic Chaos, ***Physics Letters A***, **128**, no.6-7, 339-342.

Wiggins, S., 1991, book on tranport theory to appear in the Springer applied math series.